Hybrid polymer/silicon materials for thermoelectric applications

Geoffrey Prunet

université de BORDEAUX

THÈSE PRÉSENTÉE

POUR OBTENIR LE GRADE DE

DOCTEUR DE

L'UNIVERSITÉ DE BORDEAUX

ÉCOLE DOCTORALE DES SCIENCES CHIMIQUES

SPÉCIALITÉ : Polymères

Par Geoffrey PRUNET

Hybrid polymer/silicon materials for thermoelectric application

Matériaux polymères/silicium hybrides pour des applications thermoélectriques

---

Sous la direction de : Prof. Georges HADZIIOANNOU et Dr Éric CLOUTET

Soutenue le 8 Novembre 2019

Membres du jury :

Prof. MAGLIONE Mario, ICMCB, Université de Bordeaux	Président
Dr HEBERT Sylvie, CRISMAT, Université de Caen	Rapportrice
Prof. MÜLLER Christian, Chalmers University of Technology, Sweden	Rapporteur
Dr SÉGUY Isabelle, LAAS-CNRS, Toulouse	Examinatrice
Prof. DILHAIRE Stefan, LOMA, Université de Bordeaux	Invité
Prof. HADZIIOANNOU Georges, LCPO, Université de Bordeaux	Directeur de thèse
Dr CLOUTET Eric, LCPO, Université de Bordeaux	Directeur de thèse

“If you want to find the secrets of the universe, think in terms of energy, frequency and vibration.”
— Nikola Tesla

Acknowledgments – Remerciements

I would like to thank all the committee members: Prof. Mario Maglione, Dr Sylvie Hébert, Prof. Chrisitian Müller, Dr Isabelle Séguy, Prof. Stéfan Dilhaire, Dr Eric Cloutet and Prof. Georges Hadziioannou for agreeing to judge this work.

Je tiens à remercier mes deux directeurs de thèse, Prof. Georges Hadziioannou et Dr Eric Cloutet pour m'avoir laissé l'opportunité de travailler sur ce sujet. Leur confiance à mon égard, à travers l'autonomie qu'ils m'ont offert, m'a permis de m'épanouir et de réussir à mener à bien ce projet. Je leur suis vraiment reconnaissant des savoirs et de la rigueur scientifique qu'ils m'ont transmis. Leur passion des polymères dans le domaine de l'électronique organique a su déteindre sur moi.

Je remercie ensuite mes encadrants « non officiels » comme je les nomme, Dr Guillaume Fleury, Dr Eleni Pavlopoulou, Dr Stéphane Grauby et Prof. Stefan Dilhaire. Guillaume, tu as su apporter ta rigueur au projet, collaborer avec toi m'a grandement aidé et je t'en remercie. Eleni, je te remercie pour toute ton aide, ta porte a toujours été ouverte quand j'en ai eu besoin. Stéphane et Stéfan, votre amour de la mesure bien faite a permis de valider ces travaux. Votre aide à travers nos réunions au LOMA m'a permis de mieux appréhender le sujet et de me remettre en question pour mieux avancer.

Merci également aux autres permanents du LCPO – B8. Cyril Brochon, pour ta bonne humeur et toutes tes anecdotes ! Gilles, pour toute ton aide en salle blanche, ta camaraderie et nos superbes « discussions ». Mélanie, pour avoir su me garder en vie dans le laboratoire. Ellena, pour ta bonne humeur et la super gestion de nos missions et autres ! Enfin Aude, pour toute ton aide, ta présence a été essentielle et a grandement facilité le déroulement de ma thèse.

Merci aux Prof. Mats Fahlman et Prof. Samson Jenekhe pour leurs collaborations. Merci également Elorprinttec pour m'avoir permis l'accès à leur infrastructure, l'équipement disponible au sein de cette salle blanche a grandement contribué aux résultats et à la compréhension de ce projet.

Je tenais à remercier tous les B8ters, 300 pages supplémentaires ne suffirait pas pour tous vous remercier. Tous les bons moments passés ensemble resteront gravés en moi. J'espère pouvoir continuer à vous voir, au travail ou en dehors.

Big up au Bu3-West. Florent, malgré le peu de temps passé ensemble, j'ai grandement apprécié ton sérieux et tes connaissances sur le thermoélectrique, continue d'améliorer ton humour, tu es presque à mon niveau. Daniele, ta bonne humeur et ton extravagance me manqueront. Camille, la plus vieille rescapée du bureau, ton grain de folie a rendu cette thèse inoubliable, nos ateliers du Vendredi me manqueront, vive le « photovoltaïme et le thermoélectrisme ». Enfin Solène, mon binôme de thermoélectricité, tu as grandement contribué à la réussite de cette thèse, ta présence m'a grandement aidé, tu es sans conteste l'âme du B8. Je suis certain que toute les portes s'ouvriront pour toi au vue de ton implication et de ton sérieux, Keep Calm and become Doctor Soso.

Merci aux membres de la soupe de Lotus ! Antoine, tes mollets musclés et ton fair-play auront été un plaisir. Florian, ton amour ouvert de la culture geek et des moustaches épaisses m'auront permis de ne pas passer pour un extra-terrestre au laboratoire.

Mille merci à mes deux stagiaires pour leur travail et leur implication dans nos projets communs. Amine, tes cornes de gazelles et ton humour auront illuminé mes journées. Etienne, sans toi cette thèse n'aurait pas été aussi aboutie, tes résultats sur les polymères de type p & n m'auront plus qu'aidé. J'ai grandement apprécié ton sérieux et ta rigueur. Partager des passions communes aura rendu cette aventure encore plus plaisante. C'est sans le moindre doute que tu trouveras rapidement un poste.

Merci à mes amis, pour leur confiance et leur présence dans cette aventure.

Merci à ma famille, pour m'avoir soutenu et porté si loin. Je ne saurais comment décrire ma gratitude envers vous.

Pour finir, je remercie ma femme, Emilie. Je ne serais pas devenu le Docteur et l'homme que je suis sans son amour, son soutien et sa patience. Tu auras été ma lumière dans mes moments de doute. Tu es mon passé, mon présent et mon avenir. Jag älskar dig – 10.08.2019.

List of abbreviations

ACN	Acetronitrile
AFM	Atomic force microscopy
Ag	Silver
$AgNO_3$	Silver nitrate
AOB	Acridine orange base dye
AsF_5	Arsenic pentafluoride
Au	Gold
BBL	Polybenzimidazobenzophenanthroline
BBT	Benzobisthiadiazole
BCP	Block copolymers
BDT	Benzo[1,2-b:4,5-b′]-dithiophene
Bi_2Te_3	Bismuth Telluride
BTFMSI	Bis(trifluoromethylsulfonyl)imide
C_{60}	Fullerene
C8TBT	Poly(N-9'-heptadecanyl-2,7-carbazole-alt-(4,7-bis(3-hexyk-thien-5-yl)-2,1,3-benzothiadiazole -2',2"-diyl)
CB	Conduction band
CB	Chlorobenzene
ClBDPPV	Chlorine functionalized benzodifurandione-based poly(p-phenylene vinylele)
CNT	Carbon nanotube
$CoCp_2$	Cobaltocene
CPE	Conjugated polyelectrolytes
Cu-BHT	Copper benzenehexathiol complex
CSA	Camphorsulfonic acid
CVD	Chemical vapour deposition
DIO	Diiodooctane
DMF	Dimethyl fomamide
DMSO	Dimethyl sulfoxide
DoS	Density of State
EA	Electron Affinity
EBSA	4-ethyl-benzenesulfonic acid
EDOT	3,4-ethyldioxythiphene
EG	Ethylene glycol
ETT	Ethenetetrathiolate
F_2TCNQ	Tetrathiafulvalene-difluorotetracyano-quinodimethane
F_4TCNQ	2,3,5,6-Tetrafluoro-7,7,8,8-tetracyano-quinodimethane
F8TBT	Poly((9,9-diotcylfluorene)-2,7-diyl-alt-(4,7-bis(3-hexylthien-5-yl)-2,1,3-benzothiadiazole)-2',2"-diyl)
FBDPPV	Fluorine functionalized benzodifurandione-based poly(p-phenylene vinylele
$FeCl_3$	Iron(III) chloride
$Fe(CN)_6$	Ferricyanide
FTS	(tridecafluoro-1,1,2,2-tetrahydrooctyl)trichlorosilane
GaAs	Gallium arsenide
GHG	Greenhouse gas
GIWAXS	Grazing-incidence wide angle X-ray scattering
H_2O_2	Hydrogen peroxide
H_2SO_4	Sulfuric acid
$HAuCl_4$	Tetrachloroauric acid
HCl	Hydrochloric acid
HF	Hydrogen fluoride
HM	High molecular mass

HNO_3	Nitric acid
HOMO	Highest occupied molecular orbital
IE	Ionization energy
IPA	Isopropyl alcohol
I_{SC}	Short-circuit current
ITO	Indium tin oxide
KOH	Potassium hydroxide
K_XNi-ett	Kx(Ni-ethylenetetrathiolate)
LM	Low molecular mass
LUMO	Lowest unoccupied molecular orbital
MACE	Metal-asssited chemical etching
MCEE	Metal-catalyzed electoless etching
Mn_3O_4	Manganese oxide
N-DMBI	4-(1,3-dimethyl-2,3-dihydro1H-benzoimidazol-2-yl)phenyl)dimethylamine
N-DPBI	4-(1,3-dimethyl-2,3-dihydro-1H-benzimidazol-2-yl)-N,N-diphenylaniline
NaOH	Sodium hydroxide
$NbCl_5$	Niobium(V) chloride
NDI	Naphthalenediimide
NDTI	Naphtho[2,3-b:6,7-b]dithiophenediimi
NMR	Nuclear Magnetic Resonnance
$NOPF_6$	Nitrosonium hexafluorophosphate
NP	Nanoparticles
NTCDA	1,4,5,8-Naphthalenetetracarboxylic dianhydride
NWs	Nanowires
OH^-	Hydroxide ion
OPV	Organic Photovoltaic
P3HT	Poly(3-hexylthiophene)
PA	Polyacetylene
PANi	Polyaniline
PbTe	Lead telluride
PBTTT	Poly(2,5-bis(3-alkylthiophen-2-yl)thieno[3,2-b]thiophene)
PCBM	Phenyl-C61-butyric acid methyl ester
PCDTBT	Poly[N-9'-heptadecanyl-2,7-carbazole-alt-5,5-(4,7-di-2-thienyl-2',1',3'-benzothiadiazole]
PDPP3T	Poly{2,2′-[(2,5-bis(2-hexyldecyl)-3,6-dioxo-2,3,5,6-tetrahydropyrrolo[3,4-c]pyrrole-1,4-diyl)dithiophene]-5,5′-diyl-alt-thiophen-2,5-diyl}
PCE	Power conversion efficiency
PEG	Poly(ethyleneglycol)
PEO	Poly(ethylene oxide)
PET	Polyethylene terephthalate
PF	Power factor
PF_6	Hexafluorophosphate
PEDOT	Poly (3,4-ethylenedioxythiophene)
PNDIBS	Naphthalenediimide-biselenophene copolymer
P(NDIOD-T2) or PNDI(2OD2T)	Poly{N,N′-bis(2-octyldodecyl)-1,4,5,8-napthalenedicarboximide-2,6-diyl]-alt-5,5-(2,2bithiophene)}
P_{out}	Power output
PPV	Polyphenylenevinylene
PPy	Polypyrrole
pSi	Porous silicon
PSS	polystyrene sulfonate
PTB7	Poly[[4,8-bis[(2-ethylhexyl)oxy]benzo[1,2-b:4,5-b']dithiophene-2,6-diyl][3-fluoro-2-[(2-ethylhexyl) carbonyl] thieno[3,4-b]thiophenediyl]]
PVD	Physical vapour deposition
Pyr	Pyridine

RSF	Relative sensitivity factor
RTG	Radioisotope thermoelectric generator
Sb_2Te_3	Antimony telluride
SEC	Size exclusion chromatography
SEM	Scanning electron microscopy
SHE	Standard hydrogen electrode
Si	Silicium
$SiCl_4$	Silicon tetrachloride
SiH_4	Silane
SiNWs	Silicon nanowires
SiO_2	Silicon oxide
SWCNT	Single walled carbon nanotubes
T_b	Boiling point temperature
TBAF	Tetra-n-butyl ammonium fluoride
TCB	1,2,4-trichlorobenzene
TDEA	Tetrakis(dimethylamino)ethylene)
TE	Thermoelectric
Te	Tellurium
TEG	Thermoelectric generator
TEM	Transmission electron miscroscopy
TFSI	Bis(trifluoromethanesulfonyl)imide
THF	Tetrahydrofurane
$TiS_2(HA)x$	Hexylammonium titanium disulfide
Tol	Toluene
Tos	Tosylate
TT	3-fluorothieno- [3,4-b]thiophene-2-carboxylate
TTF-TCNQ	Tetrathiafulvene-tetracyanoquinodimethane complex
UPS	Ultra-violet electron spectroscopy
UV-Vis-NIR	Ultraviolet – visible – near infrared
VB	Valence band
VHR	Variable range hopping
V_{OC}	Open-circuit voltage
VPP	Vapor phase polymerization
VLS	Vapour-liquid-solid
WAXS	Wide-angle X-ray scattering
XPS	X-Ray photoelectron spectroscopy
XRD	X-ray diffraction
$ZrCl_4$	Zirconium(IV) chloride
ZT	Figure of Merit

List of symbols

a	$m^2.s^{-1}$	Carrier diffusivity
ΔT	K	Temperature difference
ε	$F.m^{-1}$	Dielectric constant
$\vec{E}$	$V.m^{-1}$	Electric field
E_f	eV	Fermi level energy
E_g	eV	Energy bandgap
E_v	eV	Vacuum energy level
η		Thermoelectric efficiency
I_{sc}	A	Short-circuit curent
$\vec{J}$	A/m^2	Current density
κ	$W/(m \cdot K)$	Thermal condcutivity
K	$V.K^{-1}$	Thomson coefficient
k_B	$J.K^{-1}$	Boltzmann constant = 1.380649×10^{-23}
λ	m	Wavelength
L	$W.\Omega.K^{-2}$	Lorenz number = 2.44×10^{-8}
M_n	$g.mol^{-1}$	Molar mass
μ	$m^2.V^{-1}.s^{-1}$	Mobility
N	m^{-3}	Charge carrier density
ξ	m	Charge carrier localization length
P_e	W	Electric power
Π	V	Peltier coefficient
Q	W	Thermal (Heat) flux
q	$A.s$	Elementary charge = 1.602×10^{-19}
ρ	$\Omega.m$	Electrical resistivity
R_q	m	Roughness (Root Mean Squared)
σ	$S.m^{-1}$	Electrical conductivity
S	$V.K^{-1}$	Seebeck coefficient
τ	s	Relaxation time
T	K	Temperature
$\vec{\nabla}T$	K	Temperature gradient
ν	$m.s^{-1}$	Drift velocity
V_{oc}	V	Open-circuit voltage
Φ	eV	Work function

Table of contents

Résumé

La nourriture et le chauffage sont des besoins fondamentaux pour les êtres humains. Le feu a permis à l'homme d'améliorer sa condition de vie. Depuis, nous avons cherché à diversifier nos moyens de production d'énergie, puis à les diversifier. Initialement, la principale source d'énergie était la biomasse (bois, excréments d'animaux, etc.) via le feu. Cela a évolué au cours de l'histoire avec, par exemple, avec l'utilisation des combustibles fossiles. Les sources se sont ainsi diversifiées à travers les découvertes et les progrès techniques pour devenir les sources d'énergie actuelles telles que : l'énergie mécanique par friction, l'énergie nucléaire par fission ou l'énergie radiante via des capteurs solaires. Cette multitude de sources a permis une utilisation généralisée de l'énergie à travers le monde.

Néanmoins, la production de chaleur associée résultante n'est pas toujours souhaitée. Une grande partie reste encore inexploitée, et est libérée directement dans l'atmosphère. Chaque année, le laboratoire national Lawrence Livermore (créé par UC Berkeley) a pour objectif de répertorier la consommation d'énergie des États-Unis dans un diagramme de Sankey (Figure 1). Ce diagramme comprend la source d'énergie initiale (nucléaire, pétrole, éolienne, etc.) ainsi que l'utilisation finale (domestique, commerciale, etc.) de l'énergie produite (un quad simple équivaut approximativement à 8 milliards de gallons d'essence).

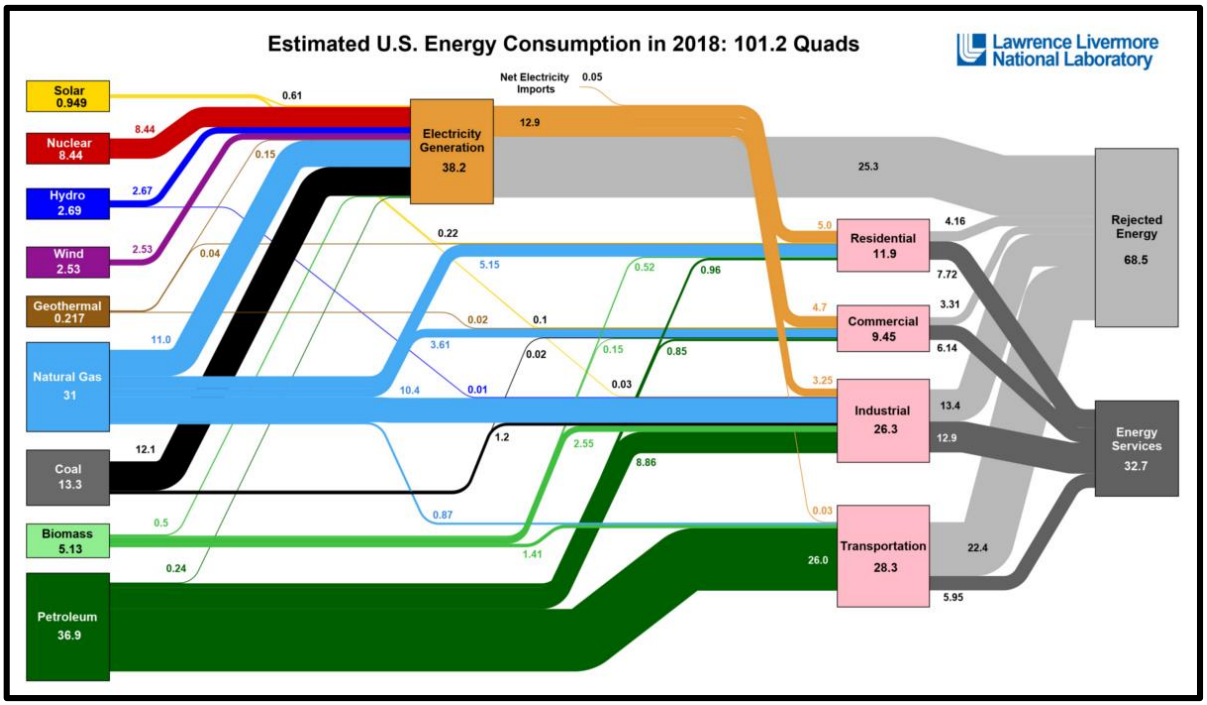

Figure 1 : Diagramme de Sankey de la consommation des Etats-Unis en 2018

Ce diagramme indique également l'énergie rejetée, ce qui représente l'énergie gaspillée. En fait, 68% de toute l'énergie produite n'est pas exploité. Cela est principalement dû au fait que les moteurs thermiques ont généralement un faible rendement d'environ 20 à 40%, même les moteurs électriques gaspillent de l'énergie, leur efficacité étant de 85 à 90%. Un certain pourcentage d'énergie est toujours libéré sous forme de chaleur, de son, de lumière ou d'autres formes difficiles à exploiter. Cette énergie perdue peut être valorisée pour augmenter les rendements énergétiques des systèmes. La récupération directe de chaleur pour le chauffage n'est pas toujours pertinente, principalement en raison de la faible quantité d'énergie. Ce problème est accentué lorsque les zones à chauffer sont trop éloignées du point de production de chaleur.

Aujourd'hui, l'homme cherche principalement à gérer les énergies et leurs utilisations dans une perspective de développement durable. Parmi les différentes énergies renouvelables, la thermoélectricité semble être une solution de choix pour la conversion des pertes de chaleur en électricité, et donc pour l'amélioration du rendement thermique. Cependant, comme l'a souligné Cronin Vining, la thermoélectricité ne sera pas la solution à la crise énergétique mondiale. En effet, en raison des faibles rendements, les dispositifs thermoélectriques seront utilisés pour des applications personnelles, ou au mieux pour des pertes énergétiques de véhicules privés. Ainsi, l'impact sur la crise énergétique mondiale serait considérablement moindre.

À cet égard, les chercheurs tentent constamment d'améliorer de manière significative les propriétés des dispositifs thermoélectriques. Actuellement, les générateurs thermoélectriques sont fabriqués à partir de matériaux inorganiques. Cependant, leurs hautes performances n'effacent pas leurs défauts, tout comme leur faible abondance. Par exemple, le matériau inorganique le plus utilisé dans les générateurs thermoélectriques (GTE), le tellurure de bismuth - Bi_2Te_3, est composé des deux « métaux » parmi les plus rares de la Terre. De plus, le poids est également une limitation pour les applications embarquées. Enfin, leur faible aptitude au traitement, leur toxicité élevée et leur coût élevé (806 $/kg) sont problématiques pour leur future généralisation.

Grâce à la découverte de Shirakawa, Mac Diarmid et Heeger en 1977, les polymères conjugués oxydés ont acquis un comportement électrique similaire aux métaux, et ont pu être utilisés comme matériaux innovants et concurrentiels pour les GTE. Les polymères conducteurs ont déjà été utilisés dans divers domaines, tels que la fabrication de cellules solaires organiques flexibles, de capteurs de lumière organique émettrice ou de divers capteurs souples. Au cours

des 10 dernières années, les propriétés thermoélectriques des polymères conducteurs ont retenu l'attention de la communauté scientifique. En effet, la force des polymères conducteurs réside dans leur faible conductivité thermique, leur conductivité électrique élevée (avec un réglage approprié de la structure), leur grande capacité de traitement (techniques d'impression) et leur faible coût. Cependant, leur faible efficacité par rapport aux GTE inorganiques limite leur application aux appareils de faible puissance à température ambiante. De nombreux efforts sont déployés pour améliorer leurs propriétés.

Objectifs

Le but de ce doctorat a été de développer un générateur thermoélectrique efficace à base de matériaux organiques pour des applications à température ambiante. Plusieurs pistes ont été explorées dans ce travail, comme l'optimisation des paramètres de synthèse et de formulation des matériaux organiques, ou encore l'association des matériaux organiques et inorganiques pour former un matériau hybride thermoélectrique.

Dans ce manuscrit, le Chapitre 1 fournit une base théorique ainsi qu'une étude bibliographique pour une meilleure compréhension de la thermoélectricité. Ainsi le Chapitre 1 résume les connaissances, la compréhension et l'utilisation des polymères dans le domaine de la thermoélectricité en tant que matériau innovant.

Les chapitres suivants décrivent les travaux et les études réalisés au cours de cette thèse. Le Chapitre 2 traite de l'optimisation des matériaux polymères et organiques pour la thermoélectricité. Ces matériaux organiques ont été optimisés, et une nouvelle approche a été développée dans notre laboratoire pour améliorer leurs propriétés thermoélectriques. Cette dernière consistait en un couplage entre des matériaux organiques (conductivité électrique élevée) et des matériaux inorganiques (coefficient Seebeck élevé) pour bénéficier des avantages de chacun des matériaux. Ainsi le silicium a été utilisé comme substrat pour tirer parti de ses propriétés thermoélectriques intéressantes. L'interface entre le matériau organique et le substrat de silicium a été la clé de voûte de l'amélioration des propriétés thermoélectriques. Les résultats obtenus sont décrits dans les Chapitres 3 et 4. Le Chapitre 5 décrit la fabrication et les performances des GTE obtenues grâce aux travaux effectués dans les chapitres précédents. Enfin, à la fin de manuscrit, différentes annexes fournissent des informations sur la théorique des polymères conjugués, les procédures expérimentales et une étude menée en parallèle de ce projet.

Chapitre 2

Grâce à diverses modifications de traitement, les propriétés structurelles, électroniques et thermoélectriques de divers polymères et matériaux organiques ont été optimisées. Les polymères de type p synthétisés présentaient de meilleures performances thermoélectriques que les matériaux de type n. Par exemple, dans le cas de PEDOT: Tos, un facteur de puissance élevé de 240 µW/mK² a été atteint.

Un nouveau polymère prometteur, le PNDIBS, analogue au PNDI(2OD)2T, a été testé en tant que matériau thermoélectrique de type n. Les performances thermoélectriques obtenues pour ce matériau étaient comparables à celles du PNDI(2OD)2T, connues comme le matériau de type n référence.

En outre, cette étude a montré l'importance du dopage des matériaux organiques. Dans la plupart des cas, le facteur de puissance suivait une courbe en forme de cloche avec un maximum pour une concentration précise en dopant.

Enfin, ces matériaux organiques serviront de « brique élémentaire » pour la conception d'un générateur thermoélectrique. Les meilleures performances thermoélectriques de chaque matériau sont résumées dans le tableau suivant (Tableau 1).

Material	**Dopant or structural agent**	**Concentration (wt% - mol%)**	**S (µV/K)**	**σ (S/cm)**	**PF (µW/m.K²)**	**Air stability**
PEDOT:Tos	DMSO Pyridine	3 3	44	1240	240	Stable
P3HT m.	F_4TCNQ	20	76	4.3	2.48	Stable
P3HT seq.	F_4TCNQ	10	127	0.87	1.40	Stable
PCDTBT	$FeCl_3$	50	37	60	8.21	Stable
PTB7	DIO	3	760	0.017	0.9	Stable
PCBM	AOB N-DPBI	10 5	-412	0.7	11.88	Instable
PNDIBS LMn	N-DMBI	20	-167	$8x10^{-4}$	$2.2x10^{-3}$	Instable
PNDIBS HMn	N-DMBI	20	-189	$9x10^{-4}$	$3.2x10^{-3}$	Instable

Tableau 1 : Performances thermoélectriques des meilleurs matériaux organiques

Chapitre 3

L'influence de l'épaisseur de matériaux organiques sur les propriétés thermoélectriques de substrats de silicium avec différents niveaux de dopage a été étudiée. Il a été démontré que le coefficient Seebeck d'une telle jonction hybride pouvait être réglé en amplitude et en signe en fonction du dopage du silicium et des propriétés des matériaux organiques (Figure 2). Ces résultats ont pu être prédits grâce à un modèle basé sur un circuit électrique. Ce modèle est utilisable pour une large gamme de matériaux organiques sur substrat inorganique. Il a également été démontré que la conductivité électrique, et donc le facteur de puissance d'un matériau inorganique nu, pouvait être améliorée en ajoutant des matériaux organiques conducteurs. Ce phénomène a été étudié par des analyses UPS et XPS. L'hypothèse principale de cette amélioration de propriété serait l'influence directe du type d'architecture du dispositif utilisé. En fait, les électrodes ont été « prises en sandwich » entre le substrat de silicium et le film mince de polymère. L'interface semble jouer un rôle important dans ces résultats. La conductivité électrique et le facteur de puissance obtenus pour les dispositifs hybrides à base de PEDOT:Tos et de silicium ont obtenu les meilleures performances. Dans le cas des matériaux de type n, les performances obtenues sont supérieures à celles enregistrées dans la littérature pour des matériaux de type n relativement stable à l'air.

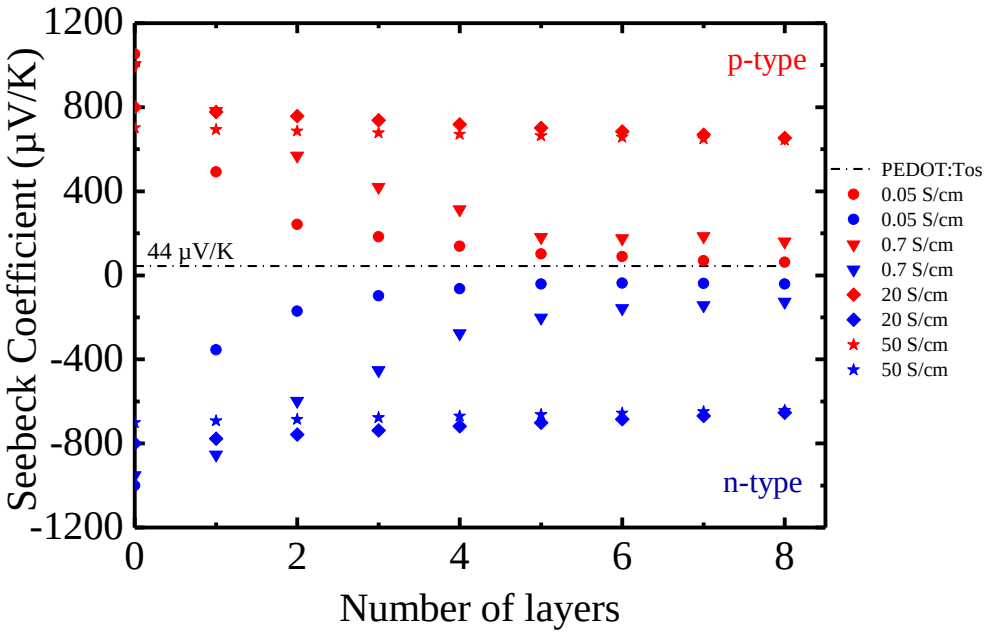

Figure 2 : Coefficient Seebeck en fonction du nombre de couche de PEDOT :Tos.

Chapitre 4

Grâce à diverses procédures de gravure, trois nanostructures de silicium ont été obtenues. Un réglage fin des paramètres de gravure a permis de réaliser des nanofils, des pores et des pyramides au-dessus de substrats de silicium. Le meilleur polymère développé dans le Chapitre 2, le PEDOT:Tos traité avec du DMSO et de la pyridine, a été déposé sur du silicium nanostructuré. Toutes les procédures de gravure ainsi que le dépôt du polymère ont été suivis microscopie électrique à balayage (MEB) (Figure 3).

Les propriétés thermoélectriques des dispositifs à base de silicium nanostructuré avec diverses couches de PEDOT:Tos à leurs sommets ont été étudiées. Les nanofils de silicium ont permis d'obtenir les meilleures améliorations du facteur de puissance par rapport au silicium nu. Grâce à une diminution de la dimensionnalité, un coefficient de Seebeck plus élevé a été obtenu et, malgré une diminution de la conductivité électrique, le facteur de puissance a été augmenté d'environ 10 à 20% dans les meilleurs des cas.

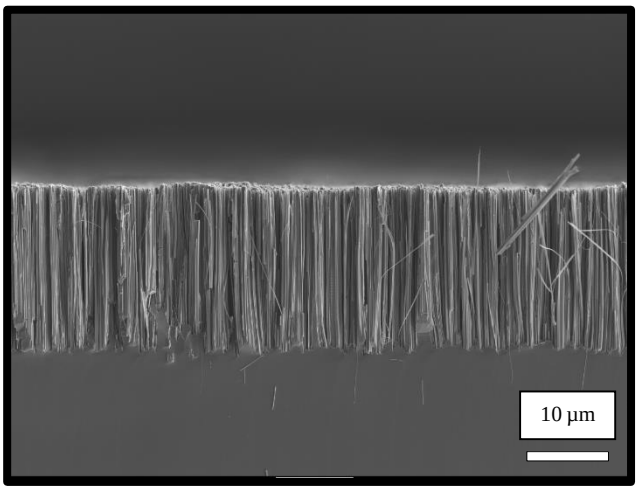

Figure 3 : Image MEB de nanofils de silicim.

Chapitre 5

Des générateurs thermoélectriques sur divers supports ont été développés pour des applications à température ambiante. Les GTE organiques, sur verre et PET, ont montré des performances similaires. Le principal problème a été la faible stabilité (absence de conductivité électrique) du matériau de type n entraînant de faibles performances.

En parallèle, des GTE sur des substrats de silicium ont été fabriqués (Figure 4). Dans le cas des substrats de silicium hautement conducteur, le couplage avec un matériau organique a

permis d'obtenir une amélioration des performances du dispositif. En nanostructurant la surface du silicium, de meilleures performances ont été obtenues pour les générateurs thermoélectriques hybrides PEDOT:Tos-silicium. Cette amélioration pourrait être expliquée en partie par un transfert de charge à l'interface silicium-organique, ce qui a permis d'atteindre une puissance record de 2350 nW pour un générateur à trois jambes à base de PEDOT:Tos sur silicium nanostructuré sous un $\Delta T = 10$ °C près de la température ambiante.

Malheureusement, cette amélioration n'a pas pu être vérifiée, même avec des techniques analytiques poussées. Ces résultats sont en accord avec les études récentes sur les systèmes hybrides. Les scientifiques se sont concentrés sur l'utilisation de diverses stratégies (transport interfacial et effets structurels/morphologiques) pour améliorer les performances thermoélectriques. Cependant, il s'est avéré difficile d'établir la physique fondamentale à l'origine de ces améliorations de performance. La mise au point de matériaux et d'un dispositif hybrides thermoélectriques de nouvelle génération nécessite une meilleure compréhension de la physique du transporteur dans les systèmes multiphases complexes.

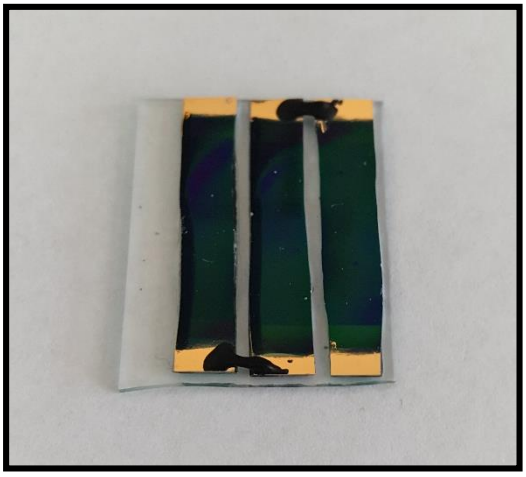

Figure 4 : Photographie d'un générateur thermoélectrique hybride à base PEDOT:Tos sur substrat de silicium.

Conclusion

La thermoélectricité organique et hybride est un domaine qui est encore à ses balbutiements et présente de nombreuses possibilités d'exploration. L'émergence récente des technologies de communication, ainsi que les problèmes d'énergie et la menace du réchauffement climatique, pourraient faire des dispositifs thermoélectriques organiques et hybrides un marché important. Pour que les produits thermoélectriques trouvent leur place dans ce contexte de nouvelles technologies émergentes, il est encore nécessaire de surmonter les obstacles liés aux performances et aux processus de fabrication des dispositifs thermoélectriques.

L'objectif principal de ce doctorat, la fabrication d'un générateur thermoélectrique à base de matériaux organiques a été abordée avec succès. La philosophie de ce travail était d'utiliser les avantages des matériaux organiques et inorganiques pour atteindre des performances thermoélectriques élevées.

Ainsi, les polymères de type p synthétisés ont été formulés avec divers agents dopants et additifs pour optimiser leurs performances thermoélectriques. Quant aux matériaux organiques de type n, ils ont également été optimisés et caractérisés, malgré leur faible stabilité à l'air. Ainsi grâce à un réglage fin des propriétés électroniques, les meilleurs matériaux pour les séries de type p & n ont été le PEDOT: Tos avec un facteur de puissance de 240 µW/mK² et PCBM avec un facteur de puissance de 2,44 µW/mK.

Tous les matériaux organiques ont été combinés avec des substrats de silicium de type p et n. Les propriétés thermoélectriques, le coefficient Seebeck, la conductivité électrique et le facteur de puissance ont été mesurés pour chaque matériau hybride. Les résultats ont montré un comportement intéressant avec l'augmentation de l'épaisseur de la couche de polymère. En fait, les propriétés thermoélectriques pourraient être ajustées avec cette stratégie. Bien que l'origine de ce comportement ne soit pas complètement clarifiée, il pourrait être envisagé comme un phénomène de transfert de charge à l'interface.

La pénurie de matériaux thermoélectriques de type n (fortement liée à leur instabilité dans l'air ambiant) a obligé à proposer de nouvelles approches de synthèse de ces matériaux. La nouvelle approche, avec un substrat en silicium et un matériau organique à la surface, a permis de développer un matériau de type n stable à l'air efficace pour les applications thermoélectriques. En fait, les impuretés à l'intérieur du substrat de silicium ont grandement influencé le type de porteur de charge dans le matériau hybride. Ainsi, avec du silicium dopé négativement, les dispositifs correspondants étaient de type n (en ce qui concerne son coefficient de Seebeck), malgré le dépôt de matière organique de type p. Le dispositif hybride à base de PEDOT: Tos et de silicium de type n a atteint une valeur record de 0,65 mW/mK², l'une des meilleures valeurs pour les matériaux hybrides de type n.

Ensuite, la surface de silicium a été nanostructurée, donnant des indications supplémentaires sur le rôle de l'interface sur les propriétés thermoélectriques. En fait, l'augmentation de la surface spécifique a produit une amélioration des propriétés thermoélectriques par rapport au silicium nu. Malgré l'utilisation exclusive de PEDOT:Tos, cette stratégie pourrait être appliquée à n'importe quel matériau organique et la même amélioration devrait être obtenue.

Enfin, des générateurs thermoélectriques ont été fabriqués à l'aide de ces systèmes hybrides. La meilleure puissance de sortie, 2350 nW, a été obtenue pour un TEG à trois jambes constitué de six couches PEDOT:Tos sur des nanofils de silicium avec une différence de températures de 10°C à température ambiante. Cette étude a été conçue pour aborder différents aspects et problématiques de la thermoélectricité dans le domaine organique.

General Introduction

Food and heating are the basic needs of human beings. A long time ago fire allowed human beings to improve their living conditions [1]. Since then we have sought to diversify our means of producing thermal energy, and then to diversify the forms of energy. Initially, the main source of thermal energy was biomass (wood, animal excrement ...) with fire. This has evolved throughout history with, for example, the use of fossil fuels. The sources then diversified through discovery and technical progress to be today's wide energy sources including: mechanical energy [2] via friction and shocks, nuclear energy [3] via fission, radiant energy [4] via solar collectors or even geothermal energy [5] can, amongst other things, produce heat. This multitude of sources allows widespread use of thermal energy and to be relatively well distributed on Earth.

Nevertheless, the production of heat is not always desired. Much of it is untapped and released directly into the atmosphere [6]. Every year, the Lawrence Livermore National Laboratory (founded by UC Berkeley) aim to chart all U.S. energy use in one Sankey diagram (Figure 1). This diagram includes the original energy source (*i.e.* nuclear, oil, wind, etc.) as well as the ultimate end-use (*i.e.* residential, commercial, etc.) for the energy that was generated (a single quad is roughly equivalent to 8 billion gallons of gasoline).

One interesting aspect of the diagram is that it also shows rejected energy, which represents the energy that is wasted due to various inefficiencies. In fact, 68% of all energy generated is not harnessed for any productive use. This is primarily due to the fact that gasoline engines are usually only about 20-40% efficient, and even electric engines waste energy since they are 85- 90% efficient. A certain percentage of energy is always released as heat, sound, light, or other forms that are hard for us to harness.

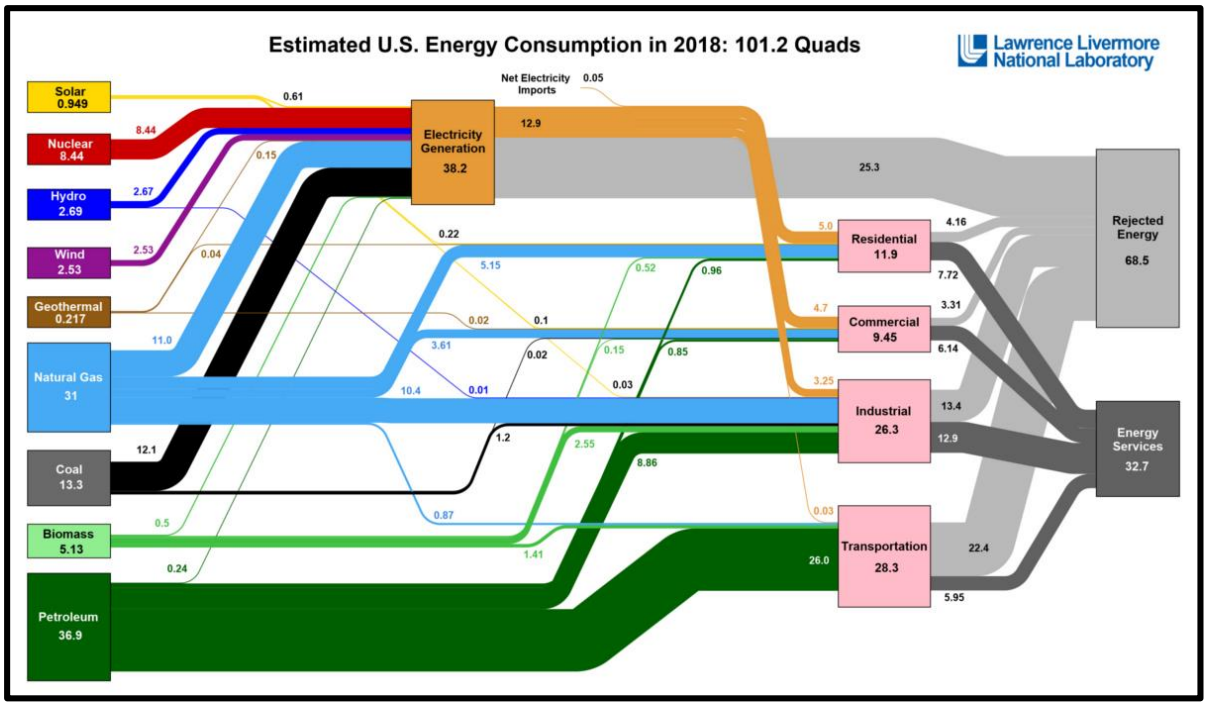

Figure 2 : Sankey diagram of U.S. energy consumption in 2018

This lost energy can be valorised in order to increase the energy yields of the systems. For example, the heat generated by a process can be recovered and sent to areas that need to be heated (homes, tertiary sector buildings, ...) [7]. Direct heat recovery for heating is not always relevant, mainly because the amount of energy and the temperature level are not sufficient. This problem is accentuated when the zones to be heated are too far from the point of heat production.

Today, human beings seek mainly to manage energies and their uses in perspectives of sustainable development. It is in this context that the various directives of the European Commission can be summarized, which can be summed up by the "20-20-20" objective for 2020 [8]:

- Decrease greenhouse gas (GHG) emissions by 20% from 1990 emissions;
- Reduce energy consumption by 20% through improved energy efficiency;
- Achieve 20% renewable energy in the energy mix.

Recently, on January 22nd, 2014, a new proposal from the European Commission supporting a reinforcement of this energy-climate policy was published [9]. The goal is to achieve a GHG reduction of 40% and a 27% renewable energy rate by 2030.

Among the various renewable energies, thermoelectricity is the solution for the conversion of heat losses into electricity, and therefore the improvement of thermal efficiency.

However, as pointed out by Cronin Vining, thermoelectricity will not be the only solution to the global energy crisis [10]. Indeed, it underlines that in view of the yields, the thermoelectric devices will be used for personal applications, or at best on the energetic losses of private vehicles. Thus, the impact on the world energetic crisis would be considerably less.

In this regard, researchers are constantly trying to significantly improve the thermoelectric device properties. Currently, thermoelectric generators are made from inorganic materials [11]. However, their high performance does not erase their defects, like their low abundance of inorganic elements in earth's crust and in oceans. For example, the most used inorganic material in thermoelectric generators (TEGs), Bismuth Telluride - Bi_2Te_3, is composed of the Earth's two rarest "metals" [12]. Furthermore, weight is also a limitation for embedded applications. Finally, their low processability, high toxicity and high cost ($806/kg) are problematic for future device use [13].

Thanks to the discovery of Shirakawa, Mac Diarmid and Heeger in 1977, oxidized conjugated polymers could behave electrically as a metal [14,15], and used as an innovative and competing material for TEGs [16]. Conducting polymers have already been used in various fields such as in the fabrication of flexible organic solar cells [17], flexible organic light emitting [18], or flexible sensors [19]. In the past 10 years, the thermoelectric properties of conducting polymers have gained a lot of attention from the scientific community [20]. Indeed, conducting polymer's strength lie in their intrinsic low thermal conductivity, a high electrical conductivity (with a proper structure tuning), a high processability (printable techniques available) and low cost [21–25]. However, their low efficiency compare to inorganic TEGs limits their application to low powered devices. Many efforts are being made to improve their properties.

The aim of this Ph.D. is to develop an efficient thermoelectric generator based on organic materials. Several optimization routes have been investigated in this work, either by fine-tuning of the synthetic parameters leading to the thermoelectric material or by associating organic and inorganic materials in a thermoelectric composite.

In this manuscript, Chapter 1 provides a basic overview of thermoelectricity. Starting with a brief history of thermoelectricity, as well as the basic theory of these related phenomena, some highlights from the literature with a focus on state-of-the-art studies in this field will be

provided. Chapter 1 summarizes the knowledge and understanding of polymers in the thermoelectric field, and their use as an innovative material in the thermoelectric generator.

The following Chapters describe the works and studies realized during this Ph. D. Chapter 2 discusses the optimization of polymer and organics materials for thermoelectricity. Most famous p-type materials, such as PEDOT, P3HT, and PCDTBT were studied. Likewise, n-type material, PCBM and a new polymer with selenium were used. When these organic materials were optimized, a novel approach developed in our laboratory was used to enhance thermoelectric properties. Silicon was used as a substrate to benefit from these properties. The interface between the organic material and the silicon substrate was the point as a keystone to achieving enhancement of thermoelectric properties, Chapter 3 and 4 described results obtained.

The last Chapter 5, describes the fabrication of TEGs based on works previously done in other Chapters. The production and characterization of various forms of thermoelectric generators were developed. Finally, at the end of this manuscript, different appendices provide some insights on the polymer theoretical background, the experimental procedures and other parallel studies, respectively.

References

[1] L. Henry, *La domestication du feu aux temps paléolithiques* ; Odile Jacob : Paris, **2017**.
[2] P. Breeze, *Power Generation Technologies*; Elsevier, **2014**.
[3] K. Saidi and M. B. Mbarek, *Progress in Nuclear Energy*, **2016**, *88*, 364-374.
[4] G. L. Smith, K. J. Priestley, N. G. Loeb, B. A. Wielicki, T. P. Charlock, P. Minnis, D. R. Doelling, D. A. Rutan, *Adv. Space Res.* **2011**, *48*, 254.
[5] J. Zhu, K. Hu, X. Lu, X. Huang, K. Liu, X. Wu, *Energy* **2015**, *93*, 466.
[6] H. Harde, *Int. J. Atmospheric Sci.* **2013**, Article ID 503727, pp26.
[7] H. Jouhara, N. Khordehgah, S. Almahmoud, B. Delpech, A. Chauhan, S. A. Tassou, *Therm. Sci. Eng. Prog.* **2018**, *6*, 268.
[8] European Commission, 2020 climate & energy package. *Clim. Action - Eur. Comm.* **2016**.
[9] European Commission, 2030 climate & energy framework. *Clim. Action - Eur. Comm.* **2016**.
[10] C. B. Vining, *Nat. Mater.* **2009**, *8*, 83.
[11] M.-K. Han, Y. Jin, D.-H. Lee, S.-J. Kim, *Materials* **2017**, *10*, 1235.
[12] O. Eibl, K. Nielsch, N. Peranio, F. Völklein, *Thermoelectric Bi2Te3 Nanomaterials*; John Wiley & Sons, **2015**.
[13] N. Lowhorn, W. K. Wong-Ng, J. Lu, E. L. Thomas, M. Otani, M. L. Green, N. Dilley, J. Sharp, T. N. Tran, *Appl. Phys. -Mater. Sci. Process.* **2009**, *96*.
[14] A. J. Heeger, *Rev. Mod. Phys.* **2001**, *73*, 681.
[15] M. Geoghegan, G. Hadziioannou, *Polymer Electronics*; Oxford Master Series in Physics; Oxford University Press: Oxford, New York, **2013**.
[16] B. Russ, A. Glaudell, J. J. Urban, M. L. Chabinyc, R. A. Segalman, *Nat. Rev. Mater.* **2016**, *1*, 16050.
[17] A. I. Hofmann, W. T. T. Smaal, M. Mumtaz, D. Katsigiannopoulos, C. Brochon, F. Schütze, O. R. Hild, E. Cloutet, G. Hadziioannou, *Angew. Chem. Int. Ed.* **2015**, *54*, 8506.
[18] M. Kuik, G.-J. A. H. Wetzelaer, H. T. Nicolai, N. I. Craciun, D. M. D. Leeuw, P. W. M. Blom, *Adv. Mater.* **2014**, *26*, 512.
[19] K. M. Persson, R. Gabrielsson, A. Sawatdee, D. Nilsson, P. Konradsson, M. Berggren, *Langmuir* **2014**, *30*, 6257.
[20] O. Bubnova, X. Crispin, *Energy Environ. Sci.* **2012**, *5*, 9345.
[21] X.-S. Wang, H.-P. Tang, X.-D. Li, X. Hua, *Int. J. Mol. Sci.* **2009**, *10*, 5257.
[22] T.-H. Le, Y. Kim, H. Yoon, *Polymers* **2017**, *9*, 150.
[23] M. Aldissi, *Mol. Cryst. Liq. Cryst. Inc. Nonlinear Opt.* **1988**, *160*, 121.
[24] C. Huang, X. Qian, R. Yang, *Mater. Sci. Eng. R Rep.* **2018**, *132*, 1.
[25] T. O. Magu, A. U. Agobi, L. Hitler, P. M. Dass, *J. Chem. Rev.* **2019**, *1*, 19.

Chapter 1

Thermoelectricity state of the art:

From origin to recent device

A Fundamentals of thermoelectric materials

1. Historic

Thermoelectricity began in 1794 with Alessandro Volta, when he highlighted the appearance of a "force" under a temperature gradient thanks to glasses of water with iron and frog parts (Figure 1) [1].

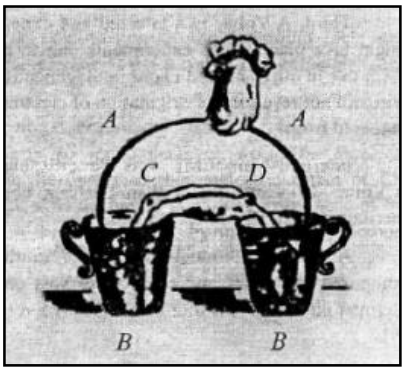

Figure 1: Volta's experiment. A – Metal bow (iron), B – Glass full of water, C & D Frog parts immerged in glasses.

It will take three decades for the interest of scientists for thermoelectricity to come back. In 1821, Thomas Johann Seebeck shown that when a temperature gradient is applied to a circuit built with two metallic conductors and a needle, the latter is deviated (Figure 2) [2]. Seebeck mistakenly thinks that this effect is due to the magnetic field induced by the difference in temperature and that it must be connected to the Earth's magnetic field. At the same time, Hans Christian Oersted and Gustav Magnus tried to explain this phenomenon. First, Hans Christian Oersted explained that the temperature gradient creates a potential difference so if the circuit is closed and allows current flow, a magnetic field is induced [3]. Then Gustav Magnus discovered the Seebeck voltage was independent on thermal distribution along the material junction, the thermopower was a thermodynamic state function [4].

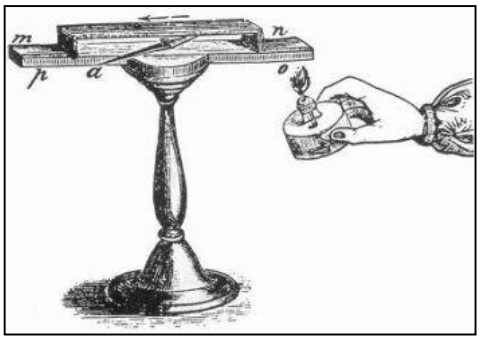

Figure 2: Thomas Johann Seebeck first experiment

Few years after these discoveries, in 1834, Jean Peltier, realized that an electrical current flow could produce or absorb heat at the junction of two metallic materials [5]. This phenomenon was explained later by Emil Lenz, he put ice around a bismuth-antimony junction, and by reversing electrical current flow, he melted the ice. So heating or cooling was dependent of current direction flow [6]. Later, in 1840's, James Prescott Joule demonstrated an irreversible phenomenon, when an electric current flowed in a material because of the internal resistance of the material, heat is produced. This heat's quantity is related to the square of current intensity and the internal resistance, it's called Joule effect [7].

It took twenty years, thanks to William Thomson (Lord Kelvin), to link Seebeck and Peltier effects (**Appendix I**) with Kelvin equations. He also predicted a third phenomenon, called Thomson effect (**Appendix I**). When a temperature gradient and an electrical current flow are present simultaneously, heat emission or absorption could happen in material [8].

Volta, Seebeck, Peltier and Thomson (Lord Kelvin) are the pioneers in the field of thermoelectricity. Their understanding of different phenomena has greatly contributed to the current advances. However, due to the complexity of this phenomena, it's only in the next century that for the first time an efficiency for a thermoelectric generator is calculated based on Seebeck coefficient thanks to Edmund Altenkirch [9]. Later, he extended his calculation on cooling and described optimal operating conditions for this devices.

2. Thermoelectric effects

This section introduces the fundamentals of thermoelectric effects, mainly focused on Seebeck coefficient and electrical and thermal conductivity (*i.e* Figure of merit *ZT*), by a general approach of their physics and in particular a focus on semiconductors material.

Thermoelectricity combines two phenomena, the heat flux (“thermos”) and the electric current (“electricity”) for a same material. Thermoelectric system can either harvest waste heat to convert it in electricity or convert an applied voltage into a cooling or heating source. The first effect, a temperature gradient results in the production of a voltage, is called Seebeck coefficient (*S*). The other effect, opposed to Seebeck coefficient, the Peltier effect (*ΠT*) described the presence of heating or cooling at the electrified junction of two conductors.

So thermoelectric effects link the fluxes between the current density $\overrightarrow{J_e}$, and heat carriers $\overrightarrow{J_q}$. In order to explain this relation, electric current density equation (Ohm’s law) and heat conduction (Fourrier’s Law) have to be considered [4–8].

Ohm’s law expresses current density $\overrightarrow{J_e}$ through material and can be related to electrical conductivity σ to a specific electric field $\vec{E}$:

$$\overrightarrow{J_e} = \sigma\, \vec{\mathrm{E}} \tag{1}$$

When a temperature gradient $\vec{\nabla}T$ is applied in the material, equation (1) becomes:

$$\overrightarrow{J_e} = \sigma\, \vec{\mathrm{E}} - \sigma S \vec{\nabla} T \tag{2}$$

Current density is expressed with two terms, one related to the electrical field and another related to the temperature gradient that will induce an internal carrier diffusion. In the last term, the Seebeck coefficient *S* appear and is expressed in volts per Kelvin (V/K). This parameter is one of the most important parameter in thermoelectricity.

2.1 Seebeck effect

The Seebeck effect gains great interest in semiconductors field, as it allows for determination of the type of the dominating charge carriers in a material as well as the relative position of the Fermi level with respect to the transport level.

Practically, when a temperature difference ΔT is applied on a material, a potential difference ΔV is generated, which is proportional to this temperature difference ΔT. The proportionality is given by an intrinsic material property called Seebeck coefficient S.

$$S = -\frac{\Delta V}{\Delta T} \tag{3}$$

Seebeck coefficient could be understood as follows: In a semiconductor, the energetic distribution of free charge carriers is shifted to higher energy states upon heating. So, if one side of the material is hotter than the other, the charge carriers on the hotter side have higher energies. This leads to a displacement diffusion current towards cold side, resulting in a charging of the two sides of the material. With increasing charge accumulation at the sides, an electric field opposite to the diffusion current builds up, limiting the total voltage being generated (Figure 3). If electrons are the dominating charge carriers, the cold side will be charged negatively, whereas for hole dominated materials the cold side is charged positively.

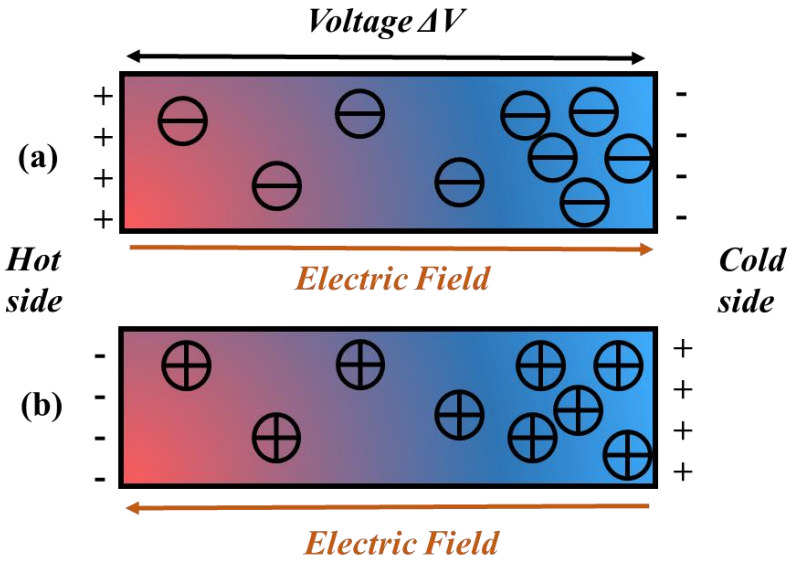

Figure 3: Sketch illustrating the thermoelectric effect.
(a) n-type material (electrons) & (b) p-type (holes) material under a temperature gradient

Seebeck coefficient could be also explained by energy band diagram. In Figure 4, an idealized n-type semi-conducting material is sandwiched between two metallic electrodes (contacts are considered perfect) [10]. However, an energy barrier Φ_{CN} at the interface is present, it's simply a difference between barrier energy of conduction band E_C and Fermi level E_F.

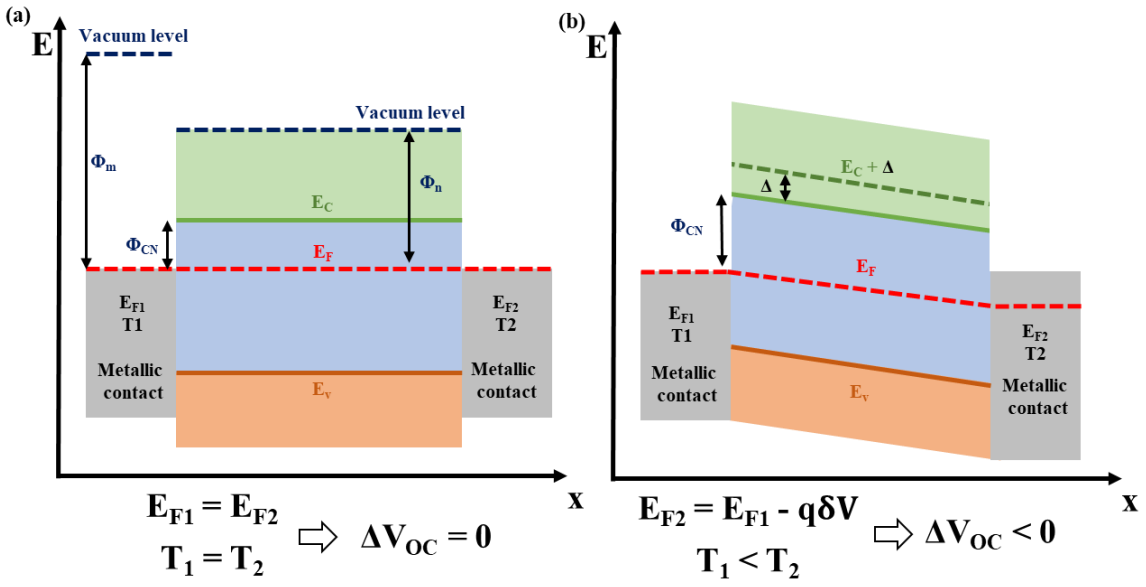

Figure 4: Analysis of Seebeck effect with energy band diagrams.
(a) Without temperature gradient. (b) With a temperature gradient.

Without temperature gradient (Figure 4 (a)), Fermi levels are aligned and no open-circuit voltage is present (V_{oc} = 0). On the other side, when temperature of metallic contact 2 increases ($T_2 > T_1$), Fermi level on the same side will decrease towards Fermi level of the intrinsic semi-conducting material (Figure 4 (b)). So electrons will cross more easily the energetic barrier of the hot side. Because density of states appears at higher energy level than E_C, average energy, where electrons are localized, will be called Δ_x (Figure 4 (b)).

So temperature gradient generates a positive voltage on hot contact 2, creating a potential difference ΔV following Fermi level difference between hot and cold contact:

$$E_{F2} = E_{F1} - q\Delta V \tag{4}$$

In an open-circuit, electrical current J is zero, so electrons can't move. Generated voltage adjusts to temperature difference to balance energy's system and stop electron movement. Thus, if J =0, the probability f_1 to have an electron hoping form cold contact to $E_C + \Delta_x$ is equal to the probability f_2 to have an electron hoping from hot contact to $E_C + \Delta_x$. This could be translated by the following equation:

$$f_1 = f_2 \rightarrow f_1\,[Ec(0) + \Delta x] = f_2\,[Ec(0) + \Delta x] \tag{5}$$

By applying Fermi-Dirac distribution on f_1 and f_2, the equation becomes:

$$\frac{1}{1+e^{(E_c+\Delta_x-E_{F1})/k_BT_1}} = \frac{1}{1+e^{(E_c+\Delta_x-E_{F2})/k_BT_2}} \quad (6)$$

Which leads to:

$$(E_c + \Delta_x - E_{F1})/k_BT_1 = (E_c + \Delta_x - E_{F1} + q\Delta V)/k_BT_2 \quad (7)$$

The equation can be express as:

$$\Delta V = -\frac{(E_c + \Delta_x - E_{F1})}{qT_1}\,\Delta T \quad (8)$$

Finally, Seebeck coefficient appears in the equation with $S = \Delta V / \Delta T$ and can be written as:

$$S = -\frac{E_c - E_{F1}}{qT_1} - \frac{\Delta_x}{qT_1} = -\left(\frac{k_B}{q}\right)\left(\frac{E_c - E_{F1}}{k_BT_1} + \frac{\Delta_x}{k_BT_1}\right) \quad (9)$$

$$S = \left(\frac{k_B}{q}\right)\left(\frac{E_{F1} - E_V}{k_BT_1} - \frac{\Delta_x}{k_BT_1}\right) \quad (10)$$

By convention for semi-conductors, Seebeck coefficient is negative for n-type and positive for p-type materials. Thanks to equation above, Seebeck coefficient is proportional to the energy difference between band energy (($E_C + \Delta_x$) or ($E_V - \Delta_x$)) and Fermi level energy. It means, in case of highly degenerated materials, like metals or highly doped semi-conductors, Fermi level is near E_C (or E_V) and so Seebeck coefficient tend to zero. Thus, semi-conducting materials will have high Seebeck coefficient.

2.2 Electrical conductivity

Electrical conductivity σ is also an important parameter in thermoelectric field. This is material inherent property to conduct current, and is linked to charge carrier transport [11]. Based on equation (1), electrical conductivity can be expressed as:

$$\sigma = \frac{\mathrm{J}}{\mathrm{E}} \tag{11}$$

In a homogenous material, current density J is equal to conduction current J_d. In semi- conductors, current density is given by the following relation:

$$J_d = J_{dn} + J_{dp} = q(\mu_n n + \mu_p p)E \tag{12}$$

Where μ_n and μ_p are electrons and holes mobility, n & p are charge carrier concentration of electrons and holes, and q is elementary charge. Thanks to the previous equations, electrical conductivity is:

$$\sigma = q(\mu_n n + \mu_p p) \tag{13}$$

Electrical conductivity thought electrical mobility is an important parameter for charge carrier transport characterization and devices performances.

2.3 Thermal conductivity

The last important parameter that is involved in thermoelectricity is the thermal conductivity [11]. Thermal conductivity κ is a thermal conduction without matter displacement that can be defined as a ratio between heat flux density $\overrightarrow{J_q}$ and temperature gradient $\vec{\nabla}T$ based on Fourier's law:

$$\kappa = -\frac{\overrightarrow{J_q}}{\vec{\nabla} T} \tag{14}$$

So dependence of thermal flux to temperature gradient shows that thermal energy transfer is a random process based on diffusivity and particles collision inside the material. In case of metals and heavily doped inorganic semi-conductors, κ is separated into two contributions, the structural, κ_s, and the electronic contribution, κ_e, as the charge carriers of the material also contribute to the propagation of the phonons in the material [6,7]. For metals the electronic contribution is dominant in the thermal conductivity and is based on the fact that the charge carriers are involved in both the heat and charge transport in the material [8]. So thermal conductivity is expressed as:

$$\kappa_e = \sigma L T \tag{15}$$

where L is Lorentz number depending on band structure, diffusivity and level of degeneration. For metals the Lorenz number is equal to the Sommerfield value, and it is commonly used to calculate the thermal conductivity from the electrical conductivity in metals [7]. However, for inorganic semiconductors, the Lorenz number deviates from the Sommerfield value, due to the introduction of disorder into the system [7].

2.4 Figure of Merit ZT

Thanks to Edmund Altenkirch in 1911 who introduced the concept of dimensionless unit (Figure of merit, *ZT*), thermoelectric materials performance can be evaluated [12]. Then Abram Fedorovich Ioffe, in 1931, applied successfully this concept to semiconductors materials [13].

Because only material properties are involved in *ZT* expression; the figure of merit express material efficiency in heat-electricity conversion. *ZT* is the reference in the classification of thermoelectric materials. The figure of merit is defined by following equation:

$$ZT = \frac{S^2\sigma}{\kappa} T \tag{16}$$

Where the electrical conductivity σ, Seebeck coefficient S, thermal conductivity κ of the material and the operating temperature T (average temperature between the hot and cold sides) are expressed [14]. The product in the numerator, $S^2\sigma$, is known as the Power Factor (PF). Sometimes PF is used to compare thermoelectric materials when κ is ignored because of its weak evolution or difficulty to be measured.

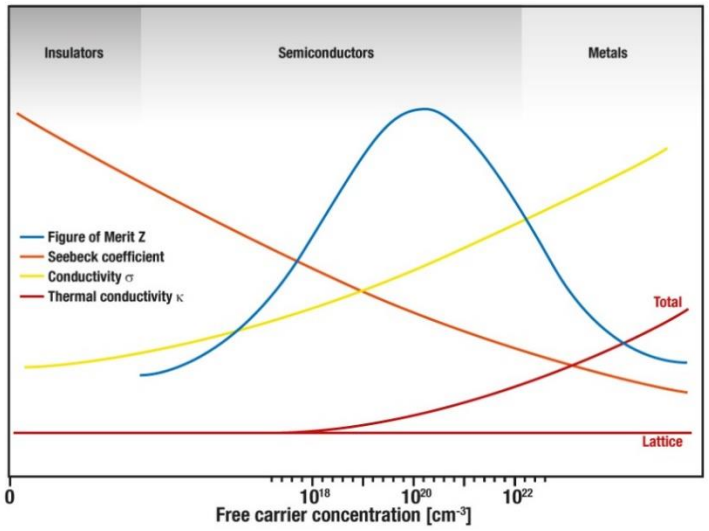

Figure 5: Seebeck coefficient, electrical conductivity, thermal conductivity and ZT as function of free carrier concentration [15 - 17].

Improving thermoelectric performance is fundamentally challenging because S and σ are anti-correlated, and coupled with κ. The enhancement challenge is graphically illustrated in Figure 5. The *ZT* relationship suggests that to improve performance one might aim to enhance the electrical conductivity, which can be done, for example, by increasing the carrier concentration, n (σ=$nq\mu$). However, increasing the carrier concentration generally leads to a reduction in the material's Seebeck coefficient and an increase in the thermal conductivity. As a result, improvements in *ZT* have been hard to achieve and limited to an optimization problem. Useful thermoelectric materials are typically doped semiconductors or semi-metals that can balance the thermal and electrical properties [14–18]. The ideal thermoelectric material, therefore has very low κ and high σ, which is often described as a "phonon-glass, electron-crystal" [18].

The best thermoelectric material in 2016, with high *ZT*, were bismuth telluride alloys at low temperature (*ZT* = 1.86 at 320K) and lead telluride at high temperature (*ZT* = 2.2 at 915K) [19].

3. Thermoelectric device

A thermoelectric device is composed of two thermoelectric materials, a n-type (electron transporting) and a p-type (hole transporting) semiconductor, connected together electrically in series and thermally in parallel. One n-type or p-type part is called “leg” or “plug”. The array is sandwiched between electrically insulating heat spreaders on both the hot side and cold side. Under an applied thermal gradient, charge carriers flow from the hot to the cold side, and the resulting electrical potential can be harnessed as usable electricity (Figure 6 (a)). If operated in reverse (flowing electricity through the material to generate a temperature difference), thermoelectric effects can also be used for cooling applications as Peltier coolers (Figure 6 (b)).

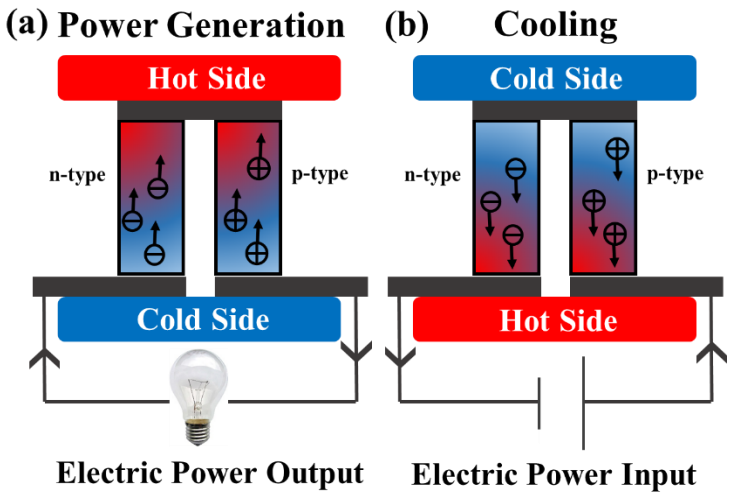

Figure 6: Schematic principle of (a) Seebeck and (b) Peltier effects under a gradient of temperature

This part is focused on power generation device. Device thermoelectric efficiency η_{TE} is defined by the ratio between electric power produced *Pe* on thermic flux crossing hot side *Qc* [14,20]. The equation is given below (equation (17)) and some hypothesis were made (more details about this equation (17) in Chapter 5):

- Material thermoelectric properties are constant;
- Temperature on each side is uniform;
- All heat flux crosses thermoelectric materials from hot side to cold side;
- Electric contact between thermoelectric materials are supposed perfect.

$$\eta_{TE} = \frac{Pe}{Qc} = \frac{T_H - T_C}{T_H} \cdot \frac{\frac{m}{m+1}}{1 + \frac{(m+1)}{Z \cdot T_C} - \frac{\frac{T_C}{T_H}}{2 \cdot T_C \cdot (m+1)}} \quad (17)$$

Where T_H is the temperature at the hot junction, T_C is the temperature at the cold junction and m is the ratio between load electric resistance on internal electric resistance of the thermoelectric module. By using an optimal value for *m* ($m_{opt} = \sqrt{1 + ZT}$), shown by Ioffe [21], device thermoelectric efficiency η_{TE} becomes maximal efficiency η_{max} [22]:

$$\eta_{TE\ max} = \frac{Pe}{Qc} = \frac{T_H - T_C}{T_H} \cdot \frac{\sqrt{1+ZT} - 1}{\sqrt{1+ZT} + 1} \quad (18)$$

In these equations, the term $\frac{T_H - T_C}{T_H}$ is related to Carnot cycle efficiency for reversible process. The second term is directly related to thermoelectric system (*ZT*) and has an huge influence on thermoelectric efficiency η_{TE} value as this shown Figure 7. But, because thermoelectric cycle isn't a reversible process, that means conversion efficiency can't achieve maximum Carnot efficiency. This limitation is due to all irreversible process from *ZT* parameters.

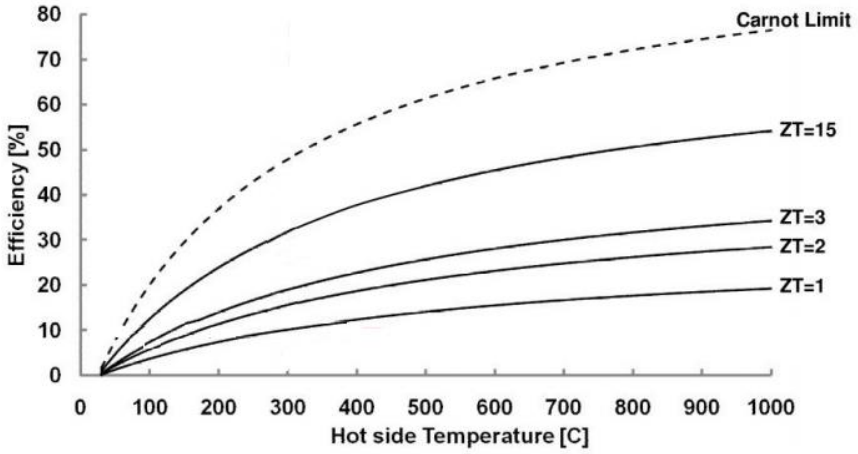

Figure 7: Thermoelectric efficiency as function of temperature for different ZT value

So performing thermoelectric material must have high *ZT* value in order to obtain the best efficiency. Thanks to Figure 5, an overview of changes in physical characteristics as a function of charge concentration is possible. Thus there exists an optimal charge density at the maximization of *ZT*, and that corresponds to the field of semiconductors. For high temperature applications, such as waste heat recovery from vehicle exhaust, only inorganic materials are stable enough to be useful and active research is ongoing into a number of inorganic classes of materials, including silicides, skutterudites, half Heusler alloys, inorganic clathrates, and oxides [18]. At low operating temperatures (below 200°C), alloys of the inorganic semiconductor, bismuth telluride (Bi_2Te_3), have long been the benchmark thermoelectric material with a *ZT* of approximately 1 (which equates to ~5% efficiency at 100 K temperature difference) [18,23,24]. In laboratory, a *ZT* higher than 2 was already obtained, but there are still a number of years before this type of material will be available for the industry [25]. However, bismuth telluride is toxic, not earth abundant, and fragile, resulting in rigid and brittle module architectures. Conducting polymers and molecular semiconductors are an attractive earth abundant alternative for low temperature applications.

B Polymer thermoelectric

1. Introduction – Motivation

These lasts years conducting polymers appeared as great candidates for thermoelectric applications [26] thanks to a unique combination of properties [27]. Semiconducting polymers can have high electrical conductivity around σ ~ 1000 S/cm [27] and a relatively low thermal conductivity compare to conventional inorganic semiconductors (κ_{pol} ~ 0.1-1 $W.m^{-1}.K^{-1}$, κ_{inorg} ~ 10-100 $W.m^{-1}.K^{-1}$) [28–31]. Furthermore, polymers have the major advantages of being printable, flexible and moldable, in comparison to their inorganic rigid counterparts [32] as its shown Figure 8 [26].

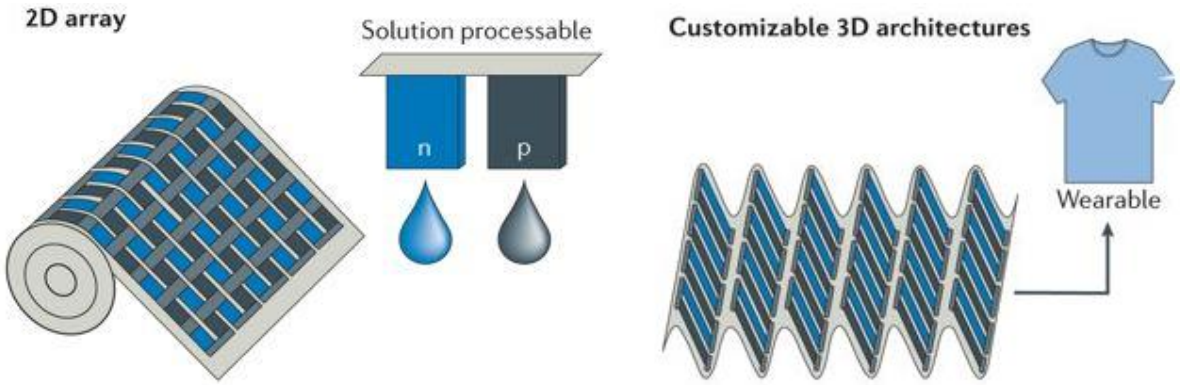

Figure 8: Organic thermoelectric materials compatible with 2D processing enable customizable and easily optimizable device architectures.
(Left) 2D thermoelectric generator obtained by roll-to-roll printing of p-type & n-type material.
(Right) 2D arrays transformable into flexible and lightweight 3D structure. [26]

Printing technology is a low-cost manufacturing technique that enables the replication of a large number of legs in order to produce a large thermos-voltage. This is achievable in a single manufacturing process without high temperature treatment and on flexible substrates. As a result, polymer thermoelectric are candidates for self-powered devices in powering everyday appliances (i.e. cellphones). Currently, in laboratory, thermoelectric generators are designed by the same way. For example, E. J. Bae et al. used a printer in order to obtain a 2D printed thermoelectric array generating a stable thermoelectric voltage of over 2 mV in response to human body heat (Figure 9 (a)) [33]. Likewise, S. Hwang et al. made a 3D drop cast thermoelectric generator consisting of 48 elements achieving an output power of almost 2.5 μW, at a temperature gradient of ~35 K (Figure 9 (b)) [34].

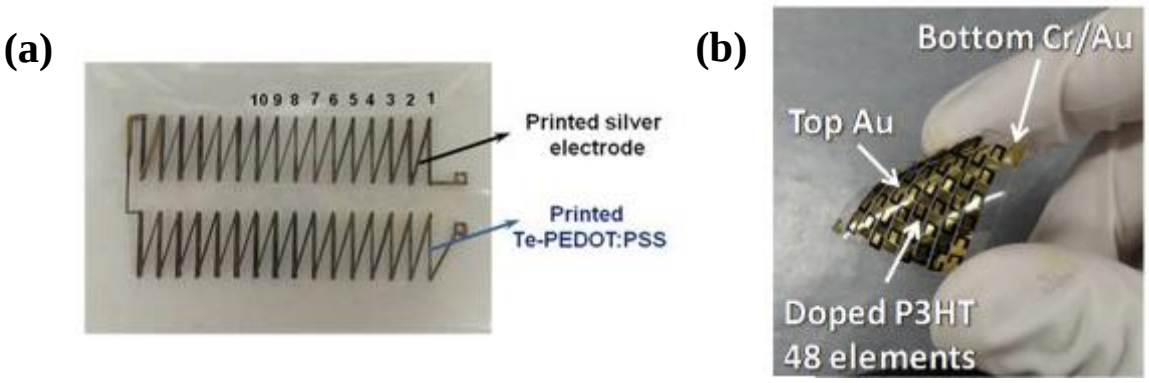

Figure 9: (a) Image of a 32-legs planar thermoelectric generator on flexible PET substrate [33]. (b) Image of a 48 elements 3D thermoelectric generator on flexible PET substrate [34].

Promising results were obtained thanks to rigorous strategic material design, in order to compete with efficiencies of inorganic thermoelectric generator. However, the main disadvantage of polymers is their lower thermoelectric efficiency in comparison to their inorganic compartments. In the next parts, several reported strategies on the enhancement of the thermoelectric properties of polymers (p- & n-type) are going to be reviewed.

2. p-Type thermoelectric material

At their beginning, conducting polymers were not envisioned as prospective thermoelectric materials. The first conducting organic polymer to be extensively studied was *trans*-polyacetylene [35–39]. Conductivities of 560 $S.cm^{-1}$ and high carrier mobilities of approximately 1 $cm^2.V^{-1}.s^{-1}$, due to polyacetylene linearity, were reported when p-doped with arsenic pentafluoride (AsF_5). The first Seebeck measurement was done on this polyacetylene to understand the nature of the charge carrier. By varying the doping level of polyacetylene, Park et *al.*, shown that the Seebeck coefficient decreases for high carrier concentrations [40]. Nevertheless, it's only thirty years later that Hiroshige *et al.* reported the first demonstration of the potential for polymers in thermoelectric (ZT = 0,1) by doping PPV with iodine [41].

The representative p-type thermoelectric polymer include poly(3,4-ethylenedioxythiopene) (PEDOT), polythiophene derivatives (more particularly poly(3-hexylthiophene, P3HT), polyaniline (PANi), polypyrrole, polyphenylenevinylene (PPV), polycarbazole (like poly[N-9'-heptadecanyl-2,7-carbazole-alt-5,5-(4,7-di-2-thienyl-2',1',3'-benzothiadiazole], PCDTBT) and poly(benzodithiophene) (like Poly[[4,8-bis[(2-ethylhexyl)oxy]benzo[1,2-b:4,5-b']dithiophene-2,6-diyl][3-fluoro-2-[(2-ethylhexyl) carbonyl] thieno[3,4-b]thiophenediyl]], PTB7) (Figure 10).

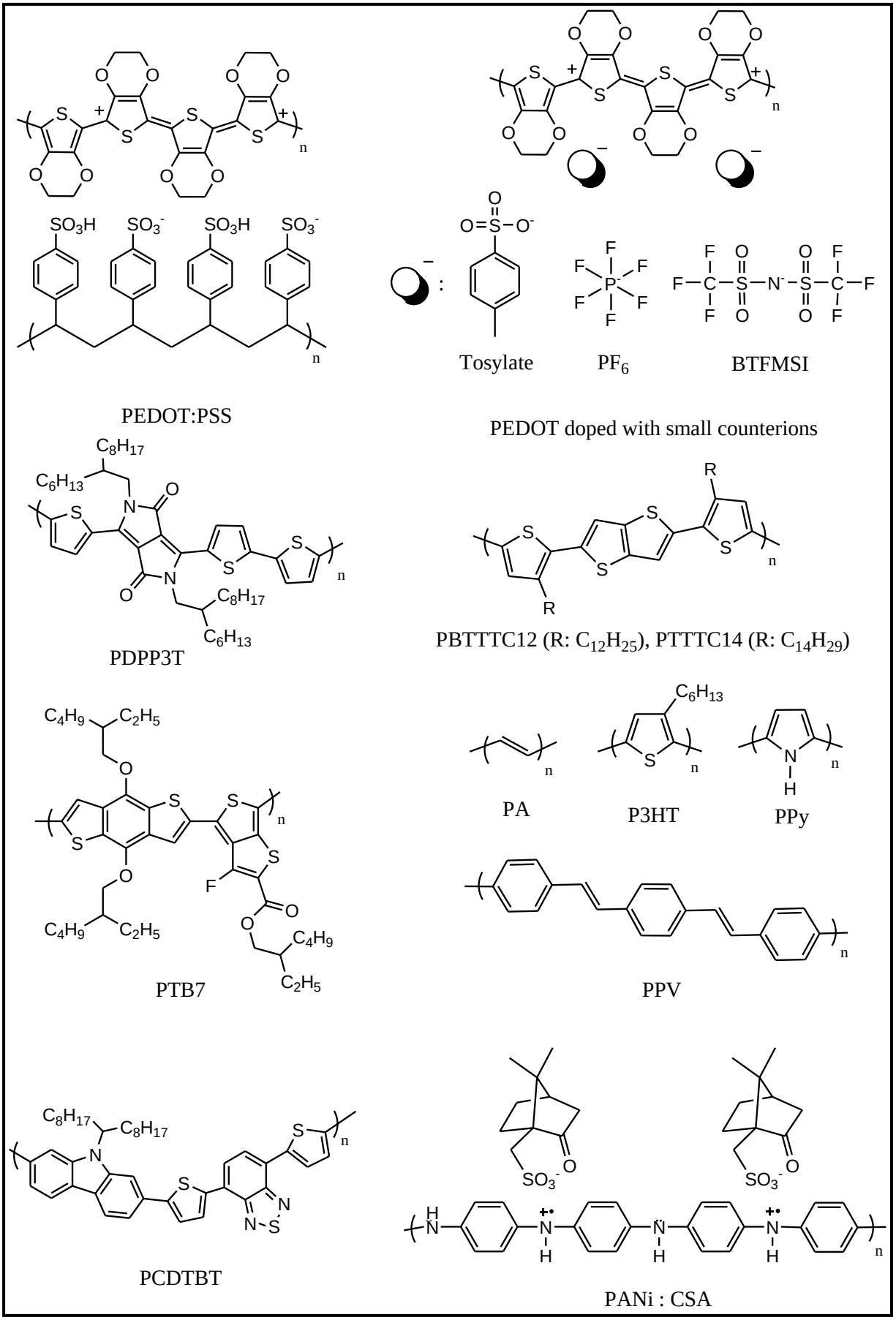

Figure 10: Chemical structure of p-types polymers

2.1 PEDOT material

The PEDOT family is the most used and developed p-type material for thermoelectric material. In particular, PEDOT:poly(styrenesulfonate) (PEDOT:PSS) and PEDOT:p- toluenesulfonate (PEDOT:Tos) have received the greatest attention [42–44].

PEDOT:PSS is water dispersible, and its solutions are commercially available. But as- prepared PEDOT:PSS film has low thermoelectric properties with low electrical conductivity <1 S/cm, and low Seebeck coefficient around 15 µV/K [45–54]. These poor properties are linked to the excess PSS that helps to stabilize PEDOT in water [46]. Thermoelectric properties, particularly electrical conductivity, can be enhanced by removing the excess PSS by a couple of methods developed recently [33,55–63]. Furthermore, Seebeck coefficient can be improved by dedoping or adding structural agent [45].

In-situ synthesized PEDOT:Tos has also been studied because of its easy fabrication and good electrical performance [64–68]. PEDOT:Tos thermoelectric efficiency has been also optimized by chemical dedoping and enhance of structural engineering [44].

2.1.1 Structural engineering – Morphology tuning

Structural engineering, also called "secondary doping", allows to enhance the electronic properties of the material [69]. In principle, higher degree of crystallinity or order means a more electrically conducting material (charge transport is facilitated) [70.71]. However, this also benefits the Seebeck coefficient of the system, as the charge carriers can diffuse easier under a thermal gradient, resulting in a high Seebeck coefficient [72,73]. So treating with solvent, vapor or solution, allows to modify the composition and film morphology without changing the doping level. The thermoelectric performance of PEDOT:PSS can be enhanced by adding dimethyl sulfoxide (DMSO), ethylene glycol (EG), or poly(ethylene oxide) (PEO) into its solution [55,56,74–76].

The effect of the high boiling point solvents like DMSO and EG on thermoelectric properties of PEDOT:PSS was highlighted by Kim *et al* [77]. PEDOT:PSS films were treated in DMSO and EG bath to remove excess of insulating PSS, in order to improve the polymer power factor to 469 µW/m.K². Later, Palumbiny *et al*. [78] demonstrated that this kind of treatment enhances the thin film crystallinity, as the high boiling point solvents act as plasticizers and slow down the crystallization kinetics. As a result, the polymer chains can rearrange in the thin film,

increasing the degree of crystallinity and assisting the charge carrier transport in the system (Figure 11) [51,78,79].

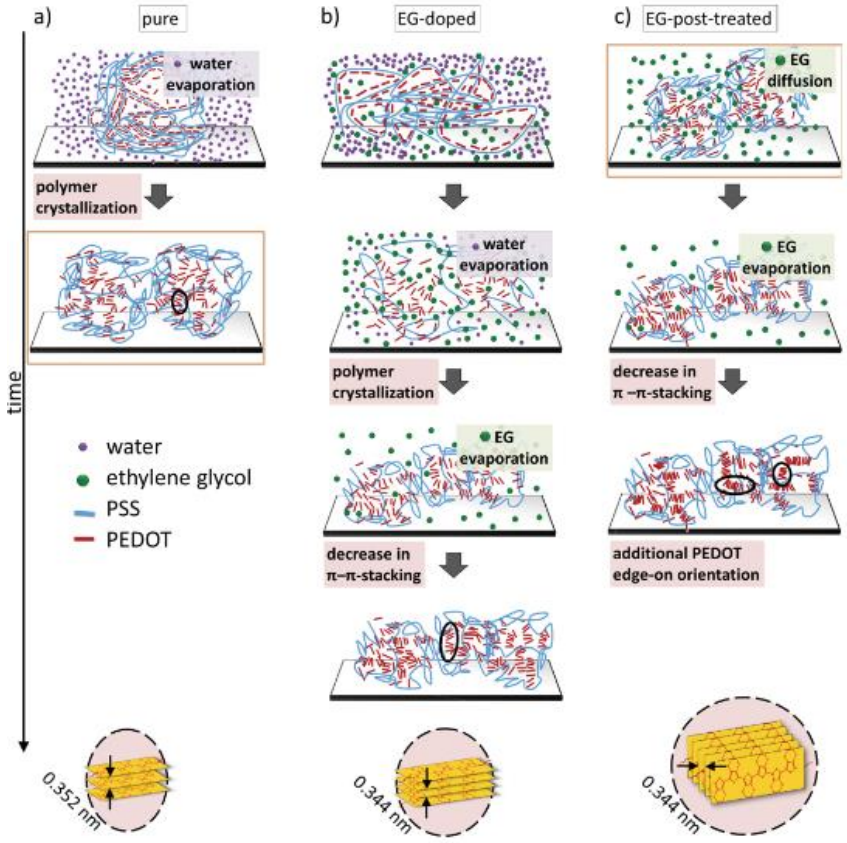

Figure 11: Plasticizing effect agents on the PEDOT:PSS structure. When EG is added to PEDOT:PSS material (b), the crystallization process is shown down resulting in better stacked chains, in comparison to the pure material (a). When the thin films are further treated with an EG bath, the system recrystallize and shift from a face-one to an edge-on configuration (c). [57] [78] [79]

More explanation was given by Bubnova *et al.* [72] proposing that PEDOT derivatives with increased crystallinity could behave as semimetals, thus having both a high electrical conductivity and a high Seebeck coefficient. In PEDOT systems of high crystallinity, the π- orbitals of the PEDOT units recombine into a bipolaron network, which broadens all the π- orbitals of the polymer, thus increasing the slope at the density of states and the Seebeck coefficient. As a result, vapor phase polymerized PEDOT:Tos films exhibit power factor as high as 454 $\mu W/m \cdot K^2$. In recent years, more studies support the beneficial effect of crystallinity on the thermoelectric properties of PEDOT derivatives [72,80–82].

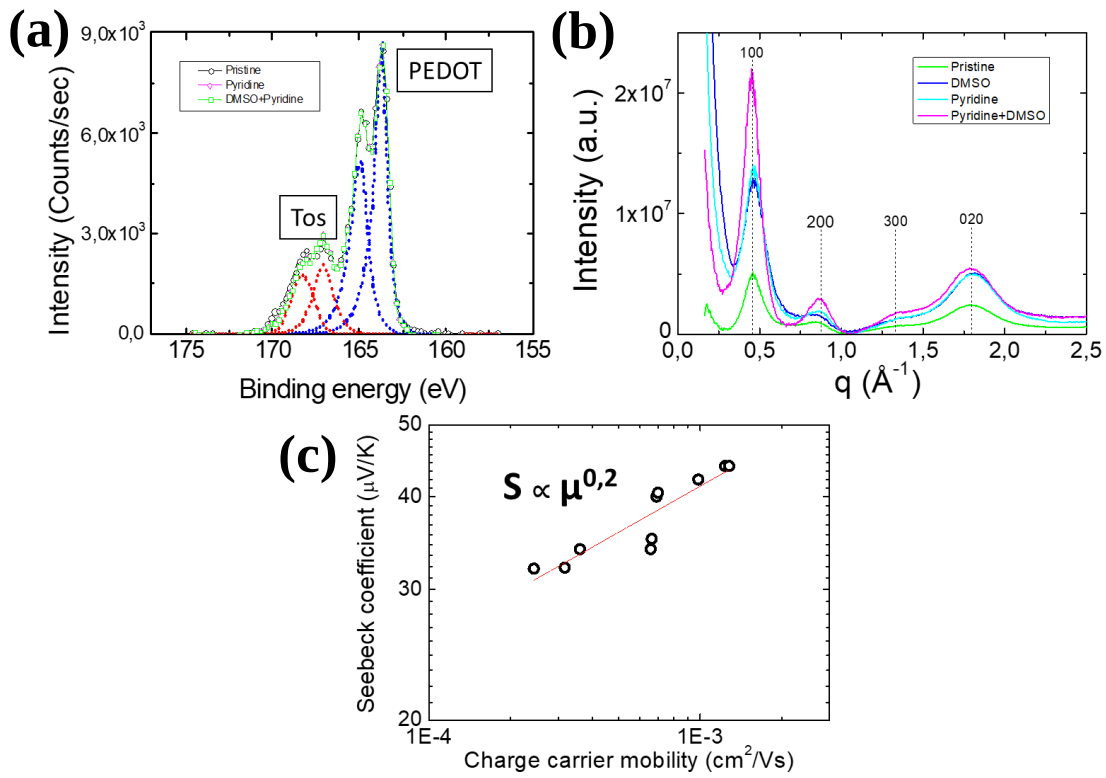

Figure 12: (a) The radially averaged intensity versus the scattering vector q for the various PEDOT :Tos samples. A higher intensity in the peak corresponding to the (100) reflection is respective to a system of higher degree of crystallinity. (b) XPS spectra of PEDOT:Tos samples with various solvent additives. (c) Extracted relationship between Seebeck coefficicent and charge carrier mobility with constant oxidation levels. [73]

In their works, Petsagkourakis *et al.* correlated charge carrier mobility, thin film crystallinity and thermoelectric properties of conducting polymers, PEDOT:Tos thin films [73]. Two additives, DMSO, a high boiling point solvent, and pyridine, an organic base were mixed to the polymer solution to enhance the degree of crystallinity of PEDOT:Tos thin films (Figure 12 (b)). This treatment didn't affect the oxidation level of the polymers, as proven by X-Ray photoelectron spectroscopy (XPS) (Figure 12 (a)). So the conductivity of these samples is directly related to the mobility, because the oxidation level is the same. A relationship between Seebeck coefficient and charge carrier mobility was extracted for those films, $S \sim \mu^{0.2}$ (Figure 12 (c)).

2.1.2 Tuning of the doping level

One of the biggest concerns about thermoelectric development is the modest electrical conductivity of intrinsic polymer materials (pristine PEDOT:PSS σ = 0.1 – 0.5 S/cm) [83]. In case of PEDOT, it was shown that the thermoelectric properties of films could be enhanced by

removing the unionized portion of the counter-anion molecules, which reduces charge-carrier mobility [84]. This process is called "de-doping".

As reference study, Bubnova *et al.* optimized thermoelectric properties of PEDOT:Tos by an exposure to reductive vapors. By de-doping the material, the Seebeck coefficient increased while the electrical conductivity decreased, showing a similar behavior as inorganic materials (Figure 13). The power factor was optimized from 38 to 324 µW/m.K², and a figure of merit of 0.25 at room temperature was obtained (thermal conductivity of 0.25 W/m.K²) [44].

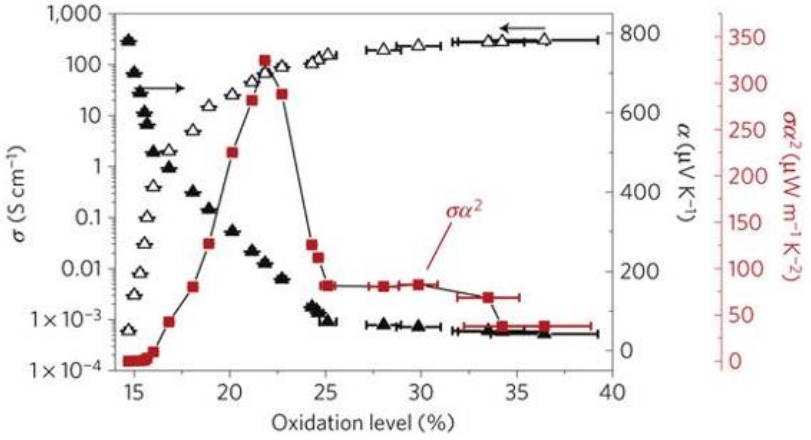

Figure 13: Electrical conductivity σ, Seebeck coefficient S, and the power factor σS², versus the oxidation levels of the PEDOT:Tos films [44].

The degree of de-doping in a material is heavily affected by the electrochemical potential and the chemical nature of the reducing agent itself as shown by Massonnet *et al.* [85] upon dipping films of PEDOT:PSS in different reducing agents like tetrakis(dimethylamino)ethylene) (TDAE) or hydrazine. Khan *et al.* [86] shown the impact of the pH on thermoelectric properties of PEDOT films (Figure 14). The pH of the solutions impacted the electrical conductivity and the Seebeck coefficient, allowing for optimization of the system. Later, Fan *et al.* [87] washed pristine PEDOT:PSS with sulfuric acid then a reducing agent. The sulfuric acid increases the electrical conductivity both by oxidation and by changing morphology. The power factor of PEDOT:PSS was enhance from 0.0045 µW/m.K² to 334 µW/m.K².

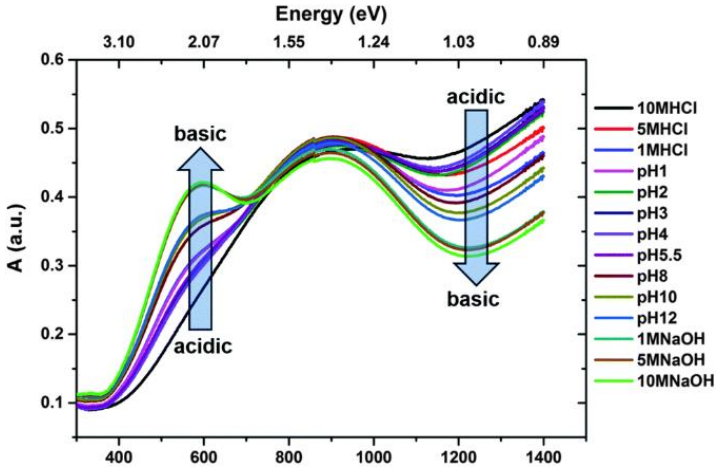

Figure 14:UV-Vis spectra of acid and base treated PEDOT:Tos with respect the pH of the treating solution [41]

All previous works concerned conventional chemical redox reaction, an alternative approach for doping optimization is electrochemical methods, offering a better control. A typical electrochemical setup is composed of three electrodes: a working, a reference and a counter electrode. This technique consists in depositing a polymer film by oxidation (anodic polymerization) on the surface of a noble metal electrode (gold, platinum) [88]. The films obtained by electrochemical polymerization are films whose properties and structure are better defined and controlled. Parameters such as temperature, current density, frequency, electrolyte, counter-ions for PEDOT could be used to modify the morphology and film properties [89]. Park *et al.* [90] synthesized PEDOT:Tos by this process, and obtained a record power factor of 1270 µW/m.K^2. Another use was reported by Bubnova *et al.* [91] where an organic electrochemical transistor was used to optimize their thermoelectric properties of PEDOT:PSS.

2.2 Other p-type polymers

Historically, the first conductive polymer was *trans*-polyacetylene [35–39], a "non-PEDOT family" p-type polymer. Despite, PEDOT:PSS and derivatives are widely represented in thermoelectric field, a lot of groups worked on other p-type polymers to obtain the best thermoelectric generator. As in case of PEDOT, works have been carried out to improve the thermoelectric properties of p-type polymers through an optimization of their morphology and level of doping.

2.2.1 Polyacetylene (PA)

When polyacetylene is doped with halogens such as chlorine, bromine or iodine vapors and with pentafluoride (AsF_5) the electrical conductivity could be further increase to 20.000 S/cm [35,92,93]. Stretching also caused enhancement in conductivity from 3000 to 6000 S/cm in iodine doped films [94]. Roth *et al.* were the first to measure thermoelectric properties of polyacetylene doped with metal halides like $FeCl_3$, $ZrCl_4$ and $NbCl_5$ [94,95]. Despite being the first polymer showing "huge" electrical conductivity of 44 S/cm resulting in the highest power factor of 9.9 $x10^{-4}$ $\mu W/m.K^2$ after doping [96], polyacetylene is unsuitable for thermoelectric applications, mainly due to its poor solubility and poor oxidative stability in air. Those promising results on polyacetylene were the beginning for the course of more stable p-type materials under atmospheric conditions.

2.2.2 Polyaniline (PANI)

Polyaniline (PANI) is a very popular conducting polymer because of its easy synthesis and properties such as good stability, mechanical flexibility and solution processability. One interesting property of polyaniline is ability to change Seebeck coefficient sign by varying pH level of dopants or adding organic/inorganic groups [97–99]. Furthermore, polyaniline synthesis is easy and can be carried out chemically or electrochemically, leading to materials with differing electrical conductivities [100]. Because electrical conductivity depends upon its oxidation states, and that polyaniline has three distinct oxidation states and acid/base doping response, conductivity can be varied between 10^{-7} to 3 $x10^2$ S/cm [101,102].

The dependence of the doping concentration (HCl) on the thermoelectric properties of PANI was studied by Li and co-workers and the maximum *ZT* value of 2.7 $x10^{-4}$ at 423 K was achieved [103]. Nath *et al.* used camphor sulphonic acid (CSA) to dope PANI and obtained high *ZT* value of 0.77 and 2.17 at 45 K and 17 K [104]. The outcome of this study can be used for low temperature devices like Peltier coolers. An alternative strategy to increase thermoelectric properties was the cross-linking of monomer repeat units in polyaniline. Due to a better order between chains, charge transport was improved so mobility and conductivity increased by almost 25% compare to linear polymer [105].

2.2.3 Polypyrrole (PPy)

Like polyaniline, polypyrrole (PPy) is a very popular conducting polymer. Polypyrroles are a good choice for thermoelectric applications thanks to a good conductivity and mechanically stable flexible films. It exists various ways to fabricate flexible conducting PPy film like oxidative polymerization by using pyrrole monomers and iron(III) trichloride ($FeCl_3$) or electrochemically [106–108]. The electrochemical synthesis is often preferred because polymer chains are directly doped, by $(Fe(CN)_6)^{-3}$ [109]. The best method is freezing interfacial polymerization which allows to obtain high electrical conductivity of 2000 S/cm due to an increase in order in polymeric structure [108]. The main drawback of these polymers could be their low Seebeck coefficient at room temperature [110], best value of power factor reported was 3.9 $\mu W/m.K^2$ [111].

2.2.4 Poly(3-hexylthiophene) (P3HT)

Regioregular P3HT is an alkylated derivative of polythiophene, and one of the most studied conjugated polymers. He has an excellent solubility and film forming properties, moreover is commercially available [112]. Without surprise, after P3HT successfully introduced into organic photovoltaics and organic field effect transistors, many scientists were interested in exploiting this polymer in thermoelectric field.

Crispin *et al.* were interested in evaluating the thermoelectric properties of P3HT film using nitrosonium hexafluorophosphate ($NOPF_6$) as dopant [38b]. The maximum power factor was obtained at doping levels ranging from 20 to 31%, giving a power factor of 14 $\mu W/m.K^2$. This result was explained as following, at low doping levels the large PF_6^- anions prevent an ordered structure within the P3HT, but with increasing doping levels the disorder within the polymer matrix diminishes and so does the Seebeck coefficient, whilst the electrical conductivity increases. Similarly, Zhu *et al.* doped P3HT with ferric salt of $TFSI^-$ in order to obtain power factor of 20 $\mu W/m.K^2$ [113].

More recently, scientist community shows more interested in organic dopant, such as the electron acceptor 2,3,5,6-tetrafluoro-7,7,8,8-tetracyanoquinodimethane (F4TCNQ) [114–116]. Molecular dopants undergo ground-state charge transfer with their host semiconductor, yielding polarons or bipolarons on the semiconductor [116-117]. The dopant anions remain in the film. One main drawback is the solution processing of doped films, doping often results in drastically reduced solubility of polymers, so mixed polymer:dopant solutions must be kept at high temperatures and dilute concentrations to avoid aggregate [118,119]. With this conventional

solution processing, an electrical conductivity around 4 x 10^{-4} S/cm and a power factor around 6 x 10^{-3} µW/m.K^{-2} were obtained [120a]. A major problem with the bulk doping method is that the large amount of F4TCNQ negatively affects the morphology of the P3HT film and leads to F4TCNQ aggregation, preventing to achieve higher conductivity [121].

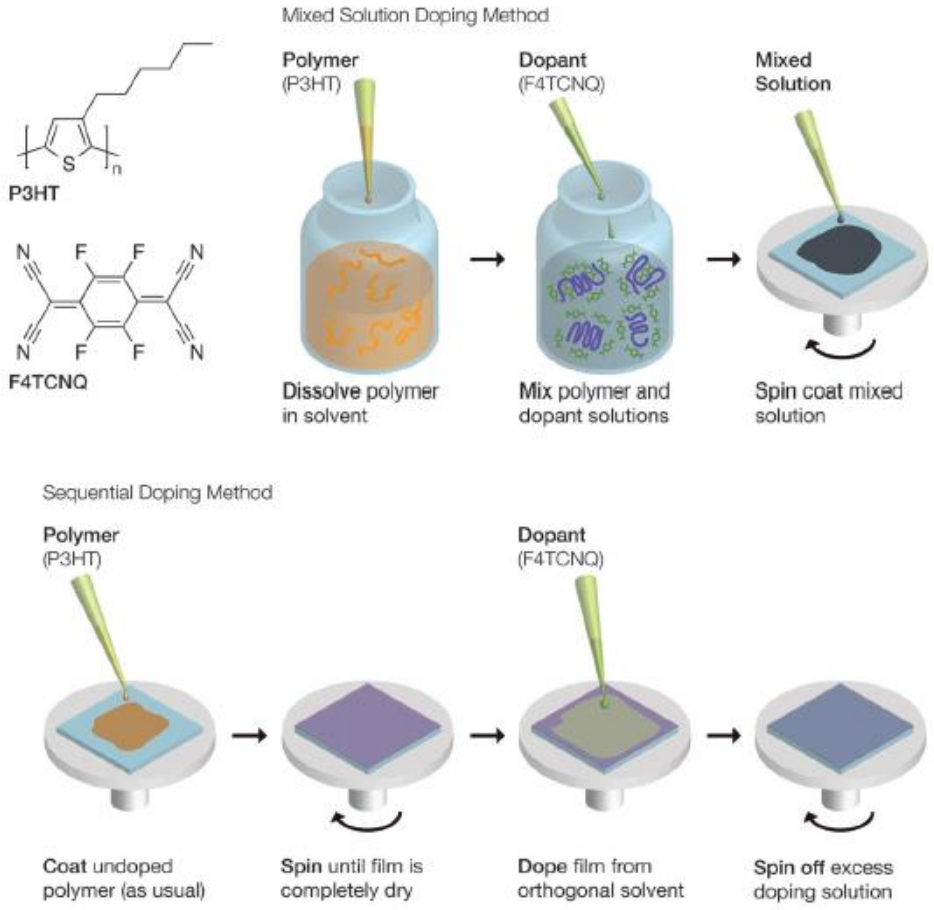

Figure 15: Schematic of the two methods of P3HT doped with F4TCNQ. [115]

In their study, Jacobs *et al.* compared film properties from a standard mixed-solution versus a sequential method (Figure 15) [115]. They observed that sequentially doped films were much easier to process significantly less rough, and show higher conductivity at a given doping ratio. This higher conductivity (factor 5 to 15) was assigned to morphology improvement and a large number of tie molecules between doped crystalline domains as shown on Figure 16. Sequential procedure achieved 5.5 S/cm and a power factor of 8 µW/m.K^{-2} for thin films [122,123]. Last year, Zuo *et al.* adapted this procedure to obtain thick films (> 1µm) with almost the same properties than thin films, 3 S/cm and a power factor of 5 µW/m.K^{-2} [123].

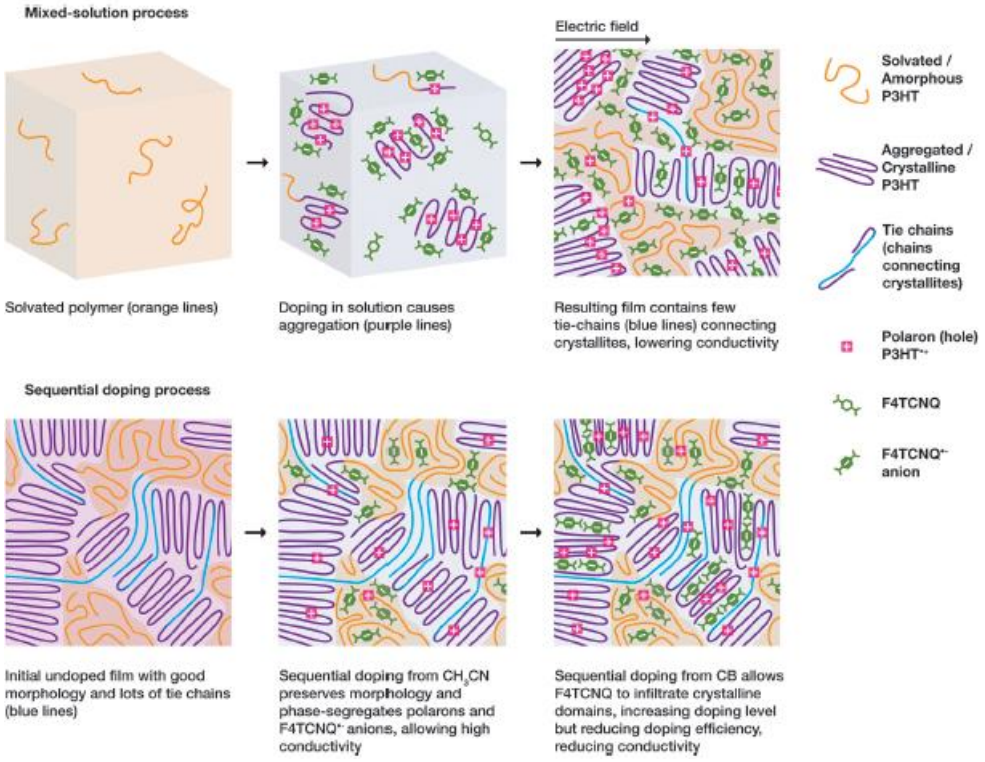

Figure 16: Morphological development in mixed-solution and sequential doping.[115]

Currently, it is not known which polymer configuration (regioregularity, molecular mass) and nanostructure (degree of order) should be selected to maximize the electrical conductivity of F4TCNQ-doped P3HT. In their work, Hynynen *et al*. tried to correlate electrical conductivity and solid-state order by using sequential processing and exposed thin P3HT films to F4TCNQ vapor [117a]. They were able to manipulate various parameters of interest and have a better control of doping step. They also shown that molecular mass didn't strongly affect the electrical conductivity (M_n range 5 to 64 kg/mol). Finally, thanks to a fine tuning of dopant level, they achieved to "control" the crystallinity to obtain 2.7 µW/m.K^2 of power factor (maximum Seebeck coefficient = 63 µV/K and electrical conductivity = 12.7 S/cm) [117b].

2.2.5 Other p-type polymer like PBTTT, PCDTBT, PTB7, …

i. Poly(2,5-bis(3-alkylthiophen-2-yl)thieno[3,2-b]thiophene) (PBTTT)

Research on the high mobility polymer poly(2,5-bis(3-alkylthiophen-2-yl)thieno[3,2-b]thiophene) (PBTTT) investigated the relationships between its morphology, doping, method, and thermoelectric performance. The first dopants used to improve PBTTT's thermoelectric properties was chemical oxidants, $NOPF_6$:acetronitrile solution [124]. Zhang *et al.* compared as-cast and annealed films, doping efficiency was similar for both films based on optical measurements but thermoelectric properties of the annealed PBTTT films (S= 13.5 µV/K and

σ=55 S/cm) were higher than those of as-cast films (S= 11 µV/K and σ= 33 S/cm). The power factor in annealed films was three times higher than as-cast films, which was attributed to the increased structural ordering and domain size [124].

Later, acid dopants like (tridecafluoro-1,1,2,2-tetrahydrooctyl)trichlorosilane (FTS) and 4-ethyl-benzenesulfonic acid (EBSA) were used on PBTTT films [125]. The conductivity of PBTTT films was increased to similar levels, 1000 S/cm and 1300 S/cm for FTS and EBSA. However, the two doping agents led to different Seebeck coefficients, 33 µV/K for FTS and 25 µV/K for EBSA. So significantly different power factors were obtained, 110 µW/m.K² for FTS and 25 µW/m.K² for EBSA, thanks to GIWAXS measurements on PBTTT films shown that both doping agents generally preserved the edge-on structure of PBTTT crystallites and that the changes in short-range order could not explain the difference in Seebeck coefficient [125].

Like for P3HT, F_4TCNQ was used for PBTTT and F_4TCNQ solution-doped PBTTT has reached a power factor of 1.3 µW/m.K² [126]. Vapor process with F_4TCNQ on PBTTT films shown a higher power factor of 32 µW/m.K² [127]. The increase resulted from a significant difference in the electrical conductivity of the films. Vapor-doped films had more than hundred times increase in conductivity compared to solution-doped films with comparable charge carrier concentration [126,127]. This increase in conductivity was attributed to both a higher molar ratio of F4TCNQ in the vapor-doped film. PBTTT was also been doped with 2,5-dufluoro-7,7,8,8-tetracyanoquinodimethane (F2TCNQ), which has a smaller electron affinity than F4TCNQ. Due to the lower doping efficiency, the vapor-doped film with F2TCNQ had a lower conductivity of 36 S/cm and higher Seebeck of 140 µV/K. Despite the lower doping efficiency, F2TCNQ vapor-doped film had a higher power factor, 70 µW/m.K² than the equivalent F4TCNQ-doped film [127]. The Seebeck coefficient was not strongly dependent on morphology at comparable carrier levels. These studies have begun to illuminate the connections between dopant choice, morphology, and thermoelectric properties in PBTTT and suggest that further improvement can be realized by increased charge carrier mobility and controlling dopant concentration [127–129].

ii. Co-polymers

Co-polymerization of donors and acceptors allow for tuning of the electronic properties of semiconducting polymers. Some efforts have been made to measure and improve the thermoelectric properties of these donor-acceptor copolymers, doping method, and processing have not yet been well-explored in this class of polymers.

Several studies on copolymers' thermoelectric properties have focused on carbazole-containing copolymers. Copolymers of carbazole and three different acceptors were synthesized and compared. Poly [N- 9'-heptadecanyl-2,7-carbazole-alt-5,5-(4,7-di-2-thienyl-2',1',3'-benzothiadiazole] (PCDTBT) films doped with $FeCl_3$ were found to have the highest power factor, 19 µW/m.K², of the three polymers [130]. Later, the effect of the carbazole unit on thermoelectric properties was studied by comparing the copolymers poly((9,9-dioctylfluorene)-2,7-diyl-*alt*-(4,7-bis(3-hexylthien-5-yl)-2,1,3-benzothiadiazole)-2',2"-diyl) (F8TBT) and poly(*N*-9'-heptadecanyl-2,7-carbazole-*alt*-(4,7-bis(3-hexyk-thien-5-yl)-2,1,3-benzothiadiazole -2',2"-diyl) (C8TBT). F8TBT has a fluorine unit as the donor, while C8TBT has a carbazole unit. Comparing the properties of these two polymers tests the effect of the nitrogen atom on the thermoelectric properties. The doped C8TBT films had higher conductivity and Seebeck coefficient than the doped F8TBT, leading to a higher power factor [131].

More recently, poly{2,2′-[(2,5-bis(2-hexyldecyl)-3,6-dioxo-2,3,5,6- tetrahydropyrrolo [3,4-c] pyrrole-1,4-diyl)dithiophene]- 5,5′-diyl-alt-thiophen-2,5-diyl} (PDPP3T) films have demonstrated a high power factor compared to other thiophene-containing polymers like P3HT and PBTTT. The power factors of $Fe(TFSI)_3$-doped PDPP3T, P3HT, and PBTTT were compared [132]. PDPP3T's optimum power factor of 25 µW/m.K² was higher than PBTTT, 14 µW/m.K², and comparable to P3HT, 30 µW/m.K². Although their power factors were similar, PDPP3T films had a lower conductivity and higher Seebeck coefficient than other films even at low doping levels (Figure 17) [89,132]. The optimized power factor obtained for PDPP3T films was 276 µW/m.K². This great performance was attributed to the smaller volume of dopants in the PDPP3T films compare to P3HT or PBTTT [133]. This increased power factor suggests that methods of further improving the thermoelectric properties of donor-acceptor copolymers will emerge as future research explores this broad class of polymers.

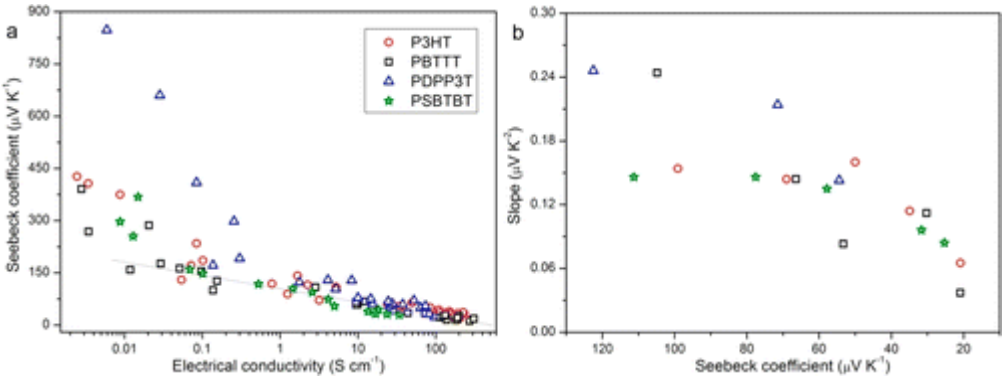

Figure 17: (a) Seebeck coefficient versus the logarithm of electrical conductivity unifying P3HT, PBTTT, PDPP3T, and PSBTBT. (b) Evolution in the slope S/T with Seebeck coefficients, the slope derived from linear-fitting of the positive temperature dependence of Seebeck coefficients. [89][132]

3. n-type "organic" material

N-type polymers have not been as studied for thermoelectric applications as p-type polymers. The stability of n-type polymers is related to the lowest unoccupied molecular orbital (LUMO). The LUMO level can be lowered by introducing electron-withdrawing units in the backbone or as side groups. A couple of n-type organic small molecules were reported, such as naphthalenetetracarboxylic dianhydride [134], benzotriazole [135], perylene bisimide [136], naphthodithiophenediimide [137], and fullerenes [138]. The representative n-type thermoelectric polymer/molecule are presented Figure 18.

N-type doping of polymers is difficult because n-type dopants have small ionization energies, making them more unstable and vulnerable to reactions with air [139]. Organic donor molecules, such as 4-(1,3-dimethyl-2,3-dihydro1H-benzoimidazol-2-yl)phenyl)dimethylamine (N-DMBI) [140a], tetra-n-butyl ammonium fluoride (TBAF) [140b], and cobaltocene ($CoCp_2$) [140c], were employed to dope these n-type molecules. Development of new types of stable dopants and polymers with higher miscibility with dopants is currently under investigation [141].

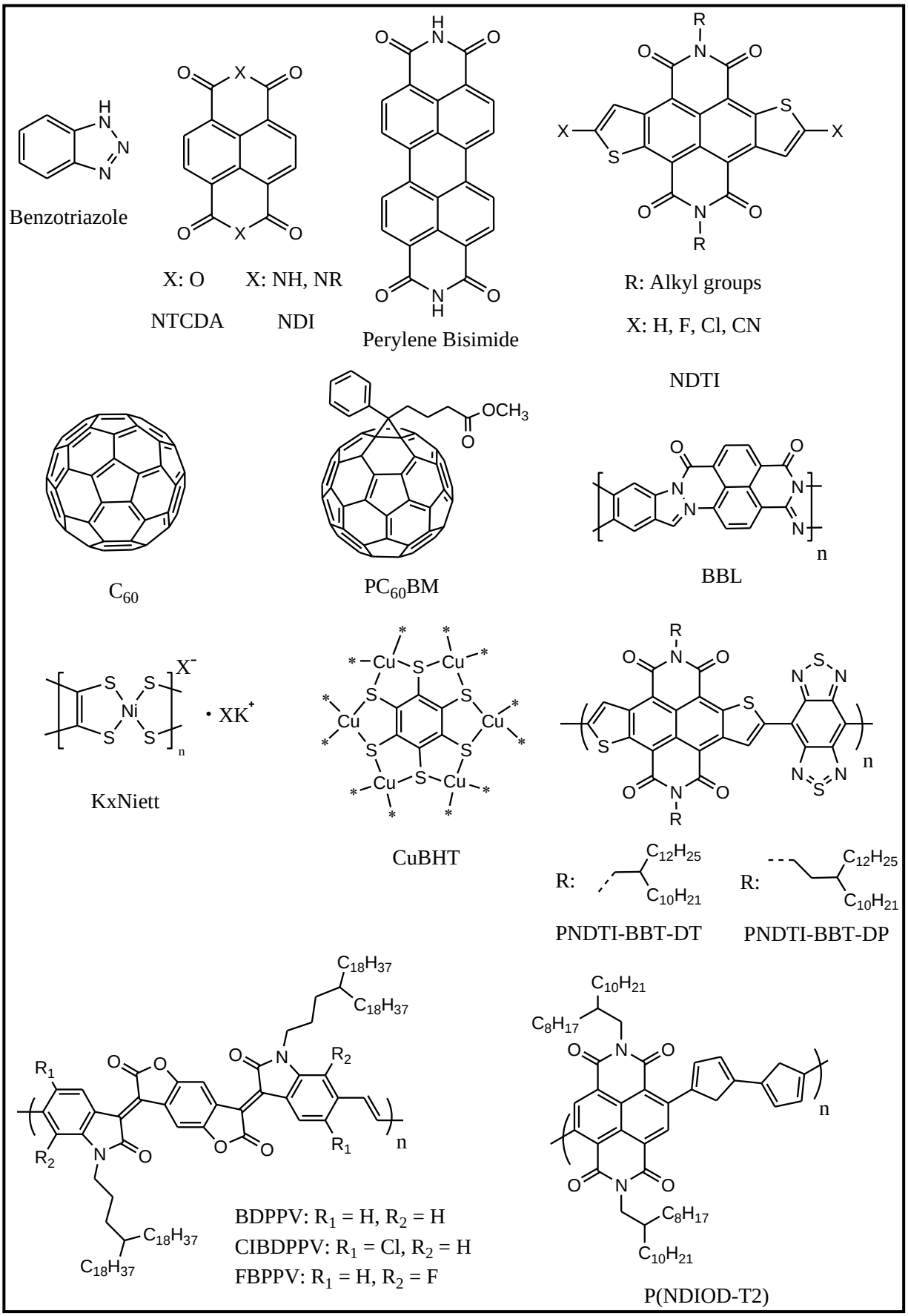

Figure 18: Chemical structure of n-types polymers

Heeger was the first to report n-type behavior for polymer (S = -43.5 μV/K) with polyacetylene doped with TBAF by electrochemical reduction [142]. Conjugated polymers with metal atoms in the backbone can show n-type behavior and have good air stability [143–147]. Currently the best performance as *n*-type is an organometallic polymer based on metal-ethenetetrathiolate (ETT), Poly(Ni-1,1,2,2-ethentetrathiolate) (poly(Ni-ETT)). As a pellet, poly(K_x(Ni-ETT) reached power factors to 66 μW/m.K² [148], and 344 μW/m.K² in an electrochemically polymerized poly(Ni-ETT) film [141]. Besides K_xNiett, the thermoelectric performance of other polymers with the Ni-S coordinate bonds, such as copper benzenehexathiol complex (Cu-BHT), was investigated [149]. Cu-BHT can have a high electrical conductivity over 1500 S/cm and a Seebeck coefficient of -4 to -10 μV/K. However, these polymers are insoluble in common solvents and are difficult to process, limiting the ability to study how they can be further optimized.

Later, Pei and co-workers introduced electron withdrawing elements like Cl and F to *p*- phenylene vinylene (PPV) [150]. FBDPPV (fluorine functionalized benzodifurandione-based poly(*p*-phenylene vinylele) (FBDPPV) doped with N-DMBI had a power factor of 28 μW/m.K² [151]. Like p-type polymers, n-type polymers thermoelectric properties also depend on the morphology. Ma et al. investigated the effect of dopant on the crystallinity on FBDPPV [152]. The GIWAXS indicates that the crystallinity of the polymer varies with the doping level of N-DMBI. FBDPPV with the optimal doping level can exhibit an electrical conductivity of 6.2 S/cm, a Seebeck coefficient of −210 μV/K and a power factor of 25.5 μW/m.K². ClBDPPV (chlorine functionalized benzodifurandione-based poly(*p*-phenylene vinylele) (ClDPPV) doped with TBAF also demonstrated good air stability for a solution-processed *n*-type polymer. Measured in air, doped films had a conductivity of 0.62 S/cm and power factor of 0.63 μW/m.K². After storage in air for one week, films retained a conductivity of 0.1 S/cm [153].

Another group of high-performance solution-processable *n*-type polymers are the naphthalenediimide (NDI) copolymers. Poly{N,N′-bis(2-octyldodecyl)-1,4,5,8-napthalenedicarboximide-2,6-diyl]-alt-5,5-(2,2bithiophene)} (P(NDIOD-T2) with the electron-deficient imidazole groups is one of the most famous n-type polymers for thermoelectric applications. The PNDIOD-T2 polymers in the doped state show better air stability than PPV derivatives. Additionally, they can be dispersed in organic solvents like 1,2- dichlorobenzene and can be thus processed by solution processing techniques. Chabinyc *et al*. investigated this polymer with different dopants including 4-(1,3-dimethyl-2,3-dihydro-1H-benzimidazol-2-yl)-N,N-diphenylaniline (N-DPBI) and N-DMBI [154]. The optimally doped

film had a power factor of 0.6 μW/m.K². Atomic force microscopy (AFM) images shown that N-DMBI had largely aggregated on the films surface, only 1% of dopant molecules contributed a free carrier in the film [154]. These results highlight the importance of dopant-polymer miscibility in improving the thermometric performance of solution-processable n-type polymers. Recent studies have tried to improve the miscibility of N-DMBI in PNDIOD-T2 by replacing the alkyl chains of the NDI unit with PEG chains [155] or by adding polar side chains to both the NDI and thiophene units [156]. Other studies worked on polymer solubility, inspired by PVDIOD-T2, copolymers of naphtho[2,3-b:6,7-b]dithiophenediimide (NDTI) and benzobisthiadiazole (BBT) units like PNDTIBBT-DT and PNDTI-BBT-DP were synthesized [157]. They exhibit an electrical conductivity of 5 S/cm and a PF of 14 μW/m.K².

Conjugated polymers with ladder structures can have high solubility in organic solvents. They were investigated as n-type TE polymers. Ladder-type polymers such as polybenzimidazobenzophenanthroline (BBL) doped with TDAE was reported [158]. Although its PF is only 0.43 μW/m.K², it is soluble in organic solvents like o-dichlorobenzene. Hence, it can be processed in large scale like the p-type PEDOT:PSS.

These studies on n-type polymers with dopant show that the most crucial issues in improving the thermoelectric properties are stability and the miscibility of the dopant in the polymer host.

4. Afterword on polymer/organic n- & p-type materials

Thermoelectric performance of polymer/organic n- & p-type materials could be summarized in a graphical (Figure 19). Electrical conductivity and Seebeck coefficient are obviously dependent on each other, Chabinyc and co-workers [126] suggested the empirical relation $S \propto \sigma^{-1/4}$ ($S^2\sigma \propto \sigma^{1/2}$) for p-type materials, confirmed by Kemerink and co-workers [121] for n-type materials. In some cases, another exponent would result in a better fit of the experimental data. Grey/white lines present a constant figure of merit *ZT* which was estimated assuming a phonon contribution to the thermal conductivity of k_{ph} = 0.2 /m/K and the Wiedemann-Franz law is obeyed. So κ follows σ evolution according to the Wiedemann-Franz law. This relation between κ and σ is a limitation to obtain high *ZT* value, one possible strategy to surpass it could be the decoupling of the electronic and thermal conductivity by creating heterogeneous materials like nanocomposites with inorganic materials that enhance phonon scattering.

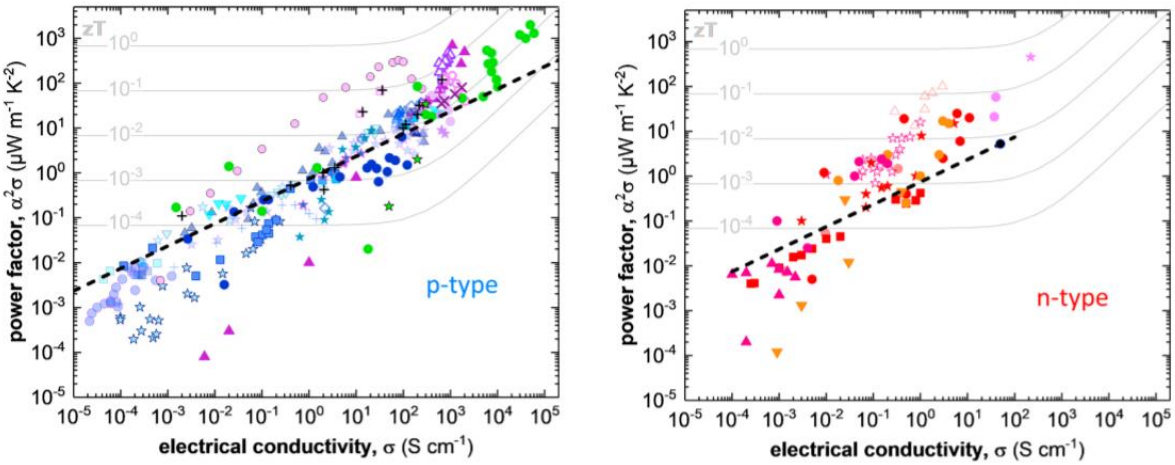

Figure 19: Thermoelectric PF as function of σ for p-type (blue: polythiphene derivates, purple: PEDOT, green: polyacetylene) and n-type materials extracted from literature of previous parts. The dashed lines represent the relation $S \propto \sigma^{-1/4}$ [130][138]. The gray lines represent lines of a constant figure of merit zT.

4.1 Composite

Organic-inorganic hybrid thermoelectrics (TEs) are a fascinating field for both organic and inorganic materials researchers. Most of the work devoted to enhancing the thermoelectric properties of organic materials focuses on increasing the electrical conductivity while, in case of inorganic materials, efforts are directed towards reducing the thermal conductivity of optimally doped systems. One key difficulty is the fact that for most systems, *S*, *σ*, and *κ*, are strongly correlated. The interaction between nanofillers and polymer matrix can often yield decoupled TE parameters, thereby leading to significantly enhanced PF compared with individual components. The fillers of TE composites can be either inorganic or organic, while the matrix can be either insulating or intrinsically conductive [146b].

4.1.1 Polymer-inorganic composites

The main purpose for research into polymer-inorganic composites for thermoelectric is to improve the performance of an already well-known material even further by lowering its thermal conductivity without significantly affecting other properties. Polymer matrices may also provide some degree of flexibility and lower volumetric cost. On the other hand, using a polymer as matrix limits the maximum operational temperature to values typically lower than 500K.

The first attempt of polymer-inorganic composites was filling an array of vertical silicon nanowires by an insulating polymer, in order to lower only κ, while benefiting from an increase

in S due to the reduced dimensionality of the nanowires [159]. Unfortunately, σ strongly decreased, making an unsuccessful attempt.

Later, PEDOT:PSS was used, instead of an insulating polymer, with ball-milled Bi_2Te_3, and power factors of 131 and 80 μW/m.K² for p-type and n-type composites were obtained [160]. While this was an improvement over neat PEDOT:PSS, it remained below the performance of bulk Bi_2Te_3, which was attributed to the contact resistance between the components.

In order to understand the increase in thermoelectric performance of polymer-inorganic material composites, Qiu *and col.* worked on composites of P3HT and Bi_2Te_3 nanowires and cited a doping dependent scattering of carriers as the reason of the improved power factor of 13.6 μW/m.K² [161]. This work suggests an energy-filtering at internal interfaces inducing an increase in thermoelectric performance of polymer-composite composites. Low energy charge-carriers are blocked, decreasing σ, otherwise S is increasing because the average energy carried per charge increases. A study on Te nanowires, PEDOT:PSS and reduced graphene composite confirms an energy filtering effect occurring at both of the distinct interfaces, obtaining a power factor of 143 μW/m.K² [162].

On another side, Liang *et al.* shown that such an effect is not necessarily present. Thanks to a rigorous control of $FeCl_3$ dopant, they tuned energy barrier between P3HT and Te- nanoparticles composites by 1eV. This change didn't affect thermoelectric performance and they concluded that energy filtering was not mandatory to explain it, a simple linear combination of parallel and series transport was relevant [163].

Another keypoint in polymer-inorganic composite is thermal conductivity. Conventional inorganic thermoelectric material possesses high thermal conductivities of 1.2 – 2.8 W/m.K [160,164], nearly one order of magnitude greater than polymers [165]. Thanks to numerous interfaces in the polymer-inorganic composites, phonons scatters and thermoelectric composite have a thermal conductivity close to that of the polymer matrix [120,121].

In case of p-type composites, a high *ZT* of 0.39 was obtained for PEDOT:PSS – Te nanowires treated with H_2SO_4 [33]. Authors explained that a structural rearrangement of PEDOT:PSS, due to the removal of PSS, induced the formation of a more crystalline structure and increased the number of charge carriers enhancing of electrical conductivity of H_2SO_4-treated Te-PEDOT:PSS. For n-type composites, Liang *et al.* dispersed a large amount of Ni nanowires inside a PVDF matrix [153] exhibiting an electrical conductivity of 4701 S/cm and Seebeck

coefficient of -20 μV/K, resulting in a power factor of 200 μW/m.K² which is a record for n-type polymer-inorganic composites.

4.1.2 Polymer-"Carbon" composites

Nanostructured carbon allotropes like carbon nanotubes (CNT) and graphene can also be used as fillers for thermoelectric composites [166–169]. Their main property is their high electrical conductivity. Similar to the inorganic/organic thermoelectric composites, the carbon-based thermoelectric composites have also shown decoupled Seebeck coefficient and electrical conductivity. Furthermore, the thermal conductivity of the composites still remains low due to the phonon scattering thus promising thermoelectric performance.

By looking the graphene properties, it's not an obvious candidate for thermoelectric application, due to its symmetric density of states without band gap, and its high thermal conductivity. Nevertheless, Du *et al.* mixed PANI and graphene nanosheets in pellets and observed a good power factor of 5.6 μW/m.K², due to a high μ in the composite [120b]. Another study shown graphene utility in thermoelectric application, Wang and co-workers used graphene with C_{60} and PEDOT:PSS to obtained a power factor of 32 μW/m.K² and a *ZT* of 0.067 [170]. Finally, another promising approach is the interface engineering in multilayer structures. Promising results were obtained with a layer-by-layer assembly of CNTs and graphene, stabilized in solution by PEDOT:PSS, and polyaniline which demonstrated power factor of 1825 μW/m.K² [171] and 2710 μW/m.K² [172]. These high power factors were due to an increase of mobility and the highly network between multilayers. The same layer-by-layer was applied to n-type material, and a power factor of 190 μW/m.K² was achieved [173].

Carbon nanotubes are one of the most popular nanofillers for thermoelectric application. Several approaches to organic thermoelectric CNT composites exist. The basic principles include electronic percolation, secondary doping (through charge carrier mobility modifications), energy filtering, interface engineering, improved CNT dispersion and chirality selection, and multiple strategies for varying charge carrier concentration.

One of the first experiment between CNT and polymers was a simple composite of CNT and PEDOT:PSS in gum Arabic matrix showing that σ can be partially decoupled from κ [174,175]. The underlying mechanism for this is the fact that electrons are transported through percolative paths, while heat flows in parallel between the insulating matrix and minute amounts of the conductive filler. The interfaces between both materials also have a strong influence, as we will

see below. The gum arabic not only decreased κ of the final film, but also stabilized the CNTs in solution, providing solution-processability. Building on low-κ CNT composites, the gum arabic has been substituted with conducting and semiconducting polymers.

Later, Grunlan *et al.* used an optimized PEDOT:PSS – CNTs composites by using single wall carbon nanotubes (SWCNTs) [176]. They managed to obtain water-processable and flexible thin films with a low thermal conductivity of 0.4-0.7 W/m.K. A thin film composed of 85 wt% SWNT achieves a power factor of 140 μW/m.K². The good modulation between CNTs and polymer matrix was helpful and permitted the formation of highly electrically connecting but thermally impeding CNT-PEDOT-CNT junctions (Figure 20).

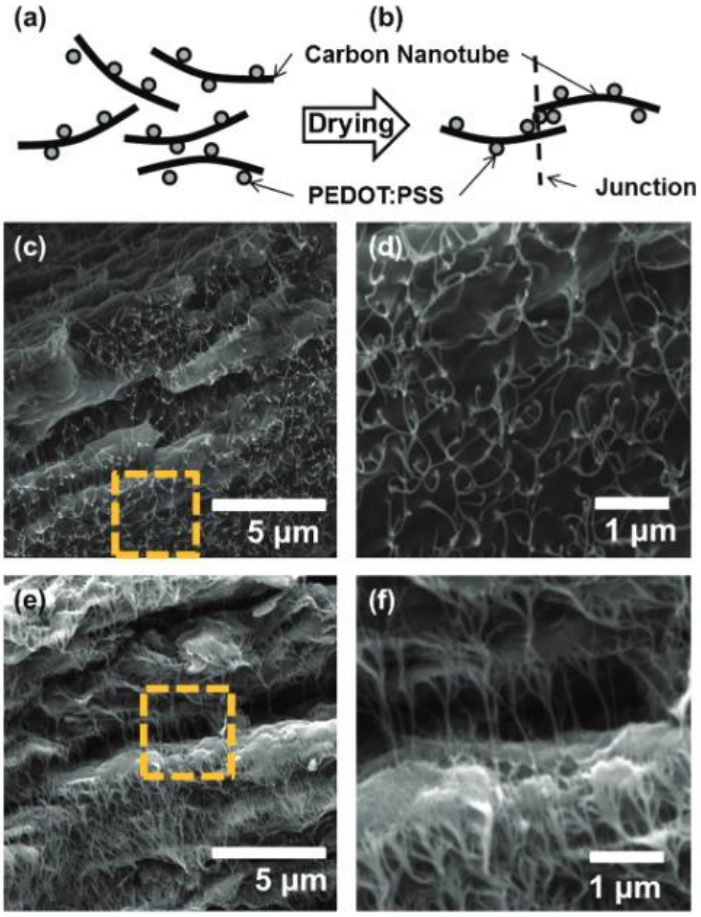

Figure 20: Schematics of CNTs coated by PEDOT:PSS particles in exfoliated state (a) and an electrically conductive junction formed between CNTs (b). SEM cross-sectional images of 20 w% SWNT film (c) and a 60 wt% SWNT film €. Images (d) and (f) are higher magnification images, marked by dotted boxes. The balance of each films is PEDOT:PSS. [176]

Post-treatments were also exploited to enhance thermoelectric properties of composites with CNTs, contributing to enhance more electrical conductivity than Seebeck coefficient. For example, formic acid and DMSO were used to treat SWCNT/PEDOT:PSS composite [177].

Thanks to this treatment, at the same CNT loading, films treated by DMSO and formic acid shown an enhancement of power factor over 300 (464 and 407 μW/m.K²).

Composites were prepared directly by synthesizing conducting polymers in presence of carbon fillers. Such synthesis is known as "template-directed in situ polymerization", thanks to the strong π-π interaction between the carbon lattice and the conjugated polymer backbone. A series of studies on the direct synthesis of carbon-based thermoelectric composites was done by Chen *et al.*. They performed the in situ polymerization of monomers, like EDOT [178], pyrrole [179a], and tried various shapes, such as pie-like [178] and cable-like [179b] (Figure 21).

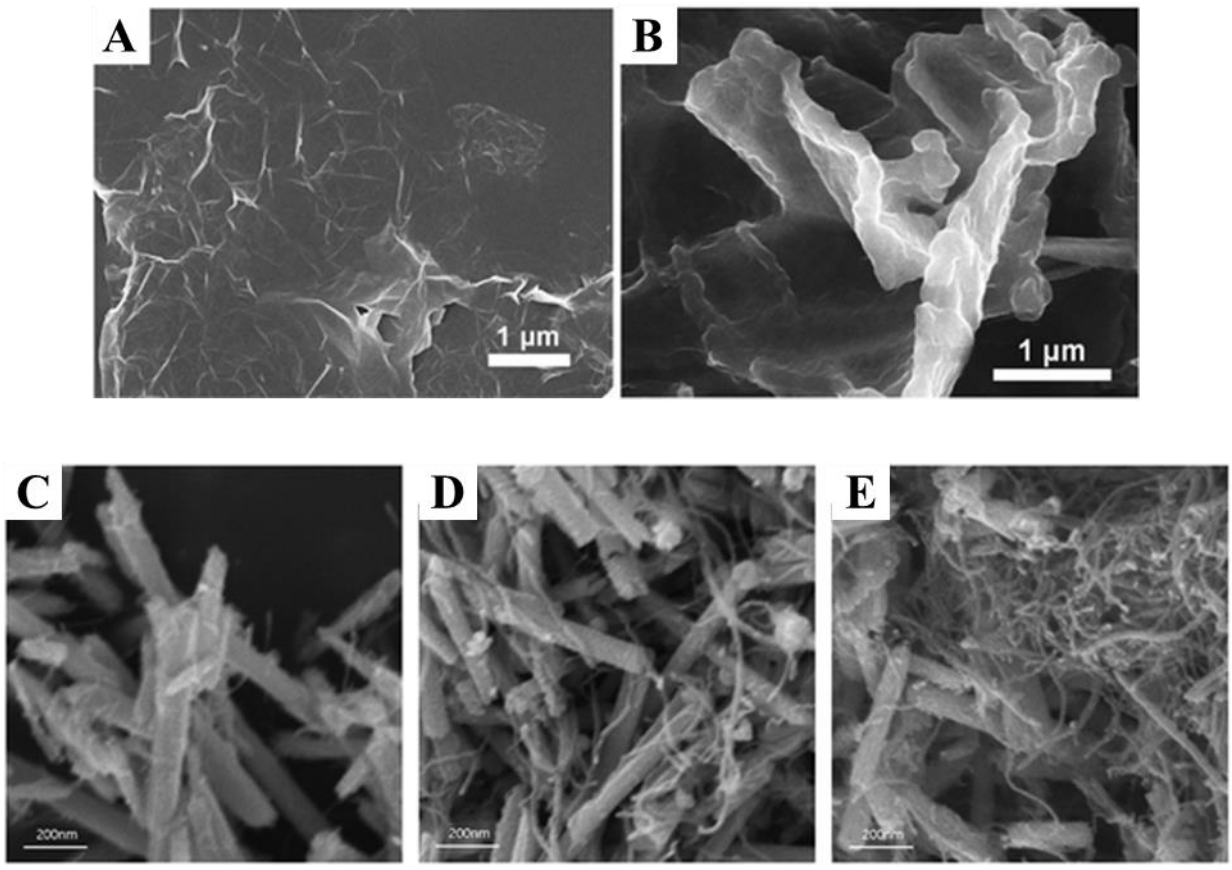

Figure 21: SEM images of (A) reduced graphene oxide (rGO) sheets & (B) PEDOT-rGO oxide [178]
SEM images MWCNT/Te nanorad composites with MWCNT contents (C) 1 wt%, (D) 3 wt% and (E) 5 wt% [179]

Their results indicate that the carbon nanofillers, the thickness of surface coating layers as well as the nanostructures of the conducting polymers can affect the thermoelectric performance of the composites. Additionally, of the contribution on thermoelectric properties, carbon nanofillers assist the alignment of the polymer chains and thus increase also the thermoelectric

properties. Composites of carbon fillers and PANi were prepared via an in situ polymerization process [180,181], both of them shown higher Seebeck coefficient and power factors than neat PANi. Pristine PANi films had a power factor of 5 μW/m.K² while the composite one exhibited a power factor of 20 μW/m.K². Carbon fillers cause the PANi chains to align in a more ordered manner as revealed by SEM, XRD, and Raman spectra (Figure 22).

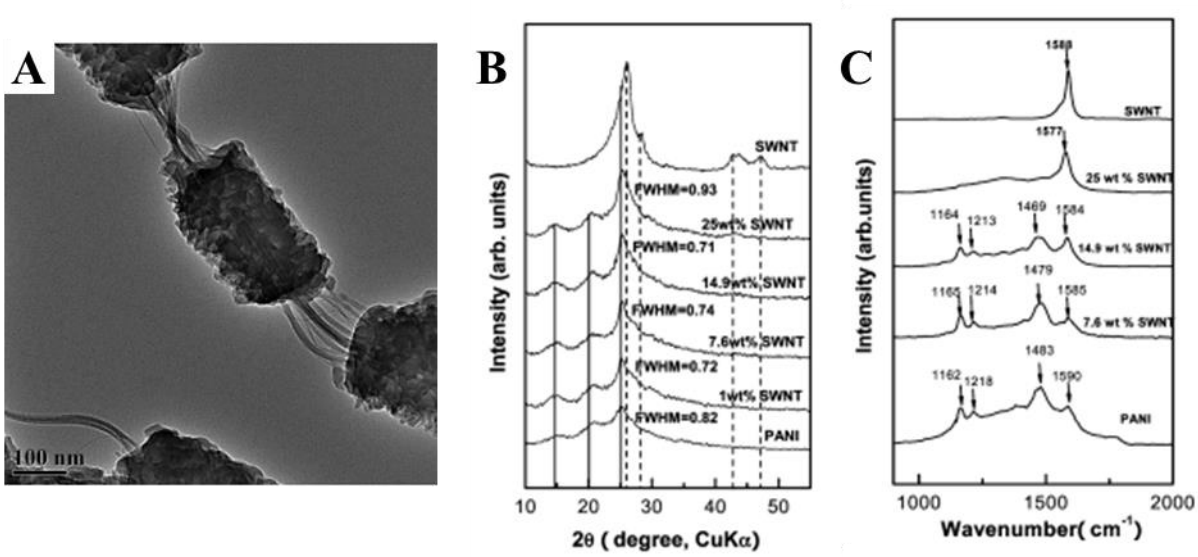

Figure 22: (A) SEM image of SWNT/PANi composites with 25 wt% SWNT. (B) XRD patterns for SWNT/PANi composites with different SWNT content (solid lines and dashed lines denote the peaks of PANi and SWNT). (C) Raman spectra for SWNT/PANi composites with different SWNT content [181][182]

4.1.3 Polymer-Polymer composite

Thermal conductivity being a problem for composite materials, scientists investigated nanostructured polymers as nanofillers for thermoelectric composites. Thanks to the polymeric nature of both the filler and matrix, a low thermal conductivity should be achieved. One of the most used nanostructured polymers is PEDOT nanowires inside PEDOT matrix. By adding, a few amount, 0.2 w% of PEDOT nanowires, composites can show a high power factor of 446.6 μW/m.K² with a Seebeck coefficient of 59.3 μV/K and σ = 1270 S/cm [182]. This high power factor could be attributed to an interfacial energy filtering effect arising from the interface (Figure 23).

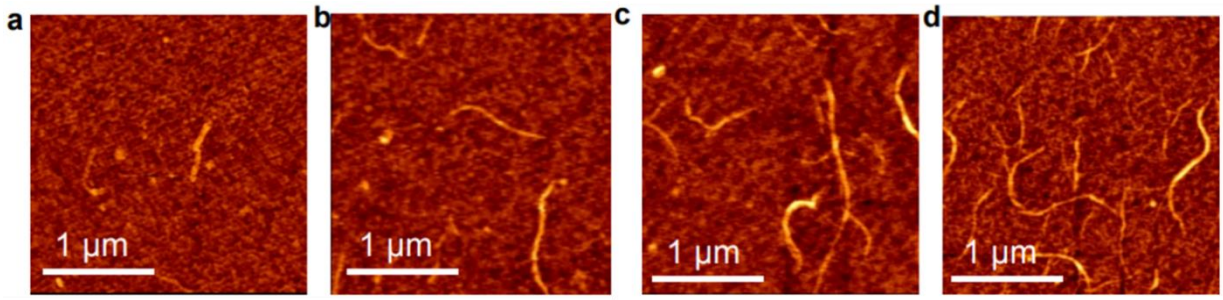

Figure 23: AFM topography images of PEDOT NWs/PEDOT :PSS hybrid films with various PEDOT NW weight fractions. (a) 0.1 wt%, (b) 0.2 wt%, (c) 0.5 wt%, (d) 1 wt% [182].

Furthermore, blending two semiconducting polymers with different HOMO levels, the density of states can be engineered by adding states close to Fermi level. An energy barrier is introduced, decreasing σ and acts more effectively on the density of state with respect to energy, leading to an increase in Seebeck coefficient [120]. To confirm the proposed mechanism, a blends of P3HT and PTB7 or TQ1 were done and were obtained record values of Seebeck coefficient near 1 mV/K [183]. This mechanism was also demonstrated on n-types blends of PCBM [184].

5. Thermoelectric devices (TEG)

5.2 Applications

The field of applications of thermoelectrics is large. Conversion of heat into electricity could be used in various sectors, like health, defense, electronics, industry, renewable energy and others. However, low *ZT* value is the main drawback of thermoelectricity to be spread everywhere. Since 2014, thermoelectric generators have gained a lot of interest with benefits around 40 million of US dollar [185], and in only two years benefits doubled to achieve 90 million of US dollar. IDTechEx expects an annual benefit of 1 billion of US dollar in 2026 for thermoelectric generators [185].

Internet of things will have a huge impact on technologies market, industries and society. Wireless connected sensors will have more than billion interconnections with device and objects. So sophisticated and ubiquitous networks in permanent communication will appear, requiring more and more data to have an information with more precision, this phenomenon is called Big Data. In 2020, more than 25 billion devices will be connected [186] requiring billions of energy source.

Thermoelectric generators based on polymer could be one of this energy source with lots of advantages:

- Flexibility and adaptability to sensor size;
- Maintenance not necessary;
- Lifetime;
- Compatibility with environment;

So Internet of thing could propel thermoelectricity from niche area to major market.

5.3 TEG polymer-based

Thermoelectric devices can be fabricated in vertical (bulk) or in lateral (thin films form). The first thermoelectric device made with polymers used PEDOT:Tos as the p-type material and TTF-TCNQ as the n-type in a bulk configuration. Bubnova *et al.* fabricated this first organic thermoelectric module producing 0.128 µW with a temperature gradient of 10 K at room temperature [44]. Later, others studies tried to utilize polymers for thermoelectric devices, unfortunately, because n-type poor stability and efficiency, most reported devices used only p- type thermoelectric interconnected in-series with metal paste like silver. Obviously, this kind of devices shown lower efficiency than p-type/n-type configuration, but by managing the number of legs and the device architecture, comparable results could be obtained.

Based on this model, screen printed thermoelectric devices on paper made with PEDOT:PSS and silver connection, obtained a power output of 4 µW in a ΔT = 50 K [187]. Later, a thermoelectric device, using PEDOT:PSS, was fabricated by thermal lamination at 373 K, exhibiting a power output of 37 µW in a ΔT = 50 K at room temperature [188a]. The importance of device architecture was further explored by Lee *et al.* [188b]. The authors compared the power output of a vertical (drop-cast, thick film), and a horizontal (spin-coated, thin film) device. Vertical thermoelectric device had up to 7 times higher power (175 nW @ ΔT = 50K) than horizontal one. Cho *et al.* developed a flexible organic thermoelectric generator with PEDOT:PSS in a chevron-structure (Figure 24) [189]. They managed to integrate 24 PEDOT:PSS patterns with a high flexibility and obtained a power output of 1 µW at Δ=17.5 K in vertical heat flow.

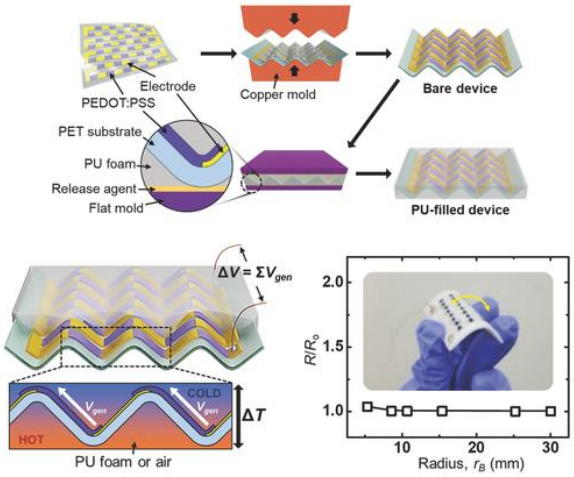

Figure 24: Schematic description of the fabrication process of a chevron-structured TEG. [189]

Gordiz *et al.* suggested that a large number of thermoelectric legs would result in high interconnect resistance that could eventually limit the device output [190]. By positioning the thermoelectric legs in a hexagonal closed-packed layout, higher fill factor can be achieved that lower the interconnect resistance and lead to higher power outputs.

Menon *et al.* proposed a new architecture, a radial thermoelectric device for polymer thermoelectric device working under natural heat convection [190,191]. Authors managed to produce 85 mV open circuit voltage and a power density of 15 nW/cm². Later, PEDOT:PSS was coated on commercial fabrics [192] and silk yarn [193] to make more applicable polymer thermoelectric devices. In the first study, wearable devices generated a voltage output of 4.3 mV at ΔT = 75 K. Meanwhile, the second one device with 26 legs gave an output voltage of 35 mV at ΔT = 66 K. Li *et al.* [194] highlighted the importance of polymer structure to the performance of a polymer thermoelectric device. In fact, by controlling the structure of free standing PEDOT:PSS films, the authors reported a 5-leg module with thermo-voltage of 2 mV at a temperature difference of 25 K.

Finally, photolithography method was used to fabricate a flexible organic module [195]. PEDOT:PSS and TTF-TCNQ were used as the p- & n-type materials. An output voltage of 250 mV, sufficient to drive electrical devices with a booster circuit, was realized at 80 K temperature difference (Figure 25). However, the high contact resistance was a problem, and it was proposed to design thermoelectric materials from the standpoints of expected module structures and mass-production processes rather than optimize ZT of the material first [195].

Figure 25: Photograph and schematic image of the module. [195]

5.4 TEG polymer-inorganic composite

Various thermoelectric modules have been fabricated using organic-inorganic hybrid materials, due to the advantages of flexibility that are conferred by the organic material and high performance of inorganic material. In a slightly unusual device structure, flexible transparent modules were reported, by using polyethylene terephthalate (PET) substrate onto which, PEDOT:PSS and a hybrid indium tin oxide (ITO)-PEDOT:PSS material were deposited as the p- & n-type legs, respectively. From 8 p-n pairs, a voltage output of 6.8 mV and power output of 0.86 nW are generated with a temperature difference of around 20 K. The n-type thermoelectric properties appear dominated by the ITO with no enhancement from the hybrid effect, however, the authors propose that the PEDOT:PSS coating on top of ITO promotes mechanical stability during the active bending of the module [196].

Ferhat *et al.* made a flexible thermoelectric device on paper entirely fabricated using inkjet printing. They used PEDOT:PSS as p-type and (TiS_2(HA)x) as n-type legs, and obtained a power output of 22.5 nW at Δ= 20 K for a small device area of 128 mm^2 [197]. Koumoto and coworkers have fabricated a thermoelectric module composed of hybrid TiS_2/organic superlattice films and PEDOT:PSS film, as the n- and p-type materials, respectively. From five p-n pairs, they obtain a voltage output of 33 mV with a maximum power density of 250 $\mu W/cm^2$ under a temperature difference of 70 K [198].

Recently, a rolled flexible TEG was fabricated by a screen printing method using PEDOT:PSS and conjugated polyelectrolytes with nickel (CPE) /CNT nanocomposite as p-type and n-type materials, respectively [199]. A maximum output power and open circuit voltage of the TE modules with 288 legs is 46 µW and 260 mV at ΔT = 65K (Figure 26).

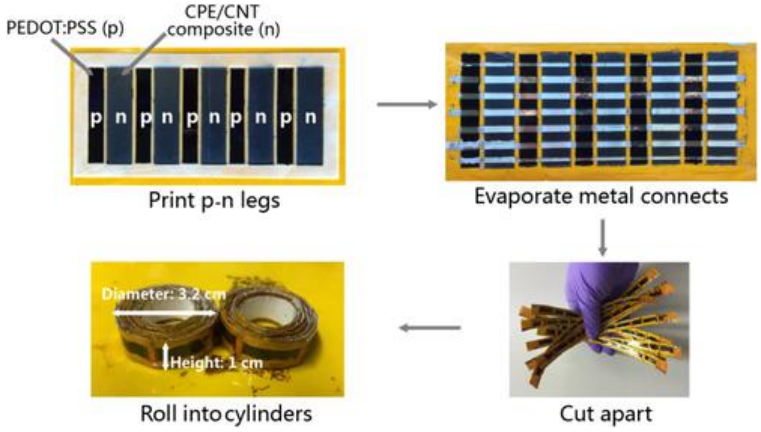

Figure 26: Fabrication process for rolled modules using PEDOT :PSS as p-type and CPE/CNT composites as n-type legs on Kapton film. [199]

C Conclusion

Thermoelectricity is not a new phenomenon, nevertheless for the production of electricity, it knows for ten years a renewed interest. Indeed, the direct conversion of heat into electricity by the thermoelectric modules makes it possible to limit both the number and the complexity of the elements that make up the TEG. It is, therefore, one of the most robust energy conversion systems.

On the other hand, the field of thermoelectric polymers can still be considered in its infancy with respect to the thermoelectric inorganic domain. Most reported studies involved p-type materials, and the optimization of their thermoelectric properties. The keystone of this optimization lies in the ability to fine-tuning to the electronic properties of materials via doping. This challenge is the main axis of research for many groups as revealed by this state of the art.

Furthermore, for a fully functional thermoelectric generator, an n-type material is also needed. To overcome the limited thermoelectric performance and stability of n-type material, inorganic/organic composite could be developed. This alternative shown a high potential to modulate the thermoelectric behavior from n-type material.

Finally, development for the fabrication of fully operational thermoelectric generator is necessary. The evaluation of the Power Output delivered by such devices is crucial to evaluate the "organic thermoelectric" technology.

The objective of this thesis work is to create a performant TEG for near room temperature. As shown in this Chapter 1, polymers appeared as great candidates for thermoelectric applications thanks to a unique combination of properties. It is essential to properly characterize the thermoelectric properties of polymer material, and then enhance them by a fine tuning of electronic structure with doping. Chapter 2 described thermoelectric properties optimization of several famous polymers such as PEDOT:Tos, P3HT, PCDTBT and PTB7. Moreover, various n-type materials were studied, particularly a n-type polymer from Prof. Jenekhe's group, a naphthalenediimide-biselenophene copolymer (PNDIBS). Then, in order to continue to improve thermoelectric properties, a novel approach designed in our laboratory, coupling inorganic semi-conducting substrate and organic materials, was developed (Chapter 3). The interface between inorganic and organic material was studied, and the surface of the inorganic substrate was etched to increase its specific surface area (Chapter 4). Silicon was chosen as

inorganic semi-conducting substrate due to its high importance in electronic and industrial field, its high range of impurities concentration (doping concentration) accessible and its good thermoelectric properties (S ≈ 500-1200 µV/K when correctly doped) at room temperature. Resulting hybrid silicon-polymer devices exhibit a significate improvement of thermoelectric properties. These "novel" hybrid materials were used as building block for the fabrication of performant TEG (Chapter 5).

References

[1] L. I. Anatychuk, *Journal of thermoelectricity No2*, **2004**, 5–11 (*ISSN 1607-8829*).

[2] T. J. Seebeck, *Magnetische Polarisation der Metalle und Erze durch Temperature Differenz*, Leipzig, W. Engelmann, « Ostwald's Klassiker Exakten Wissenschaften vol.70 », **1895**, 120 p.

[3] H. C. Ørsted, *Der Geist in der Natur*, München, Cotta, 1850.

[4] G. Magnus, *Poggendorf's Annalen der Physik*, « Poggendorfs Ann. Phys vol.83 ». **1851**, 469 p.

[5] J. C. Peltier, *Nouvelles expériences sur la caloricité des courants électriques*, « Ann. Chim vol. I. IV. », **1834**, 371–87.

[6] E. Lenz, *Ueber einige Versuche im Gebiete des Galvanismus*, St. Pétersb. « Acaf. Sci. Bull, Ann. Phys. vol. III », **1838**, *120*, 342 p.

[7] J. P. J. Esq, *On the heat evolved by metallic conductors of electricity, and in the cells of a battery during electrolysis*, Dublin, Lond. Edinb., « Philos. Mag. J. Sci. 3 » **1841**, *19*, 260 p.

[8] W. Thomson, *On the Dynamical Theory of Heat Transfer*, Edinburgh, Earth Environ. Sci. Trans. R. Soc. Edinb. **1853**, *20*, 261 p.

[9] E. Altenkirch, *Physikalische Zeitschrift*, **1991**, *12*, 120.

[10] W. Brostow, G. Granowski, N. Hnatchuk, J. Sharp, J. White, *J. Mater. Educ.* **2014**, *36*, 175.

[11] C. Kittel, *Introduction to Solid State Physics*, Wiley India Pvt. Limited, « Seventh Edition », **2007**.

[12] M. V. Vedernikov, E. K. Iordanishvili, In *Seventeenth International Conference on Thermoelectrics. Proceedings ICT98 (Cat. No.98TH8365)*; IEEE: Nagoya, Japan, 1998; pp. 37–42.

[13] G. S. Nolas, J. Sharp, J. Goldsmid, *Thermoelectrics: Basic Principles and New Materials Developments*, Berlin Heidelberg, Springer Series in Materials Science, « Springer-Verlag », **2001**.

[14] D. M. Rowe, *Thermoelectrics Handbook: Macro to Nano*, « CRC Press Book », **2006**.

[15] P. R. Sangi Reddy, *PhD Thesis: Transport of charge and energy in metal-molecule-metal junctions*, Univ. of California, Berkeley, **2007**.

[16] R. Y.-S. Wang, *PhD Thesis: Energy transport and conversion in nanostructured materials*, Univ. of California, Berkeley, **2008**.

[17] S. K. Yee, *PhD Thesis: Development of Organic-Inorganic Hybrid Thermoelectrics*, Univ. of California, Berkeley, **2013**.

[18] G. J. Snyder, E. S. Toberer, *Natur. Mater.*, **2008**, *7*, 105-114

[19] C. Uher, *Material Aspect of Thermoelectricity*, « CRC Press Book », **2016**.

[20] H. J. Goldsmid, *Introduction to Thermoelectricity*, Berlin, Heidelberg, « Springer Series in Materials Science », **2010**, pp. 7–21.

[21] A. F. Ioffe, *Semiconductor thermoelements, and Thermoelectric cooling*, London, « Infosearch First ed. », **1957**.

[22] D. M. Rowe, *Handbook of Thermoelectrics*., « CRC Press Book », **1995**.

[23] T. Caillat, J. Sakamoto, A. Jewell, C.-K. Huang, J. Cheng, J. Paik, P. Gogna, P.-J. Fleurial, R. Ewell, "Status of skutterudite-based segmented thermoelectric technology components development at JPL", in *STAIF 23rd Symposium on Space Nuclear Power and Propulsion*, Albuquerque, New Mexico, **2006**.

[24] T. Caillat, S. Firdosy, S. C. B. Li, J.-A. Paik, C.-K Huang, J. Cheng, J.-P. Fleurial, V. Ravi, E. J. Brandon, "Advanced high-temperature thermoelectric devices", in *DOE Thermoelectric Applications Workshop*, **2009**.
[25] R. L. Cataldo, G. L. Bennett, *Radioisot. - Appl. Phys. Sci.* **2011**.
[26] B. Russ, A. Glaudell, J. J. Urban, M. L. Chabinyc, S. Segalman, *Nature Reviews Materials*, **2016**, *1*.
[27] S. M. Haque, J. A. A. Rey, A. A. Masud, Y. Umar, R. Albarracin, *Electrical Properties of Different Polymeric Materials and their Applications: The Influence of Electric Field Chapter 3*, Boxue Du, « IntechOpen », **2017**, 25 p.
[28] A. B. Robbins, A. J. Minnich, *Appl. Phys. Lett.* **2015**, *107*, 201908.
[29] C. L. Choy, *Polymer* **1977**, *18*, 984.
[30] C. L. Yaws, *Viscosity, Thermal Conductivity, and Diffusivity of C1 to C100 Organics and Ac to Zr Inorganics*, « Transport Properties of Chemicals and Hydrocarbons - 1st Edition », **2009**, pp. 403-406.
[31] M. Culebras, C. M. Gómez, A. Cantarero, *Materials* **2014**, *7*, 6701.
[32] M. Orrill, S. LeBlanc, *J. Appl. Polym. Sci.* **2017**, *134*.
[33] E. J. Bae, Y. H. Kang, K.-S. Jang, S. Y. Cho, *Sci. Rep.* **2016**, *6*, 18805.
[34] S. Hwang, W. J. Potscavage, R. Nakamichi, C. Adachi, *Org. Electron.* **2016**, *31*, 31.
[35] C. K. Chiang, C. R. Fincher, Y. W. Park, A. J. Heeger, H. Shirakawa, E. J. Louis, S. C. Gau, A. G. MacDiarmid, *Phys. Rev. Lett.* **1977**, *39*, 1098.
[36] H. Shirakawa, E. J. Louis, A. G. MacDiarmid, C. K. Chiang, and A. J. Heeger, J*ournal of the Chemical Society, Chemical Communications*, **1977**, *578*.
[37] W. P. Su, J. R. Schrieffer, A. J. Heeger, *Phys. Rev. Lett.* **1979**, *42*, 1698.
[38] (a) W. P. Su, J. R. Schrieffer, A. J. Heeger, *Physical Review B*, **1980**, *22*, 2099. (b) Y. Xuan, *Phys. Rev. B*, **2010**, *82*, 115454-9.
[39] W. P. Su, J. R. Schrieffer, *Proc. Natl. Acad. Sci. U. S. A.* **1980**, *77*, 5626.
[40] Y. W. Park, A. Denenstein, C. K. Chiang, A. J. Heeger, A. G. MacDiarmid, *Solid State Commun.* **1979**, *29*, 747.
[41] Y. Hiroshige, M. Ookawa, N. Toshima, *Synthetic Metals*, **2007**, *157*, 467-474.
[42] M. Scholdt, H. Do, J. Lang, A. Gall, A. Colsmann, U. Lemmer, J. D. Koenig, M. Winkler, H. Boettner, *J. Electron. Mater.* **2010**, *39*, 1589.
[43] L. Groenendaal, F. Jonas, D. Freitag, H. Pielartzik, J. R. Reynolds, *Advanced Materials*, **2000**, *12*, 481.
[44] O. Bubnova, Z. U. Khan, A. Malti, S. Braun, M. Fahlman, M. Berggren, X. Crispin, *Nat. Mat.*, **2011**, *10*, 429-433.
[45] S. Kirchmeyer, K. Reuter, *J. Mater. Chem.* **2005**, *15*, 2077.
[46] A. Elschnet, S. Kirchmeyer, W. Lovenich, U. MErker, K. Reuter, *PEDOT: Principles and Applications of an Intrinsically Conductive Polymer*, Boca Raton, FL, USA, « CRC Press Book », **2010**.
[47] Y. Xia, J. Ouyang, *ACS Appl. Mater. Interfaces* **2012**, *4*, 4131.
[48] J. Ouyang, *ACS Appl. Mater. Interfaces* **2013**, *5*, 13082.
[49] J. Luo, D. Billep, T. Waechtler, T. Otto, M. Toader, O. Gordan, E. Sheremet, J. Martin, M. Hietschold, D. R. T. Zahn, T. Gessner, *J. Mater. Chem. A* **2013**, *1*, 7576.
[50] J. Xiong, F. Jiang, W. Zhou, C. Liu, J. Xu, *RSC Adv.* **2015**, *5*, 60708.
[51] S. Liu, H. Deng, Y. Zhao, S. Ren, Q. Fu, *RSC Adv.* **2014**, *5*, 1910.
[52] L. Zhang, H. Deng, S. Liu, Q. Zhang, F. Chen, Q. Fu, *RSC Adv.* **2015**, *5*, 105592.
[53] S. Zhang, Z. Yu, P. Li, B. Li, F. H. Isikgor, D. Du, K. Sun, Y. Xia, J. Ouyang, *Org. Electron.* **2016**, *32*, 149.
[54] Y. Xia, J. Fang, P. Li, B. Zhang, H. Yao, J. Chen, J. Ding, J. Ouyang, *ACS Appl. Mater. Interfaces* **2017**, *9*, 19001.

[55] F. Kong, C. Liu, H. Song, J. Xu, Y. Huang, H. Zhu, J. Wang, *Synth. Met.* **2013**, *185–186*, 31.
[56] C. Yi, A. Wilhite, L. Zhang, R. Hu, S. S. C. Chuang, J. Zheng, X. Gong, *ACS Appl. Mater. Interfaces* **2015**, *7*, 8984.
[57] D. A. Mengistie, C.-H. Chen, K. M. Boopathi, F. W. Pranoto, L.-J. Li, C.-W. Chu, *ACS Appl. Mater. Interfaces* **2015**, *7*, 94.
[58] K. Sun, S. Zhang, P. Li, Y. Xia, X. Zhang, D. Du, F. H. Isikgor, J. Ouyang, *J. Mater. Sci. Mater. Electron.* **2015**, *26*, 4438.
[59] Y. Xia, K. Sun, J. Chang, J. Ouyang, *J. Mater. Chem. A* **2015**, *3*, 15897.
[60] H. Shi, C. Liu, Q. Jiang, J. Xu, *Adv. Electron. Mater.* **2015**, *1*,1500017.
[61] Z. Yu, Y. Xia, D. Du, J. Ouyang, *ACS Appl. Mater. Interfaces* **2016**, *8*, 11629.
[62] Z. FAn, D. DU, Z. Yu, P. Li, Y. XIa, J. Ouyang, *ACS Appl. Mater. Interfaces*, **2016**, *8*, 23204
[63] S. Zhang, Y. Xia, J. Ouyang, *Org. Electron*., **2017**, *45*, 139.
[64] D. M. De Leeuw, P. A. Kraakman, P. F. G. Bongaerts, C. M. J. Mutsaers, D. B. M. Klaassen, *Synth. Met.* **1994**, *66*, 263–273.
[65] G. Heywang, F. Jonas, *Adv. Mater.*, **1992**, *4*, 116-118.
[66] M. Fabretto, K. Zuber, C. Hall, P. Murphy, *Macromol. Rapid Commun*, **2008**, *29*, 1403-1409.
[67] M. Fabretto, C. Jariego-Moncunill, J. -P. Autere, *Polymer*, **2011**, *52*, 1725-1730.
[68] B. Winther-Jensen, O. Winter-Jensen, M. Forsyth, D. R. MacFarlane, *Science*, **2008**, *321*, 671-674.
[69] R. Noriega, J. Rivnay, K. Vandewal, F. P. V. Koch, N. Stingelin, P. Smith, M. F. Toney, A. Salleo, *Nat. Mater.* **2013**, *12*, 1038.
[70] I. Petsagkourakis *et al.*, *Scientific Reports*, **2016**, *6*:30501.
[71] A. B. Kaiser, V. Skákalová, *Chem. Soc. Rev.* **2011**, *40*, 3786.
[72] O. Bubnova *et al.*, *Nat. Mater.* **2014**, *13*, 190.
[73] I. Petsagkourakis *et al.*, *Organic Electronics*, **2018**, *52*, 335-341
[74] J. Y. Kim, J. H. Jung, D. E. Lee, J. Joo, *Synth. Met.* **2002**, *126*, 311.
[75] C. Liu, B. Lu, J. Yan, J. Xu, R. Yue, Z. Zhu, S. Zhou, X. Hu, Z. Zhang, P. Chen, *Synth. Met*. **2010**, *160*, 2481.
[76] F.-F. Kong, C.-C. Liu, J.-K. Xu, F.-X. Jiang, B.-Y. Lu, R.-R. Yue, G.-D. Liu, J.-M. Wang, *Chin. Phys. Lett.* **2011**, *28*, 037201.
[77] G. H. Kim, L. Shao, R. Zhang, K. P. Pipe, *Nat. Mater*, **2013**, *12*, 719-723.
[78] C. M. Palumbiny *et al.*, *Adv. Mater.*, **2015**, *27*, 3391-3397.
[79] E. Liu, C. Liu, Z. Zhu, H. Shi, Q. Jiang, F. Jiang, J. Xu, J. Xiong, Y. Hu, *J. Polym. Res.* **2015**, *22*, 240.
[80] N. Kishi, Y. Kondo, H. Kunieda, S. Hibi, Y. Sawada, *J. Mater. Sci. Mater. Electron.* **2018**, *29*, 4030.
[81] J. Wang, K. Cai, S. Shen, *Organic Electronics*, **2014**, *15*, 3087-3095.
[82] D. Beretta *et al.*, *ACS Appl. Mater. Interfaces*, **2017**, *9*, 18151-18160.
[83] H. Yu, *Soft Materials*, **2018**, *16:1*, 31-36.
[84] S. H. Lee, H. Park, W. Son, H. H. Choi, J. H. Kim, *J. Mater. Chem. A*, **2014**, *2*, 13380.
[85] N. Massonnet, A. Carella, O. Jaudouin, P. Rannou, G. Laval, C. Celle, J.-P. Simonato, *J. Mater. Chem. C*, **2014**, *2*, 1278.
[86] Z. U. Khan, O. Bubnova, M. J. Jafari, R. Brooke, X. Liu, R. Gabrielsson, T. Ederth, D. R. Evans, J. W. Andreasen, M. Fahlman, X. Crispin, *J. Mater. Chem. C*, **2015**, *3*, 10616.
[87] Z. Fan, P. Li, J. Ouyang, *Advanced Energy Materials*, **2017**, *7*, 1602116.

[88] K. Gurunathan, A. V. Murugan, R. Marimuthu, U. P. Mulik, D. P. Amalnerkar, *Mater. Chem. Phys.*, **1999**, *61*, 173.
[89] L. Zhang, T. Goto, I. Imae, Y. Sakurai, Y. Harima, *J. Polym. Sci. Part B Polym. Phys.*, **2017**, *55*, 524.
[90] T. Park, C. Park, B. Kim, H. Shin, E. Kim, *Energy Environ. Sci.*, **2013**, *6*, 788.
[91] O. Bubnova, M. Berggren, X. Crispin, *J. Am. Chem. Soc.*, **2012**, *134*, 16456-16459.
[92] J. L. Bredas, G. B. Street, *Accounts of Chemical Research*, **1985**, *18*, 309.
[93] N. Basescu, Z.-X. Liu, D. Moses, A. J. Heeger, H. Naarmann, N. Theophilou, *Nature*, **1987**, *327*, 403.
[94] R. Zuzok, A. B. Kaiser, W. Pukacki, S. Roth, *J. Chem. Phys.*, **1991**, *95*, 1270.
[95] Y. W. Park, C. O. Yoon, B. C. Na, H. Shirakawa, K. Akagi, *Synth. Met.*, **1991**, *41*, 27.
[96] H. Kaneko, T. Ishiguro, A. Takahashi, J. Tsukamoto, *Synth. Met.* **1993**, *57*, 4900.
[97] Y. W. Park, Y. S. Lee, C. Park, L. W. Shacklette, R. H. Baughman, *Solid State Commun.*, **1987**, *63*, 1063.
[98] Y. W. Park, J. S. Moon, M. K. Bak, J.-I. Jin, *Synth. Met*,. **1989**, *29*, 389.
[99] E. Dalas, S. Sakkopoulos, E. Vitoratos, *J. Mater. Sci.*, **1994**, *29*, 4131.
[100] S. Bhadra, N. K. Singha, and D. Khastgir, *Science*, **2007**, *104*, 1900.
[101] B. Abad *et al.*, *Journal of Materials Chemistry* A, **2013**, *1*, 10450-7.
[102] H. Yan, N. Sada, N. Toshima, *J. Therm. Anal. Calorim.* **2002**, *69*, 881.
[103] J. Li, X. Tang, H. Li, Y. Yan, Q. Zhang, *Synth. Met.* **2010**, *160*, 1153.
[104] C. Nath, A. Kumar, Y. -K. Kuo, G. S. Okram, *Appl. Phys. Lett.*, **2014**, *105*, 133108-5.
[105] Y. Yang, S. Chen, L. Xu, *Macromol. Rapid Commun.* **2011**, *32*, 593.
[106] S. P. Armes, *Synth. Met.* **1987**, *20*, 365.
[107] P. Jha *et al.*, *Macromolecules*, **2011**, *44*, 4583-5.
[108] G. Qi, L. Huang, H. Wang, *Chem. Commun.* **2012**, *48*, 8246.
[109] D. Oukil *et al.*, *Sensors and Actuators B: Chemical*, **2014**, *204*¸203.
[110] N. T. Kemp, A. B. Kaiser, C.-J. Liu, B. Chapman, O. Mercier, A. M. Carr, H. J. Trodahl, R. G. Buckley, A. C. Partridge, J. Y. Lee, C. Y. Kim, A. Bartl, L. Dunsch, W. T. Smith, J. S. Shapiro, *J. Polym. Sci. Part B Polym. Phys.* **1999**, *37*, 953.
[111] M. Culebras, B. Uriol, C. M. Gomez, A. Cantarero, *Phys. Chem.*, **2015**, *17*, 15140-5.
[112] B. Endrdi *et al.*, *J . Chem. C*, **2015**, *119*, 8472-9.
[113] Q. Zhang, Y. Sun, W. Xu, D. Zhu, *Energy Environ. Sci.* **2012**, *5*, 9639.
[114] D. T. Duong, H. Phan, D. Hanifi, P. S. Jo, T.-Q. Nguyen, A. Salleo, *Adv. Mater. Deerfield Beach Fla* **2014**, *26*, 6069.
[115] I. E. Jacobs, E. W. Aasen, J. L. Oliveira, T. N. Fonseca, J. D. Roehling, J. Li, G. Zhang, M. P. Augustine, M. Mascal, A. J. Moulé, *J. Mater. Chem. C* **2016**, *4*, 3454.
[116] C. Wang, D. T. Duong, K. Vandewal, J. Rivnay, A. Salleo, *Phys. Rev. B* **2015**, *91*, 085205.
[117] (a) J. Hynynen *et al.*, **2017**, *50*, 8140-8148. (b) E. Justin *et al.*, *Macromolecules*, **2014**, *47* (19), 6836-6846.
[118] E. J. Cochran *et al.*, *Macromolecules*, **2014**, *47* (19), 6836-6846.
[119] D. T. Duong, C. Wang, E. Antono, M. F. Toney, A. Salleo, *Org. Electron.* **2013**, *14*, 1330.
[120] (a) J. Sun *et al.*, *Macromolecules*, **2010**, *43* (6), 2897-2903. (b) Y. Du *et al.*, *Synth. Met.*, **2012**, *161*, 2688-2692.
[121] G. Zuo *et al.*, *J. Phys. Chem. C*, **2017**, *121* (14), 7767-7775.
[122] D. T. Scholes, S. A. Hawks, P. Y. Yee, H. Wu, J. R. Lindemuth, S. H. Tolbert, B. J. Schwartz, *J. Phys. Chem. Lett.* **2015**, *6*, 4786.
[123] G. Zuo, O. Andersson, H. Abdalla, M. Kemerink, *Appl. Phys. Lett.* **2018**, *112*, 083303.
[124] Q. Zhang, Y. Sun, F. Jiao, J. Zhang, W. Xu, D. Zhu, *Synth. Met.* **2012**, *162*, 788.

[125] Q. Zhang, *Macromolecules*, **2014**, *47* (2), 609-615.
[126] A. M. Glaudell, J. E. Cochran, S. N. Patel, M. L. Chabinyc, *Adv. Energy Mater.*, **2014**, *5* (4), 1401072.
[127] S. N. Patel, A. M. Glaudell, K. A. Peterson, E. M. Thomas, K. A. O'Hara, E. Lim, M. L. Chabinyc, *Sci. Adv.* **2017**, *3*, e1700434.
[128] E. Lim, K. A. Peterson, G. M. Su, M. L. Chabinyc, *Chem. Mater.* **2018**, *30*, 998.
[129] S. N. Patel, A. M. Glaudell, D. Kiefer, M. L. Chabinyc, *ACS Macro Lett.* **2016**, *5*, 268.
[130] R. B Aïch, N. Blouin, A. Bouchard, M. Leclerc, *Chem. Mater.*, **2009**, *21* (4), 751-757
[131] L. Wang, C. Pan, A. Liang, X. Zhou, W. Zhou, T. Wan, L. Wang, *Polym. Chem.* **2017**, *8*, 4644.
[132] Q. Zhang, Y. Sun, W. Xu, D. Zhu, *Macromolecules* **2014**, *47*, 609.
[133] I. H. Jung *et al.*, *Scientific Reports*, **2017**, 7, 44704.
[134] A. Nollau, M. Pfeiffer, T. Fritz, K. Leo, *J. Appl. Phys.* **2000**, *87*, 4340.
[135] (a) W. W. H. Wong, J. Subbiah, S. R. Puniredd, W. Pisula, D. J. Jones, A. B. Holmes, *Polym. Chem.* **2014**, *5*, 1258. (b) J. L. Banal, J. Subbiah, H. Graham, J.-K. Lee, K. P. Ghiggino, W. W. H. Wong, *Polym. Chem.* **2013**, *4*, 1077.
[136] R. Schmidt, J. H. Oh, Y.-S. Sun, M. Deppisch, A.-M. Krause, K. Radacki, H. Braunschweig, M. Könemann, P. Erk, Z. Bao, F. Würthner, *J. Am. Chem. Soc.* **2009**, *131*, 6215.
[137] Y. Fukutomi *et al.*, *J. Am. Chem. Soc.*, **2013**, *135* (31), 11445-11448.
[138] T. Menke, D. Ray, J. Meiss, K. Leo, M. Riede, *Appl. Phys. Lett.* **2012**, *100*, 093304.
[139] B. Lüssem *et al.*, *Chem. Rev.*, **2016**, *116* (22), 13714-13751.
[140] (a) P. Wei, J. H. Oh, G. Dong, Z. Bao, *J. Am. Chem. Soc.* **2010**, *132*, 8852. (b) C. D. Weber, C. Bradley, M. C. Lonergan, *J. Mater. Chem. A* **2014**, *2*, 303 (c) J. Lu, S. Nagase, D. Yu, H. Ye, R. Han, Z. Gao, S. Zhang, L. Peng, *Phys. Rev. Lett.* **2004**, *93*, 116804.
[141] J. Liu, M. P. garman, J. Dong, L. Qiu, G. Portale, J. C. Hummelen, L. J. A. Koster, *ACS Appli. Energy Mater.* **2019**, (DOI: 10.1021/acsaem.9b01179).
[142] D. Moses, J. Chen, A. Denenstein, M. Kaveh, T. Chung, A. J. Heeger, A. G. MacDiarmid, Y. W. Park, *Solid State Commun.* **1981**, *40*, 1007.
[143] J. R. Reynolds, J. C. W. Chien, C. P. Lillya, *Macromolecules*, **1987**, *20*, 1184.
[144] J. R. Reynolds, F. E. Karasz, C. P. Lillya, J. C. W. Chien, *J. Chem. Soc., Chem. Commun.* **1985**, 268.
[145] C. Faulmann, J. Chahine, K. Jacob, Y. Coppel, L. Valade, D. De Caro, *J. Nanoparticle Res.* **2013**, *15*, 1.
[146] (a) K. Oshima, J. Inoue, S. Sadakata, Y. Shiraishi, N. Toshima, *J. Electron. Mater.* **2017**, *46*, 3207. (b) T. Naoki, *Synhth. Met.* , **2017**, *225*, 3-21
[147] Y. Sun, J. Zhang, L. Liu, Y. Qin, Y. Sun, W. Xu, D. Zhu, *Sci. China Chem.* **2016**, *59*, 1323.
[148] C. D. Weber, C. Bradley, M. C. Lonergan, *J. Mater. Chem. A* **2013**, *2*, 303.
[149] X. Huang, P. Sheng, Z. Tu, F. Zhang, J. Wang, H. Geng, Y. Zou, C.-A. Di, Y. Yi, Y. Sun, W. Xu, D. Zhu, *Nat. Commun.* **2015**, *6*, 7408.
[150] T. Lei, J.-H. Dou, X.-Y. Cao, J.-Y. Wang, J. Pei, *J. Am. Chem. Soc.* **2013**, *135*, 12168.
[151] K. Shi, F. Zhang, C.-A. Di, T.-W. Yan, Y. Zou, X. Zhou, D. Zhu, J.-Y. Wang, J. Pei, *J. Am. Chem. Soc.* **2015**, *137*, 6979.
[152] W. Ma, K. Shi, Y. Wu, Z.-Y. Lu, H.-Y. Liu, J.-Y. Wang, J. Pei, *ACS Appl. Mater. Interfaces* **2016**, *8*, 24737.
[153] X. Zhao, D. Madan, Y. Cheng, J. Zhou, H. Li, S. M. Thon, A. E. Bragg, M. E. DeCoster, P. E. Hopkins, H. E. Katz, *Adv. Mater.* **2017**, *29*, 1606928.

[154] R. A. Schlitz, F. G. Brunetti, A. M. Glaudell, P. L. Miller, M. A. Brady, C. J. Takacs, C. J. Hawker, M. L. Chabinyc, *Adv. Mater. Deerfield Beach Fla* **2014**, *26*, 2825.
[155] J. Liu *et al.*, *Advanced Materials*, **2018**, *30* (7), 1704630.
[156] D. Kiefer *et al.*, *ACS Energy Lett.*, **2018**, *3* (2), 278-285.
[157] Y. Wang *et al.*, *Macromolecules*, **2017**, *50* (3), 857-864.
[158] S. Wang, H. Sun, U. Ail, M. Vagin, P. O. Å. Persson, J. W. Andreasen, W. Thiel, M. Berggren, X. Crispin, D. Fazzi, S. Fabiano, *Adv. Mater. Deerfield Beach Fla* **2016**, *28*, 10764.
[159] A.R. Abramson, W.C. Kim, S.T. Huxtable, H. Yan, Y. Wu, A. Majumdar, C.-L. Tien, P. Yang, *J. Microelectromech. Syst.*, **2004**, *13*, 505–513.
[160] B. Zhang *et al.*, *ACS Appl. Mater. Interfaces*, **2010**, *2* (11), 3170-3178.
[161] M. He, J. Ge, Z. Lin, X. Feng, X. Wang, H. Lu, Y. Yang, F. Qiu, *Energy Environ. Sci.* **2012**, *5*, 8351.
[162] J. Choi *et al.*, *Ad. Energy Mat.*, **2016**, *6* (9), 1502181.
[163] Z. Liang, M. J. Boland, K. Butrouna, D. R. Strachan, K. R. Graham, *J. Mater. Chem. A* **2017**, *5*, 15891.
[164] K. C. See, J. P. Feser, C. E. Chen, A. Majumdar, J. J. Urban, R. A. Segalman, *Nano Lett.* **2010**, *10*, 4664.
[165] B. T. McGrail, A. Sehirlioglu, E. Pentzer, *Angew. Chem. Int. Ed Engl.* **2015**, *54*, 1710.
[166] D. Tasis, N. Tagmatarchis, A. Bianco, M. Prato, *Chem. Rev.* **2006**, *106*, 1105.
[167] B. Fan, X. Mei, K. Sun, J. Ouyang, *Appl. Phys. Lett.* **2008**, *93*, 143103.
[168] C. Soldano, A. Mahmood, E. Dujardin, *Carbon* **2010**, *48*, 2127.
[169] B. A. MacLeod, N. J. Stanton, I. E. Gould, D. Wesenberg, R. Ihly, Z. R. Owczarczyk, K. E. Hurst, C. S. Fewox, C. N. Folmar, K. H. Hughes, B. L. Zink, J. L. Blackburn, A. J. Ferguson, *Energy Environ. Sci.* **2017**, *10*, 2168.
[170] K. Zhang, Y. Zhang, S. Wang, *Sci. Rep.* **2013**, *3*, 3448.
[171] C. Cho, B. Stevens, J.-H. Hsu, R. Bureau, D. A. Hagen, O. Regev, C. Yu, J. C. Grunlan, *Adv. Mater. Deerfield Beach Fla* **2015**, *27*, 2996.
[172] C. Cho, K. L. Wallace, P. Tzeng, J. H. Hsu, J. C. Grunlan, *Adv. Energy Mater.*, **2016**, *6* (7), 1502168-1502176.
[173] C. Cho, M. Culebras, K. L. Wallace, Y. Song, K. Holder, J.-H. Hsu, C. Yu, J. C. Grunlan, *Nano Energy* **2016**, *28*, 426.
[174] C. Yu, Y. S. Kim, D. Kim, J. C. Grunlan, *Nano Lett.* **2008**, *8*, 4428.
[175] D. Kim, Y. Kim, K. Choi, J. C. Grunlan, C. Yu, *ACS Nano* **2010**, *4*, 513.
[176] G. P. Moriarty, *J. Polym. Sci. Part B*, **2013**, *51*, 119.
[177] J.-H. Hsu, W. Choi, G. Yang, C. Yu, *Org. Electron.* **2017**, *45*, 182.
[178] K. Xu, G. Chen, D. Qiu, *J. Mater. Chem. A* **2013**, *1*, 12395.
[179] (a) L. Liang, C. Gao, G. Chen, C.-Y. Guo, *J. Mater. Chem. C* **2016**, *4*, 526. (b) X. Hu, G. Chen, X. Wang, *Compos. Sci. Technol.* **2017**, *144*, 43.
[180] C. Meng, C. Liu, S. Fan, *Adv. Mater. Deerfield Beach Fla* **2010**, *22*, 535.
[181] Q. Yao, L. Chen, W. Zhang, S. Liufu, X. Chen, *ACS Nano* **2010**, *4*, 2445.
[182] K. Zhang, J. Qiu, S. Wang, *Nanoscale* **2016**, *8*, 8033.
[183] G. Zuo, X. Liu, M. Fahlman, M. Kemerink, *Adv. Functional Mater.*, **2018**, *28* (15), 1703280
[184] G. Zuo, Z. Li, E. Wang, M. Kemerink, *Adv. Electron. Mater.* **2018**, *4*, 1700501.
[185] ReportBuyer, (July 2016), *Thermoelectric Energy Harvesting 2016-2026: Technologies, devices & applications for thermoelectric generators*, see on https://www.prnewswire.com/news-releases/thermoelectric-energy-harvesting-2016-2026--technologies-devices--applications-for-thermoelectric-generators-300305111.html (21st June 2019)

[186] Rob van der Meulen, Janessa Rivera, (November 2014), *Gartner Says 4.9 Billion Connected "Things" Will Be in Use in 2015*, see on https://www.gartner.com/en/newsroom/press-releases/2014-11-11-gartner-says-nearly-5-billion-connected-things-will-be-in-use-in-2015 (21st June 2019)
[187] Q. Wei, M. Mukaida, K. Kirihara, Y. Naitoh, T. Ishida, *RSC Adv.* **2014**, *4*, 28802.
[188] (a) P. Aranguren, A. Roch, L. Stepien, et al, *Appl. Therm. Eng.* **2016**, *102*, 402. (b) W. Lee *et al., Scientific Reports,* **2016**, *6*, 33795.
[189] D. Kim *et al., Adv. Materials. Tech.,* **2018**, *3* (4), 1700335.
[190] K. Gordiz, A. K. Menon, S. K. Yee, *J. Appl. Phys.* **2017**, *122*, 124507.
[191] A. K. Menon, S. K. Yee, *Journal of Applied Physics,* **2016**, *119*, 055501.
[192] Y. Du, K. Cai, S. Chen, H. Wang, S. Z. Shen, R. Donelson, T. Lin, *Sci. Rep.* **2015**, *5*, 6411.
[193] J. D. Ryan *et al., ACS Appl. Mater. Interfaces*, **2017**, *9* (10), 9045-9050.
[194] Z. Li, H. Sun, C.-L. Hsiao, Y. Yao, Y. Xiao, M. Shahi, Y. Jin, A. Cruce, X. Liu, Y. Jiang, W. Meng, F. Qin, T. Ederth, S. Fabiano, W. Chen, X. Lu, J. Birch, J. W. Brill, Y. Zhou, F. Zhang, *Adv. Electron. Mater.* **2018**, 1700496.
[195] N. Satoh, M. Otsuka, T. Ohki, A. Ohi, Y. Sakurai, Y. Yamashita, T. Mori, *Sci. Technol. Adv. Mater.* **2018**, *19*, 517.
[196] X. Dong *et al., ACS Appl. Mater. Interfaces*, **2018**, *10* (31), 26687-26693.
[197] S. Ferhat, C. Domain, J. Vidal, D. Noël, B. Ratier, B. Lucas, *Org. Electron.* **2019**, *68*, 256.
[198] R. Tian, C. Wan, Y. Wang, Q. Wei, T. Ishida, A. Yamamoto, A. Tsuruta, W. Shin, S. Li, K. Koumoto, *J. Mater. Chem. A* **2017**, *5*, 564.
[199] H. Fang *et al., Journal of Applied Polymer Science,* **2017**, *134* (3), 44208.

Chapter 2
Formulation and structural engineering of polymer films

Recently, thermoelectricity appears to be a promising renewable energy source, thanks to the potential to convert waste of heat into electricity. Inorganic thermoelectric materials have been largely studied for this purpose, *ZT* as high as 2.2 could be achieved with these materials. On another side, organic thermoelectric materials, with a majority of polymers, have some appealing properties such as low density, low thermal conductivity, low cost and easy synthesis and/or processing. Unfortunately, polymers can't compete with inorganic materials for medium/high temperatures due to their low thermal range application [1], they can still find a practical application in low-end waste heat management and flexible portable device [2].

Two mains strategies exist to improve the conversion efficiency of thermoelectric materials: lower their thermal conductivity (κ), or enhance the power factor ($S^2\sigma$). In order to obtain a larger *ZT*, high electrical conductivity, large Seebeck coefficient and a low thermal conductivity are targeted. As descussed in Chapter 1, all of these parameters are interdependent, making the optimization of *ZT* challenging and more difficult [3].

Thermoelectric polymers must be conducting polymers, and depending on the main charge carrier type, they could be classified in two categories: p-type (holes) and n-type materials (electrons). In this Chapter 2, studies and optimization of thermoelectrics properties of polymers/organics materials have been done, p-type synthesized polymers are presented Figure 1 while n-type materials used are presented in Figure 2.

First, a study of the effect of several solvent additives and base on thermoelectric properties of Poly(3,4-ethylenedioxythiophene doped with *p*-toluenesulfonate (PEDOT:Tos) thin films was conducted. The additives were selected based on increase of their boiling point temperatures. Then a base, the pyridine, was selected to reduce the polymerization rate. Both of this additives will contribute to promote crystallization and so improve thermoelectric properties of the resulting thin films. This approach, already described in our laboratory, was performed to test its robustness and reliability on our new equipment [4].

Then, three well-known p-type conjugated polymers were synthesized, Poly-3-hexylthiophene (P3HT), Poly[N- 9′- heptadecanyl- 2,7- carbazole- 5,5- (4′,7′- di- 2- thienyl- 2′,1′,3′-benzothiadiazole)] (PCDTBT) and Polythieno [3,4-b]-thiophene-co-benzodithiophene (PTB7). These polymers are widely used in organic optoelectronic and transistors devices [5,6]. Although all conducting polymers are conjugated, not all conjugated polymers are conducting. So a doping step was necessary in order to obtain conducting polymers with good electrical properties. Thus, thanks to a fine tuning of their electronic and morphology properties,

thermoelectric properties of these polymers were largely increased. Values comparable with the literature were obtained.

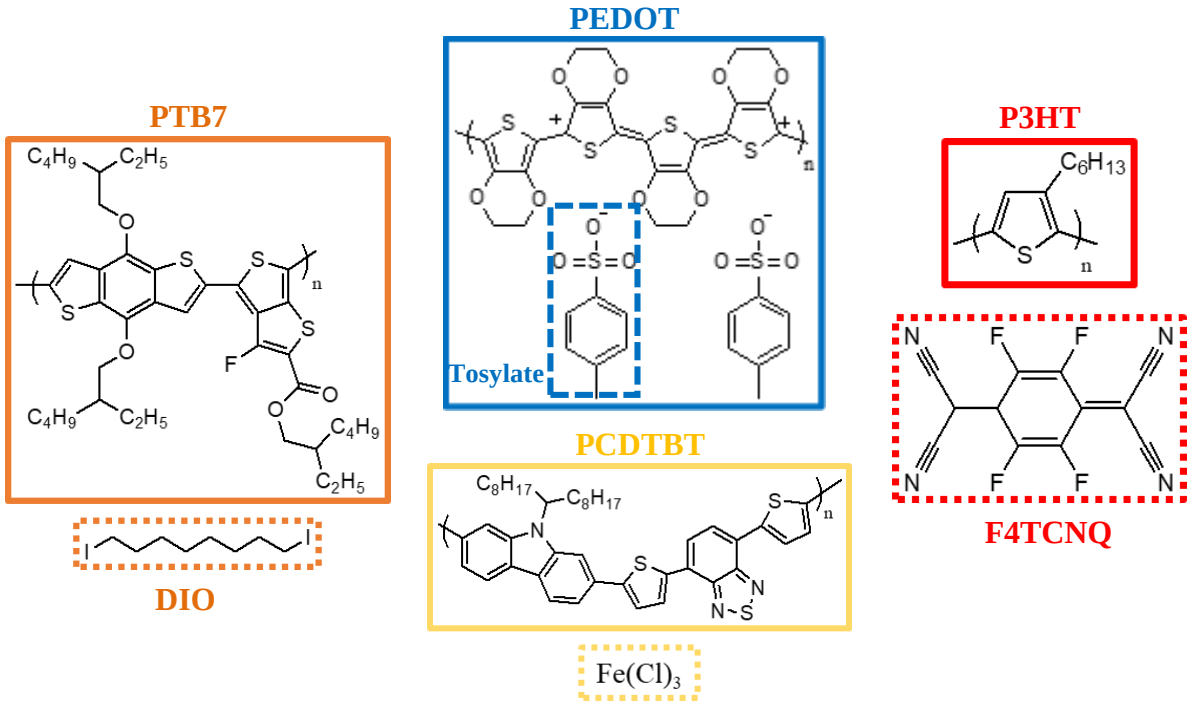

Figure 1: p-type polymer synthesized (full line) and their «dopants » (dashed line).

An optimized thermoelectric module consists of units of n- and p- type semiconducting material connected electrically in series and thermally in parallel [7]. Therefore, two n-type polymers and organic materials were studied (Figure 2). Initially, PCBM as a n-type reference material was studied due to its large use as n-type material in various field [8]. A novel approach by liquid way was used in order to improve the thermoelectric properties of resulting thin films. Finally, a collaboration with the *Prof.* Jenekhe's group allowed to obtain a n-type polymer, NDI-biselenophene copolymer (PNDIBS), with two molecular mass. PNDIBS is a derivative of Poly{[N,N'-bis(2-octyldodecyl)naphthalene-1,4,5,8-bis(dicarboximide)-2,6-diyl]-alt-5,5'-(2,2'-bithiophene)} (PNDI(2OD2T)) (the most famous n-type conducting polymer), the main difference is their heteroatom, selenium for the first one and sulfur for the last.

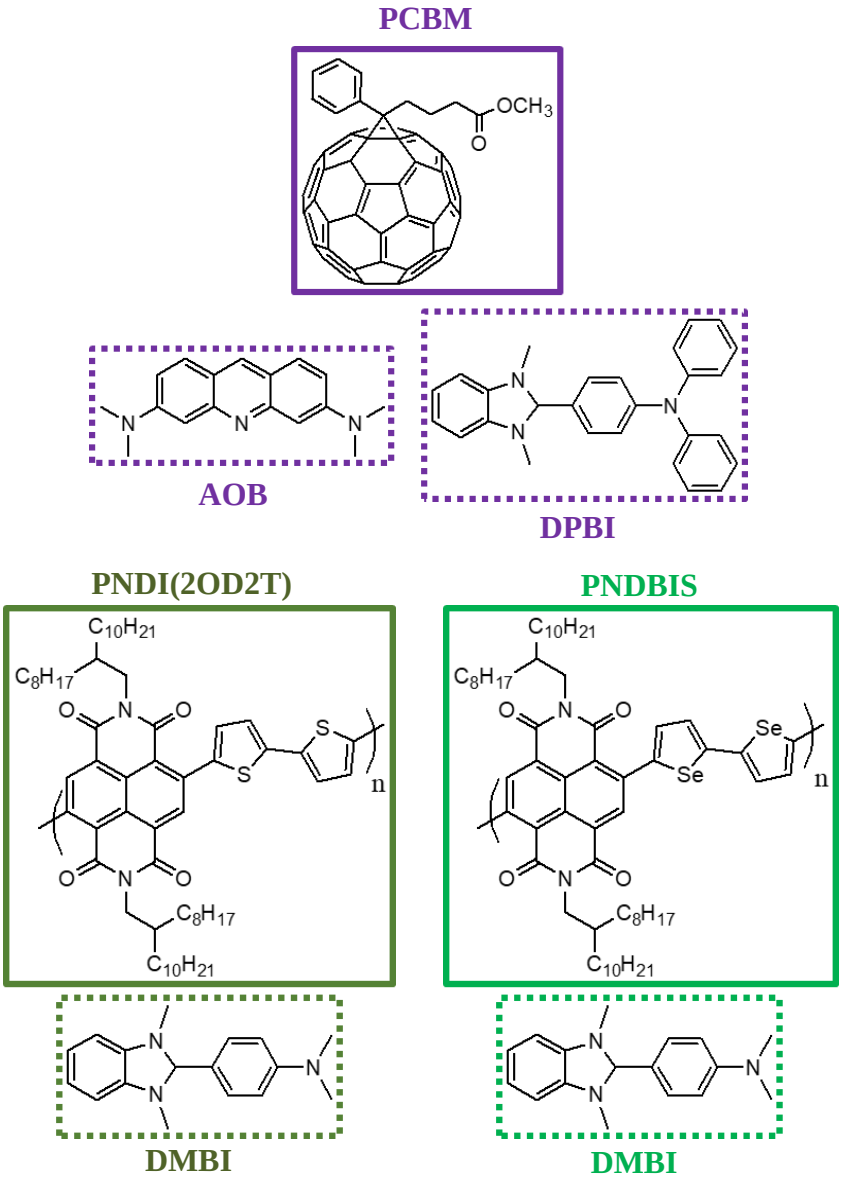

Figure 2: n-type materials used (full line) and their dopants (dashed line).

A p-type polymer engineering

1. PEDOT:Tos

Poly(3,4-ethylenedioxythiophene) (PEDOT) derivatives are promising material for low-cost printed thermo-generators for room temperature applications. Thin films of poly(3,4-ethylenedioxythiophene) (PEDOT) derivatives doped with *p*-toluenesulfonate (Tos) molecules can exhibit a *ZT* as high as 0.25 at room temperature, which is only 4 times lower than that of conventional Bi_2Te_3 at room temperature [9], thus underlining the high potential of such systems for future applications. Furthermore, conducting polymers have lot of advantages like easy processability, low toxicity and a low thermal conductivity [10,11].

As shown in Chapter 1, thermoelectric materials could be compared thanks to the figure of merit ZT at a given temperature. However, scientists focus on the optimization of the power factor, $S^2\sigma$, because of the negligible effect of the thermal conductivity (0.2-0.5 W/m.K) and its difficulty to be measured with precision [10,12–14].

Regrettably, Seebeck coefficient of conducting polymers are quite low because of their high conductivity and the antagonist behaviour with the respect of charge carrier concentration (Chapter 1) [11,13]. In case of PEDOT:Tos, the optimization of the power factor was done by focusing on the doping level. As shown by Bubnova *et* al, a proper tuning of PEDOT doping level is crucial for improving thermoelectric properties, enhanced Seebeck coefficient without losing the high conductivity [13]. Another strategy developed by Petsagkourakis *et al.* to increase thermoelectric properties, mainly electrical conductivity, is the engineering of the PEDOT structure with high boiling point solvent leading a noticeable enhancement of the charge carrier mobility ($\sigma = [N\mu_{e+} P\mu_h] e$) by affecting the carrier delocalization with the improvement of crystallinity [15]. The structural optimization has a side effect on thermoelectric properties, in particular on the Seebeck coefficient. In fact, due to a notable change of the Fermi level position and in the shape and filling to the DoS slope, Seebeck coefficient is enhanced (S is proportional to the DoS at the Fermi level, see in **Appendix I**) [12,16]. In case of PEDOT:Tos, improvement of the π-orbital overlapping thanks to a proper doping level tuning and structural engineering allows a transition from a Fermi glass to a semi-metallic behaviour [17–19]. Crispin *and coll.*, worked a bipolaron network band structure for this polymer system with a positive improvement of both electrical and Seebeck conductivity by band structure modification [12].

Processing parameters and synthetic pathway strongly affect the crystallinity of semi-conducting polymers thin films [20–23]. In case of PEDOT formulations, addition of high boiling point solvent improves the crystallinity of the films by acting as a plasticizer during the polymerization, as confirmed by grazing incidence X-ray scattering experiments (GIWAXS) [15]. Another strategy to improve the crystallinity is by controlling the conjugated polymer molecular mass [24–26]. PEDOT derivatives polymerization occurs with an oxidative polymerization where the release of protons during its process induces an acceleration of the polymerization kinetics which is harmful for a proper polymerization control and chain length control [27]. To limit this auto-catalysed mechanism, an organic base can be introduced in PEDOT formulations in order to obtain higher molecular mass [28,29].

Recently, PEDOT:Tos thin films power factor were optimized by introducing additives like DMSO and pyridine [30]. This processing methodology of adding a high boiling point solvent and an organic base inducts an increase of the thin film crystallinity. Thus electrical conductivity and carrier mobility were improved for the same constant carrier concentration without affecting the Seebeck coefficient. This improvement was due to a synergistic effect of the high boiling point solvent, as plasticizer, and the organic base, as controlling polymerization agent on the crystallinity and DoS. So a tenfold increase of the thermoelectric power with respect of pristine films was achieved.

This strategy developed few years ago in our laboratory, was used and its repeatability and robustness were controlled over month for solutions and thins polymers films thermoelectric properties.

1.1 Structural engineering with high boiling point solvent

The difference of boiling point between different solvent and PEDOT:Tos was studied in order to investigate their effect on thermoelectrics properties of thin films. Electrical conductivity σ, Seebeck coefficient S and power factor PF of all polymer films are presented Table 1. Polymer films were made in accordance with the procedure described in **Appendix II**. The boiling point of solvent didn't have a significant impact on Seebeck coefficients, which stayed constant at 35 ± 5 µV/K. However, the electrical conductivity wasn't constant with respect of boiling temperature, a maximum was reached for DMSO at 635 S/cm (Table 1). With a constant Seebeck coefficient and an electrical conductivity with a maximum, the power factor,

$S^2\sigma$, followed the trend of the electrical conductivity (bell-shape curve), and reached a maximum of 69.2 µW/m.K² for DMSO (Figure 3).

High boiling point solvent	Tb (°C)	S (µV/K)	σ (S/cm)	PF (µW/m.K²)
Pristine (no additive)	-	33 ± 5	230 ± 11	25.0
Acetronitrile (ACN)	82	33 ± 5	264 ± 10	28.7
Toluene (Tol)	110	33 ± 5	301 ± 12	32.8
Chlorobenzene (CB)	137	36 ± 5	315 ± 14	40.8
Dimethylformamide (DMF)	153	32 ± 5	630 ± 20	64.5
Dimethylsulfoxide (DMSO)	189	33 ± 5	635 ± 18	69.2
Ethylene Gycol (EG)	197	32 ± 5	145 ± 8	14.8

Table 1 : Thermoelectric properties of the corresponding PEDOT:Tos films with high boiling point solvent (class with respect of their boiling point Tb)

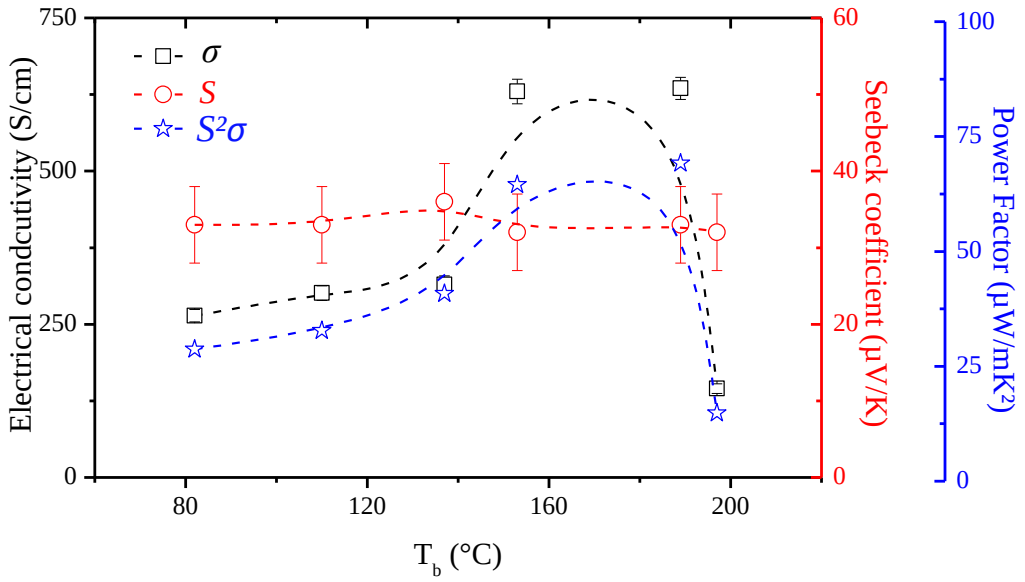

Figure 3: Seebeck coefficient, electrical conductivity and power factor of PEDOT :Tos thin films treated with various high boiling point solvent

To find an origin of the electrical conductivity increase, the oxidation level and the morphology of PEDOT:Tos films were compared. First, the oxidation level and *N* (density of charge carrier) are correlated, in polymer chain of semiconducting polymers, the doping is able thanks to an oxidation process [10,13]. Besides, oxidized sulfur atoms are stabilized by the anion of the dopant molecule, the tosylate counter-ion [31]. With a positive Seebeck coefficient, the charge carrier in this systems were holes. In order to determine the oxidation level of each PEDOT:Tos samples with additive, X-ray photoelectron spectroscopy (XPS) was used, this is an analytical experiment allowing to obtain chemical nature of the surface, a survey spectrum

of PEDOT:Tos thin film is presented Figure 4. As σ is directly linked to *N* through doping, probing the oxidation level of PEDOT:Tos films by XPS could be a way to study the possible modification of the carrier concentration. With a magnification on 160-170 eV area of the survey spectrum (red rectangle), two kinds of sulfur atoms are visible for PEDOT:Tos thin films; one in the tosylate counter-ion molecule and the other in the polymer backbone, in the thiophene unit.

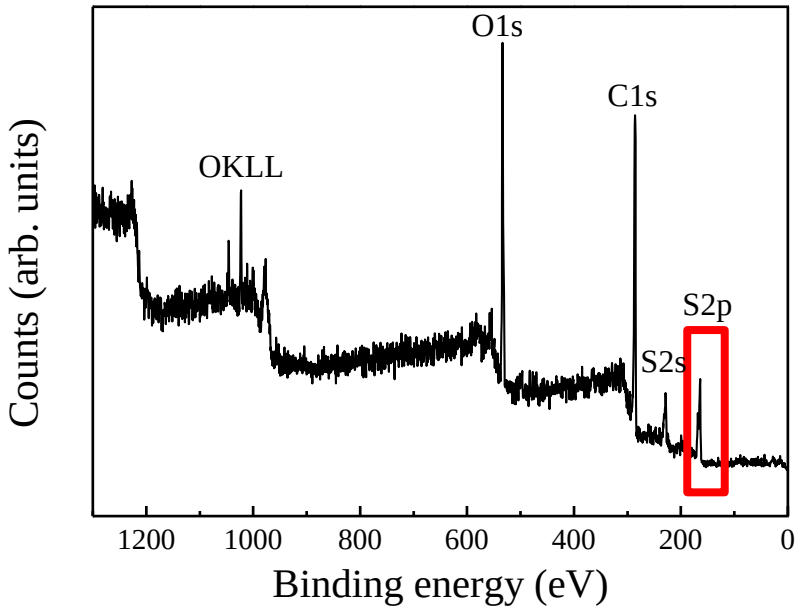

Figure 4: XPS Survey spectrum of a PEDOT :Tos thin film

Because the chemical environment of two sulfurs is different, XPS shows distinct signatures. For more visibility, only XPS spectra for sulfur S(2p) for PEDOT:Tos with DMSO thin film is presented Figure 5. The grey curve is the experimental data obtained by the measurement, and the black one is the fitting. This fitting was obtained by considering the relative sensitivity factor (RSF) for sulfur, carbon and oxygen [32]. The light red, at high binding energies 167-171 eV, could be attributed to sulphur of tosylate counter-ion "linked" to the polymer backbone while the dark red, at binding energies 167-169 eV, could be attributed to sulfur from free tosylate counter-ion. Then the light blue, at lower binding energies 165-168 eV, is from the positively charge thiophene unit, and the dark blue at binding energies 163-166 eV is related to the neutral thiophene unit [33] . Based on this analysis, the oxidation levels of PEDOT:Tos thin films can be determined. The oxidation level is relative to the amount of tosylate counter-anion per unit of thiophene unit. So, the ratio of the area for neutral tosylates contribution on

the area for all thiophenes unit contribution gives the oxidation level (More details in **Appendix II**). All oxidation levels for PEDOT:Tos films are presented in Table 2, the treatment process didn't impact the oxidation levels of PEDOT:Tos films.

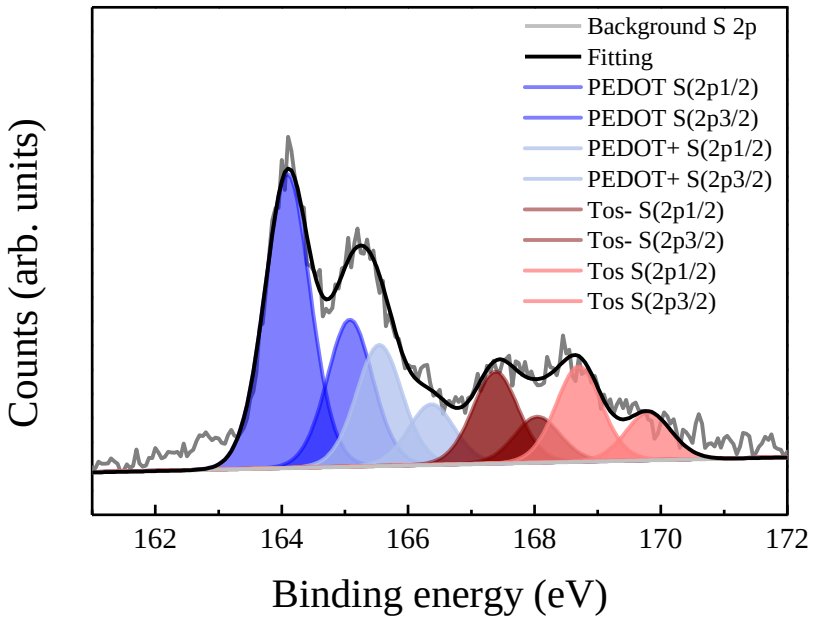

Figure 5: S2p XPS spectra of PEDOT :Tos (grey curve) with its fitting (black curve). Blue peaks correspond to thiophene unit and red peaks correspond to tosylate.

High boiling point solvent	Oxidation level (%)
Pristine (no additive)	20.77
Acetronitrile (ACN)	21.45
Toluene (Tol)	22.12
Chlorobenzene (CB)	21.89
Dimethylformamide (DMF)	22.52
Dimethylsulfoxide (DMSO)	22.12
Ethylene Gycol (EG)	21.78

Table 2 : Oxidation levels calculated from XPS data for PEDOT :Tos films treated with high boiling point solvent.

Therefore, the charge concentration, *N*, of PEDOT:Tos films remains constant, implying that the electrical conductivity increased was linked to the mobility μ ($\sigma = Nq\mu$). But, because PEDOT-based polymers are heavily doped semiconductors [34], conventional transistors aren't appropriate for the determination of the mobility to the screening of the applied electric field by the charge carriers. In literature, electrolyte gated transistors have been described as an alternative for transport properties' measurement [34–36]. Unfortunately, an ion gel is incorporated in this transistors' type, modifying the density of charge carriers, meaning an

under-estimation of field effects and so mobility. Another way to indirectly observe an increase in mobility could be to look at the morphology and more particularly the degree of crystallization of pristine and solvent treated PEDOT:Tos samples. In fact, in organic semiconductors, transport properties are strongly related to their film morphology [22,23,25,37–39]. Thanks to Grazing Incidence Wide Angle X-ray Scattering (GIWAXS), the structural properties of the PEDOT:Tos thin films were probe to correlate the nature of the additive on the conductivity, by an increase of the mobility. The (q_r, q_z) 2D scattering pattern recorded for the pristine PEDOT:Tos film as well as those recorded for the acetonitrile-treated and DMSO-treated films are presented in Figure 6 (a). Only three samples are presented to have easier clarity on the graph. These films scatter anisotropically, with the majority of scattered intensity along the near out-of-plane axis ($q_r = 0$), so perpendicularly to the substrate. In Figure 6 (b), the radially averaged scattered intensity is plotted with respect to the scattering vector q. In all cases, the scattered intensity is presented after normalization for film thickness and background subtraction, to allow for quantitative comparison between samples. Based on work of Aasmundtveit *et al.*, the strong peak at 0.44 $Å^{-1}$ and 0.88 $Å^{-1}$ are attributed on the (100) and (200) reflections for all the PEDOT:Tos thin films [40]. The third peak observed at 1.3 $Å^{-1}$ can be assigned to the (300) reflection. The very low intensity of this peak means a limited long-range order along this axis, indicating a material with paracrystalline distortions. Finally, at 1.77 $Å^{-1}$ a broad and intense peak, the (020) reflection can be assigned as the π-π stacking direction [40].

On top of that, when the PEDOT:Tos thin films were treated by the high boiling point solvent, an increase of the scattered intensity for the (100) and (020) peaks could be observed. Furthermore, the area below the scattering peaks is directly correlated with the degree of crystallinity, so adding a high boiling point solvent in the film increases its crystallinity and so its mobility (increase of the conductivity without N modification). The increase of crystallinity is due to a slower evaporation rate of the main solvent, 1-butanol (T_b = 115°C), when T_b of the additive is higher, delaying the crystallization kinetics of the polymer chains and allowing further crystallization. Many works in the literature confirmed this behaviour for conducting polymers [21,34].

Then the anisotropic nature of the 2D images were examined, the in-plane and near out-of-plane line-cuts are presented in Figure 6 (c) and (d). In the near out-of-plane pattern ($I(q_z)$ vs q_z, Figure 6 (d)), the (h00) group and the (020) reflection, similarly to the $I(q)$ vs q pattern, while in the in-plane pattern ($I(q_y)$ vs q_y, Figure 6 (c)) the (h00) reflections are absent and only the broad (020) reflection at 1.77 $Å^{-1}$ is observed. In the in-plane pattern, the absence of the

(h00) group can be interpreted by a preferential orientation of the crystallites in the film with respect to the substrate. PEDOT chains are oriented in an edge-on configuration, where the thiophene ring are aligned with their planes normal to the substrate. Nevertheless, the (020) peak corresponding to the π-π stacking is also present, some crystallites are oriented with face-on, with the thiophene ring parallel to the film plate.

In case of crystalline semiconducting polymers, chain & crystallite orientation and thin film crystallinity have an important influence on the charge transport properties [12,25,34,38,41]. For PEDOT, where the most efficient charge transport occurs by hopping between doped conjugated chains [41], charge transport is anisotropic, and is dictate by the presence of highly conducting crystallites "metallic" islands embedded in amorphous polymer matrix (less conductive) [42]. Higher crystallinity can exhibit higher mobility and so electrical conductivity, only if a majority of the crystallites orientation is edge-on orientation, thus inter-chain and intra-chain hopping transport are promoted. This methodology developed in our laboratory, enhanced charge transport improves thermoelectric properties by increasing the electrical conductivity from 230 S/cm (pristine) to 635 S/cm (DMSO, best additive) to obtain the power factor of 69.2 µW.mK² for PEDOT:Tos thin films treated with DMSO [30].

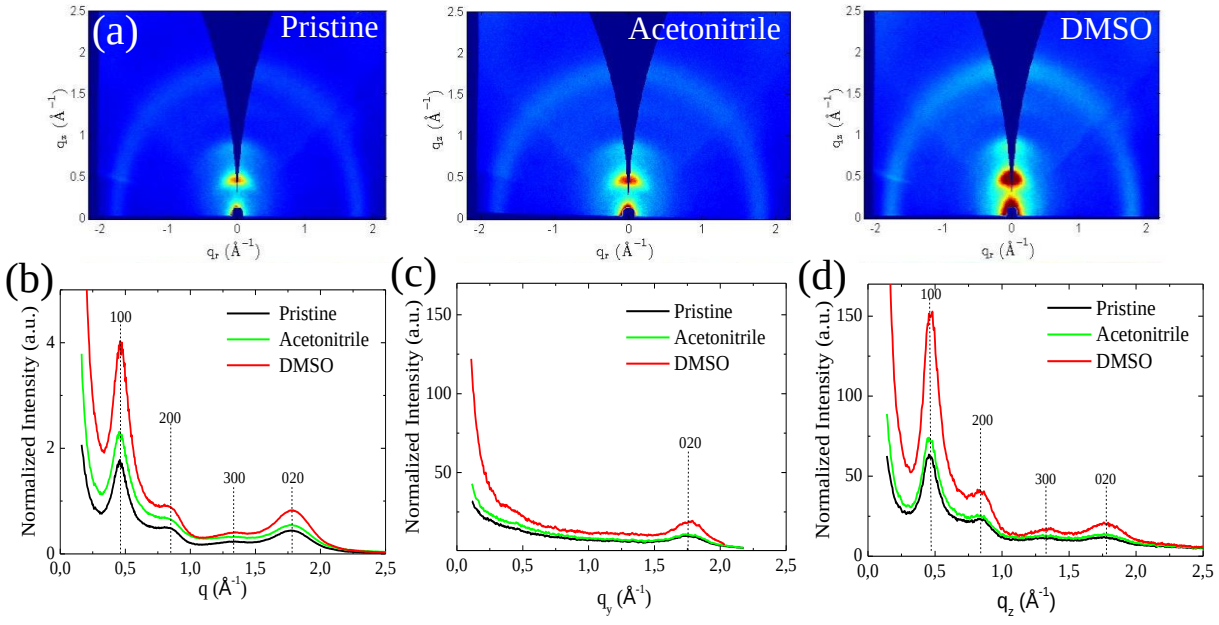

Figure 6: GIWAXS characterization of PEDOT :Tos films with additives.
(a) 2D GIWAXS images of PEDOT:Tos films.
The corresponding 1D scattering patterns: (b) radially average intensity with respect to the scattering vector q, (c) the in-plane intensity line-cut and (d) the near out-of-plane intensity line-cut. The scattering intensity was normalized by film thickness (substrate scattering was substracted).

1.2 Thermoelectric properties enhancement by formulation with an organic base, pyridine

Thermoelectric properties of PEDOT:Tos thin films could be tuned by tuning the crystallisation degree via structural engineering. PEDOT:Tos thin films were prepared by following the reaction procedure described in **Appendix II** [43,44]. The reaction is a thermally activated in-situ solution oxidative polymerization of EDOT monomers in presence of $Fe(Tos)_3$. The polymerization prepared by in-situ polymerization techniques, using oxidants based on Fe^{3+} derivate, are highly acidic and reactive, making the polymerization uncontrollable and resulting in many structural defects in the thin film. With the addition of an organic base to the PEDOT:$Fe(Tos)_3$ formulation, the polymerization process can be slow down in order to obtain higher molecular mass polymer chains [28,43–45]. This organic base will play the role of an inhibitor, by increasing the pH in order to control the reaction rate. Based on previous work in our laboratory, the organic base chosen is pyridine. To follow the polymerization kinetics, UV-visible spectroscopy in formulations with and without pyridine was done. Similar absorbance curves shape, with only absorbance intensity difference, due to a thickness difference, were obtained (Figure 7).

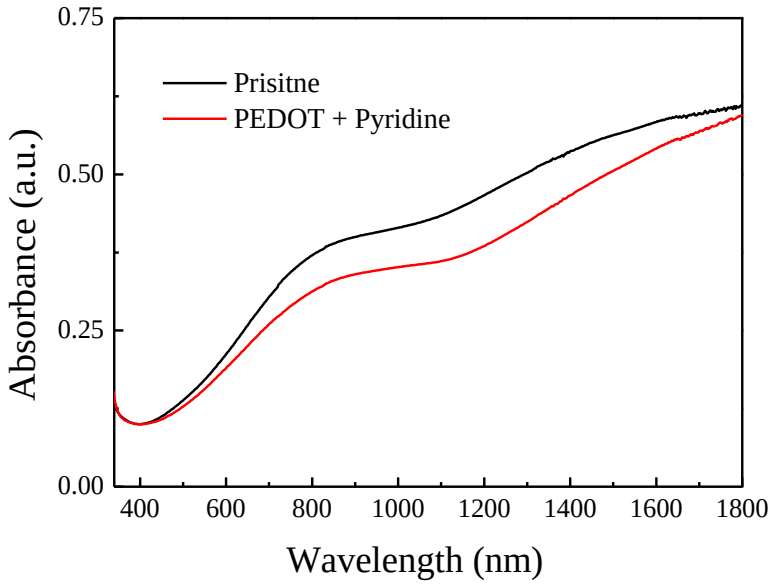

Figure 7: UV-visible spectra of pristine and pyridine treated PEDOT:Tos "solutions".

The influence of the pyridine on the kinetics is observable thanks to the absorbance at 1600 nm, corresponding to the bipolaron signature and is plotted Figure 8.

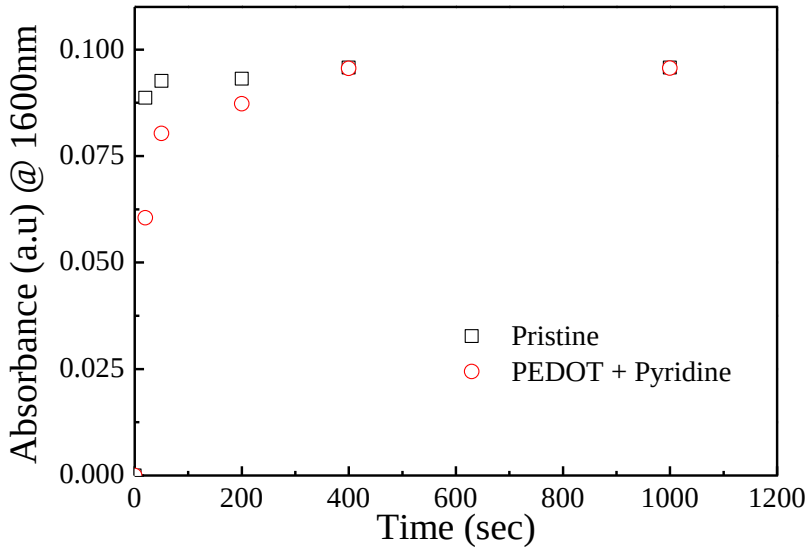

Figure 8: Absorbance at 1600 nm versus polymerization time for pristine PEDOT :Tos film and treated with pyridine

In case of PEDOT:Tos pristine formulation, polymerization is quick as shown the increase of the bipolaron band at 1600 nm, the absorbance maximum is reached at 20 sec and stays constant over the time, confirming the fast polymerization process from the oxidative polymerization mechanism [43,44]. However, in presence of pyridine, the maximum conversion of the EDOT monomers can only be observed after at least 200 sec of reaction time. The treatment of UV-Vis data over the time allow to confirm the capture of protons by the pyridine during the polymerization or the complexation of the pyridine with the iron catalyst, resulting in a reduction of the polymerization rate. Based on literature and previous results [28], higher molecular mass PEDOT chains could be produced even if this is not possible to measure the molecular mass of PEDOT:Tos with size exclusion chromatography (SEC).

The effect of organic base was studied in order to investigate its effect on thermoelectrics properties. The organic base was also added in high boiling point solvent formulation to observe any influence on thermoelectrics properties. Electrical conductivity σ, Seebeck coefficient S and power factor PF of all polymer films are presented in Table 3. Polymer films were made in accordance with the procedure described in **Appendix II**. The pyridine had an impact on the Seebeck coefficient, which increased from 33 ± 5 µV/K to 40 ± 3 µV/K. Furthermore, the electrical conductivity increased by a factor 3, reaching 600 S/cm, almost the electrical conductivity of PEDOT:Tos + DMSO formulation (635 S/cm). PEDOT:Tos films prepared

with pyridine formulation also shown an overall 4-fold increase of the Power factor to achieve 96 µW/m.K² (Figure 9).

High boiling point solvent	Tb (°C)	S (µV/K)	σ (S/cm)	PF (µW/m.K²)
Pristine (no additive)	-	33 ± 5	230 ± 11	25.0
Pyridine	-	40 ± 3	600 ± 20	96
ACN + pyridine	82	41 ± 2	609 ± 11	102.4
Tol + pyridine	110	42 ± 4	615 ± 9	108.5
CB + pyridine	137	41 ± 4	1120 ± 8	188.3
DMF + pyridine	153	39 ± 3	1054 ± 16	160.3
DMSO + pyridine	189	44 ± 3	1240 ± 12	240.1
EG + pyridine	197	40 ± 5	1045 ± 10	167.2

Table 3 : Thermoelectric properties of the corresponding PEDOT :Tos films with high boiling point solvent and pyridine.

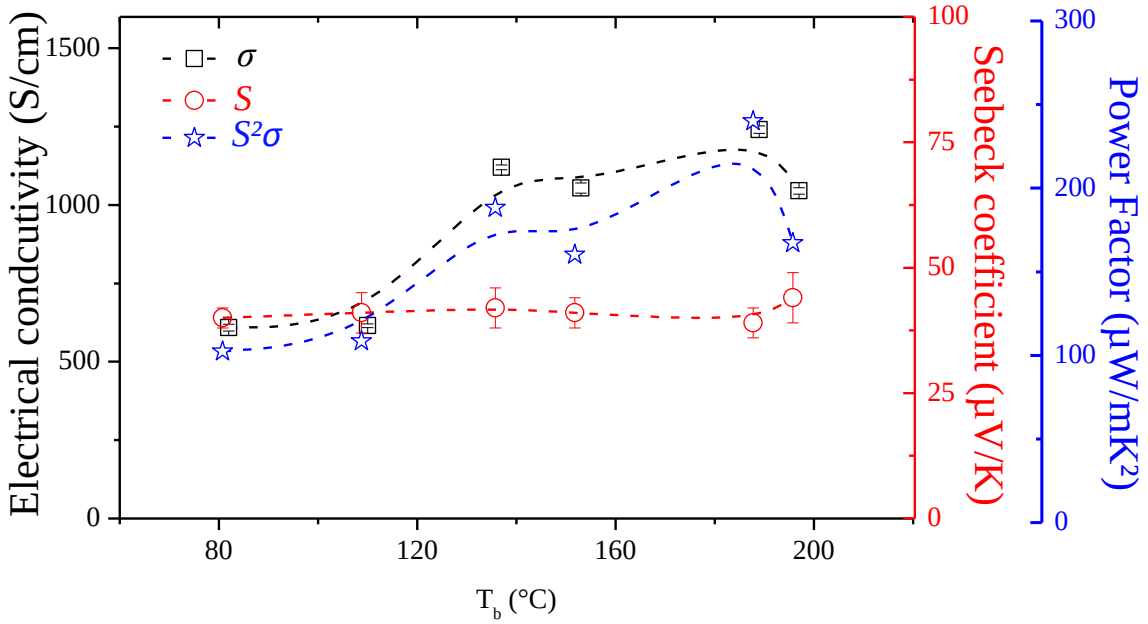

Figure 9: Seebeck coefficient, electrical conductivity and power factor of PEDOT:Tos thin films treated with high boiling point solvent and pyridine.

In the previous part, the introduction of high boiling point solvent allows an overall increase of crystallinity as well as an improvement of the thermoelectric properties for PEDOT:Tos films, the follow-up consists to make same formulations with high boiling point solvent and pyridine to optimize thermoelectric properties [15]. A synergy effect could be observed when the boiling point of the additive is higher than the boiling point of 1-butanol (T_b = 115°C), the main solvent. This synergy could be observed as both the electrical conductivity and the

Seebeck coefficient increase compare to PEDOT:Tos pristine films, from σ = 230 to σ = 1240 S/cm and from S = 33 to S = 44 µV/K, resulting to a Power factor of 240.1 µW/m.K² (without modification of the oxidation level). As previously (Part on high boiling point solvent), XPS spectroscopy was used to determine and compare the oxidation level of PEDOT:Tos samples without additive, with pyridine and pyridine + high boiling point solvent (Table 4).

High boiling point solvent	Oxidation level (%)
Pristine (no additive)	20.77
Pyridine	21.55
ACN + pyridine	20.74
Tol + pyridine	21.19
CB + pyridine	21.54
DMF + pyridine	22.32
DMSO + pyridine	21.48
EG + pyridine	21.98

Table 4 : Oxidation levels calculated from XPS data for PEDOT :Tos films treated with high boiling point solvent and pyridine.

Based on the results presented Table 4, treatment process didn't impact the oxidation levels of PEDOT:Tos films. Therefore, the charge concentration, *N*, of PEDOT:Tos films remains constant, implying that the electrical conductivity increased was linked to the mobility μ ($\sigma = Nq\mu$).

In organic semiconductors, transport properties are strongly related to their film morphology. In order to elucidate the structural origin of the increase of thermoelectric properties [15,23,46], GIWAXS experiments were done. The 2D scattering patterns for the various films are presented in Figure 10 (a) (corrected by incident photon flux, acquisition time of 30 sec and scattering volume to allow direct comparison). As previously with PEDOT:Tos thin films treated with high boiling point solvent, a clear anisotropy signature could be observed on the pyridine treated films pattern. Besides, this is along the near out-of-plane q_z axis that the majority of the scattered intensity is placed, confirming the preferential orientation of the PEDOT crystallites, perpendicular to the substrate (Figure 10 (c)) [40]. A large increase of the scattered intensity is apparent for PEDOT thin films prepared with pyridine and pyridine + DMSO formulations. The radially averaged scattered intensity profiles are plotted Figure 10 (b). Three reflections corresponding to the (h00) peak family (qh00 = 0.44, 0.88, 1.3 Å) and a (020) broader peak at

1.77 Å are present. Furthermore, the radially averaged scattered intensity depicted in Figure 10 (b) allows to relate the film crystallinity to the formulation process by comparing the area of the (100) peak. A gradual increase of crystallinity is evident from the pristine sample to the pyridine + DMSO sample.

The increase of the crystallinity for PEDOT:Tos thin film by the addition of DMSO (high boiling point solvent), acting as a plasticizer during the evaporation of the solvents, was shown in the first part of this Chapter [15,21]. Pyridine can also increase the crystallinity of PEDOT:Tos thin films by lowering the polymerization rate allowing the formation of higher molecular mass chains [26]. Furthermore, the pyridine is probably evaporating simultaneously with the main solvent, 1-butanol, due to their near boiling point. A synergetic effect happens when the two additives, DMSO and pyridine are coupled, leading to PEDOT:Tos thin films with highest crystallinity.

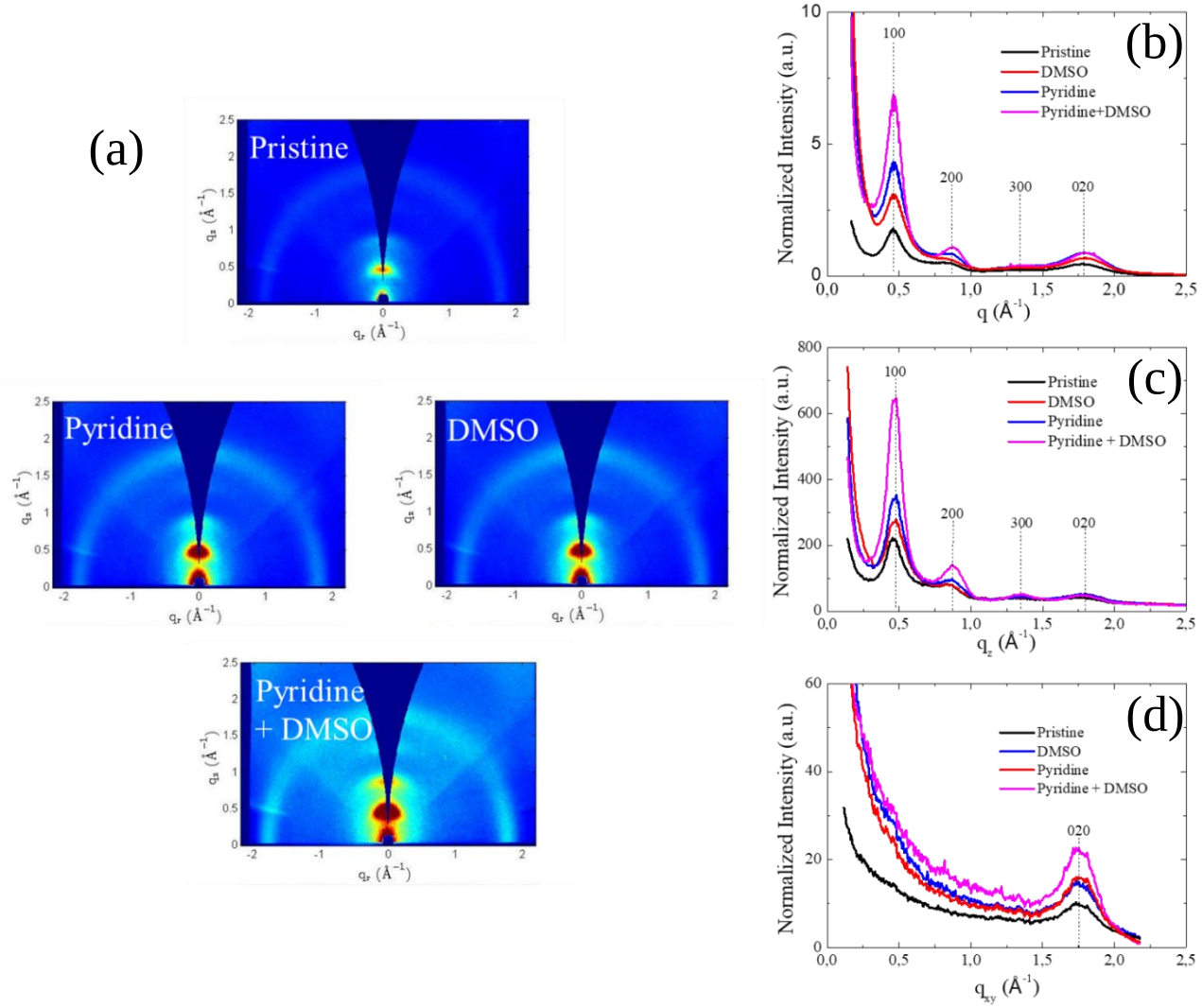

Figure 10: GIWAXS characterization of PEDOT :Tos films with additives. (a) GIWAXS images of PEDOT:Tos films.
The corresponding 1D scattering patterns: (b) radially average intensity with respect to the scattering vector q, (c) the near out-of-plane intensity line-cut and (d) the in-plane intensity line-cut. The scattering intensity was normalized by film thickness (substrate scattering was substracted).

In order to understand the increase of the Seebeck coefficient, the study of the DoS near the Fermi level is necessary. In Crispin's team [12], they proved that Seebeck coefficient of semi-crystalline conjugated materials benefits from the asymmetry of the DoS. A way to achieved to this asymmetry is to perform proper doping, leading to bipolaron bands extending the valence and conduction bands, and ultimately generate a bipolaron network. From a structural point of view, a higher charge carrier delocalization can originate from both a longer conjugation length of the doped chains and from an increased structural order [10,12]. In both cases, overlapping of the π-orbitals into a widened π-system is promoted leading to an asymmetry in the DoS. This can be true for polymers that exhibit a high crystallization degree and/or highly doped chains [12], as it is the case for the highly crystalline PEDOT films under study.

To enlighten electronic structure of PEDOT thin films treated with additives and try to relate it with the increase of thermoelectric properties, Ultra-violet Photoelectron Spectroscopy (UPS) measurements were performed. In Figure 11, normalized UPS spectra of PEDOT:Tos pristine, treated with DMSO or pyridine and with both are presented. The distinct signatures observed at 4.5, 12 and 15 eV correspond to the inelastic electron scattering at the film surface and σ states. The work function of these materials is between 4.6 – 4.8 eV which is in agreement with literature [12].

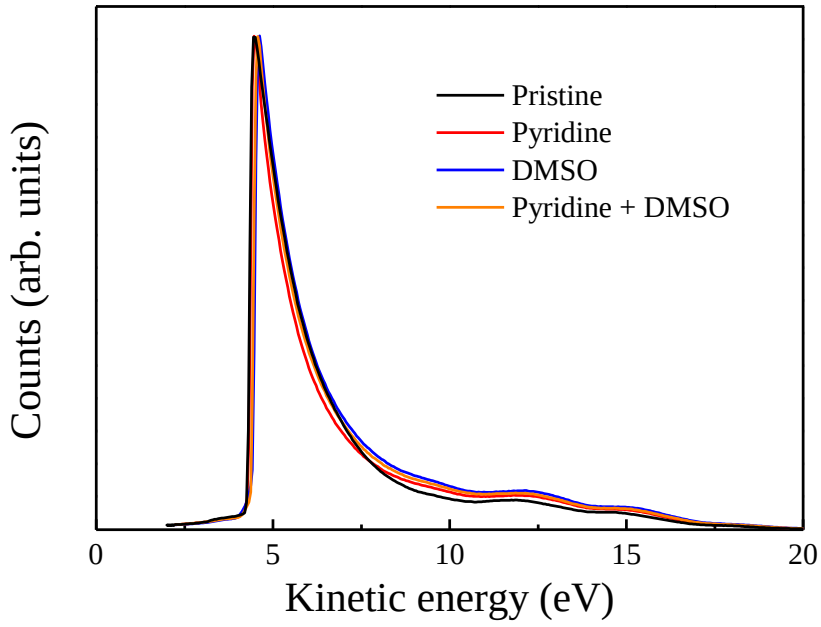

Figure 11: UPS spectra of PEDOT :Tos thin films pristine and with additives.

Figure 12 shows a magnified view at the higher kinetic energies (lower binding energies), at which the band edge corresponding to deeper π-orbitals is localized. A broadening of the band edge is evident for the PEDOT:Tos DMSO + Pyridine sample (orange curve) which is related to a higher delocalization of the charge carriers in these deeper π-orbitals [47,48]. A similar broadening should extend to all π-bands (including the ones near the Fermi position) which would result in a more asymmetric DoS at the Fermi level. This is further translated into an increase of the Seebeck coefficient for the PEDOT:Tos DMSO + pyridine material (orange curve) since the DoS slope is proportional to S through the Mott formula (purple arrow) [12].

This extended overlapping of the π orbitals retrieved from the UPS analysis and intrinsic of the increased thin film crystallinity, is also beneficial for the electrical conductivity of the polymer film [12]. In conducting polymers, the main charge transport mechanism is hopping transport of the charge carriers between low-energy "metallic" islands inside the amorphous polymer matrix [42]. From an electronic point of view, these areas can be considered as the overlapping π orbitals of the crystalline doped conjugated chains [49]. Hence, the hopping of the carriers along these regions is assisted by decreasing the structural disorder of the PEDOT:Tos thin films. This macroscopically results in higher carrier mobility and thus higher σ, as observed for the thin films treated with DMSO and pyridine (Table 3).

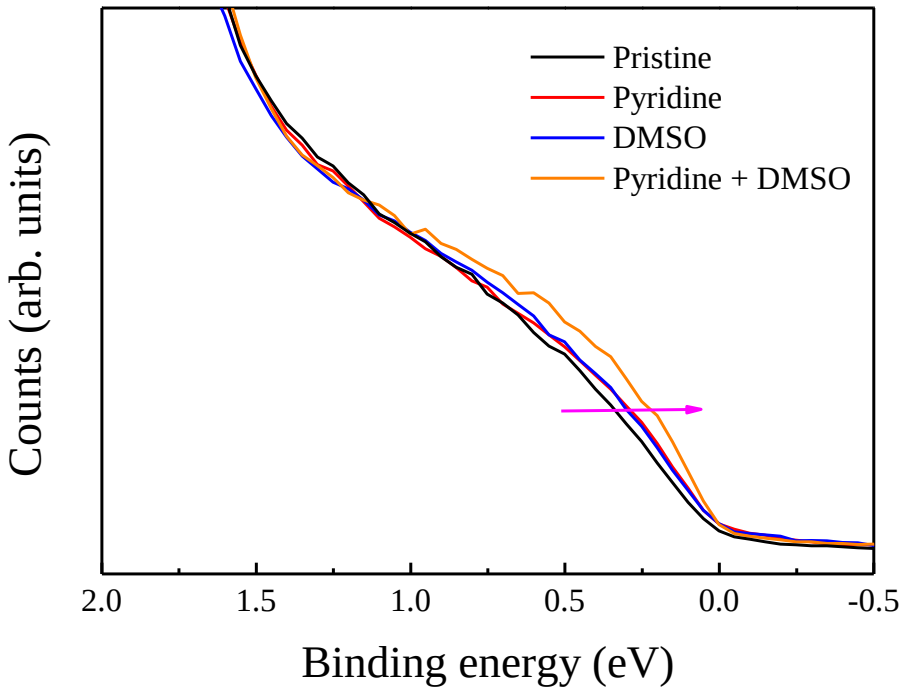

Figure 12: Magnification to low binding energy region of UPS previous spectra.

Thanks to a fine tuning of polymerization kinetics for PEDOT:Tos thin films with pyridine, an enhancement of thermoelectrics properties was achieved, as attested by both a mild increment of the Seebeck coefficient and a three-fold increase of the electrical conductivity. Then by adding pyridine to DMSO formulations, resulting PEDOT:Tos thin films obtained a high Power factor of 237 μW/m.K² inherent to an increased charge carrier mobility and a higher degree of crystallinity, thanks to a synergistically effect. Origins of these effects have been found by UPS to a band broadening near the Fermi level due to a more extended π-orbital system and by GIWAXS to a confirmation of a higher degree of crystallinity. These discoveries are consistent with the current understanding on the correlation between electronic and structural properties. In fact, PEDOT:Tos thin films with the highest crystallinity exhibits as well the most broadened band edge due to extended π-orbital overlapping, and thus, the higher thermoelectric efficiency.

1.3 Aging control

Thermoelectric properties, Seebeck coefficient and electrical conductivity, were tested over a long period of time in order to check the stability of PEDOT:Tos pyridine and DMSO formulations and films. The formulations and films were made in accordance to procedure described in **Appendix II**. Oxidant solutions were stored at 4°C and resulted films were stored in a petri dish inside a clean room (temperature, 22°C, and moisture level, 50%, were quite stable).

In Figure 13, Seebeck coefficient and electrical conductivity are plotted versus time and correspond to stability of the oxidant formulation. Thermoelectric properties are remaining unaltered at least one month (27 days), however after this month, electrical conductivity drops from 1250 to 850 S/cm in one month. Seebeck coefficient decrease is less important. This decrease could be from pyridine evaporation during swab, explaining that the electrical conductivity value is almost equal to PEDOT:Tos films only treated with DMSO (σ (pyridine/DMSO) = 850 S/cm and σ (DMSO) = 635 S/cm).

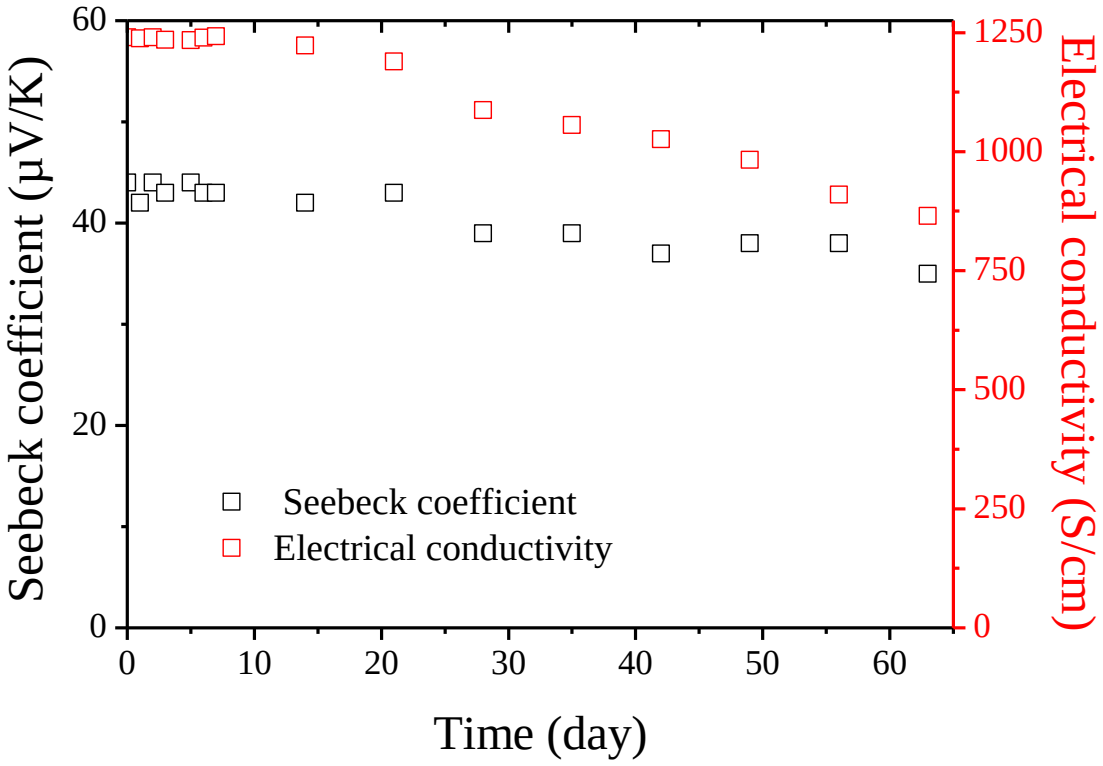

Figure 13: Seebeck coefficient (black square) and electrical conductivity (red square) of PEDOT:Tos samples from the same oxidant formulation versus time.

Then the stability over time of PEDOT:Tos thin film was evaluated though probing of thermoelectric properties. The Figure 14 corresponds to thermoelectric properties for the same PEDOT:Tos thin film treated with pyridine and DMSO. Electrical conductivity stays constant for 150 days (5 months) then drops to 0 S/cm in one more month. The decrease of the Seebeck coefficient is harder to spot due to its low value and standard deviation (Table 1 and Table 3). The hypothesis formulate is related to macroscopic defect appearing after 5 months (cracks), and degrading film order/crystallinity inducing a huge drop of electrical conductivity. This degradation is probably due to evaporation of additive or solvent trap inside the polymer thin film matrix or the interaction between the polymer thin film surface and moisture.

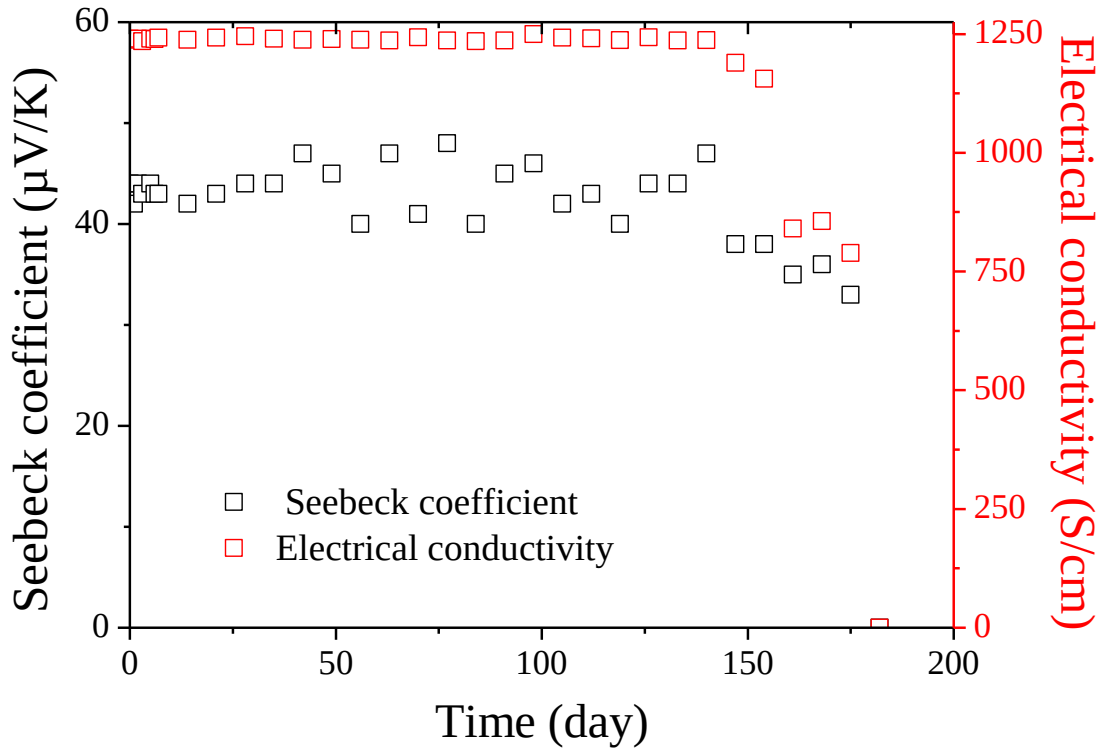

Figure 14: Seebeck coefficient (black square) and electrical conductivity (red square) of the same PEDOT:Tos thin film versus time.

2. P3HT

Poly-3-hexylthiophene (P3HT) is an alkylated derivate of polythiophene, P3HT is one of the most studied conjugated polymers thanks to its excellent intrinsic properties such as a good solubility, appropriate energy gap, doping reversibility and excellent electrical properties (high exciton mobility along its backbone) [50]. P3HT solutions, with easy processability, are suitable for a variety of solution processes such as spray-coating [51], roll-to-roll printing [52], inkjet printing [53] and spin-coating [54]. Thus, P3HT has been very successfully introduced in optoelectronic [55–59] and organic field effect transistors [60,61] , these days scientists try to explore its properties for organic thermoelectric applications [62–65].

Intrinsic P3HT electrical conductivity at room temperature is low, 3.15 x 10^{-7} S/m [66], researcher found several options to address this problem. Some common techniques are done by varying experimental condition such as solvent nature, temperature, deposition methods, and annealing conditions during film formation, order to control the structural properties and so electrical/electronic properties [67–69]. Another method to increase electrical conductivity is to use dopant molecule (molecular electron acceptors or donors) to mimic p- & n-doping of inorganic systems [70]. Doping of P3HT could be achieved by number of methods, but the most famous is by "chemical doping" with a molecule that has a high electron affinity (electron acceptors) into the film as described in Chapter 1 [71–73].

Scientific community focus its interest in F4TCNQ as dopant for P3HT films. The nature of the interaction between F4TCNQ and P3HT in solution phase and film has been invested intensely these past years [74–78]. Indeed, solvent and dopant concentration have drastically impact on P3HT solution and film properties, as proven by various studies [78]. Solvent plays an important role on π-π stacking of polymer chains and dopant/P3HT solubility [79]. Then dopant concentration affects directly the structural characteristics of P3HT films, Gao *and coll.* shown that doping efficiency depends on the ability of P3HT to form aggregates in presence of F4TCNQ [80].

Furthermore, processing method have also a high influence on P3HT/F4TCNQ film properties, especially on electrical conductivity [81–83]. Recently, three main processes were investigated, solution doping [81], sequential doping [84] and vapour phase doping [63]. For solution doping, P3HT and F4TCNQ are mixed together and directly casted into a thin film. In contrast, sequential doping is a two steps process, with cast of the neat P3HT thin film than F4TCNQ is deposited on top from an orthogonal solvent. Sequentially doped films have been

shown to have higher conductivity than that of solution doped samples at the same dopant concentration [85,86]. Indeed, with a solution mixed doping, the microstructure of the film is more disturbed than with sequential casting that allows tie-chains connecting crystalline domains formed in neat P3HT to be retained leading to high conductivity. Furthermore, in solution doping, more aggregates are formed during the charge transfer in solution, causing a different morphology in the cast films with poorly connected domains, decreasing the electrical conductivity. The main drawback of these processing methods are the post-treatment thermal annealing that can decompose or remove the dopant from the films at elevated temperature. One of the solution to this post-treatment is the vapour phase deposition, allowing the infiltration of F4TCNQ in P3HT thin film at mild temperature without disturbing too much P3HT morphology (crystallinity) [63]. Unfortunately, this process is difficult to adapt due to generally a lack of experimental information (dopant quantity, container size, atmosphere temperature, etc.) and adapted material to the laboratory.

In this work, thanks to rigorous state of the art, solution mixed and sequential doping were adapted to obtain P3HT:F4TCNQ thin films. The influence of dopant concentration on thermoelectric properties was studied in order to obtain P3HT thin film with the best power factor. Finally, the doping process efficiency was followed by UV-visible-IR analysis and correlated to the morphology thanks to AFM analysis.

2.1 Solution-mixed doping method

The effect of dopant concentration, F4TCNQ, on P3HT thin film, prepared via solution-mixed doping method, was studied in order to investigate their effect on thermoelectric properties. All thermoelectric properties are presented in Table 2. Polymers films were made in accordance with the procedure described in **Appendix II**. F4TCNQ concentration had a significant impact on electrical conductivity and Seebeck coefficient, an antagonist behaviour between these both parameters was observed. The highest electrical conductivity was reached for 20 mol% of F4TCNQ at 4.3 S/cm and the highest Seebeck coefficient for pristine P3HT at 1458 µV/K (Table 5). Evidently, the power factor, $S^2\sigma$, followed a trend with a maximum at 2.48 µW/m.K² (Figure 15).

F4TCNQ concentration (mol%)	S (µV/K)	σ (S/cm)	PF (µW/m.K²)
P3HT pristine	1458 ±101	1 x10^{-6}	2.12 x10^{-4}
P3HT + 10 mol% F4TCNQ	387 ±10	0.02 ±0.01	0.30
P3HT + 20 mol% F4TCNQ	76 ±3	4.3 ±0.2	2.48
P3HT + 30 mol% F4TCNQ	45 ±5	1.8 ±0.1	0.36

Table 5 : Thermoelectric properties of the P3HT :F4TCNQ with different F4TCNQ concentration.

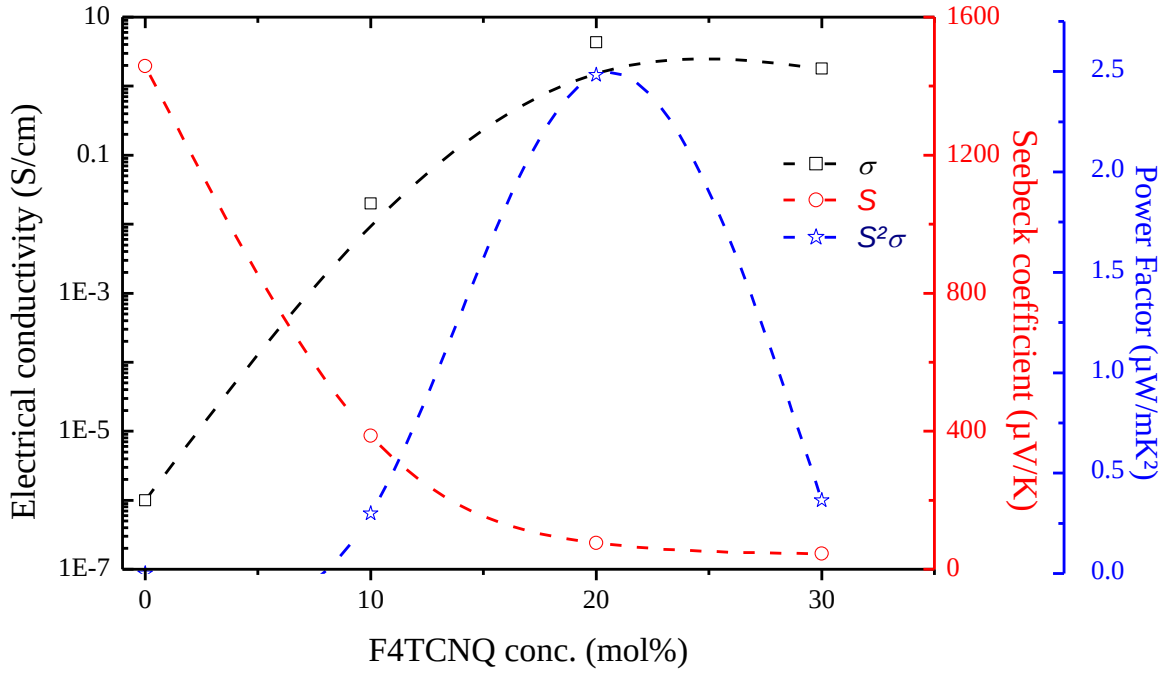

Figure 15: Seebeck coefficient, electrical conductivity and power factor of P3HT thin films doped with F4TCNQ by solution –mixed doping method.

The doping efficiency was followed by UV-visible-NIR analysis in addition to thermoelectric measurements. UV-visible is perfect for the characterization of doped film, thanks to sub-gap absorptions from charge carrier species. In case of P3HT:F4TCNQ films, the main charge carriers are singly-charged polarons, confirmed by Wang *et al.* and their fitting to optical spectra [87]. Positive polarons give rise to two allowed sub-gap transition bands; in P3HT, these transitions occur at about 826 nm and 2400 nm [88]. Furthermore, the F4TCNQ counter-ion shows four distinctive absorption band at 413, 688, 751 and 855 nm. Figure 16 shows UV-visible-IP spectra, normalized to 1 at the P3HT π-π* maximum absorption (560 nm), of all films prepared using the solution-mixed doping method at doping levels between 0 and

30 mol% F4TCNQ. With F4TCNQ mole ratio rising, absorption bands corresponding to the $F4TCNQ^{\bullet-}$ radical anion (413, 688, 751 and 855 nm) grew in. $P3HT^{\bullet-+}$ presence was confirmed by an increase of absorption band at 826 nm and the appearance of the tail of 2400 nm absorption polaron band. Additionally, hypsochromic shift (≈ 50nm) occurs for the absorption band at 560 nm corresponding to the P3HT π-π* related to F4TCNQ's action. These results are consistent with literature [89].

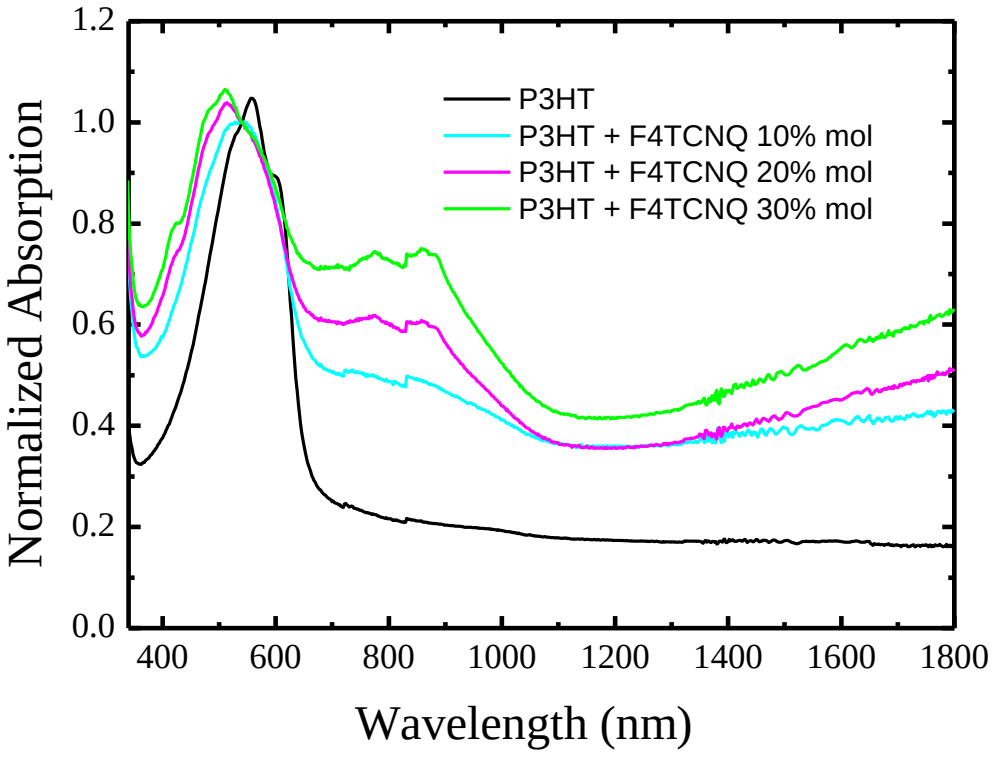

Figure 16: UV-visible spectra of P3HT :F4TCNQ thin films (solution-mixed doping).

Then the film morphology was studied by atomic force microscopy (AFM). All images of films doped using the solution-mixed method are presented Figure 17. As is clearly visible, this method yields significantly rougher films, RMS roughness was calculated directly from images. Furthermore, a phase aggregation is visible when F4TCNQ is added to P3HT film. These structures are almost certainly phase-segregated F4TCNQ domains. The vast differences in film roughness and the phase segregation are related to the difficulty of processing for solution-mixed doping method. Gao *et al.* proposed a mechanism by which doping could cause aggregation [80]. They noticed an increase in J-aggregate which are indicative of significantly increased polymer backbone rigidity thanks to resonance Raman studies of doped films. Implying the F4TCNQ primarily injects holes into aggregated P3HT domains, and resulting of

reduction in ionization potential of aggregates as compared to amorphous domains by approximately 0.3 eV, explaining aggregation in solution. Jacobs *et al.* also proposed a mechanism where they studied several aspects of doping-induced aggregation isn't accounted by a shift in dielectric constant of the polymer:dopant system [76]. The doping-induced formation of aggregates in solutions has strong detrimental effects on chain morphology/orientation and so on the electrical properties of the resulting films. Polymer chains of undoped P3HT adopted preferentially edge-on orientation [91]. This edge-on orientation with respect to the substrate means the π-π stacking direction in-plane, inducing a higher in-plane hole motilities and so electrical conductivity [91]. However, in solution-mixed doping films, more isotropic orientation of the polymer chains occurs, resulting of solution-state aggregation. This increase in anisotropy and the reduction in edge-on orientation likely plays a role in the reduced conductivity above 20 mol% of F4TCNQ (reduction in connectivity between crystalline domains).

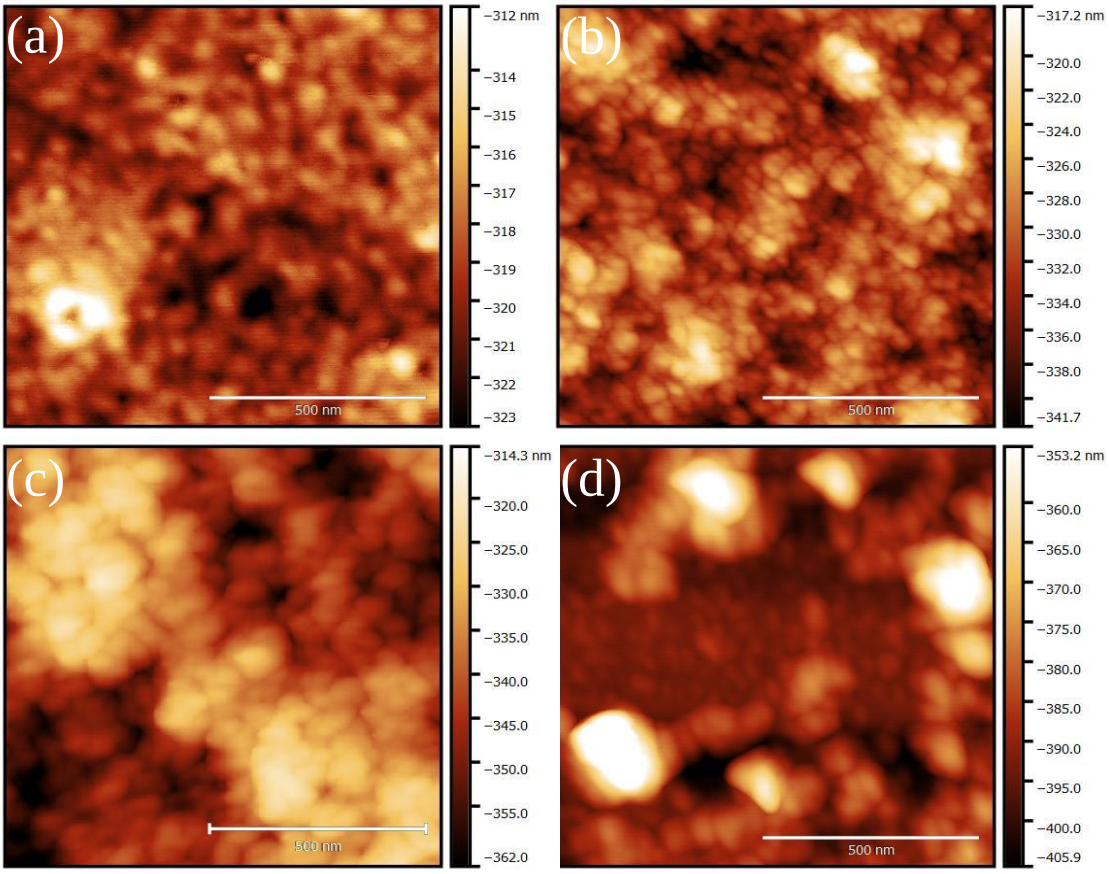

Figure 17: AFM height images of (a) Pristine P3HT, (b) P3HT with 10 %mol F4TCNQ, (c) P3HT with 20 %mol F4TCNQ and (d) P3HT with 30 %mol (scale bar = 500 nm).

2.2 Sequential doping method

The processing method for P3HT:F4TCNQ films was studied and their thermoelectric properties was investigated. Commonly, doped films are completely insoluble in organic solvent, but chemical or optical de-doping methods can recover intrinsic material properties [92]. A method, called doping-induced solubility control (DISC), could be used to stack mutually soluble materials. P3HT can be doped by F4TCNQ by simply exposing coated P3HT films to a F4TCNQ solution in a solvent orthogonal to the polymer. This method, the sequential doping, simplifies the processing of doped films compare to the traditional mixed-solution method. All thermoelectric properties are presented Table 6. Polymers films were made in accordance with the procedure described in **Appendix II**. Acetonitrile was used as an orthogonal solvent for the first layer, then different F4TCNQ concentrations in chlorobenzene were used: 0.01, 0.1 and 1 mg/ml on P3HT films. As previously observed for solution-mixed doping method, F4TCNQ concentration had a significant impact on electrical conductivity and Seebeck coefficient, an antagonist behaviour between these both parameters was observed. Nevertheless, the electrical conductivity does not reach a maximum but increased with the F4TCNQ concentration. The power factor, $S^2\sigma$, followed a trend with a maximum at 1.48 µW/m.K² (Figure 18), lower than power factor of previous method (2.48 µW/m.K²).

Doping method	F4TCNQ conc. (mg/ml)	F4TCNQ conc. (mol%)	S (µV/K)	σ (S/cm)	PF (µW/m.K²)
	P3HT pristine	/	1458 ±101	1 x10^{-6}	2.12 x10^{-4}
Sequential	0.01	5 mol%	756 ±9	0.003 ±0.001	0.17
	0.1	10 mol%	127 ±3	0.87 ±0.1	1.40
	1	20 mol%	52 ±4	2.4 ±0.3	0.65
Mixing	/	10 mol%	387 ±10	0.02 ±0.01	0.30
	/	20 mol%	76 ±3	4.3 ±0.2	2.48
	/	30 mol%	45 ±5	1.8 ±0.1	0.36

Table 6 : Thermoelectric properties of the P3HT :F4TCNQ thin films made by solution-mixed doping and sequential deposition method with different F4TCNQ concentration

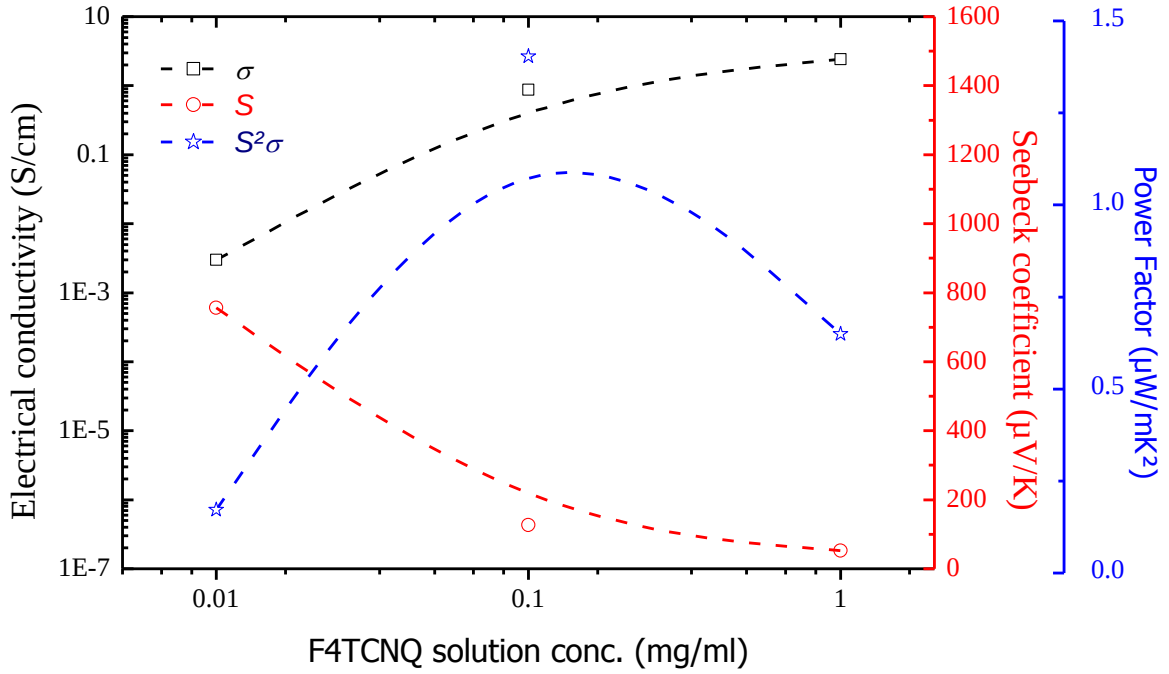

Figure 18: Seebeck coefficient, electrical conductivity and power factor of P3HT thin films doped with F4TCNQ by sequential method.

As previously, the doping efficiency was followed by UV-visible-IR analysis. Figure 19 shows UV-visible-IR spectra of all P3HT films prepared, light color and dark color are corresponding to solution-mixed doping method and sequential processing method respectively. All spectra are normalized to 1 at the P3HT π-π* maximum absorption (560 nm). Characteristic peaks of P3HT doped by F4TCNQ are visible for sequential processing doping (413, 688, 751, 826, 855 and tail of 2400 nm) confirming the availability of this method. By comparing the intensity of these characteristic peaks, an approximate doping level could be determined for sequential processing method (Table 6).

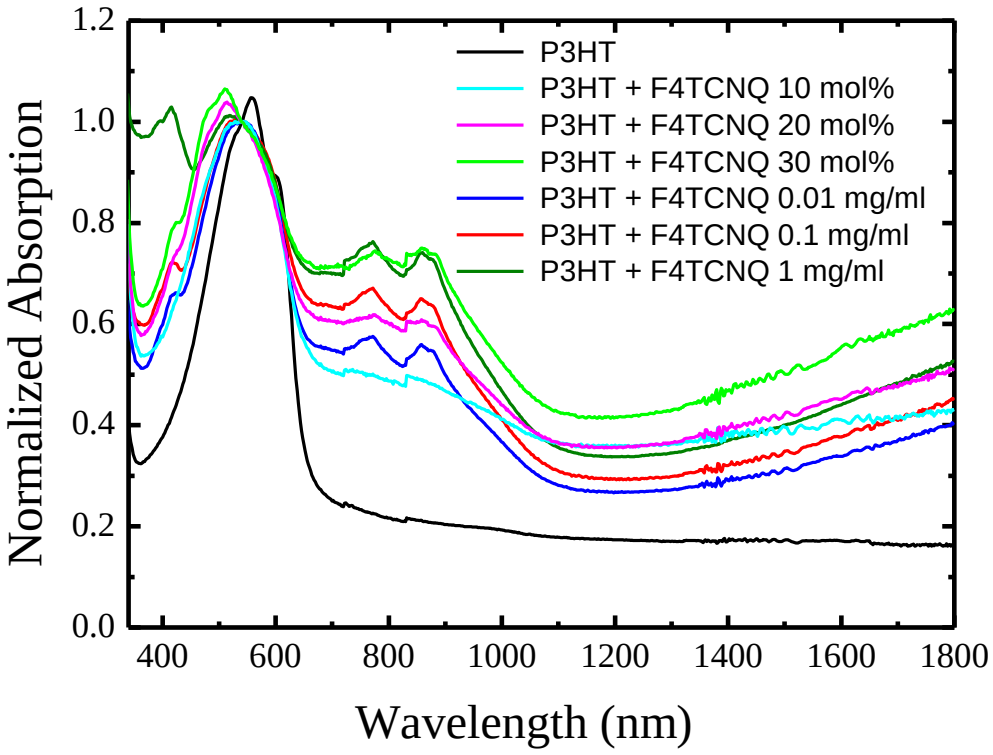

Figure 19: Comparison of UV-visible spectra for P3HT :F4TCNQ thin films made by solution-mixed doping and sequential process.

Comparable doping level were obtained with these two different methods and almost the same thermoelectric properties were achieved, Figure 20 allows to compare these methods in function of F4TCNQ molar concentration. As described previously, electrical properties of films are related to the doping-induced formation of nanoparticles in solution, sequential doping method overcomes this issue. In their work, Jacobs *et al*. clearly established that P3HT films are insoluble after sequential doping from a F4TCNQ/acetonitrile solution [92]. Despite this insolubility, these films have shown a solvatochromic absorption shift in good solvents for P3HT (*i.e.* chlorobenzene), indicating that solvents were able to infiltrate crystallites in the film without causing dissolution.

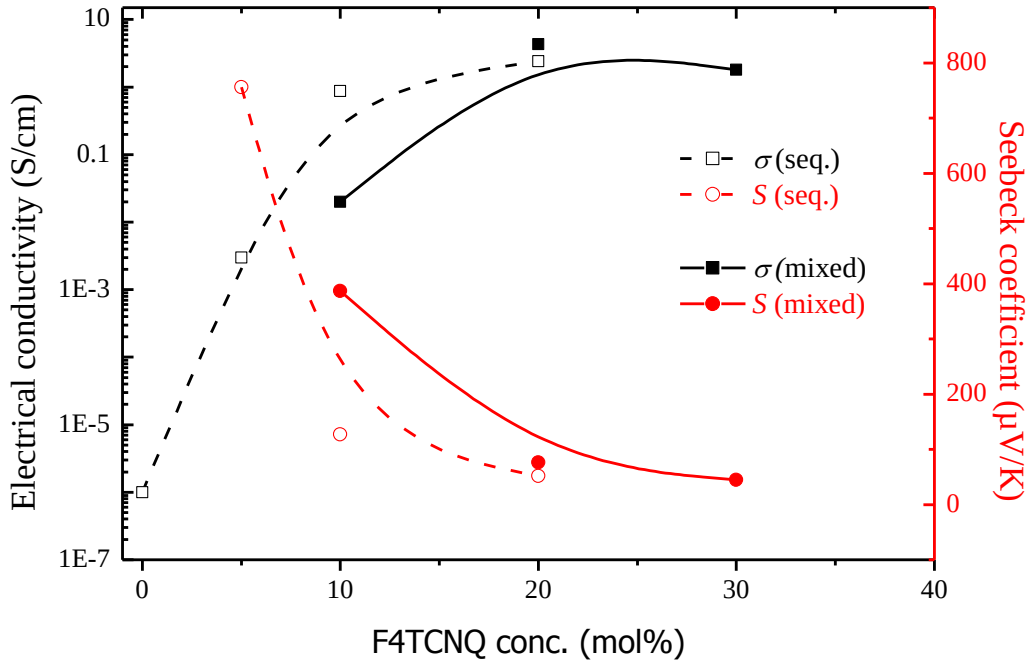

Figure 20: Comparison of Seebeck coefficient and electrical conductivity of P3HT:F4TCNQ thin films doped by solution-mixed doping (full colour symbols) and sequential process (empty colour symbols).

In order to understand this phenomenon, atomic force microscopy (AFM) was used. All images of films doped using both the solution-mixed and sequential method are presented Figure 21. Unlike the mixed-solution films which have high roughness and phase segregation, the films for the sequential process show the same morphology and have a lower roughness. Furthermore, no significant phase segregation is visible in these films, very probably F4TCNQ does not infiltrate P3HT crystallites but intercalate into P3HT crystallites. These results confirm that doping from acetonitrile solution does not affect P3HT crystallinity and allows to obtain an increase of electrical conductivity.

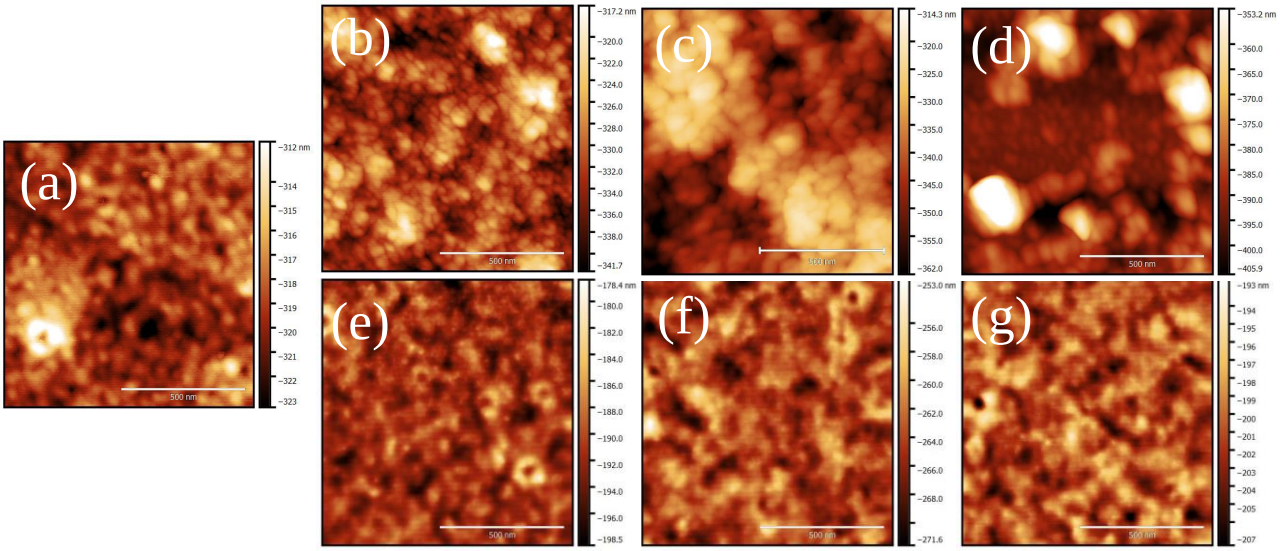

Figure 21: Comparison of AFM height images for solution-mixed (b, c, d) and sequential (e, f, g) doping process. (a) Pristine P3HT, (b) 10 %mol F4TCNQ, (c) 20 %mol F4TCNQ, (d) 30 %mol F4TCNQ, (e) 5 %mol F4TCNQ, (f) 10 %mol F4TCNQ and (g) 20 %mol F4TCNQ (scale bar = 500 nm).

3. PCDTBT

Poly[N-9′-heptadecanyl-2,7-carbazole-alt-4-5,5-(4′,7′-di-2-thienyl-2′,1′,3′-benzothiadiazole)] (PCDTBT) is a donor-acceptor copolymers also called "push-pull" copolymers, composed of carbazole (Cz) unit for the donor moiety and dithienyl-benzothiadiazole (DTBT) units for the acceptor moiety. These past two decades, PCDTBT was widely studied as a promising donor material for photovoltaic applications thanks to its exceptional structural, optical and electronic properties [93–95]. PCDTBT is a low band polymer (1.88 eV) with a relatively large ionization potential corresponding to a HOMO level of -5,35 eV. This larger ionization potential also affords the polymer with greater air stability as oxidation is suppressed [95]. Furthermore, good thermoelectrics performances are expected due to this highly polarized properties indicating well-ordered molecular structures which leads to intermolecular interactions such as heteroatom contacts or π-π interactions [96].

As described previously, semi-conducting polymers have to be doped in order to increase their electrical conductivity. In case of PCDTBT, iron(III) chloride ($FeCl_3$) was used as a dopant agent due to its oxidizing properties [97] and also thanks to thermoelectric results obtained with other carbazole-based polymers [98,99]. During the oxidation process the resulting positive charges on the polymer chains are balanced by the presence of $FeCl_4^-$ counter-ions. Martin-Gonzalez's team studied the influence of $FeCl_3$ concentration on thermoelectric properties of PCDTBT films [100]. The highest electrical conductivity was obtained from the doped PCDTBT film with one $FeCl_3$ molecule per monomer unit. For this 1:1 doped PCDTBT film, electrical conductivity increased up to nine orders of magnitude with the addition of $FeCl_3$, from 1×10^{-7} S/cm for the undoped PCDTBT film to 63 S/cm. Seebeck coefficient reached 35 µV/K leading to a power factor of 9 µW/m.K² for this film [100]. On another side, Leclerc's team used PCDTBT with a higher molecular mass in order to obtain higher thermoelectric properties, and reached at maximum 500 S/cm and 70 µV/K for 1:1.5 PCDTBT:$FeCl_3$ film (optimized data were 160 S/cm and 34 µV/K) [101].

In this work, solutions mixed doping were adapted to obtain PCDTBT:$FeCl_3$ thin films to try to enhance thermoelectric properties. The influence of dopant concentration on thermoelectric properties was studied in order to obtain PCDTBT thin film with the best power factor. Finally, the doping process efficiency was followed by UV-visible analysis and correlated to the morphology thanks to AFM analysis.

The effect of dopant concentration, $FeCl_3$, on PCDTBT thin film, prepared via solution-mixed doping method, was studied in order to investigate their effect on thermoelectric properties. All thermoelectric properties are presented in Table 7. Polymers films were made in accordance with the procedure described in **Appendix II**. In their work, Lévesque *et al.* showed the interesting behaviour of polycarbazoles under their doping, the nitrogen atom is oxidized prior to the backbone by $FeCl_4^-$ counter anion [98]. In this case, charges are very localized, resulting in a large Seebeck coefficient, nevertheless charge-carrier pinning could occur, affecting the electrical conductivity. $FeCl_4^-$ concentration had a significant impact on thermoelectric properties. The electrical conductivity increased with the dopant concentration, and achieved a maximum of 60 S/cm for one $FeCl_4^-$ per PCDTBT unit, before decreasing at high dopant concentration. The electrical conductivity dependence with the doping level can be explained in terms of "trapping". When the doping level is low, the extra introduced carriers into the polymer chains remain localized into the traps created by counter-anions, and the mobility is not sharply increased. When the doping is increased, and hence, the counter-anions are also increased, the Coulomb traps start to overlap and the energy barriers between them decrease. Then, an energy disorder decrease would take place so that both mobility and Seebeck coefficient would increase [10]. But the Seebeck coefficient decreased with the rising of the dopant concentration, a maximum of 56 µV/K was obtained in case of PCDTBT unit doped with 0.66 $FeCl_4^-$ counter anion. In fact, with the increase of doping level, the electrical conductivity forces between counter-anions increase, and so their distance and therefore the charge hopping is not facilitated. So the Seebeck coefficient decreases with the doping level decreasing due to the increase in the carrier density as explained by Snyder *et al* [102]. Finally, the best power factor, $S^2\sigma$, followed electrical conductivity trend with a maximum at 8.21 µW/m.K² (Figure 22).

Dopant concentration	S (µV/K)	σ (S/cm)	PF (µW/m.K²)
PCDTBT	/	1×10^{-7}	/
PCDTBT unit : $FeCl_4^-$ (1:0.5)	50 ±4	85 ±5	2
PCDTBT unit : $FeCl_4^-$ (1:0.66)	56 ±5	12 ±1	3.76
PCDTBT unit : $FeCl_4^-$ (1:1)	37 ±2	60 ±3	8.21
PCDTBT unit : $FeCl_4^-$ (1:2)	28 ±4	22 ±4	1.72

Table 7 : Thermoelectric properties of the PCDTBT:$FeCl_3$ thin films with different $FeCl_3$ concentration.

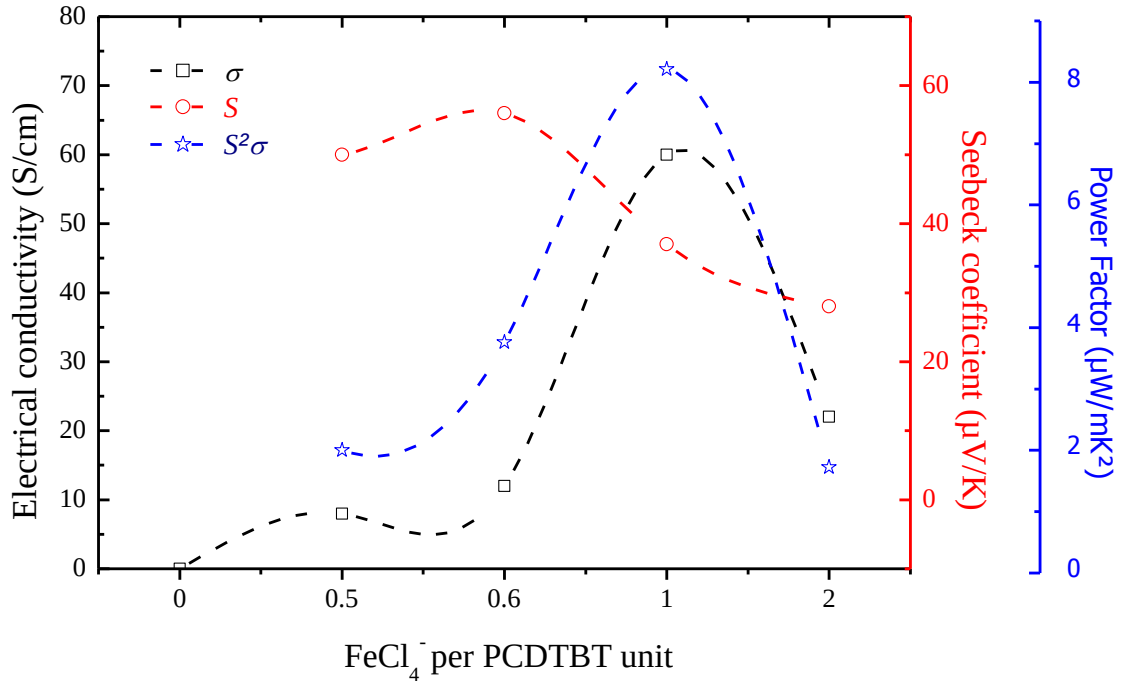

Figure 22: Seebeck coefficient, electrical conductivity and power factor of PCDTBT thin films doped with $FeCl_3$.

The doping efficiency was followed UV-visible-NIR analysis in addition to thermoelectric measurements. UV-visible is perfect for the characterization of doped polymer films. The thin film spectrum of the pristine PCDTBT consists of a peak at around 395 nm and a peak at around 550 nm, which could be attributed to carbazole and benzothiadiazole units respectively [98]. Doping results in a gradual bathochromic effect (red shift) of both absorption peak from 395 nm and 550 nm for the pristine PCDTBT to 402 nm and 570 nm for PCDTBT doped with two $FeCl_4^-$ counter anions per PCDTBT unit (Figure 23, grey dots lines).

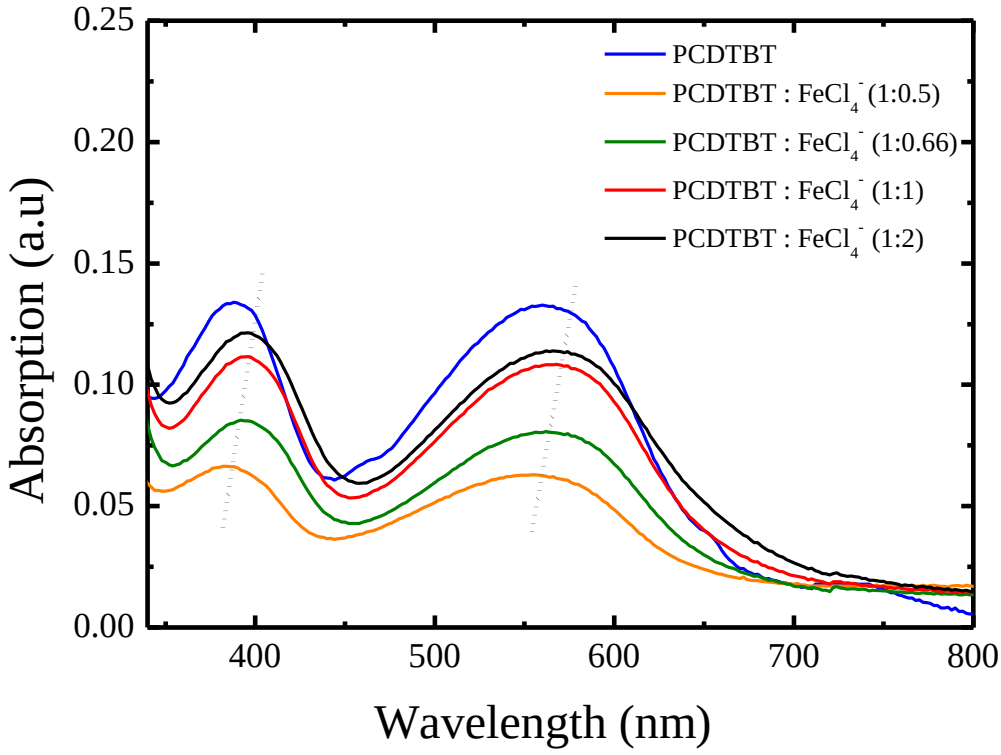

Figure 23: UV-visible spectra of PCDTBT : $FeCl_3$ thin films.

Maiz *et al.* studied the morphology of PCDTBT: $FeCl_4^-$ thin film with wide-angle X-ray scattering (WAXS), and they found that PCDTBT adopted a lamellar packing for the undoped and doped films. Furthermore, they noticed a slightly difference between undoped and doped samples from WAXS data, doping producing a more compact packing of the layers. In this study, the film morphology was studied by atomic force microscopy (AFM) to see the macroscopic influence of $FeCl_4^-$ and try to correlate it to thermoelectric properties. All images of films doped using the solution-mixed method are presented Figure 24. By increasing the $FeCl_4^-$ concentration, film roughness increases, indeed this dopant is not soluble in the polymer matrix. Furthermore, adding $FeCl_4^-$ changes the film morphology, nanostructures ($FeCl_4^-$ aggregate probably) are visible from 0.5 $FeCl_4^-$ per PCDTBT unit to 1 $FeCl_4^-$ per PCDTBT unit. This change in morphology could be the reason of the increase of electrical conductivity. However, when the amount of $FeCl_4^-$ is to high (2 $FeCl_4^-$ per PCDTBT units), the film morphology changes drastically, dewetting is observable and PCDTBT film isn't homogeneous and continuous anymore. In this case, the loss of thermoelectric properties is directly linked to the film morphology.

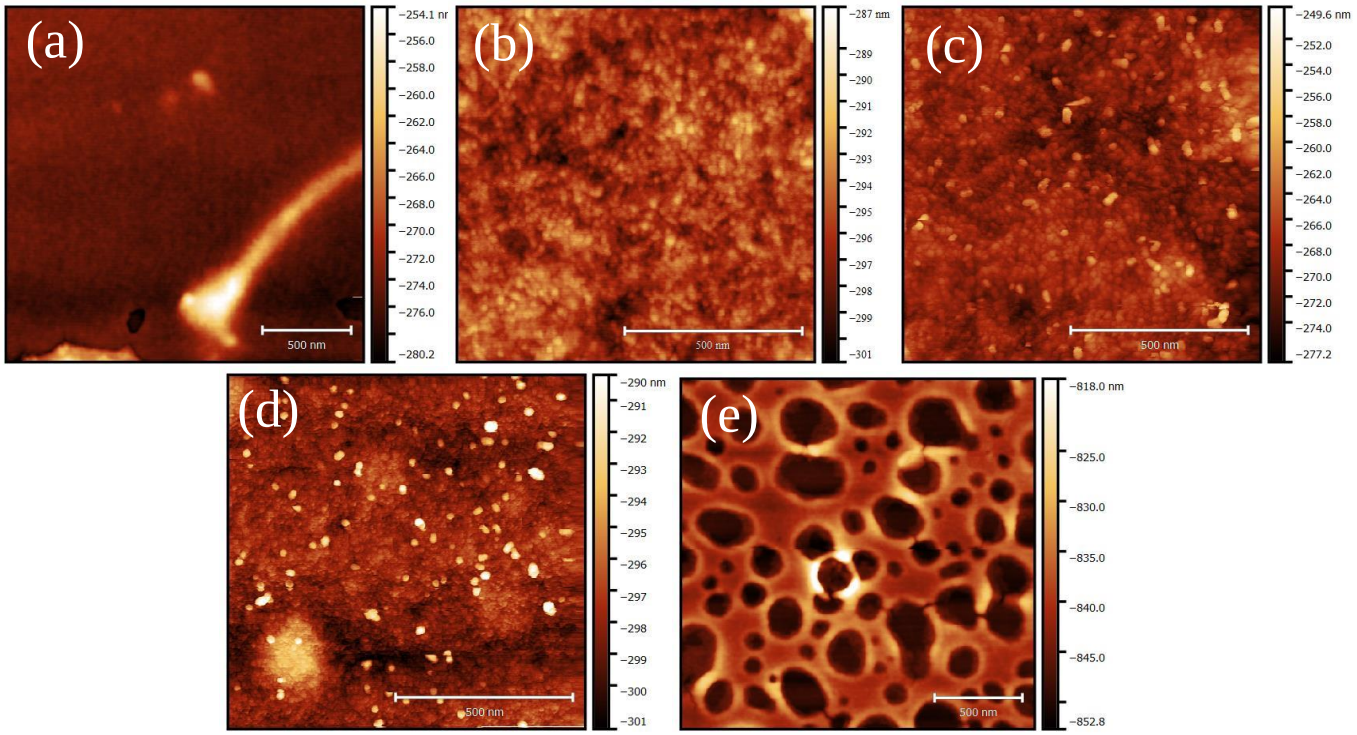

Figure 24: AFM height images of (a) Pristine PCDTBT, (b) PCDTBT: $FeCl_3$ (1:0.5), (c) PCDTBT: $FeCl_3$ (1:0.66), (d) PCDTBT: $FeCl_3$ (1:1) and (e) PCDTBT: $FeCl_3$ (1:2) thin films (scale bar = 500 nm).

4. PTB7

Poly [[4,8-bis[(2-ethylhexyl)oxy]benzo[1,2-b:4,5-b']dithiophene-2,6-diyl][3-fluoro-2-[(2-ethylhexyl)carbonyl]thieno[3,4-b]thiophenediyl]] (PTB7) is a polymer from the low bandgap family, composed alternately of 3-fluorothieno- [3,4-b]thiophene-2-carboxylate (TT) and benzo[1,2-b:4,5-b′]- dithiophene (BDT) moieties. PTB7 has shown very promising properties [103–106] especially in organic field effect transistors field [107] and in photovoltaic application as donor material leading to power conversion efficiency (PCE) as high as 9.2% [108,109]. This high efficiency could be attributed to the large transition-state dipole moment μ_{tr} = 8.23 D, an excited-state dipole moment μ_e = 7.13 D and a ground-state dipole moment μ_g = 3.76 D of the thienothiophene (TT) monomer [110]. As a comparison, the dipole moment of the P3HT polymer is in the range 1.0–1.6 D [111]. This large dipole moment value of PTB7 allows a better molecular orientation under an external application of an electric field.

Rastegaralam *et al.* used PTB7 as active layer for thermoelectric applications by adapting a strategy developed to increase the PCE in solar cells [112]. They studied the influence of a structuring agent, 1,8-diiodooctane (DIO), in various high boiling point chlorinated solvent in order to increase the polymer's crystallinity expecting to increase the charge carrier mobility. The electrical conductivity and Seebeck coefficient values are as follows: 0.5 S/m & 670 µV/K, 0.8 S/m & 702 µV/K, and 1.2 S/m & 726 µV/K for samples made of chlorobenzene (CB), 1,2-dichlorobenzene (DCB) and 1,2,4-trichlorobenzene (TCB) without DIO, respectively. Then, by adding DIO, they only managed to increase electrical conductivity and Seebeck coefficient for TCB from 1.2 S/m to 1.78 S/m and 726 µV/K to 758 µV/K. Thus, they managed to increase the electrical conductivity and the Seebeck coefficient for higher boiling point solvent TCB, leading a power factor of 1 µW/m.K².

Despite this low power factor value compared to PEDOT, P3HT or PCDTBT values previously cited, the most interesting part is the high Seebeck coefficient obtained (around 700 µV/K) with proper electrical conductivity value (0.018 S/cm) comparable to Seebeck coefficient of inorganic material like silicon (440 µV/K) [113].

In this work, the same procedure than P3HT: F4TCNQ and PCDTBT:$FeCl_3$ thin films was applied. The solution mixed doping procedure was applied to this polymer to try to enhance thermoelectric properties. The influence of structural agent on thermoelectric properties was studied in order to obtain PTB7 thin film with the best power factor. Finally, the increase of

thermoelectric properties was followed by UV-visible analysis and correlated to the morphology thanks to AFM analysis.

In this part, based on Rastegaralam *et al.* work, only the PTB7 in trichlorobenzene (TCB) was used with DIO as structural agent [112]. The effect of DIO on PTB7 thin film, prepared via solution-mixed method, was studied in order to obtain the best thermoelectric properties. Polymers films were made in accordance with the procedure described in **Appendix II**. DIO had a positive impact on thermoelectric properties, electrical conductivity and Seebeck coefficient, thus a power factor of 0.9 µW/m.K² was obtained (Figure 25).

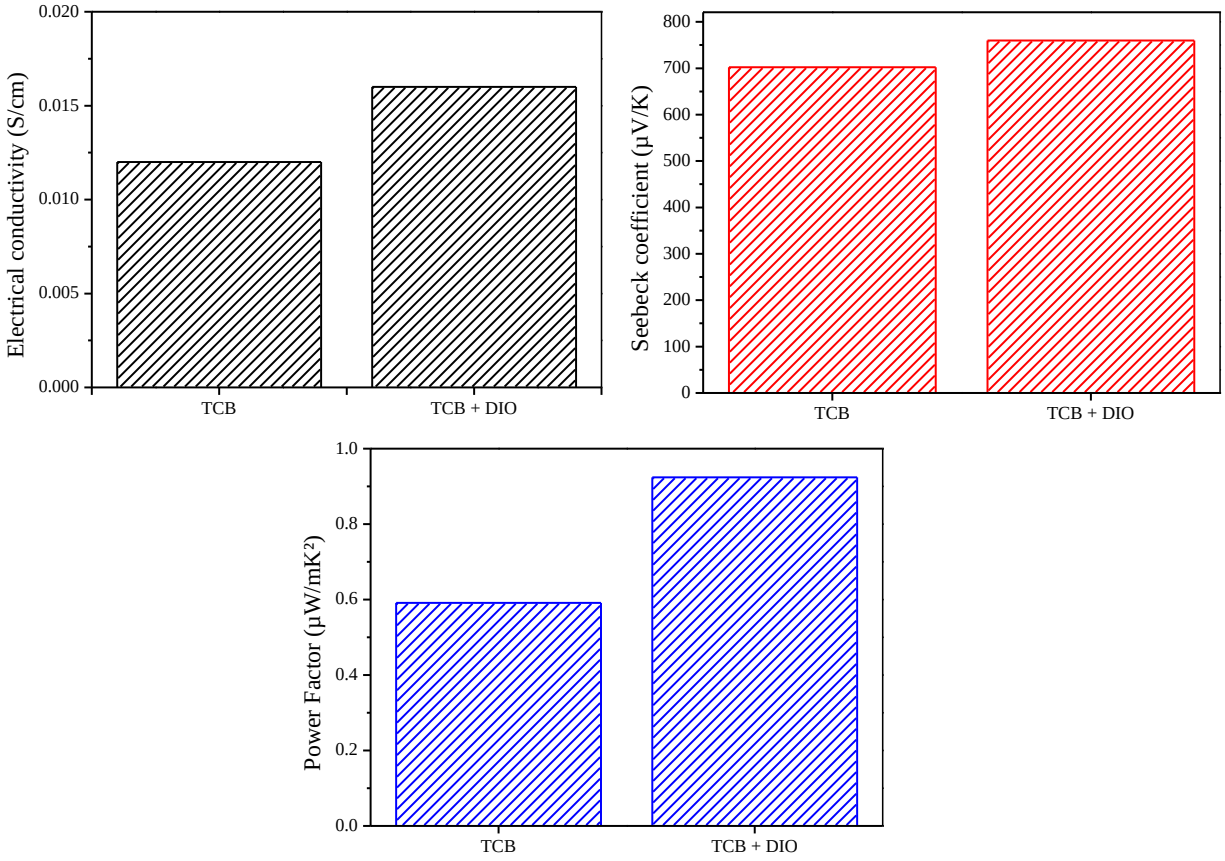

Figure 25: Thermoelectric properties (Seebeck coefficient, electrical conductivity and power factor) of the PTB7 and PTB7 + DIO thin films.

As shown by UV-visible analysis, no difference is noticeable between the pristine PTB7 and the PTB7 with DIO (Figure 26). The difference in absorbance is due to a difference of thickness, confirmed by a profilometer. This is well-known that DIO acts as a structural agent influencing the nanostructured morphology [114]. So, to find an origin of both increase of electrical conductivity and Seebeck coefficient, morphology study, by AFM, was conducted (Figure 27).

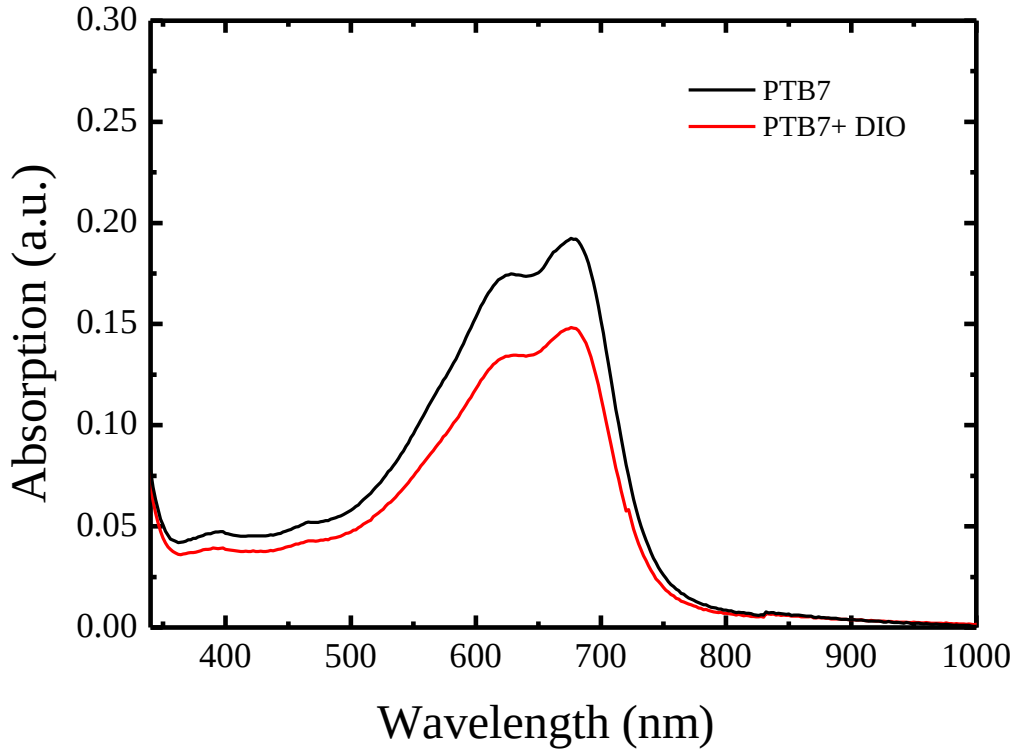

Figure 26: UV-visible spectra of PTB7 and PTB7 + DIO thin film.

The neat PTB7 is homogeneous as expected for homopolymer films. When DIO is added to the formulation, the film morphology changes and the root-mean-square (RMS) surface roughness decreased from 4.9 to 0.51 nm. DIO with its high boiling point of 332.5°C should allow PTB7 fibers to "move" more freely during the film formation, DIO inhibiting the evaporation of the solvent. These results are consistent with the UV-visible (decrease of thickness) and the increase of thermoelectric properties.

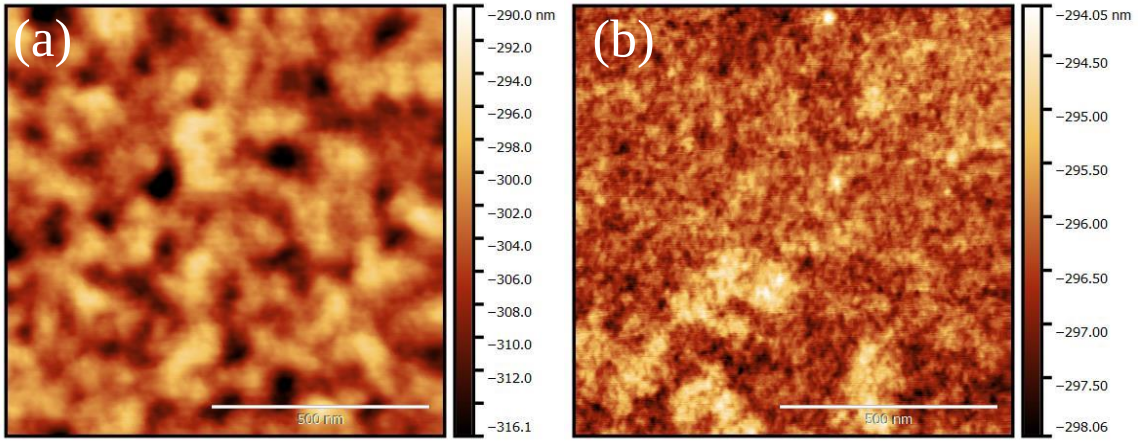

Figure 27: AFM height images of (a) Pristine PTB7 and (b) PTB7 with DIO (scale bar = 500 nm).

B n-type materials engineering

1. PCBM

Fullerenes family, such as PCBM and PC71BM, are the most commonly used acceptors in optoelectronic field. Indeed, fullerenes were widely studied due to their excellent electron transport properties, high electron affinity and their ability to form favorable nanoscale network with donor molecules. However, fullerene derivatives also exhibit several non-trivial drawbacks that hinder their use in practical applications. First, the relatively low lowest unoccupied molecular orbital (LUMO) energy level (~4.1 to -4.3 eV). set a limitation [115]. Second, fullerene derivatives have strong tendency to crystallize and aggregate causing a performance degradation in long term [116,117]. Finally, fullerenes are limited by their intrinsic low electron mobility and electrical conductivity [118,119].

For thermoelectric application, fullerene derivatives (PCBM) stay among the best n-type organic semi-conductors with high electron mobility and good thermal stability [120]. Bao's group developed an efficient and stable n-type dopant, N-DPBI, and thanks to a doping solution-processed achieved 1.9 x10^{-3} S/cm for PCBM films [121]. Gao *et al.* developed an other methods based on co-doping with N-DPBI and acridine orange base (3,6-bis(dimethylaminoacridine) (AOB) resulting in PCBM films with high electrical conductivity and Seebeck coefficient [122]. The doping mechanism of AOB was studied by Li *et al.* [123] and proposed that during the process (co-evaporation), AOB and fullerene formed a dyad of a positively charged acridine dye and a C_{60} anion radical connected by a C-N chemical bond.

In this work, $PC_{71}BM$ was formulated with N-DPBI and AOB. The protocol was adapted from a co-evaporation process to obtain a more suitable process for liquid deposition. The thermoelectric properties (electrical conductivity and Seebeck coefficient) for different dopant concentrations in PCBM films were evaluated and followed by UV-visible analysis

The influence of AOB, a heterogeneous guest, on PCBM:N-DPBI thin films, prepared via an inverse-sequential doping, was studied in order to investigate its effect on thermoelectric properties. All thermoelectric properties are presented in Table 8. Organic films were made in accordance with the procedure described in **Appendix II**. Based on Kemerink and coll. work, N-DPBI was used as dopant with a concentration of 5 wt% [124]. AOB concentration had a

significant impact on thermoelectric properties. Despite, Seebeck coefficient decreases with the increase of AOB amount, electrical conductivity followed a bell-shape trend with a maximum at 0.7 S/cm which is a high value for n-type material (*c.f.* Chapter 1), leading to a power factor of 11.88 µW/m.K² (Figure 28).

AOB conc. (mol%)	S (µV/K)	σ (S/cm)	PF (µW/m.K²)
0	-775 ±12	$8.5x10^{-8}$	$5x10^{-6}$
5 mol%	-554 ±11	0.05 ±0.01	1.53
10 mol%	-412 ±10	0.7 ±0.1	11.88
20 mol%	-332 ±11	0.22 ±0.1	2.44
30 mol%	-239 ±15	$1x10^{-3}$	$5.7x10^{-4}$

Table 8 : Thermoelectric properties of the PCBM:N-DPBI thin films with different AOB concentration

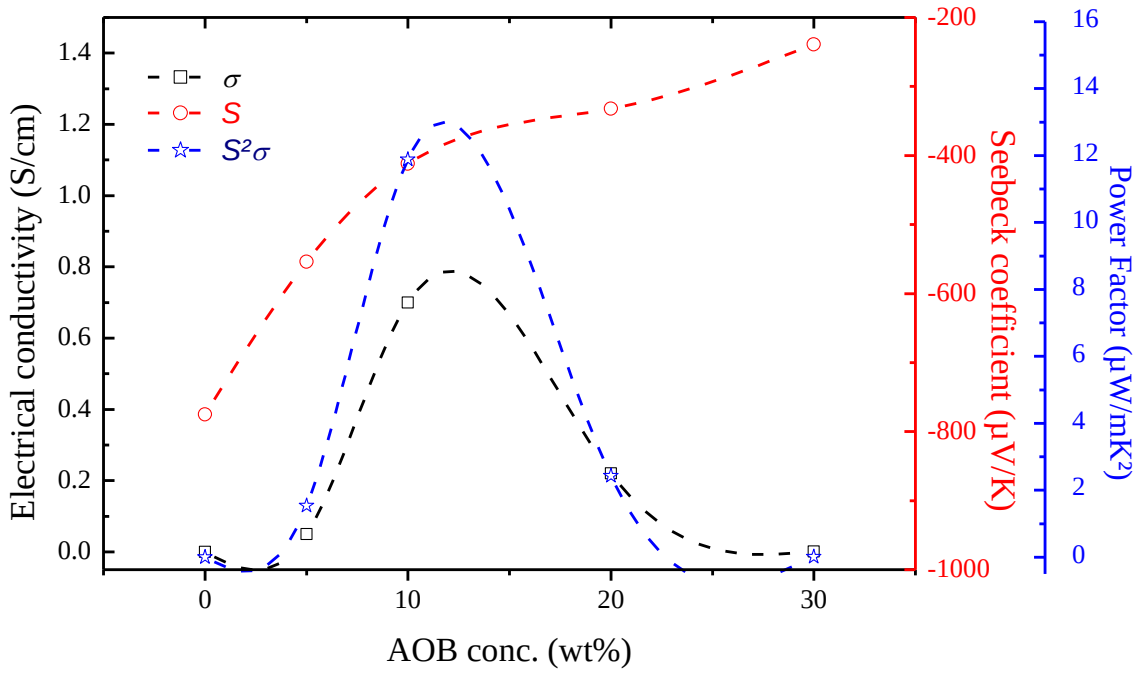

Figure 28: Seebeck coefficient, electrical conductivity and power factor of PCBM:N-DPBI thin films with different AOB concentration.

The effect of AOB was followed by UV-visible-NIR analysis in addition to thermoelectric measurements (Figure 29). AOB is a dye with a maximum of absorption around 500 nm [125]. When AOB is added to the PCBM:N-DPBI a shoulder (gain in intensity) appears around 500nm and could be attributed to the presence of the dye. No more information could be extracted from this analysis. So the thin film morphology was studied by atomic force microscopy (AFM). All images of films are presented Figure 30.

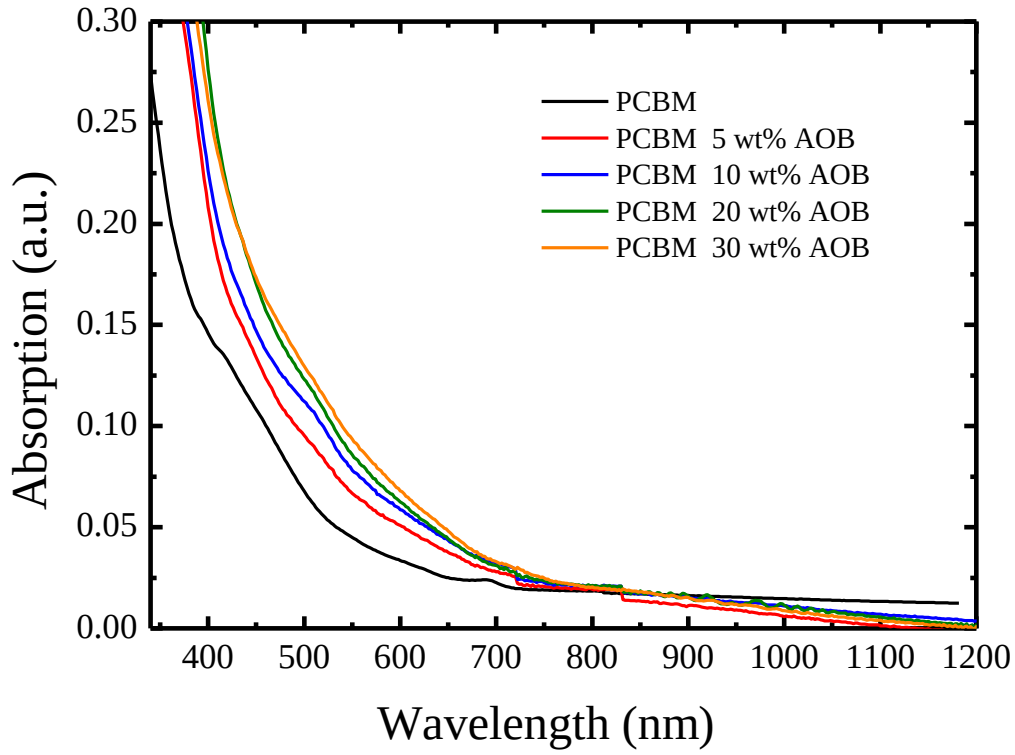

Figure 29: UV-visible spectra of PCBM:N-DPBI thin films with different AOB concentration

The "pristine" PCBM:N-DPBI film shows a smooth film with few aggregates due to the dopant. When 5 %wt of AOB are introduced, the film remains unchanged, smooth without too much aggregates. At 10 %wt of AOB, the thin morphology changes drastically to a blend with the starting material and the dye resulting in higher roughness. Above this previous AOB concentration, the roughness of the film is very high and a phase segregation is observable with large aggregates of AOB. By correlating AFM data and thermoelectric properties, the addition of a small amount of AOB is beneficed. This result was surprising, considering that adding a heterogeneous specie to a common casting solution, the morphology should be compromise and so the electrical conductivity should decrease. One hypothesis could be an improve attributed to the process, the inverse-sequentially doping of samples, leading a better

morphology allowing a faster charge carrier mobility. Lu *et al.* worked the benefit of the process on film morphology and so on electrical properties [126].

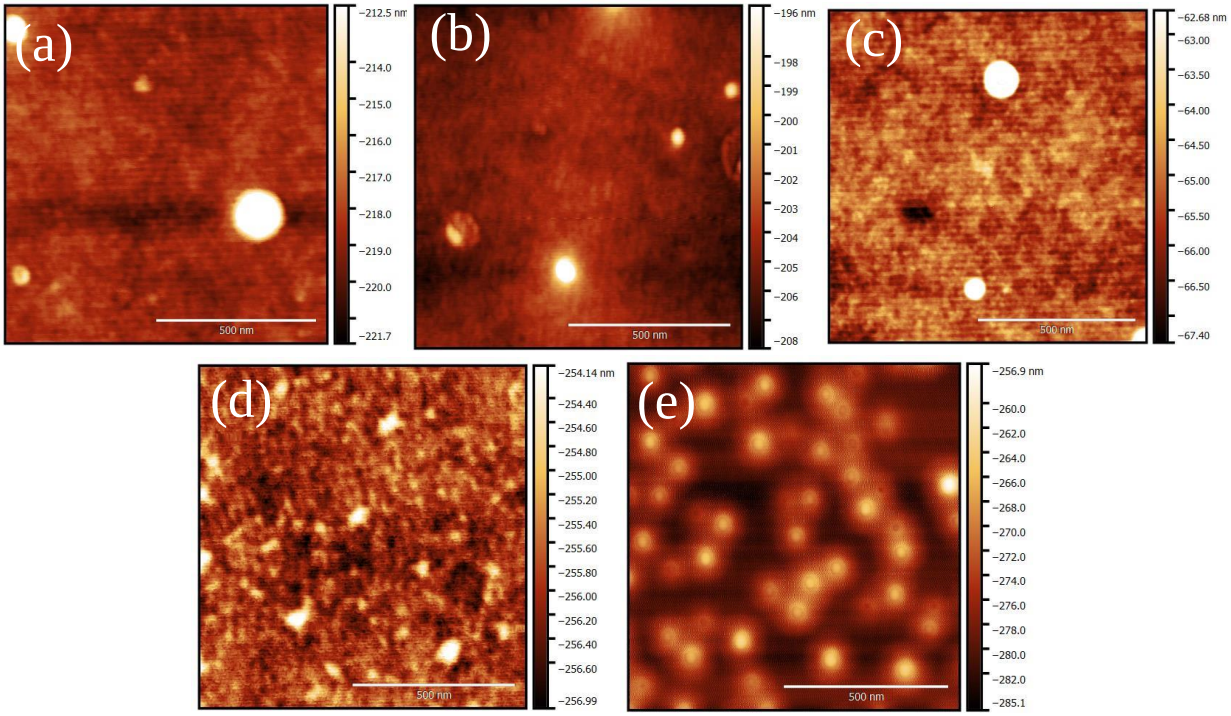

Figure 30: AFM height images of (a) Pristine PCBM:N-DPBI, (b) PCBM:N-DPBI with 5 wt% AOB, (c) PCBM:N-DPBI with 10 wt% AOB, (d) PCBM:N-DPBI with 20 wt% AOB and (e) PCBM:N-DPBI with 30 wt% AOB thin films (scale bar = 500 nm).

2. PNDIBS

NDI-biselenophene copolymer (PNDIBS) [127] is promising n-type material for thermo-generators for room temperature applications. He is Poly{[N,N'-bis(2-octyldodecyl)naphthalene-1,4,5,8-bis(dicarboximide)-2,6-diyl]-alt-5,5'-(2,2'-bithiophene)} (PNDI(2OD)2T) analogue, which is known as a high-mobility n-type semiconductor (μ_e = 0.45-0.85 cm²/V/s) [128].

PNDI(2OD)2T is also well-known for thermoelectric applications. Chabinyc's team developed two formulations, with dopants N-DMBI and N-DPBI as dopant, showing good thermoelectric performances and processability [129]. Power factor of $6x10^{-7}$ and $2x10^{-7}$ W/m-K² were obtained for N-DMBI and N-DPBI formulation respectively. Despite a high Seebeck coefficient around -800 µV/K, the main drawback was the low electrical conductivity of these doped materials, 10^{-3} S/cm. Thus, PNDI(2OD)2T is still a promising candidate for organic thermoelectrics.

The main difference between PNDI(2OD2T) and PNDIBS is their heteroatom, sulfur for the first one and selenium for others. The replacement of the sulfur by the more polarizable selenium atoms depicts a novel approach for the fine-tuning of the electrochemical and optical properties of the corresponding polymer [130]. The differences in the chemistry of selenium versus sulfur includes [131]:

- Increase in metallic behaviour;
- Involvement of filled 3d orbitals;
- Decrease in electronegativity.

Furthermore, the higher electron donating character of selenophene implied that different composition of heteroatoms in similar systems could differ greatly in their electrical properties and chemical stability [132–134].

In this work, two PNDIBS with different molar mass (30 000 and 60 000 g/mol), provided by Prof.. Jenekhe's group, were formulated with well-known n-type dopant, N-DMBI [135], and their thermoelectric properties (electrical conductivity and Seebeck coefficient) were evaluated. Finally, the doping process efficiency was followed by UV-visible analysis and correlated to the morphology thanks to AFM analysis.

The effect of n-doping on thermoelectric properties of PNDIBS was explored, results are worked in Table 9. Polymer films were made in accordance with the procedure described in **Appendix II**. Based on results Table 9 and Figure 31, molecular mass does not seem to have a huge influence on thermoelectric properties. PNDBIS pristine thin films features an electrical conductivity of 1.21 x 10^{-6} and 6.21 x 10^{-5} S/cm for 30 000 and 60 000 g/mol respectively. These values are more than one order of magnitude higher than P(NDIOD-T2) doped with N-DMBI [107]. N-DMBI concentration had a significant impact on thermoelectric properties. The highest electrical conductivity was reached for 20 mol% of dopant for both molecular mass, 8 x 10^{-4} and 9 x 10^{-4} S/cm. After further doping, electrical conductivity dropped by nearly one order of magnitude. For Seebeck coefficient, a decrease (absolute value) from -778 and -831 to -125 and -156 µV/K happens when dopant concentration is increased. The power factor, $S^2\sigma$, followed a bell-shape trend with a maximum at 2.2 x 10^{-3} and 3.2 x 10^{-3} µW/m.K² for the low and the high molecular mass respectively.

Molecular mass (g/mol)	N-DMBI conc. (mol%)	S (µV/K)	σ (S/cm)	PF (µW/m.K²)
30 000	0	-778 ±25	$2x10^{-8}$	$1.21x10^{-6}$
	5 mol%	-378 ±18	$5x10^{-6}$	$7.14x10^{-5}$
	10 mol%	-223 ±11	$6x10^{-5}$	$2.98x10^{-4}$
	20 mol%	-167 ±12	$8x10^{-4}$	$2.2x10^{-3}$
	30 mol%	-125 ±10	$1x10^{-4}$	$1.56x10^{-4}$
60 000	0	-831 ±17	$9x10^{-7}$	$6.21x10^{-5}$
	5 mol%	-456 ±11	$9x10^{-6}$	$1.87x10^{-4}$
	10 mol%	-264 ±20	$4x10^{-5}$	$2.78x10^{-4}$
	20 mol%	-189 ±8	$9x10^{-4}$	$3.2x10^{-3}$
	30 mol%	-156 ±12	$1x10^{-5}$	$2.43x10^{-5}$

Table 9 : Thermoelectric properties of PNDIBS:N-DMBI thin films with different N-DMBI concentration

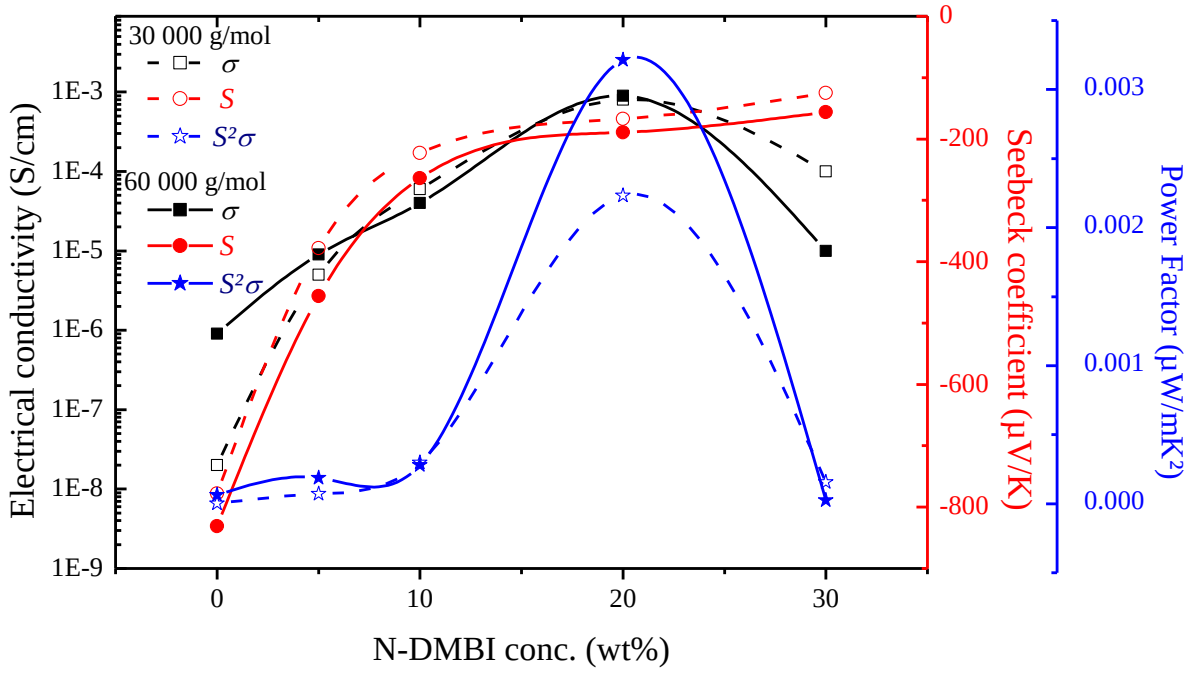

Figure 31: Seebeck coefficient, electrical conductivity and power factor of PNDIBS:N-DMBI thin films (30 000 g/mol empty and 60 000 g/mol full colour symbols) with different N-DMBI concentrations.

The doping process was followed by UV-visible-NIR analysis in addition to thermoelectric measurements (Figure 32). The thin films spectrum of the pristine polymer consists of a peak around 400 nm and a broad spectral feature between 500 and 950 nm, which could be attributed to the π-π* transition and a strong intramolecular charge transfer complex as a consequence of strong donor-acceptor interactions [137]. N-DMBI incorporation into polymer thin films has a strong influence on UV-visible-NIR spectra for both molecular mass. Actually, increasing the concentration of N-DMBI in both thin films affect peak at 400 and 750 nm.

In case of low molecular mass, an increase of intensity for the peak at 400 nm happens with the increase of dopant concentration, furthermore an hypsochromic shift occurs corresponding to the PNDIBS π-π* related to N-DMBI's action. On the other hand, for the peak at 750 nm, a decrease of the intensity is observed, an hypsochromic shift occurs too. These trends are in agreement with the work of Giovannitti *et al* [138]. Then the hypsochromic shift could be attributed to a planarization of the polymer backbone based on Kiefer *et al*. study [139].

However, the spectrum of high molecular mass is slightly different from the previously one. The intensity of the peak at 400 nm increased at the same point with the dopant concentration

of 5, 10 and 20 mol% but the decrease for 30 mol% to achieve almost the pristine intensity. Then for the peak at 750 nm, the same phenomena as previously are observed, an intensity decreasing and an hypsochromic shift.

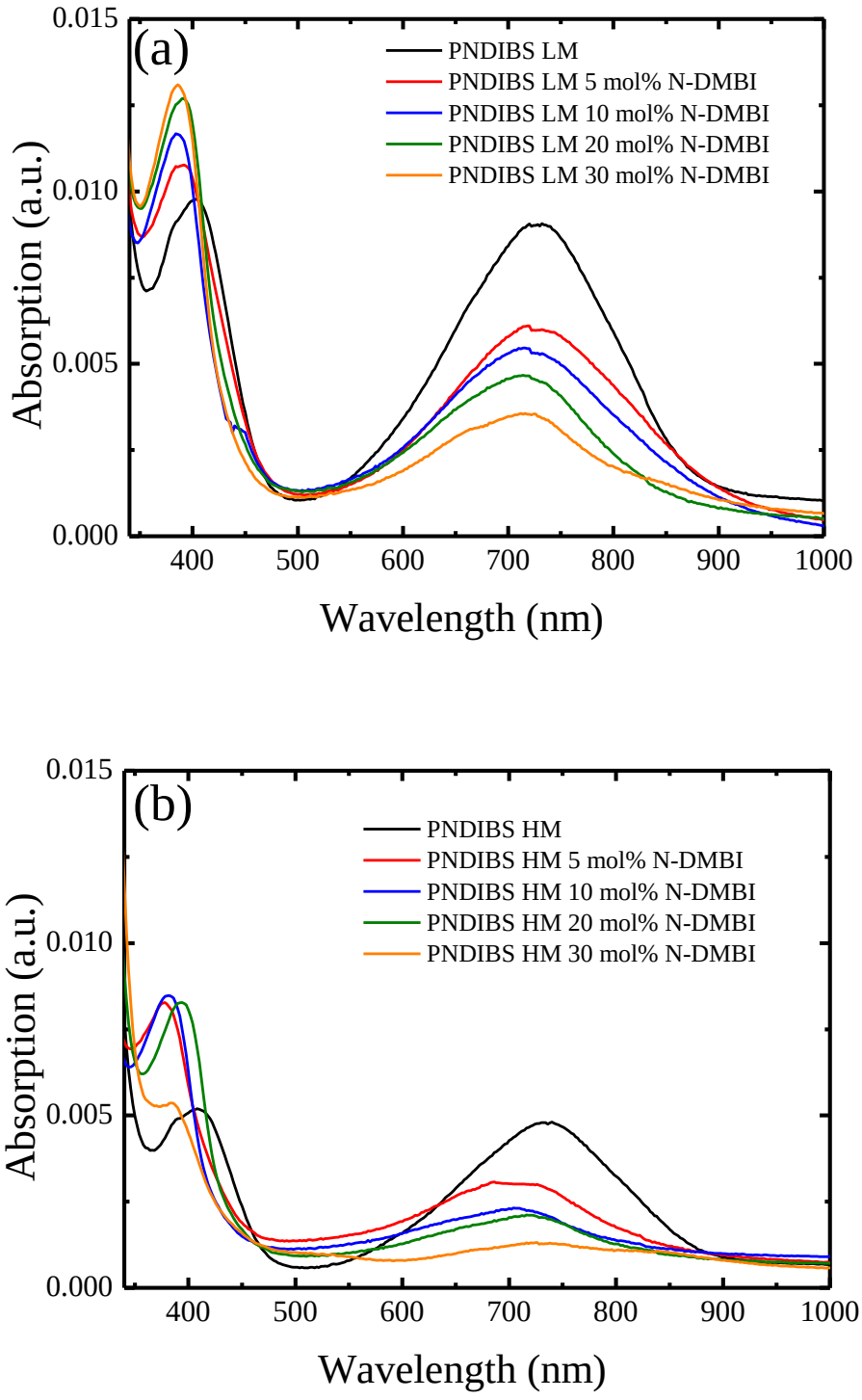

Figure 32: UV-visible spectra of (a) low molecular mass PNDIBS:N-DMBI and (b) high molecular mass PNDIBS:N-DMBI thin films with different N-DMBI concentration

Thin film morphology was studied by atomic force microscopy (AFM). All images of films with low and high molecular mass doped with N-DMBI are presented Figure 33 and 34. The dopant concentration has an influence on thin films morphology for both PNDIBS. On pristine films, crystallites are clearly visible, nucleation points also. These AFM images indicate formation of dopant aggregates on the surface of the blend films that increase the quantity and size with an increase amount of N-DMBI. The morphology and the roughness change slightly from pristine to 20 mol% N-DMBI but increase sharply for 30 mol%.

These results confirm the behaviour of thermoelectric properties (Table 9). At low dopant concentration (under 10 mol %) N-DMBI is still "soluble" in polymer matrix and affects only the charge carrier mobility. When the concentration increases, aggregates of inactive N-DMBI are formed on the top surface, affecting slightly the morphology without disturbing the thermoelectric properties. Finally, at high dopant concentration, above 20 mol%, the amount an aggregates have an important effect on the morphology, decreasing the mobility with the loss of crystallinity and so the thermoelectric properties are decreased. This hypothesis, based on thermoelectric data, UV-visible-NIR and AFM were confirmed by Schiltz *et al.* in their study [129].

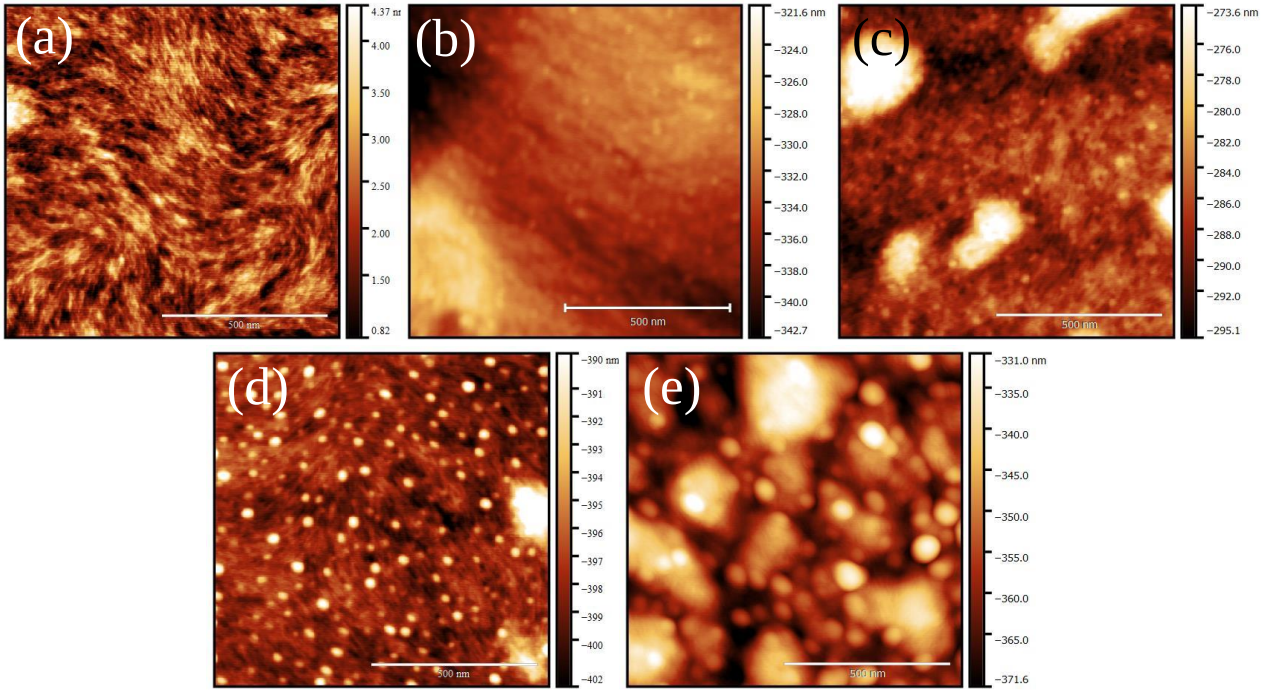

Figure 33: AFM height images of low molecular mass (a) Pristine PNDIBS:N-DMBI, (b) PNDIBS:N-DMBI with 5 wt% N-DMBI, (c) PNDIBS:N-DMBI with 10 wt% N-DMBI, (d) PNDIBS:N-DMBI with 20 wt% N-DMBI and (e) PNDIBS:N-DMBI with 30 wt% N-DMBI thin films (scale bar = 500 µm).

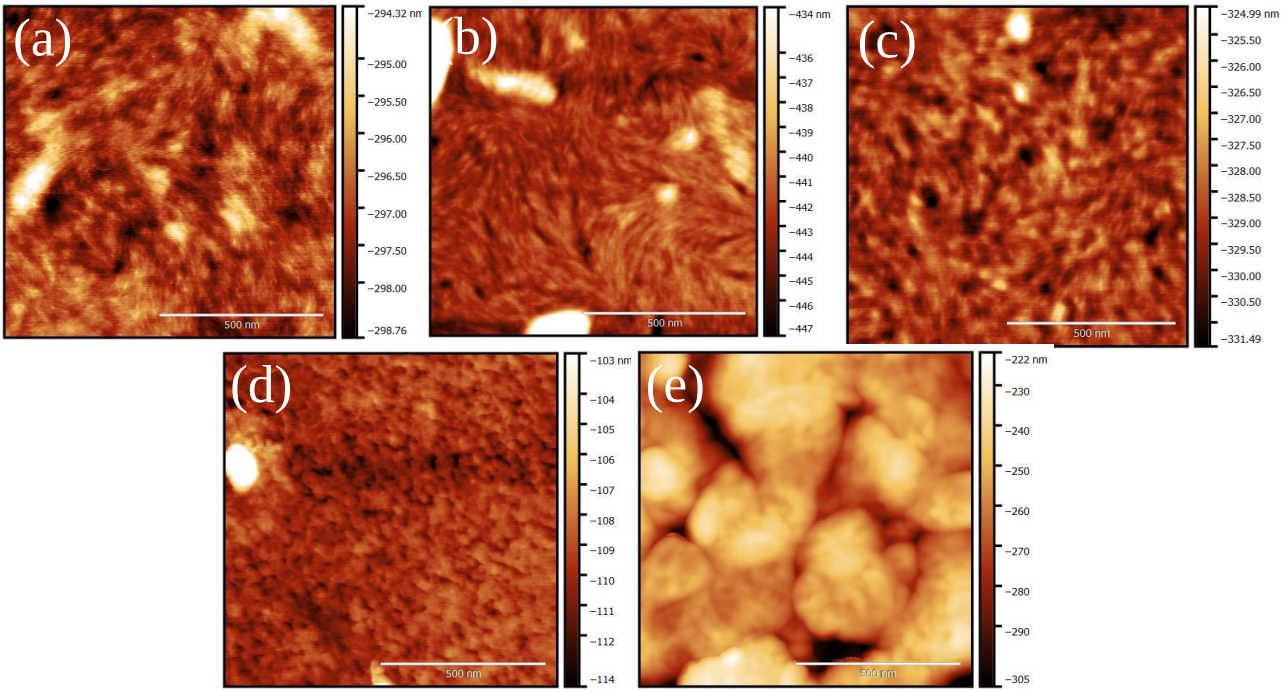

Figure 34 : AFM height images of high molecular mass (a) Pristine PNDIBS:N-DMBI, (b) PNDIBS:N-DMBI with 5 wt% N-DMBI, (c) PNDIBS:N-DMBI with 10 wt% N-DMBI, (d) PNDIBS:N-DMBI with 20 wt% N-DMBI and (e) PNDIBS:N-DMBI with 30 wt% N-DMBI thin films (scale bar = 500 µm).

C Conclusion

Through various processing modifications, the structural, electronic and thermoelectric properties of various polymers and organic materials were tuned. Synthesized p-type polymers showed better thermoelectric performances than supplied n-type materials. For instance in case of PEDOT:Tos, a high power factor of 240 µW/mK² was achieved.

A novel polymer PNDIBS, analogue to PNDI(2OD)2T with selenium atoms, was tested as a promising n-type thermoelectric material. Thermoelectric performances obtained for this material were comparable with the PNDI(2OD)2T, known as a reference n-type material. Unfortunately, the typical air sensibility of n-type material was noted.

Furthermore, this study shown the importance of fine doping of organic materials. In most cases, the power factor followed a bell-shape curve with a maximum for a precise dopant concentration.

Finally, these organic materials will be used as "brick" for the building of a thermoelectric generator. Their performances will be enhanced thanks to inorganic materials and a novel approach developed in our laboratory. Best thermoelectric performances of each material are summarized in the Table 10.

Material	Dopant or structural agent	Concentration (wt% - mol%)	S (µV/K)	σ (S/cm)	PF (µW/m.K²)	Air stability
PEDOT:Tos	DMSO Pyridine	3 3	44	1240	240	Stable
P3HT m.	F_4TCNQ	20	76	4.3	2.48	Stable
P3HT seq.	F_4TCNQ	10	127	0.87	1.40	Stable
PCDTBT	$FeCl_3$	50	37	60	8.21	Stable
PTB7	DIO	3	760	0.017	0.9	Stable
PCBM	AOB N-DPBI	10 5	-412	0.7	11.88	Instable
PNDIBS LMn	N-DMBI	20	-167	$8x10^{-4}$	$2.2x10^{-3}$	Instable
PNDIBS HMn	N-DMBI	20	-189	$9x10^{-4}$	$3.2x10^{-3}$	Instable

Table 10 : Thermoelectric performances of best p- & n-type materials studied

References

[1] Myer Kutz, *Handbook of Environmental Degradation of Materials*, Elsevier, "3rd Edition", **2018**, 684 (*ISBN: 9780323524728*).

[2] (a) J.-H. Bahk, H. Fang, K. Yazawa, A. Shakouri, *J. Mater. Chem. C* **2015**, *3*, 10362. (b) L. K. Allison, T. L. Andrew, *Adv. Mater. Technol.* **2019**, *4*, 1800615

[3] O. Bubnova, *"Thermoelectric properties of conducting polymers"*, PhD manuscript, Department of Science and Technology, Linköping University: Norrköping, Sweden, **2013**, 63 (*ISBN: 978-91-7519-741-8*).

[4] I. Petsagkourakis, *"High performance polymer and polymer/inorganic thermoelectric materials"*, PhD manuscript, LCPO-LOMA, Université de Bordeaux, Bordeaux France, **2016** (*NNT: 2016BOR0351*).

[5] B. Lüssem, C.-M. Keum, D. Kasemann, B. Naab, Z. Bao, K. Leo, *Chem. Rev.* **2016**, *116*, 13714.

[6] L. Lu, T. Zheng, Q. Wu, A. M. Schneider, D. Zhao, L. Yu, *Chem. Rev.* **2015**, *115*, 12666.

[7] S. LeBlanc, *Sustain. Mater. Technol.* **2014**, *1–2*, 26.

[8] J. C. Hummelen, B. W. Knight, F. LePeq, F. Wudl, J. Yao, C. L. Wilkins, *J. Org. Chem.* **1995**, *60*, 532.

[9] Y. Lan, A. J. Minnich, G. Chen, Z. Ren, *Adv. Funct. Mater.*, **2010**, *20* (3), 357-376.

[10] O. Bubnova, X. Crispin, *Energy Environ. Sci.* **2012**, *5*, 9345.

[11] G. J. Snyder, E. S. Toberer, *Nature Materials*, **2008**, *7*, 105-114.

[12] O. Bubnova, Z. U. Khan, H. Wang, S. Braun, D. R. Evans, M. Fabretto, P. Hojati-Talemi, D. Dagnelund, J.-B. Arlin, Y. H. Geerts, S. Desbief, D. W. Breiby, J. W. Andreasen, R. Lazzaroni, W. M. Chen, I. Zozoulenko, M. Fahlman, P. J. Murphy, M. Berggren, X. Crispin, *Nat. Mater.* **2014**, *13*, 190.

[13] O. Bubnova, Z. U. Khan, A. Malti, S. Braun, M. Fahlman, M. Berggren, X. Crispin, *Nat. Mater.* **2011**, *10*, 429.

[14] G.-H. Kim, L. Shao, K. Zhang, K. P. Pipe, *Nat. Mater.* **2013**, *12*, 719.

[15] I. Petsagkourakis, E. Pavlopoulou, G. Portale, B. A. Kuropatwa, S. Dilhaire, G. Fleury, G. Hadziioannou, *Scientific Works*, **2016**, *6*, 30501.

[16] S. Ihnatsenka, X. Crispin, I. V. Zozoulenko, *Phys. Rev. B* **2015**, *92*, 035201.

[17] N. Kim, B. H. Lee, D. Choi, G. Kim, H. Kim, J.-R. Kim, J. Lee, Y. H. Kahng, K. Lee, *Phys. Rev. Lett.* **2012**, *109*, 106405.

[18] B. B.-Y. Hsu, C.-M. Cheng, C. Luo, S. N. Patel, C. Zhong, H. Sun, J. Sherman, B. H. Lee, L. Ying, M. Wang, G. Bazan, M. Chabinyc, J.-L. Brédas, A. Heeger, *Adv. Mater.* **2015**, *27*, 7759.

[19] J. Sun, M.-L. Yeh, B. J. Jung, B. Zhang, J. Feser, A. Majumdar, H. E. Katz, *Macromolecules* **2010**, *43*, 2897.

[20] J. T. Rogers, K. Schmidt, M. F. Toney, G. C. Bazan, E. J. Kramer, *J. Am. Chem. Soc.*, **2012**, *134* (6), 2884-2887.

[21] C. M. Palumbiny, F. Liu, T. P. Russell, A. Hexemer, C. Wang, P. Müller-Buschbaum, *Advanced Materials*, **2015**, *27* (22), 3391-3397.

[22] C. H. Woo, C. Piliego, T. W. Holcombe, M. F. Toney, J. M. J. Fréchet, *Macromolecules*, **2012**, *45* (7), 3057-3062.

[23] B. W. Boudouris, V. Ho, L. H. Jimison, M. F. Toney, A. Salleo, R. A. Segalman, *Macromolecules* **2011**, *44*, 6653.

[24] B. Endrődi, J. Mellár, Z. Gingl, C. Visy, C. Janáky, *J. Phys. Chem. C* **2015**, *119*, 8472.

[25] C. Goh, R. J. Kline, M. D. McGehee, E. N. Kadnikova, J. M. J. Fréchet, *Appl. Phys. Lett.* **2005**, *86*, 122110.
[26] A. Zen *et al.*, *Macromolecules*, **2006**, *39* (6), 2162-2171.
[27] B. Winther-Jensen, D. W. Breiby, K. West, *Synth. Met.* **2005**, *152*, 1.
[28] J.-H. Huang, C.-W. Chu, *Electrochimica Acta* **2011**, *56*, 7228.
[29] C. Badre, L. MArquant, A. M. Alsayed, L. A. Hough, *Advanced Functional Materials*, **2012**, *13* (22), 2723-2727.
[30] I. Petsagkourakis, E. Pavlopoulou, E. Cloutet, Y. F. Chen, X. Liu, M. Fahlman, M. Berggren, X. Crispin, S. Dilhaire, G. Fleury, G. Hadziioannou, *Org. Electron.* **2018**, *52*, 335.
[31] L. Groenendaal, F. Jonas, D. Freitag, H. Pielartzik, J. R. Reynolds, *Adv. Mater.* **2000**, *12*, 481.
[32] XPS-Fitting, **2009**, *X-ray Photoelectron Spectroscopy (XPS) Reference Pages*, view on http://www.xpsfitting.com/2009/04/relative-sensitivity-factors-rsf.html (July, **2019**).
[33] M. Fabretto, K. Zuber, C. Hall, P. Murphy, H. J. Griesser, *J. Mater. Chem.* **2009**, *19*, 7871.
[34] Q. Wei *et al.*, *Adv. Mater.*, **2015**, *25*, 2831-2836.
[35] N. Massonnet, A. Carella, A. de Geyer, J. Faure-Vincent, J.-P. Simonato, *Chem. Sci.* **2014**, *6*, 412.
[36] K. Zhang, S. Wang, J. Qiu, J. L. Blackburn, X. Zhang, A. J. Ferguson, E. M. Miller, B. L. Weeks, *Nano Energy* **2016**, *19*, 128.
[37] D. Deribew *et al.*, *Macromolecules*, **2013**, *46* (8), 3015-3024.
[38] E. J. W. Crossland *et al.*, *Adv. MAter.*, **2012**, *24*, 839-844.
[39] X. Shen, V. Duzhko, T. P. Russell, *Adv. Energy Mater.* **2013**, *Sept 2012*.
[40] K. E. Aasmundtveit, E. J. Samuelsen, L. A. A. Pettersson, O. Inganäs, T. Johansson, R. Feidenhans'l, *Synth. Met.* **1999**, *101*, 561.
[41] H. Sirringhaus, P. J. Brown, R. H. Friend, M. M. Nielsen, K. Bechgaard, B. M. W. Langeveld-Voss, A. J. H. Spiering, R. a. J. Janssen, E. W. Meijer, P. Herwig, D. M. de Leeuw, *Nature* **1999**, *401*, 685.
[42] A. B. Kaiser, V. Skákalová, *Chem. Soc. Rev.* **2011**, *40*, 3786.
[43] W. Lövenich, *Polym. Sci. Ser. C* **2014**, *56*.
[44] A. Elschner, S. Kirchmeyer, W. Lovenich, U. Merker, K. Reuter, *PEDOT: Principles and Applications of an Intrinsically Conductive Polymer*, CRC Press, **2010**, 377 (*ISBN: 9781420069112*).
[45] Y-H. Ha *et al.*, *Adv. Funct. Mater.*, **2004**, *14*, No. 6, *June*.
[46] J.T. Rogers, K. Schmidt, M.F. Toney, G.C. Bazan, E.J. Kramer, *J. Am. Chem. Soc.*, **2012**, *134* (6), 2884-7.
[47] G. Kollet *et al.*, *Science*, **2007**, *317* (5836), 351-355.
[48] X. Crispin *et al*. *J. Am. Chem. Soc.*, **2004**, *126* (38), 11889-11899.
[49] J. Clark, C. Silva, R. H. Friend, F. C. Spano, *Phys. Rev. Lett.* **2007**, *98*, 206406.
[50] R. D. McCullough, *Adv. Mater.* **1998**, *10*, 93.
[51] Y. Xie, S. Gao, M. Eslamian, *Coatings* **2015**, *5*, 488.
[52] F. C. Krebs, S. A. Gevorgyan, J. Alstrup, *J. Mater. Chem.* **2009**, *19*, 5442.
[53] Y. Lin, C.-F. Liu, Y.-J. Song, L. Yang, W.-J. Zeng, W.-Y. Lai, W. Huang, *RSC Adv.* **2016**, *6*, 40970.
[54] J.-F. Chang, B. Sun, D. W. Breiby, M. M. Nielsen, T. I. Sölling, M. Giles, I. McCulloch, H. Sirringhaus, *Chem. Mater.* **2004**, *16*, 4772.
[55] M. L. Chabinyc, Y.-L. Loo, *J. Macromol. Sci. Part C* **2006**, *46*, 1.

[56] L. J. A. Koster, E. C. P. Smits, V. D. Mihailetchi, P. W. M. Blom, *Phys. Rev. B* **2005**, *72*, 085205.
[57] S. E. Shaheen, C. J. Brabec, N. S. Sariciftci, F. Padinger, T. Fromherz, J. C. Hummelen, *Appl. Phys. Lett.* **2001**, *78*, 841.
[58] G. Xie, Y. Jiang, X. Du, H. Tai, W. Li, *Sensors*, **2015**, *15* (1), 2086-2103.
[59] J. W. Jeong, Y. W. Park, T. H. Park, J. H. Choi, H. J. Choi, E. H. Song, J. I. Lee, H. Y. Chu, B. K. Ju, *IEEE Electron Device Lett.* **2011**, *32*, 348.
[60] Y. Yang, H. E. Katz, *J. Mater. Chem. C* **2017**, *5*, 2160.
[61] M. Y. Lee, H. J. Kim, G. Y. Jung, A.-R. Han, S. K. Kwak, B. J. Kim, J. H. Oh, *Adv. Mater.* **2015**, *27*, 1540.
[62] E. Lim, K. A. Peterson, G. M. Su, M. L. Chabinyc, *Chem. Mater.* **2018**, *30*, 998.
[63] J. Hynynen, D. Kiefer, C. Müller, *RSC Adv.* **2018**, *8*, 1593.
[64] E. Jang, A. Poosapati, D. Madan, *ACS Appl. Energy Mater.* **2018**, *1*, 1455.
[65] M. Tonga, L. Wei, E. Wilusz, L. Korugic-Karasz, F. E. Karasz, P. M. Lahti, *Synth. Met.* **2018**, *239*, 51.
[66] J. Obrzut, K. A. Page, *Phys. Rev. B* **2009**, *80*, 195211.
[67] J. Yu, Y. Zheng, J. Huang, *Polymers* **2014**, *6*, 2473.
[68] M. Chang, G. T. Lim, B. Park, E. Reichmanis, *Polymers* **2017**, *9*, 212.
[69] M. Brinkmann, *J. Polym. Sci. Part B Polym. Phys.* **2011**, *49*, 1218.
[70] S. D. Bergin, Z. Sun, D. Rickard, P. V. Streich, J. P. Hamilton, J. N. Coleman, *ACS Nano* **2009**, *3*, 2340.
[71] C. J. Brabec, N. S. Sariciftci, J. C. Hummelen, *Adv. Funct. Mater.* **2001**, *11*, 15.
[72] Y. Lin, X. Zhan, *Mater. Horiz.* **2014**, *1*, 470.
[73] A. J. Heeger, *J. Phys. Chem. B* **2001**, *105*, 8475.
[74] P. Pingel, D. Neher, *Phys. Rev. B* **2013**, *87*, 115209.
[75] E. F. Aziz, A. Vollmer, S. Eisebitt, W. Eberhardt, P. Pingel, D. Neher, N. Koch, *Adv. Mater.* **2007**, *19*, 3257.
[76] L. Ma, W. H. Lee, Y. D. Park, J. S. Kim, H. S. Lee, K. Cho, *Appl. Phys. Lett.* **2008**, *92*, 063310.
[77] P. Pingel, L. Zhu, K. S. Park, J.-O. Vogel, S. Janietz, E.-G. Kim, J. P. Rabe, J.-L. Brédas, N. Koch, *J. Phys. Chem. Lett.* **2010**, *1*, 2037.
[78] I. Salzmann, G. Heimel, *J. Electron Spectrosc. Relat. Phenom.* **2015**, *204*, 208.
[79] L. Müller, D. Nanova, T. Glaser, S. Beck, A. Pucci, A. K. Kast, R. R. Schröder, E. Mankel, P. Pingel, D. Neher, W. Kowalsky, R. Lovrincic, *Chem. Mater.* **2016**, *28*, 4432.
[80] J. Gao, E. T. Niles, J. K. Grey, *J. Phys. Chem. Lett.* **2013**, *4*, 2953.
[81] C. E. Johnson, D. S. Boucher, *J. Polym. Sci. Part B Polym. Phys.* **2014**, *52*, 526.
[82] M. Sapolsky, D. Boucher, *J. Polym. Sci. Part B Polym. Phys.* **2018**, *56*, 999.
[83] C. E. Johnson, M. P. Gordon, D. S. Boucher, *J. Polym. Sci. Part B Polym. Phys.* **2015**, *53*, 841.
[84] D. T. Scholes, P. Y. Yee, J. R. Lindemuth, H. Kang, J. Onorato, R. Ghosh, C. K. Luscombe, F. C. Spano, S. H. Tolbert, B. J. Schwartz, *Adv. Funct. Mater.* **2017**, *27*, 1702654.
[85] I. E. Jacobs, E. W. Aasen, J. L. Oliveira, T. N. Fonseca, J. D. Roehling, J. Li, G. Zhang, M. P. Augustine, M. Mascal, A. J. Moulé, *J. Mater. Chem. C* **2016**, *4*, 3454.
[86] G. Zuo, O. Andersson, H. Abdalla, M. Kemerink, *Appl. Phys. Lett.* **2018**, *112*, 083303.
[87] C. Wang, D. T. Duong, K. Vandewal, J. Rivnay, A. Salleo, *Phys. Rev. B* **2015**, *91*, 085205.
[88] R. Österbacka, *Science* **2000**, *287*, 839.

[89] D. T. Duong, C. Wang, E. Antono, M. F. Toney, A. Salleo, *Org. Electron.* **2013**, *14*, 1330.
[90] I. E. Jacobs, E. W. Aasen, J. L. Oliveira, T. N. Fonseca, J. D. Roehling, J. Li, G. Zhang, M. P. Augustine, M. Mascal, A. J. Moulé, *J. Mater. Chem. C* **2016**, *4*, 3454.
[91] D. T. Scholes, S. A. Hawks, P. Y. Yee, H. Wu, J. R. Lindemuth, S. H. Tolbert, B. J. Schwartz, *J. Phys. Chem. Lett.* **2015**, *6*, 4786.
[92] I. E. Jacobs, J. Li, S. L. Burg, D. J. Bilsky, B. T. Rotondo, M. P. Augustine, P. Stroeve, A. J. Moulé, *ACS Nano* **2015**, *9*, 1905.
[93] J. Y. Lek, Y. M. Lam, J. Niziol, M. Marzec, *Nanotechnology* **2012**, *23*, 315401.
[94] J. S. Moon, J. Jo, A. J. Heeger, *Adv. Energy Mater.* **2012**, *2*, 304.
[95] S. Cho, J. H. Seo, S. H. Park, S. Beaupré, M. Leclerc, A. J. Heeger, *Adv. Mater. Deerfield Beach Fla* **2010**, *22*, 1253.
[96] S. Wakim, B-R Aïch, Y. Tao, M. Leclerc, *Polymer Reviews*, **2007**, *48* (3), 432-462.
[97] M. Culebras, C. M. Gómez, A. Cantarero, *Materials* **2014**, *7*, 6701.
[98] I. Lévesque, P.-O. Bertrand, N. Blouin, M. Leclerc, S. Zecchin, G. Zotti, C. I. Ratcliffe, D. D. Klug, X. Gao, F. Gao, J. S. Tse, *Chem. Mater.* **2007**, *19*, 2128.
[99] I. Lévesque, X. Gao, D. D. Klug, J. S. Tse, C. I. Ratcliffe, M. Leclerc, *React. Funct. Polym.* **2005**, *65*, 23.
[100] J. Maiz, M. M. Rojo, B. Abad, A. A. Wilson, A. Nogales, D.-A. Borca-Tasciuc, T. Borca-Tasciuc, M. Martín-González, *RSC Adv.* **2015**, *5*, 66687.
[101] R. B. Aïch, N. Blouin, A. Bouchard, M. Leclerc, *Chem. Mater.* **2009**, *21*, 751.
[102] G. J. Snyder, *Energy Harvesting Technologies*, Springer, Boston, MA, **2009**; pp. 325–336.
[103] L. Lu, L. Yu, *Adv. Mater.* **2014**, *26*, 4413.
[104] Y. Liang, Z. Xu, J. Xia, S.-T. Tsai, Y. Wu, G. Li, C. Ray, L. Yu, *Adv. Mater.* **2010**, *22*, E135.
[105] W. Kim, J. K. Kim, E. Kim, T. K. Ahn, D. H. Wang, J. H. Park, *J. Phys. Chem. C* **2015**, *119*, 5954.
[106] S. Das, J. K. Keum, J. F. Browning, G. Gu, B. Yang, O. Dyck, C. Do, W. Chen, J. Chen, I. N. Ivanov, K. Hong, A. J. Rondinone, P. C. Joshi, D. B. Geohegan, G. Duscher, K. Xiao, *Nanoscale* **2015**, *7*, 15576.
[107] T. Han, L. Liu, M. Wei, C. Wang, X. Wu, Z. Xie, Y. Ma, *Phys. Chem. Chem. Phys.* **2017**, *19*, 17653.
[108] Z. He, C. Zhong, S. Su, M. Xu, H. Wu, Y. Cao, *Nat. Photonics* **2012**, *6*, 591.
[109] Z. He, C. Zhong, X. Huang, W.-Y. Wong, H. Wu, L. Chen, S. Su, Y. Cao, *Adv. Mater.* **2011**, *23*, 4636.
[110] B. Carsten, J. M. Szarko, H. J. Son, W. Wang, L. Lu, F. He, B. S. Rolczynski, S. J. Lou, L. X. Chen, L. Yu, *J. Am. Chem. Soc.* **2011**, *133*, 20468.
[111] A. Solanki *et al.*, *J. Phys. Chem. C*, **2014**, *118* (21), 11285-11291.
[112] M. Rastegaralam, C. Lee, U. Dettlaff-Weglikowska, *Crystals* **2017**, *7*, 292.
[113] C. J. M. Lasance, **2006**, *The Seebeck Coefficient., view on* https://www.electronics-cooling.com/2006/11/the-seebeck-coefficient/ (July, **2019**).
[114] S. J. Lou, N. Zhou, X. Guo, R. P. H. Chang, T. J. Marks, L. X. Chen, *J. Mater. Chem. A* **2018**, *6*, 23805.
[115] J. Ho Youn, Y. Il Lee, H. Tae Moon, M. Sun Ryu, J. Kim, J. Jang, *Curr. Appl. Phys.* **2010**, *10*.
[116] Y.-Y. Lai, Y.-J. Cheng, C.-S. Hsu, *Energy Environ. Sci.* **2014**, *7*, 1866.
[117] P. Cheng, C. Yan, T.-K. Lau, J. Mai, X. Lu, X. Zhan, *Adv. Mater.* **2016**, *28*, 5822.
[118] W. Chen, Y. Wu, Y. Yue, J. Liu, W. Zhang, X. Yang, H. Chen, E. Bi, I. Ashraful, M. Grätzel, L. Han, *Science* **2015**, *350*, 944.

[119] P.-W. Liang, C.-C. Chueh, S. T. Williams, A. K.-Y. Jen, *Adv. Energy Mater.* **2015**, *5*, 1402321.
[120] J. Yang, H.-L. Yip, A. K.-Y. Jen, *Adv. Mater. Funct.* **2013**, *3* (5), 549-565.
[121] P. Wei, J. H. Oh, G. Dong, Z. Bao, *J. Am. Chem. Soc.* **2010**, *132*, 8852.
[122] F. Gao, Y. Liu, Y. Xiong, P. Wu, B. Hu, L. Xu, *Front. Optoelectron.* **2017**, *10*, 117.
[123] F. Li, M. Pfeiffer, A. Werner, K. Harada, K. Leo, N. Hayashi, K. Seki, X. Liu, X.-D. Dang, *J. Appl. Phys.* **2006**, *100*, 023716.
[124] G. Zuo, Z. Li, E. Wang, M. Kemerink, *Adv. Electron. Mater.* **2018**, *4*, 1700501.
[125] M. Pietrzak, M. Szabelski, A. Kasparek, Z. Wieczorek, *Chem. Phys. Lett.* **2017**, *669*, 85.
[126] Y. Lu, J.-Y. Wang, J. Pei, *Angew. Chem. Int. Ed.*, **2019**, *58*, 1-6.
[127] N. B. Kolhe, H. Lee, D. Kuzuhara, N. Yoshimoto, T. Koganezawa, S. A. Jenekhe, *Chem. Mater.* **2018**, *30*, 6540.
[128] H. Yan, Z. Chen, Y. Zheng, C. Newman, J. R. Quinn, F. Dötz, M. Kastler, A. Facchetti, *Nature* **2009**, *457*, 679.
[129] R. A. Schlitz, F. G. Brunetti, A. M. Glaudell, P. L. Miller, M. A. Brady, C. J. Takacs, C. J. Hawker, M. L. Chabinyc, *Adv. Mater.* **2014**, *26*, 2825.
[130] E. Aqad, M. V. Lakshmikantham, M. P. Cava, *Org. Lett.* **2001**, *3*, 4283.
[131] M. D. Bezoari, P. Kovacic, S. Gronowitz, A.-B. Hörnfeldt, *J. Polym. Sci. Polym. Lett. Ed.* **1981**, *19*, 347.
[132] S. J. Xie, L. M. Mei, D.L. Lin, *Phys. Rev. B Condens. Matter* **1994**, *50*, 13364.
[133] H. O. Villar, P. Otto, M. Dupuis, J. Ladik, *Synth. Met.* **1993**, *59*, 97.
[134] J. Xu, J. Hou, S. Zhang, G. Nie, S. Pu, L. Shen, Q. Xiao, *J. Electroanal. Chem.* **2005**, *578*, 345.
[135] L. Tu, X. Wang, J. Wang, X. Meng, J. Chu, *Adv. Electron. Mater.* **2018**, *4*, 1870051.
[136] R. A. Schlitz, F. G. Brunetti, A. M. Glaudell, P. L. Miller, M. A. Brady, C. J. Takacs, C. J. Hawker, M. L. Chabinyc, *Adv. Mater. Deerfield Beach Fla* **2014**, *26*, 2825.
[137] Y.-J. Hwang, G. Ren, N. M. Murari, S. A. Jenekhe, *Macromolecules* **2012**, *45*, 9056.
[138] A. Giovannitti, C. B. Nielsen, D.-T. Sbircea, S. Inal, M. Donahue, M. R. Niazi, D. A. Hanifi, A. Amassian, G. G. Malliaras, J. Rivnay, I. McCulloch, *Nat. Commun.* **2016**, *7*, 13066.
[139] D. Kiefer, A. Giovannitti, H. Sun, T. Biskup, A. Hofmann, M. Koopmans, C. Cendra, S. Weber, L. J. Anton Koster, E. Olsson, J. Rivnay, S. Fabiano, I. McCulloch, C. Müller, *ACS Energy Lett.* **2018**, *3*, 278.

Chapter 3
Hybrid polymer-inorganic material tailoring

The main drawback of organic/polymeric materials for thermoelectricity is the intrinsically low Seebeck coefficient [1,2] leading to a limited power factor compare to their inorganic counterpart [3]. Researchers developed different strategies to enhance the Seebeck coefficient of the organic materials [1,2,4]. Another limitation is that n-type thermoelectric organic/polymeric materials which are unstable in the air and even with fine doping, their electrical properties (especially the electrical conductivity) are lower than p-type counterpart [4]. The main approaches involved to minimize n-type materials drawbacks are novel synthetic pathways to obtain more stable n-type materials [5], engineering of their properties such as structural tuning [6,7], charge carriers optimization [7–9], macromolecular engineering [5,10,11] and coupling polymer/inorganic nanocomposites [12–15]. Based on Dorling *et al.*'s approach [14], where they mixed p- & n-type doped carbon nanotubes with P3HT in order to modulate Seebeck coefficient with the nature of the carbon nanotubes doping (stable and performant n-type material), an alternative strategy was developed in our laboratory.

Our strategy was to use a semi-conducting inorganic material as substrate for different polymers to have a positive and a synergistic effects with both of organic (low thermal conductivity [16] and relative high electrical conductivity [17]) and inorganic (high Seebeck coefficient [18]) materials without losing properties of polymers thin films, *i.e.* crystallinity for semi-crystalline polymers.

Silicon substrates were chosen as semi-conducting inorganic materials due to their important role in electronic and industrial field [19], their high range of impurities concentration (doping concentration) accessible [20] and their good thermoelectric properties ($S \approx 500\text{-}1200$ µV/K when correctly doped) at room temperature [21]. The main drawbacks of silicon substrates are First a high thermal conductivity ($\kappa \approx 50$ W/m.K) that can be decreased by doping [22] ,and a low electrical conductivity (0.05-50 S/cm) compare to conventional inorganic material such as bismuth telluride (> 2000 S/cm) [23].

Different p- & n-type polymers described in Chapter 2 were combined with silicon substrates (wafer) of various electrical conductivities and Seebeck coefficient [24] (Table 1) in order to obtain hybrid materials that benefit from the advantages of the two components, hindering their corresponding drawbacks. All deposition methods (spin-coating, drop-casting, etc.) and measurement techniques (Seebeck coefficient measurement, 4-probe measurement, etc.) are described in **Appendix II**.

Charge carriers type	Nickname	σ (S/cm)	S (µV/K)
Positive type silicon (holes)	p-Si (0.05)	0.05	1052
	p-Si (0.7)	0.7	1001
	p-Si (20)	20	851
	p-Si (50)	50	760
Negative type silicon (electrons)	n-Si (0.05)	0.05	-1000
	n-Si (0.7)	0.7	-951
	n-Si (20)	20	-800
	n-Si (50)	50	-701

Table 1: Electrical conductivity and Seebeck coefficient measured of different Silicon wafers used.

1. Hybrid PEDOT:Tos-silicon material

PEDOT:Tos thin films were deposited on top of silicon wafers, by *in-situ* polymerization, following the procedure described in **Appendix II**. The best formulation, with pyridine and DMSO, was used (electrical conductivity = 1200 S/cm and Seebeek coefficient = 44 µV/K). The influence of PEDOT:Tos thickness on thermoelectric properties of the hybrid material was investigated. Results obtained were confirmed by UPS and XPS analysis.

1.1 Seebeck coefficient

First, the influence of PEDOT:Tos thickness on Si substrates of various doping/conductivities was studied by measuring the Seebeck coefficient (Figure 1). The doping type (positive or negative) does not have an effect on absolute Seebeck coefficient value, a superposition of Seebeck coefficient for p- & n-type Silicon for each PEDOT:Tos thicknesses is possible. However, depending on the Si substrates conductivities, the Seebeck coefficient has different behaviour with respect of PEDOT:Tos thicknesses.

For silicon with low conductivities (0.05 and 0.7 S/cm), Seebeck coefficient decreases rapidly when the PEDOT:Tos thickness increases, and reaches a plateau value after five polymer layers near the Seebeck coefficient of PEDOT:Tos (44 µV/K). In case of silicon with high conductivities (20 and 50 S/cm), Seebeck coefficient decreases slowly with the increase of PEDOT:Tos thickness, and a plateau value is achieved after two/three polymer layers. PEDOT:Tos on p-type silicon has a positive Seebeck coefficient and a negative one on n-type silicon, showing the strong influence of the substrate doping nature on Seebeck coefficient. The

plateau value for thick polymer thicknesses shows a strong dependence to the intrinsic properties of the substrate. This approach allows the tuning of the Seebeck coefficient (value and type of charge carriers) depending on the doping of the substrate and the polymer thickness.

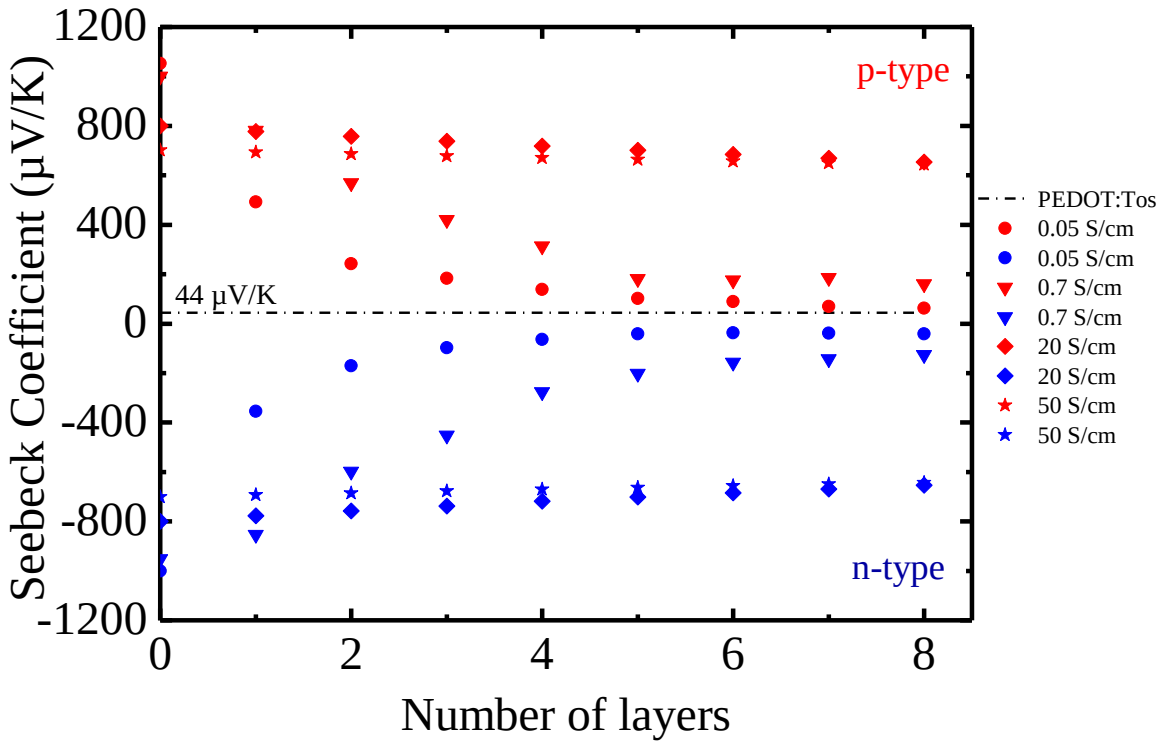

Figure 14: Seebeck coefficient plotted versus number of PEDOT:Tos layers. Blue symbols are for n-type silicon and red symbols are for p-type silicon. Each symbols correspond to an electrical conductivity of a silicon substrate: dots 0.05 S/cm, inverted triangles 0.7 S/cm, diamonds 20 S/cm and stars 50 S/cm. Dashed line is the Seebeck coefficient of bare PEDOT:Tos.

This behaviour was investigated thanks to a model considering the PEDOT:Tos-silicon system as described in Figure 2b. From an electrical point of view, the thermoelectric layers are modelled as a Seebeck generator ($S.\Delta T$) in series with its electrical sheet resistance ($\sigma.t$) (Figure 2a). In case of PEDOT:Tos-silicon system, the same basic system is applied, giving two sources with resistances in parallel (Figure 2b). When this "more" complex model is applied to the experimental data, the total Seebeck coefficient for this kind of junction is calculated with the following expression (Equation 1):

$$S_{Junction} = S_{Si} \cdot \frac{1 + \frac{S_{pol} \cdot \sigma_{pol} \cdot t_{pol}}{S_{Si} \cdot \sigma_{Si} \cdot t_{Si}}}{1 + \sigma_{pol} \cdot \frac{t_{pol}}{\sigma_{Si} \cdot t_{Si}}} \quad (1)$$

$$t_{pol} \to 0 \; ; \; S_{junction} = S_{Si}$$

$$t_{pol} \to \infty \; ; \; S_{junction} = S_{pol}$$

where the Seebeck coefficient (S_{pol} and S_{Si}), the electrical conductivity (σ_{pol} and σ_{Si}) and the thickness (t_{pol} and t_{Si}) of PEDOT:Tos and silicon substrate are expressed, respectively.

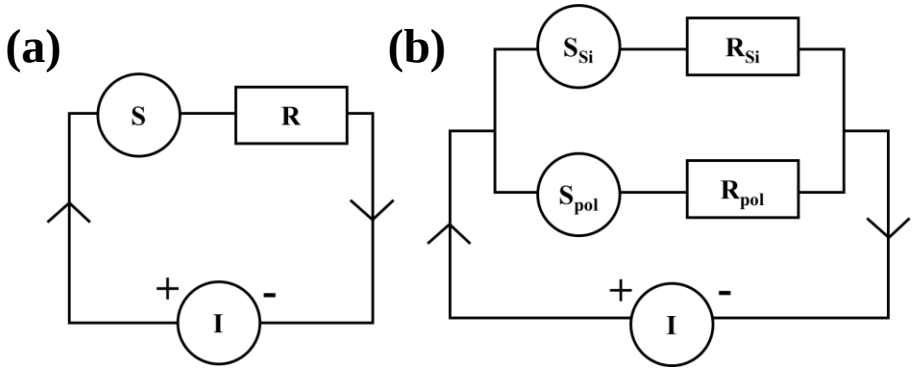

Figure 2: (a) Model system for a thermoelectric material composed of voltage source (S) and resistance (R) connected in series.
(b) Model system for hybrid material (silicon and PEDOT:Tos) composed of two identical model from (a) in parallel.

Resulting calculated Seebeck coefficient data are plotted and compared to experimental Seebeck coefficient in Figure 3. This model (dashed line) allows to satisfactorily fit the experimental data ("dots") for PEDOT:Tos-silicon junction with high electrical conductivities. However, depending on the silicon substrates conductivities, the Seebeck coefficient has a different behaviour with respect of PEDOT:Tos thicknesses (number of layers). In case of low conductive silicon substrates (circles and inverted triangles), the measured Seebeck coefficient of the thinner PEDOT:Tos samples (zero to five polymer layers) decreases when the polymer thickness increases, and then reaches the same order of magnitude as the one of the PEDOT:Tos on glass (black dashed lines) after five polymers layers. On the other hand, for high conductive silicon substrate (diamonds and stars), the measured Seebeck coefficient of PEDOT:Tos samples reaches a plateau after only one layer. Consequently, this approach allows the tuning of the Seebeck coefficient value and sign depending on the doping of the substrate. Hybrid PEDOT:Tos–silicon samples with a negative Seebeck coefficient are air stable. Interestingly the plateau value obtained for PEDOT:Tos film shows a strong dependence to the intrinsic

conductivity of the Si substrates. One hypothesis to understand the poor fitting at lower thicknesses could be the presence of an additional interaction at the interface, which was not take into account in the model, between the silicon substrate and the polymer. More analysis, UPS and XPS analysis would give information about this possible phenomenon.

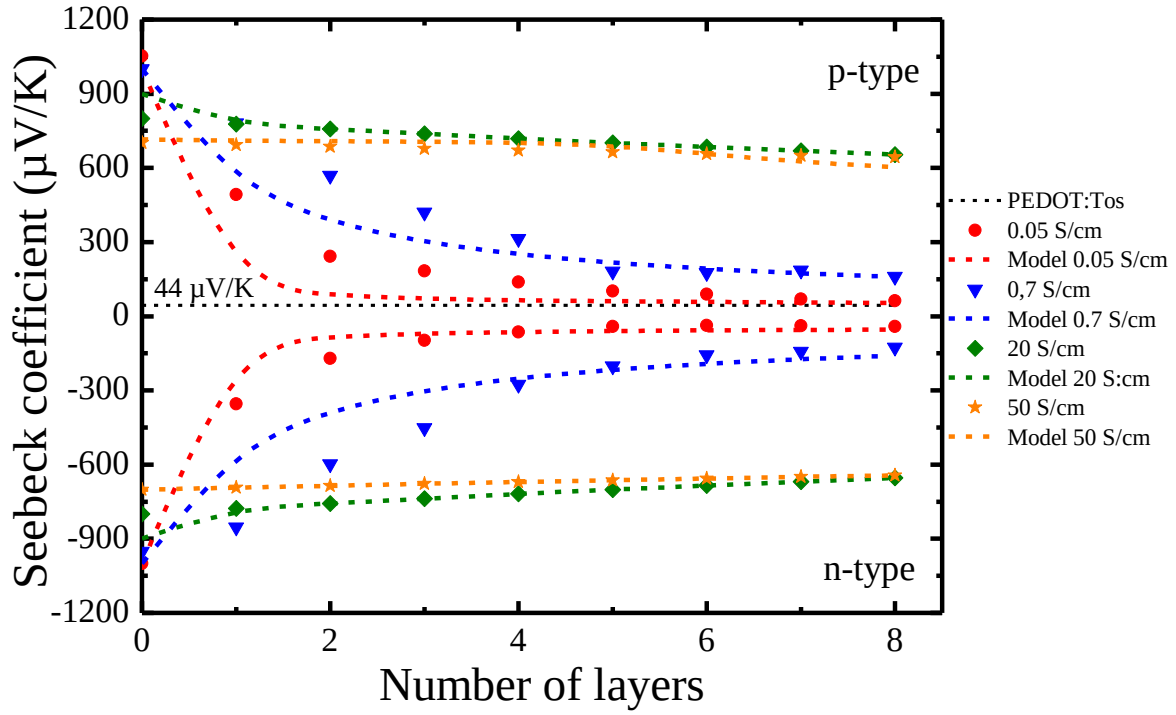

Figure 3: Seebeck coefficient plotted versus number of PEDOT:Tos layers. Color dashed lines are for the model obtained with Equation 1 and symbols are for experimental data. Each color/symbol corresponds to an electrical conductivity of a silicon substrate: red dots 0.05 S/cm, blue inverted triangles 0.7 S/cm, green diamonds 20 S/cm and orange stars 50 S/cm. Black dashed line is the Seebeck coefficient of bare PEDOT:Tos.

As shown in Chapter 2, the Seebeck coefficient of polymers is dependent of their Density of States (DoS). So, if the shape of the DoS, the filling of the DoS, or the Fermi level position change, that will affect the material thermoelectric behaviour [7,9]. As described in the literature, the shape of DoS for a polymer/nanocomposite material is affected by both the DoS of the polymer and the DoS of the inorganic part [15]. So PEDOT:Tos on various silicon substrates should result in hybrid materials of different DoS, and confirm Seebeck coefficients observed.

First, Ultraviolet Photoelectron Spectroscopy (UPS) was performed on bare silicon, the influence of the doping (type and concentration of impurities) was studied (Figure 4a). The shape of bare silicon curves is in accordance with results in literature [25], the work function extracted is 4.2 eV and 4.3 eV for low and high conductive bare silicon respectively. Thanks to

a magnification at low binding energy (Figure 4b), 0 – 2 eV, HOMO level could be scanned and no energy states are visible in this area, that is typical for semi-conducting material [26]. Furthermore, based on this magnification is difficult to see a difference of the slope at the Fermi level, and so the correlation with the Seebeck coefficient is impossible in this condition.

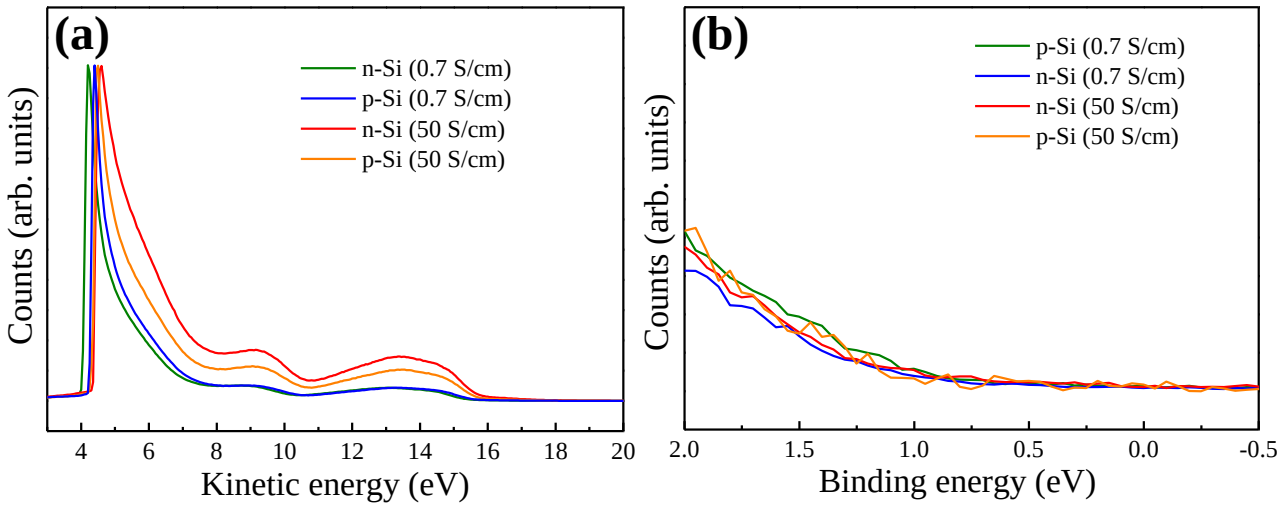

Figure 4: (a) UPS spectra of bare silicon with different electrical conductivity.
(b) Magnified view of band edge for the same UPS spectra in low binding energy region.

Then PEDOT:Tos pyridine + DMSO was deposited on low and high conductive silicon substrate and UPS measurement was used in order to correlate Seebeck coefficient and DoS of the hybrid material. The UPS spectra of one layer of polymer on various silicon are presented in Figure 5a and signatures of the inelastic scattering of the PEDOT:Tos HOMO bands are retrieved (*cf*. Chapter 2). PEDOT:Tos behaviour is similar on various silicon substrates, the characteristic signal of silicon disappeared. Thanks to a magnification at low binding energy (Figure 5b), 0 – 2 eV, HOMO level could be scanned and energy states are visible in this area, that is typical for semi-metal material [9]. Based on this magnification, the slope at the Fermi level gives an information on the Seebeck coefficient (Figure 5b). These results are in agreement with the Seebeck coefficient data obtained Figure 1. No slope difference is observed between the p- & n-type silicon with the same conductivity with one PEDOT:Tos layer on-top, this result confirms the symmetry behaviour observed previously, impurities type in the silicon do not affect the absolute value of Seebeck coefficient. However, a steeper curve is obtained for composite polymer/silicon with the highest conductivity, corresponding to a high Seebeck coefficient observed previously.

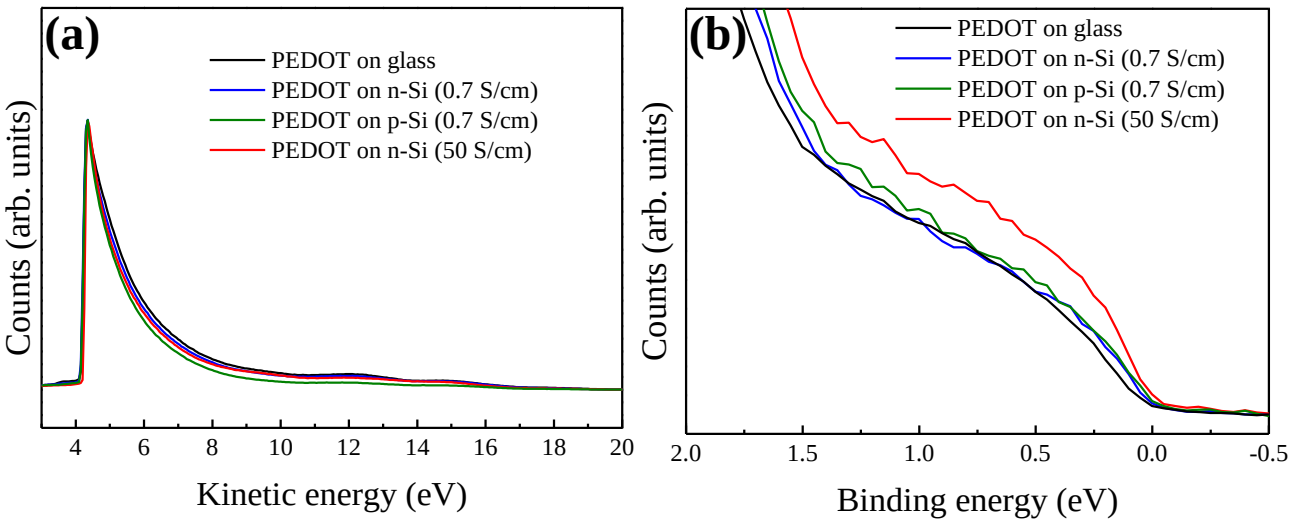

Figure 55: (a) UPS spectra of 1 layer of PEDOT:Tos on silicon with different electrical conductivities. (b) Magnified view of band edges for the same UPS spectra in low binding energy region.

Thereafter, UPS analysis was conducted on PEDOT:Tos-silicon composite with different PEDOT:Tos thicknesses in order to investigate and confirm the influence of polymer on the Seebeck coefficient (Figure 6). For more readability, only magnification (0 – 2 eV area) of one low (σ=0.7 S/cm) and one high conductive silicon is presented. In case of low conductive silicon, the addition of polymer on-top of silicon have an influence on the slope at the Fermi level, which is less steep with the addition of PEDOT:Tos. So, the Seebeck coefficient follow the same trend by being lower with PEDOT:Tos addition as found from measurement and model. On the other side, polymer thickness do not have any influence for PEDOT:Tos-high conductive silicon as expected (Figure 1).

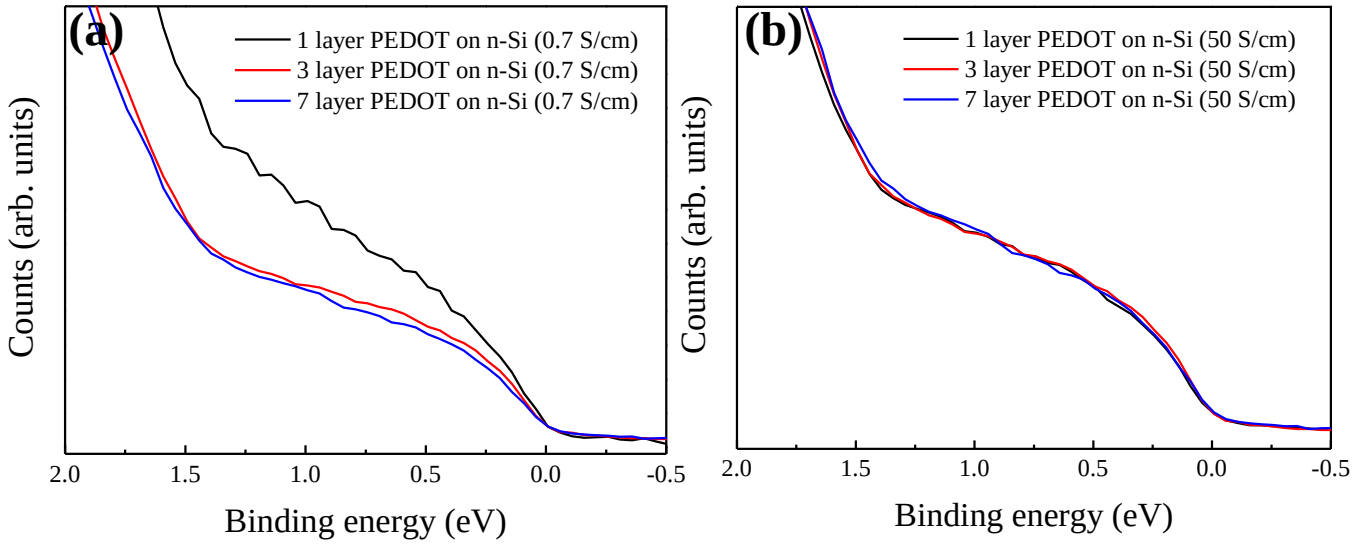

Figure 6: Magnified view of UPS spectra in low binding energy region for different PEDOT:Tos thickness on silicon with (a) low electrical conductivity and (b) high electrical conductivity.

The change of Seebeck coefficient for this hybrid materials can't be properly attributed to a charge transfer between PEDOT:Tos and silicon substrate based on UPS measurement. However, despite UPS is a strong tool, is limited to the surface effects [27]. As it was shown Chapter 1, the Seebeck coefficient is dependant of charge carriers concentration, *N*. Increasing *N* results in a decreasing of the Seebeck coefficient value. So in order to determine the oxidation level linked to *N*, XPS analysis was conducted on Si (σ=50 S/cm)/PEDOT:Tos composite at different polymer thicknesses (Figure 7). The oxidation level extracted from these analysis (*cf.* Chapter 2 for Oxidation level calculation and **Appendix II**) is similar, indicating that the polymer thickness does not affect the number of charge carriers. It seems this behaviour could be only explained by the average of contribution for each Seebeck coefficient from each material as proven by the developed model.

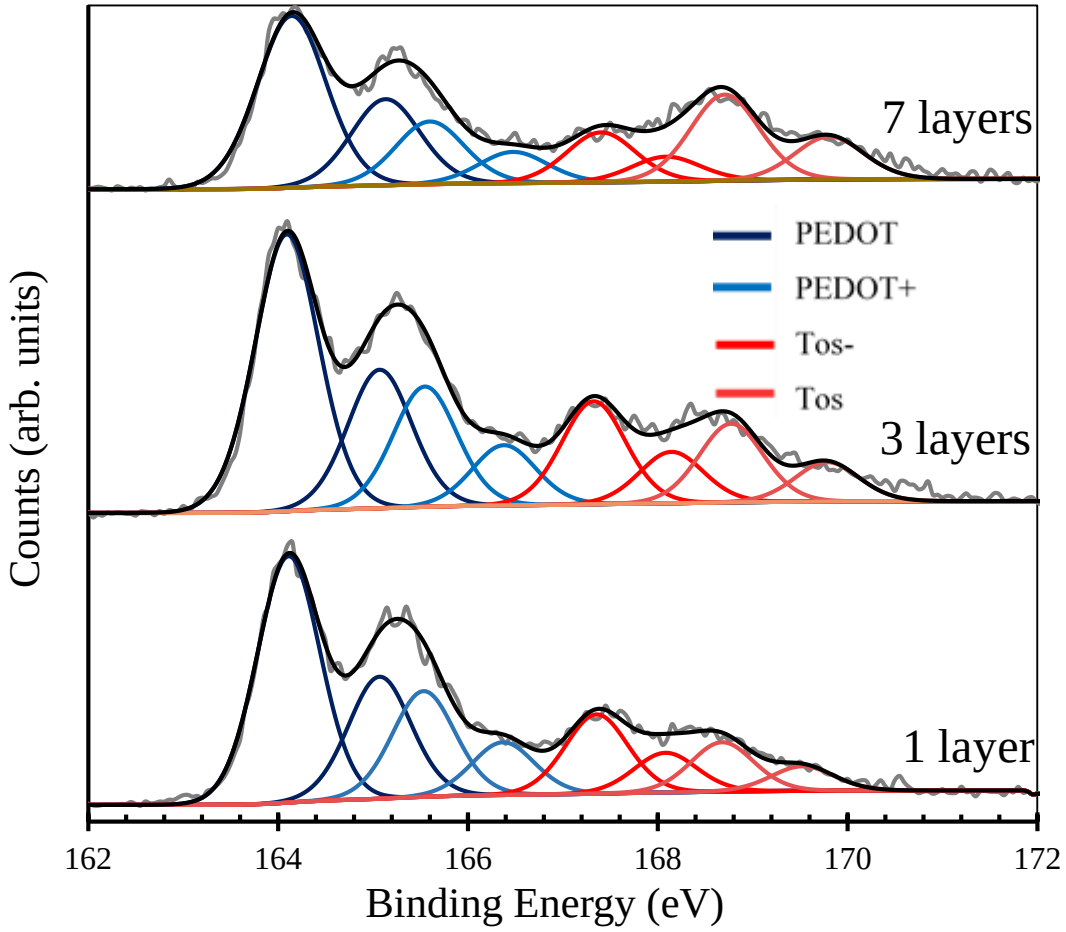

*Figure 7: S(2p) XPS spectra for different PEDOT :Tos film thicknesses on silicon (σ= 50 S/cm). Blue and red lines represent the fit of PEDOT unit and tosylate counter-ion, respectively (More details in the **Appendix II**).*

1.2 Electrical conductivity

The effective electrical conductivity of previous devices, $\sigma_{junction}$, was measured to investigate the role of the interface in these PEDOT:Tos-silicon junctions. $\sigma_{junction}$ could be extracted from the sheet resistance ($R\square$) of the hybrid device (Equation 2). The same substrate architecture and treatment, described in **Appendix II**, was used for the measurement.

$$\frac{1}{R_{\square}} = \sigma_{Junction}.\left(t_{Si}+t_{pol}\right) = \sigma_{Si}t_{Si} + \sigma_{pol}t_{pol}$$
$$\Rightarrow \sigma_{Junction} = \frac{\sigma_{Si}t_{Si} + \sigma_{pol}t_{pol}}{t_{Si}+t_{pol}} \quad (2)$$

As seen before, a thermoelectric material could be interpreted, from electrical point of view, as a Seebeck generator ($S.\Delta T$) in series with its electrical sheet resistance ($\sigma.t$). The electrical sheet resistance of hybrid PEDOT:Tos/Si have to be determine without the "Seebeck generator" that could interfere. The experimental translation was to apply an "high current" (compare to Seebeck measurement = 1 nA) of 1 mA to "supress" the generators (Figure 8).

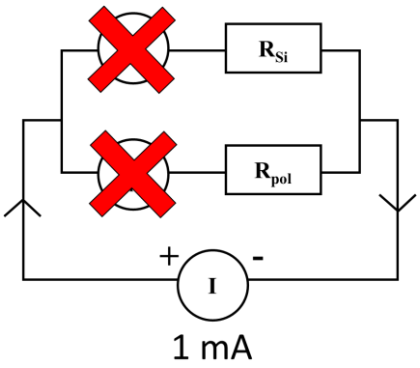

Figure 86: Model system for a hybrid thermoelectric material composed of resistances (R) connected in parallel. Voltage sources are suppressed due to "high" current applied.

Unfortunately, by applying a current on a thermoelectric material, Thomson or Joule effect could occur and interfere in electrical conductivity measurement (**Appendix II**). In case of Thomson effect, when a material is submitted to a temperature gradient and an electrical current, heat from outside environment can be exchanged (absorption or release) [28]. Furthermore, an electrical current passing through an electrical conductor increases the internal

energy of the system producing heat increase, so-called Joule effect, a temperature gradient could be generated and modified the system [29]. In order to investigate these possible interferences, a thermal imaging camera was used and pictures are presented Figure 9.

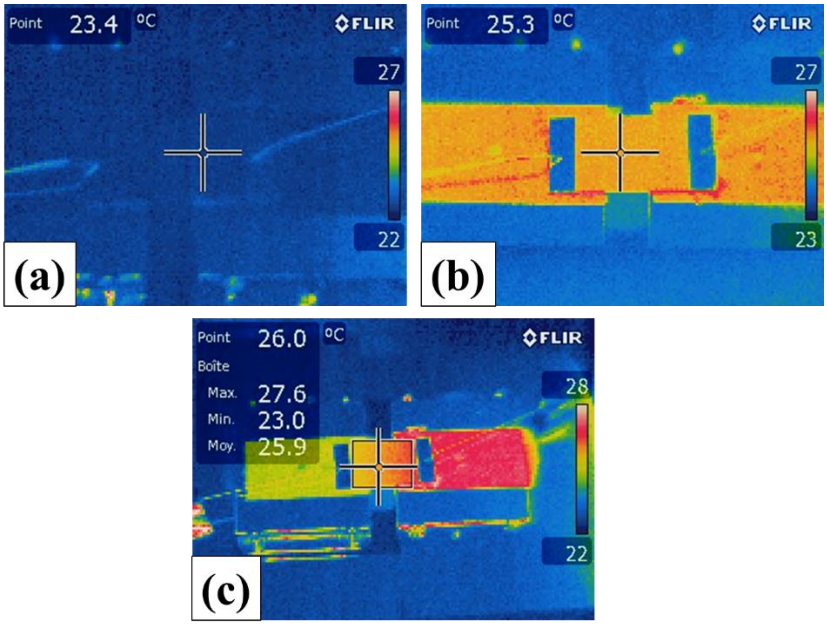

Figure 9: Thermal images of home-made Seebeck coefficient measurement system in various conditions captured with an infrared thermal camera.

In all cases, an electrical current of 1 mA was applied during recording, three different experiments were done:

- Figure 9a, without temperature difference at room temperature;
- Figure 9b, 25 °C applied on both sides;
- Figure 9c, a temperature gradient of 5°C applied (23 °C on left and 28 °C on right side).

Due to the low emissivity of metals, scotch tape was put on Peltier plates in order to measure and confirm the temperature applied [30]. For image (a), the same homogeneous colour on Peltier plates and sample allow to say that no Joule effect happens when a "high" current is applied. Then, image (b) where each side are heated at 25 °C confirm the absence of Thomson effect, no hot point is visible on the sample when temperature and "high" current is applied at the same time. Finally, the last image (c), a temperature difference is applied between each Peltier plates, a temperature gradient is visible on the sample and no heat absorption or emission is present during the measurement. In summary, thanks to these thermal imaging, none Joule effect nor Thomson effect are visible, confirming that experimental settings are valid for electrical conductivity measurement.

The influence of PEDOT:Tos thickness on the conductivity of various Si substrates was studied (Figure 10, two graphics were drawn to improve the visibility). The electrical conductivity was indirectly obtained by electrical resistance measurement and by applying the following equation (**Appendix II**):

$$\rho = \frac{1}{\sigma} = R\,\frac{w\,.\,t}{L} \tag{3}$$

Where the resistivity (ρ), the electrical conductivity (σ), the resistance (R), the width (w), the thickness (t) and the length (L) are expressed. Due to the 2-probes measurement, the contact resistance was determined [31,32] and subtracted to all resistance values as explained more precisely in **Appendix II**.

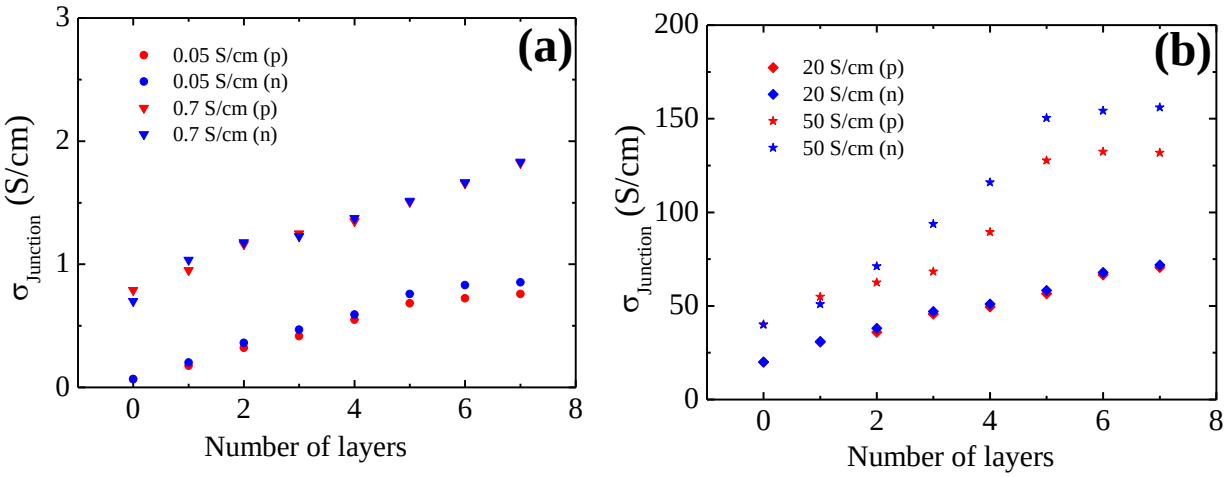

Figure 10: Electrical conductivity of the junction plotted versus number of PEDOT:Tos layers. Blue symbols are for n-type silicon and red symbols are for p-type silicon. Each symbol corresponds to an electrical conductivity of a silicon substrate: dots 0.05 S/cm, inverted triangles 0.7 S/cm, diamonds 20 S/cm and stars 50 S/cm. For more clarity, results are presented in two graphs (a) lower and (b) higher conductivity.

The doping type (positive in red and negative in blue) does not have a significant effect on electrical conductivity values regarding the experimental standard deviation. But, depending on the Si substrate conductivity, the effective conductivity values are different. Principally, an increase of polymer thickness induces an increase of the electrical conductivity until the five PEDOT:Tos layer then a plateau is achieved. In an unexpected way, the substrate conductivity has an influence on the composite material. In case of low conductive silicon, PEDOT:Tos layer stacking produces a small increase of the overall electrical conductivity. PEDOT:Tos layer

stacking on high conductive silicon produces an electrical conductivity increase by a factor three, a maximum of 156 S/cm at seven layers of PEDOT:Tos on n-Si (σ = 50 S/cm) was achieved. One hypothesis to explain this unexpected behaviour could be the way the measurements were done. The electrodes were "sandwiched" between the silicon substrate and the PEDOT:Tos thin film (**Appendix II**) allowing to measure the PEDOT:Tos film, the silicon substrate and the interface of the junction. The current pathway should be more complex than just going through the polymer film (less resistive part), the interface might play a role in these results. In a counter intuitive way, the resulting electrical conductivity might be an average contribution of each part instead of only the electrical conductivity of PEDOT:Tos. Unfortunately, UPS and XPS didn't allow to explain this phenomenon, so in order to confirm this behaviour others polymers will be tested. So if the same phenomenon occurs with other polymers, adding results could assure these results. Finally, this electrical conductivity value is among the record for n-type hybrid material stable in air (based on Chapter 1's literature).

1.3 Power factor

The power factor ($PF=S^2\sigma$) for all PEDOT:Tos/Si hybrid thermoelectric devices are represented Figure 11. When PEDOT:Tos is coated on low conductive Silicon (0.05 and 0.7 S/cm) substrates, the power factor of the hybrid devices decreases with the number of layers. This tendency is due to the negative impact of PEDOT:Tos thickness on Seebeck coefficient of Silicon with low conductivity (Figure 1). When Silicon substrate at 20 S/cm is used, the power factor is stable, the increase of electrical conductivity compensates the decrease of Seebeck coefficient when the PEDOT:Tos thickness increases. Finally, for high conductive Silicon (σ=50 S/cm), the power factor increases with the number of PEDOT:Tos' layer and achieves a plateau for 6 layers, with a maximum at five layers (0.66 and 0.56 mW/mK^2 for n-type and p-type respectively). This trend is following the same trend than electrical conductivity of hybrid PEDOT:Tos/Si(50) thanks a stable Seebeck coefficient for PEDOT:Tos/Si(50) with the increase of polymer thickness, in this case the power factor is ruled by the electrical conductivity.

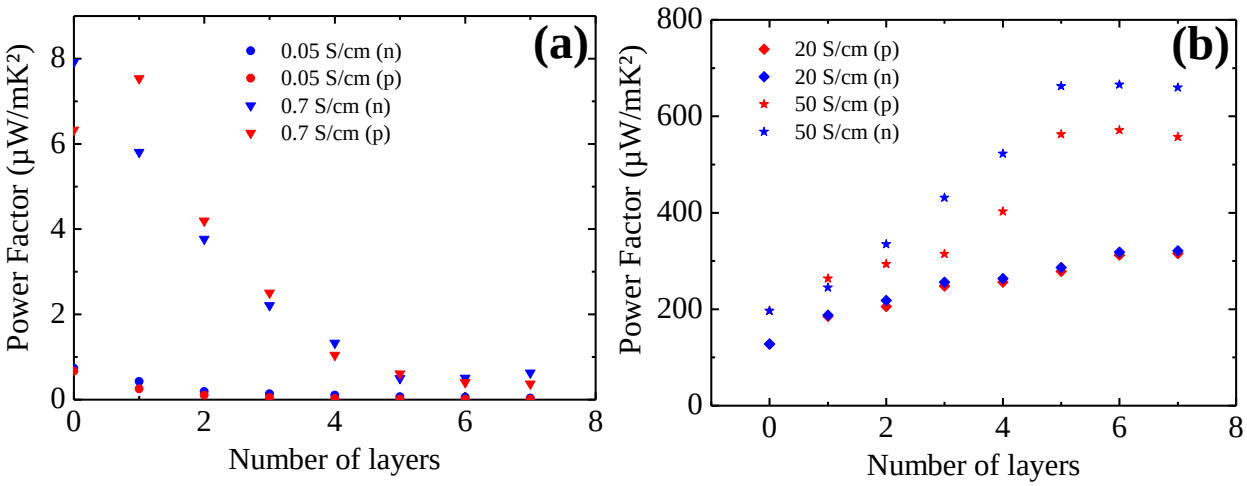

Figure 11: Power factor plotted versus number of PEDOT:Tos layers.
Blue symbols are for n-type silicon and red symbols are for p-type silicon. Each symbol corresponds to an electrical conductivity of a silicon substrate: dots 0.05 S/cm, inverted triangles 0.7 S/cm, diamonds 20 S/cm and stars 50 S/cm. For more clarity, results are presented in two graphs (a) lower and (b) higher conductivity.

To conclude, PEDOT:Tos stacking on high conductive silicon substrates has a positive effect on thermoelectric properties with a power factor from 200 µW/mK² to 660 µW/mK². In order to study more in details this behaviour, various p-type and n-type polymers/materials have been coated on the different silicon substrates cited and the previous model was applied on these hybrid junctions.

2. Hybrid p-type polymer-silicon material

The p-type polymers synthesized and optimized in Chapter 2 were deposited on silicon substrates with various electrical conductivities. All procedures are presented in **Appendix II**. Among these three p-type polymers (P3HT, PCDTBT and PTB7), two different behaviours are visible. P3HT and PCDTBT exhibit Seebeck coefficient of the same order of magnitude than PEDOT:Tos (S = 44 µV/K), 76 and 37 µV/K respectively, while PTB7 has a huge Seebeck coefficient around 750 µV/K. However, their electrical conductivity are much lower compare to PEDOT:Tos, 4.3, 60 and 0.015 S/cm for P3HT, PCDTBT and PTB7 respectively. These different thermoelectric properties will give a large overview of interaction between silicon and p-type polymers.

2.1 Seebeck coefficient

The influence of polymer thickness on Seebeck coefficient of hybrid polymer/silicon substrates was studied, all results are presented Figure 12. Furthermore, the model applied in case of PEDOT:Tos was used on the three different polymer/inorganic junctions. This model

takes into account the Seebeck coefficient of each material and their electrical conductivity weighted by their thickness, the expression is rewritten below:

$$S_{Junction} = S_{Si} \cdot \frac{1 + \frac{S_{pol} \cdot \sigma_{pol.} t_{pol}}{S_{Si} \cdot \sigma_{Si} \cdot t_{Si}}}{1 + \sigma_{pol} \cdot \frac{t_{pol}}{\sigma_{Si} \cdot t_{Si}}} \quad (1)$$

In Figure 12, “dots” are experimental data and “dashed line” are the fitting data calculated from the model (Equation 1). In case of P3HT (Figure 12a) and PCDTBT (Figure 12b), the experimental data fit well with the model for hybrid samples on high conductive silicon. In contrast, a small gap is visible for hybrid sample with low conductive silicon. This phenomenon was also observed for PEDOT:Tos and was attributed to the model center symmetry to the axis x=0 instead of Seebeck coefficient value. In fact, experimentally, when the polymer thickness increases Seebeck coefficient values tend to polymer Seebeck coefficient value. Another difference with the PEDOT:Tos occurs for the silicon σ= 20 S/cm which has its Seebeck coefficient less affected by the polymer thickness. The difference in electrical conductivity between the PEDOT:Tos and the two others polymers should explain it.

In case of PTB7, the model is satisfactory. The polymer thickness does not have any effect on the Seebeck coefficient value of the hybrid material (Figure 12c). The main reason isn’t only its high Seebeck coefficient, in fact with a low electrical conductivity, the contribution of the polymer is largely minimized. This could be explained by the model which takes into account both thermoelectric properties with respect of the thickness of each material. So the polymer low conductivity and thickness are “cancelled” compared to silicon thickness and electrical conductivity (three order of magnitude).

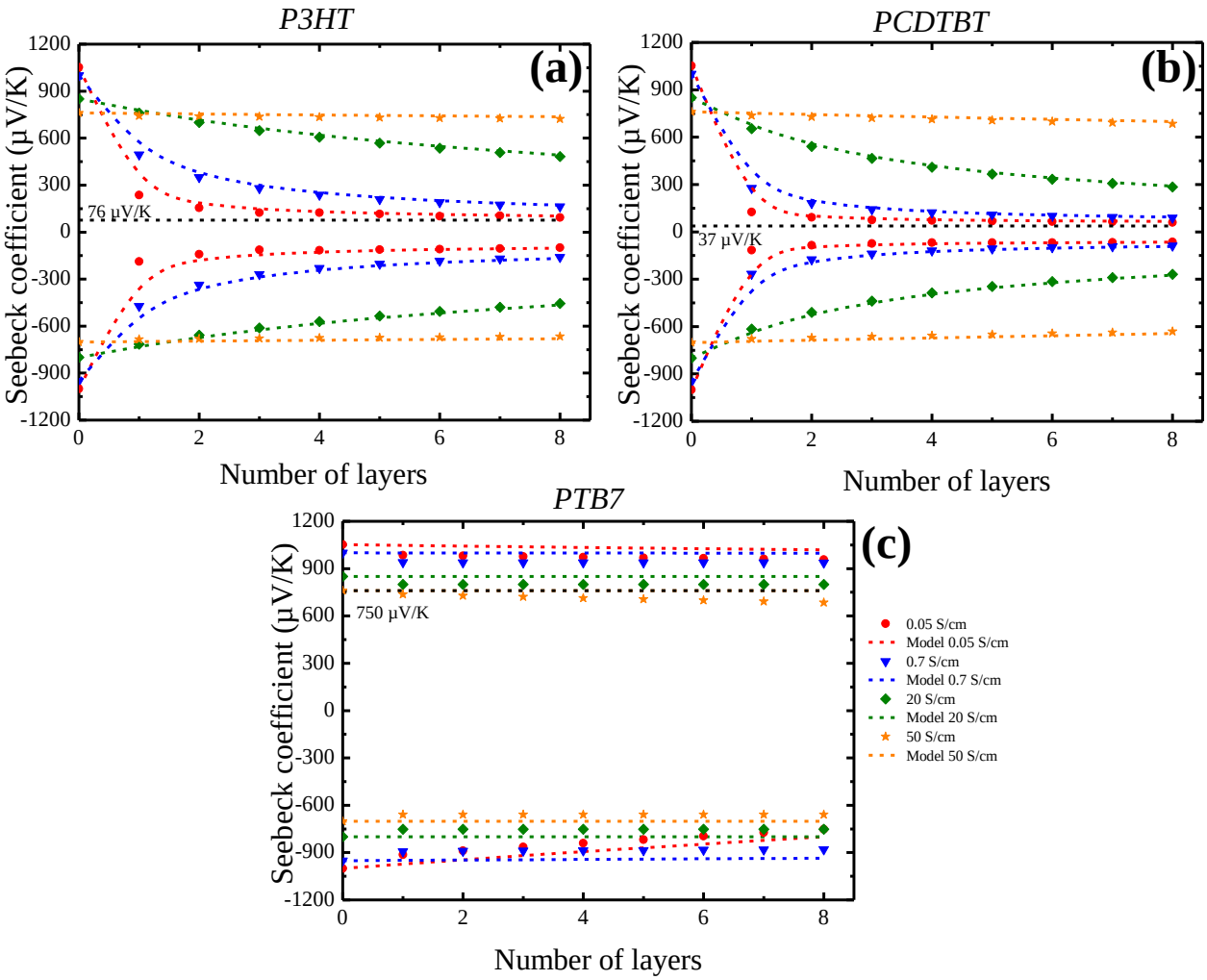

Figure 12: Seebeck coefficient plotted versus number of polymer layerss. [(a) P3HT, (b) PCDTBT and (c) PTB7] Color dashed line are for the model obtained with Equation 1 and symbols are for experimental data.

2.2 Electrical conductivity

The effective electrical conductivity of p-type polymer/silicon hybrid was studied as described previously. This measurement was indirect; the resistance was first measured then effective electrical conductivity was found by taking into account the sample geometry. Results are presented Figure 13. PTB7 on silicon electrical conductivity isn't presented because the values measured were only silicon values without any impact of polymer thickness. Most likely, the low electrical conductivity of PTB7, 0.015 S/cm, was too low to effective electrical conductivity of hybrid material.

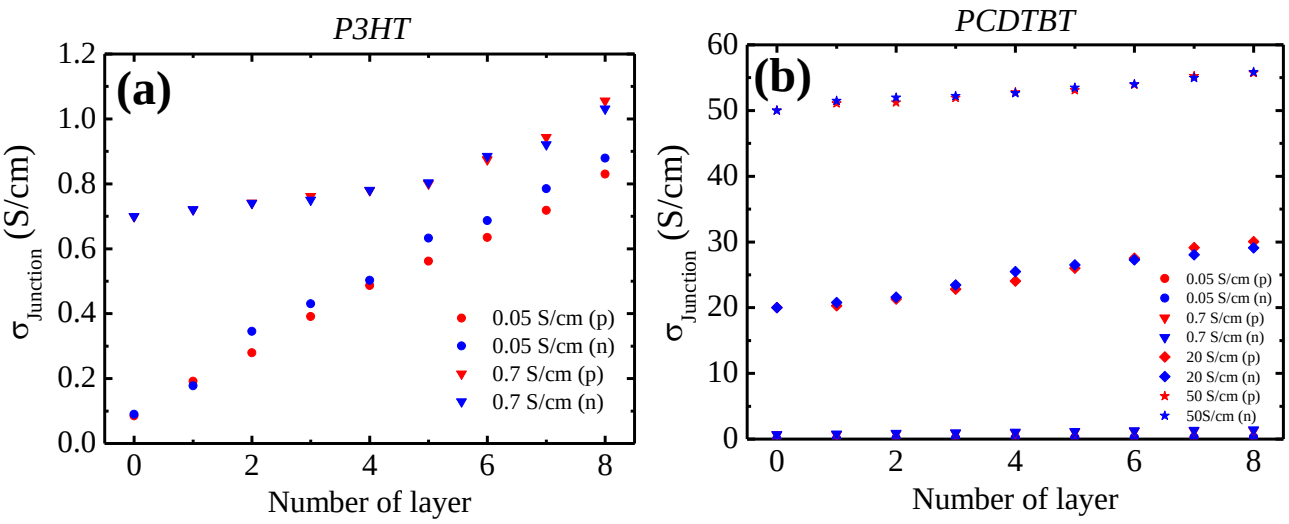

Figure 13: Electrical condcutivity plotted versus number of polymer layers. [(a) P3HT and (b) PCDTBT]. Blue symbols are for n-type silicon and red symbols are for p-type silicon.

First, the doping type (positive in red and negative in blue) does not have a high effect on electrical conductivity values. When the polymer conductivity is lower than electrical conductivity of silicon, only the silicon value is measured. The results of P3HT with high conductive silicon aren't presented because this phenomenon occurs, only electrical conductivity of silicon was probed like in PTB7 case. However, when polymer conductivity is higher than substrate one, polymer thickness has an interesting impact on electrical conductivity of hybrid material. An increase of the value is notable in each cases for P3HT and PCDTBT (even for low conductive silicon substrate with PCDTBT, the scale bar being to large). This phenomenon was also observed for PEDOT:Tos, the previous hypothesis of the impact of the measurement manner should be confirmed with these experimental data. Finally, the electrical conductivity value of these hybrid materials are a bit higher than bare materials alone.

2.3 Power factor

The power factor ($PF=S^2\sigma$) for P3HT and PCDTBT /Si hybrid thermoelectric devices are presented Figure 14. For more visibility, power factor of each polymer were speared in two graphs, one with low conductive silicon (P3HT (a) and PCDTBT (c)) and the other with high conductive silicon substrate (P3HT (b) and PCDTBT (d)). In case of PTB7, polymer thickness does not have any influence on the power factor such as Seebeck coefficient or electrical conductivity. In all cases presented below, polymer has a negative impact on the power factor of the hybrid material. Naturally, when the Seebeck coefficient decreases, the power factor follows its trend even if the electrical conductivity increase. However, contrast to PEDOT:Tos, when the Seebeck coefficient remains stable (high conductive silicon substrate), the power

factor stay unchanged or decreased. The small changes of electrical conductivity can't compensate the loss of Seebeck coefficient.

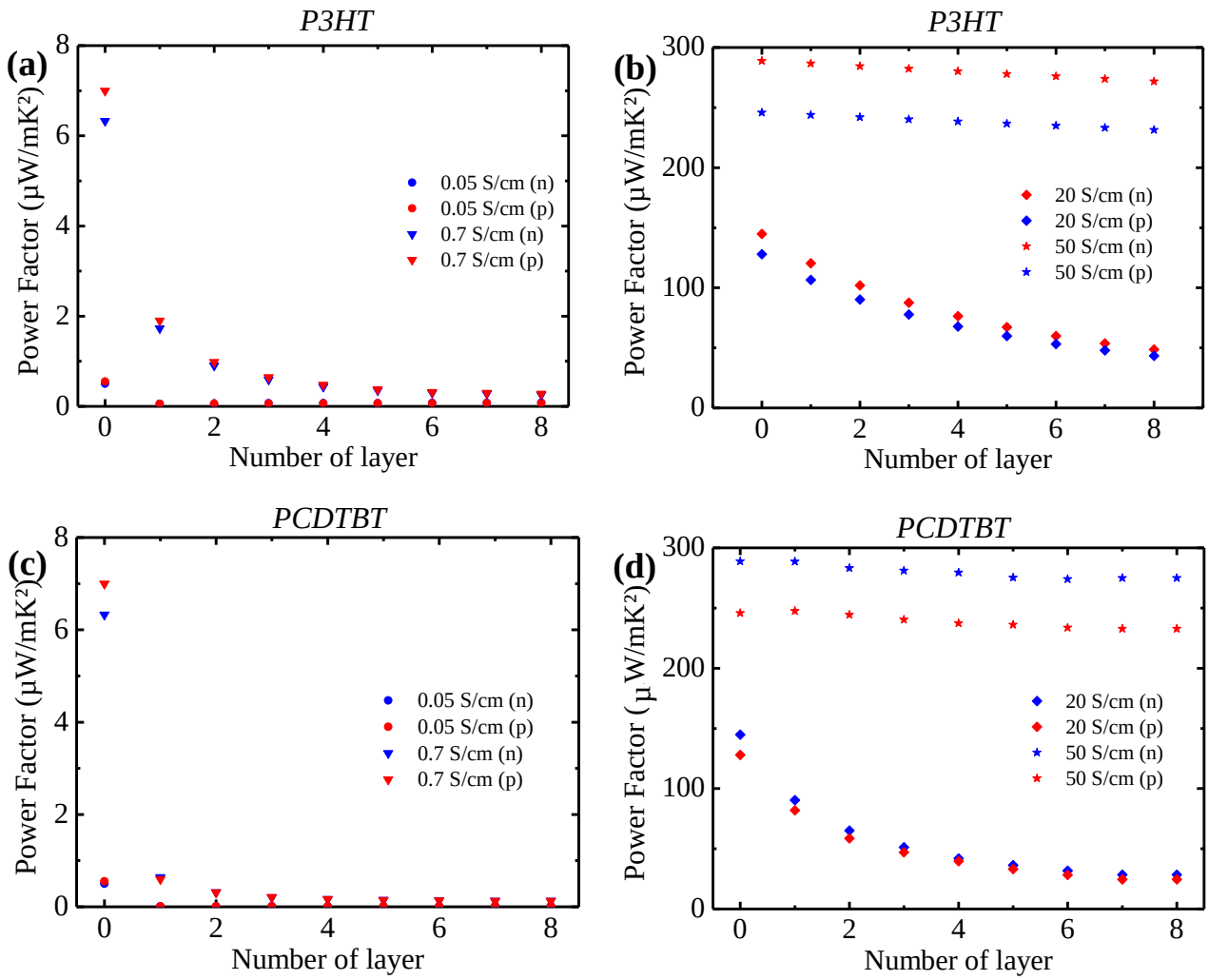

Figure 14: Power factor plotted versus number of polymer layers. [(a,b) P3HT and (c,d) PCDTBT]. Blue symbols are for n-type silicon and red symbols are for p-type silicon.

To conclude, adding stack of p-type polymer with low conductivity on silicon substrate has none impact in best cases on the performance of the final device but could have a very negative impact. These polymers were useful to have a better understanding of the interaction between polymers and silicon on Seebeck coefficient.

3. Hybrid n-type polymer-silicon material

The n-type materials optimized in Chapter 2 were deposited on silicon substrates with various electrical conductivities. All procedures are presented in **Appendix II**. As is was explained in Chapter 1, the low electrical conductivity of n-type material is their main drawback. These material, PCBM and PNDIBS, will be essentially used to confirm the previous behaviour observed.

3.1 Seebeck coefficient

As previously, the influence of polymer thickness on Seebeck coefficient of polymer/silicon substrates was studied, all results are presented Figure 15. The same model was also applied on this n-type materials, the same equation (Equation 1) was used. These experiments should control the model suitability for n-type materials.

In the Figure 15, "dots" are experimental data and "dashed line" are the fitting data calculated from the model (Equation 1). The absolute value of Seebeck coefficient of PCBM and PNDIBS are high compare to PEDOT:Tos value, so the same trend than PBT7 should be obtained for each hybrid devices. This is the case for both PNDIBS, the polymer thickness does not have any effect on the Seebeck coefficient value of the hybrid material (Figure 15a and 15b). The model is satisfactory, and the same hypothesis could be formulated, the contribution of the polymer is minimized due to the low electrical conductivity compared to silicon substrate.

In case of PCBM, similar results than P3HT or PCDTBT are obtained. Material thickness has noticeable impact on the Seebeck coefficient (Figure 15c). By increasing its, the Seebeck coefficient value tend to the bare material one. Furthermore, as expected, the Seebeck coefficient value of p-type silicon is more affected than the Seebeck coefficient value of n-type material, all results are centred around the negative Seebeck coefficient of PCBM, - 412 µV/K. The model predicted well this behaviour and seems to be suitable for n-type material also as expected.

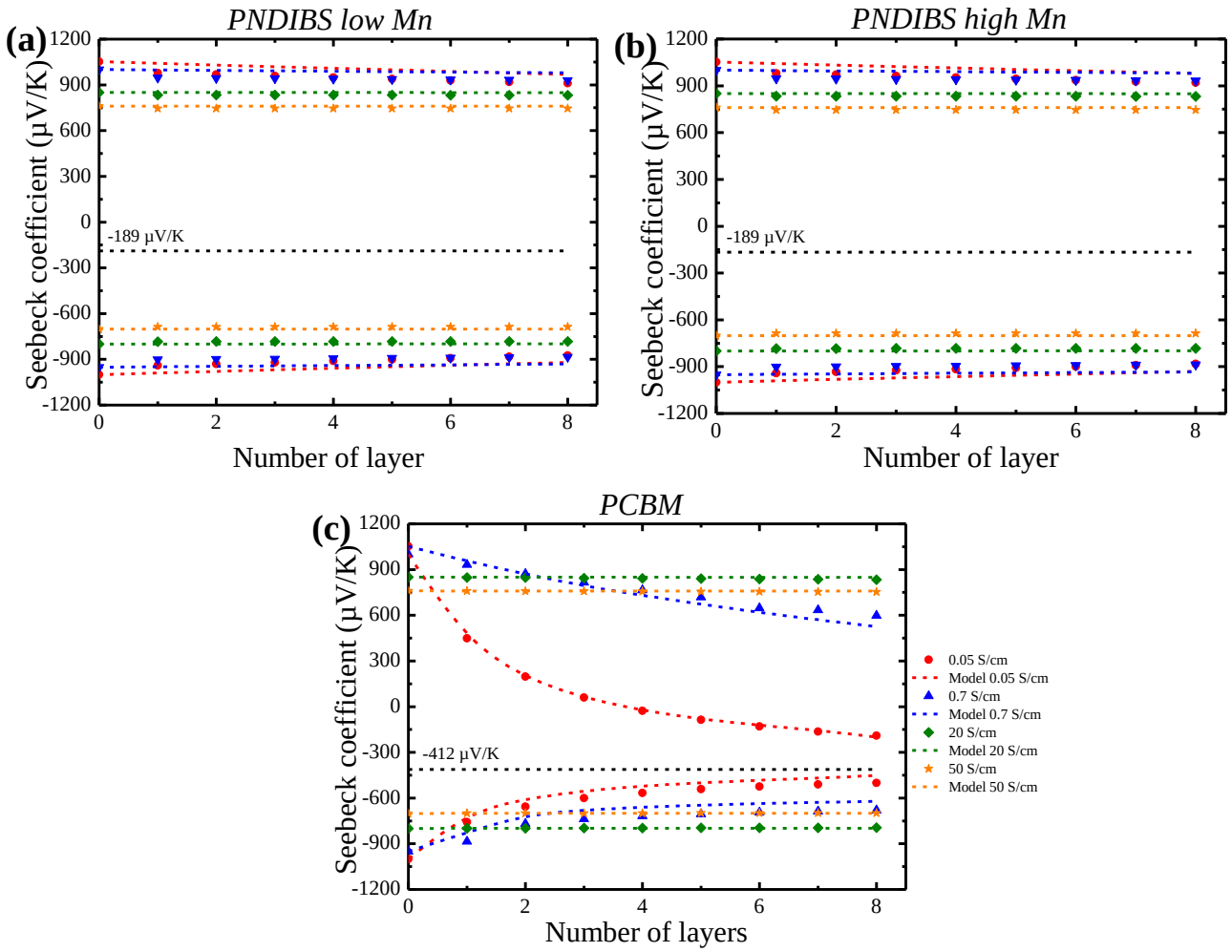

Figure 15: Seebeck coefficient plotted versus number of polymer layers [(a) PNDIBS low Mn, (b) PNDIBS high Mn and (c) PCBM].
Color dashed line are for the model obtained with Equation 1 and symbols are for experimental data.

3.2 Electrical conductivity

The effective electrical conductivity of n-type material/silicon hybrid was studied as described previously. This measurement was indirect; the resistance was first measured then electrical conductivity was found by taking into account the sample geometry. In Figure 16, only results for PCBM on low conductive silicon substrate are presented. In fact, due to the low conductivity of PNDIBS, only the electrical conductivity of the silicon was measured for the hybrid corresponding materials.

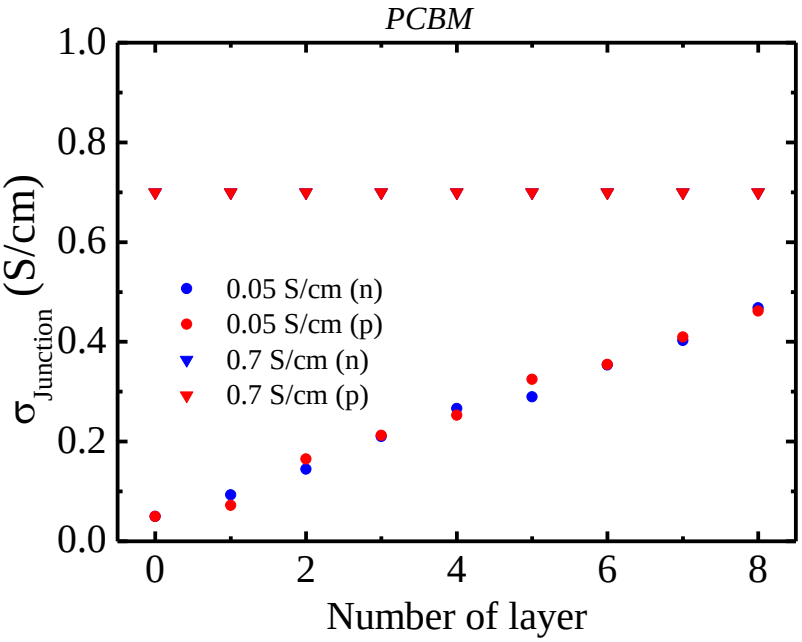

Figure 16: Electrical conductivity plotted versus number of PCBM layers.
Blue symbols are for n-type silicon and red symbols are for p-type silicon. Each symbols correspond to an electrical conductivity of a silicon substrate: dots 0.05 S/cm, inverted triangles 0.7 S/cm, diamonds 20 S/cm and stars 50 S/cm.

First, the doping type (positive in red and negative in blue) does not have a high effect on electrical conductivity values. When the conductivity is lower or equal to electrical conductivity of silicon, only the silicon value is measured. So because the PCBM conductivity on glass is equal to 0.7 S/cm, so only the conductivity of hybrid material with 0.05 S/cm silicon is changing. Adding stacks of PCBM has a positive effect on the electrical conductivity of the corresponding device, confirming the previous results observed of p-type polymers (PEDOT:Tos, P3HT and PCDTBT). Based on Chapter 1 (State of the art), electrical conductivity obtained for n-type hybrid material is high considering the air stability of corresponding hybrid materials.

3.3 Power factor

In power factor expression, $PF=S^2\sigma$, Seebeck coefficient has a huge influence compare to electrical conductivity. So, when the Seebeck coefficient is constant, the power factor will follow the same trend than electrical conductivity. In case of PNDIBS, electrical conductivity and Seebeck coefficient are constant (equal to silicon value), so the power factor is the same than bare silicon and isn't represented below. Naturally, when the Seebeck coefficient decreases, the power factor follows its trend even if the electrical conductivity increase. For

PCBM layer stacking, the small changes of electrical conductivity can't compensate the loss of Seebeck coefficient. The power factor is lower than bare silicon (Figure 17).

To conclude, adding stack of n-type material with low conductivity on silicon substrate has none impact in best cases on the performance of the final device but could have a negative impact. These materials were useful to have a better understanding of the interaction between polymers and silicon on Seebeck coefficient.

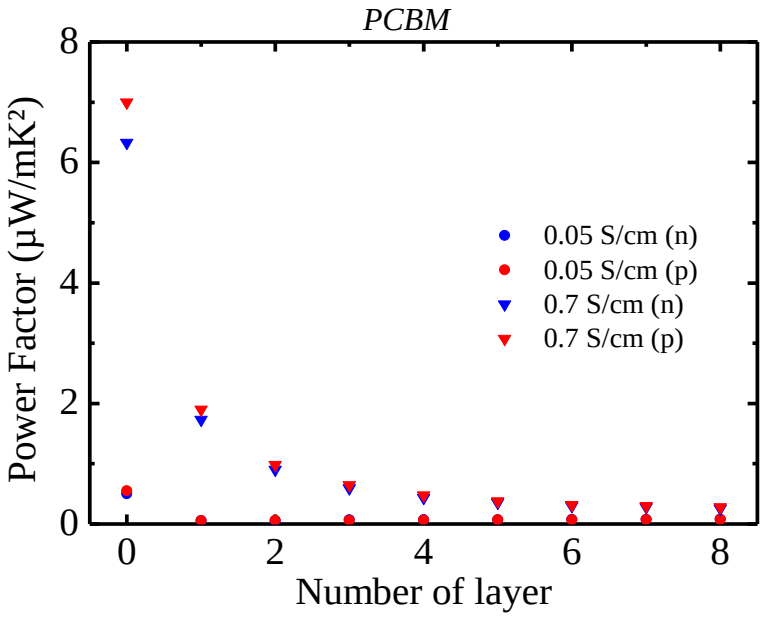

Figure 17: Power Factor plotted versus number of PCBM layers.
Blue symbols are for n-type silicon and red symbols are for p-type silicon. Each symbols correspond to an electrical conductivity of a silicon substrate: dots 0.05 S/cm, inverted triangles 0.7 S/cm, diamonds 20 S/cm and stars 50 S/cm.

D Conclusion

In the present study, the influence of various polymers, p- & n-type, coupled with a large range of silicon with different doping on thermoelectric properties was examined. It was shown that the Seebeck coefficient of such hybrid junction can be tuned in magnitude and sign depending of the silicon and organic material doping and electrical conductivity. These findings were predicted by a model based on an electric circuit. This model is usable for a large range of organic material on inorganic substrate. It was also shown that the electrical conductivity, and so the power factor of bare inorganic material could be increased by adding high conductive polymers on-top of its. This phenomenon was investigated by UPS and XPS analysis, but none of these analysis explained well the increase. The main hypothesis found was a huge influence of the device architecture. In fact, the electrodes were "sandwiched" between the silicon substrate and the PEDOT:Tos thin film (*cf.* **Appendix II**) allowing to measure the polymer film, the silicon substrate and the interface of the junction. The current pathway should be more complex than just going through the polymer film (less resistive part), the interface might play a role in these results. Electrical conductivity and power factor obtained for PEDOT:Tos on n-type silicon are among the best results described in literature for n-type material stable in the air. In a later part, this strategy will be adapted to build efficient air stable thermoelectric generator with n-type and p-type materials based on work done in this Chapter 3.

So in order to elucidate more in details this behaviour, silicon substrate surface will be modified. Nanowires, pores and pyramids will be made by etching on-top of silicon substrate allowing to obtain a larger specific area. The interface between the organic material and the new structured silicon will be different from previously, and its thermoelectric properties will be studied.

References

[1] O. Bubnova, X. Crispin, *Energy Environ. Sci.* **2012**, *5*, 9345.
[2] M. He, F. Qiu, Z. Lin, *Energy Environ. Sci.* **2013**, *6*, 1352.
[3] L.-D. Zhao, G. Tan, S. Hao, J. He, Y. Pei, H. Chi, H. Wang, S. Gong, H. Xu, V. P. Dravid, C. Uher, G. J. Snyder, C. Wolverton, M. G. Kanatzidis, *Science* **2016**, *351*, 141.
[4] C.-Y. Yang, W.-L. Jin, J. Wang, Y.-F. Ding, S. Nong, K. Shi, Y. Lu, Y.-Z. Dai, F.-D. Zhuang, T. Lei, C.-A. Di, D. Zhu, J.-Y. Wang, J. Pei, *Adv. Mater.* **2018**, *30*, 1802850.
[5] B. Russ, M. J. Robb, F. G. Brunetti, P. L. Miller, E. E. Perry, S. N. Patel, V. Ho, W. B. Chang, J. J. Urban, M. L. Chabinyc, C. J. Hawker, R. A. Segalman, *Adv. Mater.* **2014**, *26*, 3473.
[6] G-H. Kim, L. Shao, K. Zhang, K. P. Pipe, *Nature Materials*, **2013**, *12*, 719-723.
[7] O. Bubnova, M. Berggren, X. Crispin, *J. Am. Chem. Soc.* **2012**, *134*, 16456.
[8] Z. U. Khan, O. Bubnova, M. J. Jafari, R. Brooke, X. Liu, R. Gabrielsson, T. Ederth, D. R. Evans, J. W. Andreasen, M. Fahlman, X. Crispin, *J. Mater. Chem. C* **2015**, *3*, 10616.
[9] O. Bubnova *et al.*, *Nature Materials*, **2014**, *13*, 190-194.
[10] K. Shi, F. Zhang, C.-A. Di, T.-W. Yan, Y. Zou, X. Zhou, D. Zhu, J.-Y. Wang, J. Pei, *J. Am. Chem. Soc.* **2015**, *137*, 6979.
[11] Y. Sun, P. Sheng, C. Di, F. Jiao, W. Xu, D. Qiu, D. Zhu, *Adv. Mater.* **2012**, *24*, 932.
[12] N. E. Coates *et al.*, *Advance Materials*, **2013**, *25* (11), 1629-1633.
[13] S. K. Yee, N. E. Coates, A. Majumdar, J. J. Urban, R. A. Segalman, *Phys. Chem. Chem. Phys.* **2013**, *15*, 4024.
[14] B. Dörling *et al.*, *Advance Materials*, **2016**, *28* (14), 2782-2789.
[15] R. M. Ireland *et al.*, *Advanced Materials*, **2015**, *2* (6), 1500015.
[16] C. L. Choy, *Polymer* **1977**, *18*, 984.
[17] S. M. Haque, J. A. A. Rey, A. AbubakarMasúd, Y. Umar, R. Albarracin, *Prop. Appl. Polym. Dielectr.* **2017**, http://dx.doi.org/10.5772/67091.
[18] C. J. M. Lasance, **2006**, *The Seebeck Coefficient*., view on https://www.electronics-cooling.com/2006/11/the-seebeck-coefficient/ (July, **2019**).
[19] L. Venema, *Nature* **2011**, *479*, 309.
[20] B. V. Zeghbroeck, **2011**, *Principle of Semiconductor devices: 2.9 Mobility - Resistivity - Sheet resistance*, Colorado, view on ecee.colorado.edu/~bart/book/mobility.htm (July, **2019**).
[21] J. Zhou, B. Liao, B. Qiu, S. Huberman, K. Esfarjani, M. S. Dresselhaus, G. Chen, *Proc. Natl. Acad. Sci.* **2015**, *112*, 14777.
[22] J. Tang, H.-T. Wang, D. H. Lee, M. Fardy, Z. Huo, T. P. Russell, P. Yang, *Nano Lett.* **2010**, *10*, 4279.
[23] A. Yamamoto, K. Ogawa, T. Takeuchi, *Mater. Trans.* **2011**, *52*, 1539.
[24] A. W. Van Herwaarden, *Sens. Actuators* **1984**, *6*, 245.
[25] K. Ding *et al., J. Mater. Chem., **2017**, 5*, 285-291.
[26] Gerald Burns, *Solid State Physics*, Academic Press, "1st Edition", **1985**, 755 (*ISBN: 97814832886*).
[27] P. Atkins, J. de Paula, *Chimie Physique*, Bruxelles de Boeck supérieur DL, "4th Edition", **2013**, (*ISBD: 978-2-8041-6651-9br*)

[28] C. Goupil, *Continuum Theory and Modeling of Thermoelectric Elements*, Wiley-VCH Verlag GmbH & Co. KGaA: Weinheim, Germany, **2016**, 360 (*ISBN: 978-3-527-41337-9*).
[29] J. P. Joule, *The London, Edinburgh, and Dublin Philosophical Magazine and Journal of Science*, **1844**, *19* (124), 260-277.
[30] H. Crepin, **2015**, *Tableau émissivités en thermographie*, view on http://www.thethermograpiclibrary.org/index.php?title=Tableau_%C3%A9missivit%C3%A9s_en_thermographie (July, **2019**).
[31] Y. Singh, *Int. J. Mod. Phys. Conf. Ser.* **2013**, *22*, 745.
[32] M. Weis *et al.*, *Applied Physics Letters*, **2010**, 97 (26), 263304.

Chapter 4

Silicon nano-structuration: Interface influence on thermoelectric properties

As described previously, silicon has various advantages such as a high abundant earth reserves, a low cost and a matured manufacturing technology for mass production [1,2]. Unfortunately, nowadays silicon isn't used in thermoelectric devices due to its high thermal conductivity and low $ZT = 0.01$ [3–6]. Nano-structured silicon has recently attracted the attention of scientist in sensors [7] and photovoltaic cells [8] due to their small cross-sectional area, large surface-to-volume ratio, and attractive transport properties. During the past years, nano-structured silicon has also been considered as high potential thermoelectric material with a high figure of merit *ZT* value. The main reason was their ability to reduce the thermal conductivity, while retaining others thermoelectric characteristics [9]. In fact, in silicon the thermal energy is transported mostly by the lattice vibration rather than by electrons and holes, but in case of nano-structured silicon, thermal conductivity is decreased by phonon scattering by defects at the nano-structure surface [10,11]. In this study, the large surface-to-volume ratio of nano- structured silicon has been used to show the influence of silicon surface area on thermoelectric properties of hybrid PEDOT:Tos-silicon devices, thus three different structures with various specific area were made : porous, pyramids and nanowires.

A Silicon nanowires

1. Theory and principle

Silicon nanowires are one of the most successful examples of nanostructured silicon in thermoelectricity. Boukai *et al.* reported a high *ZT* ~1 at ambient temperature for a single nanowire device [12]. Thermoelectric properties, Seebeck coefficient and electrical conductivity, decreased a bit while thermal conductivity has been reduced to 1.6 W/mK. More recently, a large range of doped silicon nanowire were characterized for thermoelectric application. In both cases, silicon nanowires showed great potential for future thermoelectric application [13,14].

For device applications, a controllable fabrication of silicon nanostructure is mandatory, in fact their properties strongly depend on their preparation methods [15,16]. Low-cost and scalable production of silicon nanowires is essential to their application. Two major low-cost strategies were developed to fabricate silicon nanostructures, top-down and bottom-up approach. The most famous method for bottom-up approach is the silicon wire growth via vapour-liquid-solid (VLS) mechanism via chemical vapour deposition (CVD) developed by Wagner *et al.* [17].This method is based on an assembly process joining silicon atoms to form silicon nanowires by using gold as metallic catalyst, and SiH_4 or $SiCl_4$ as gaseous silicon precursors. Concisely, the

VLS approach involves the following steps as show Figure 1: (1) formation of liquid metal- silicon alloy droplets on substrate; (2) dissolution and diffusion of gaseous silicon precursor into the alloy droplets; and (3) silicon precipitation and axial crystal growth due to super-saturation and nucleation at the liquid/solid interface.

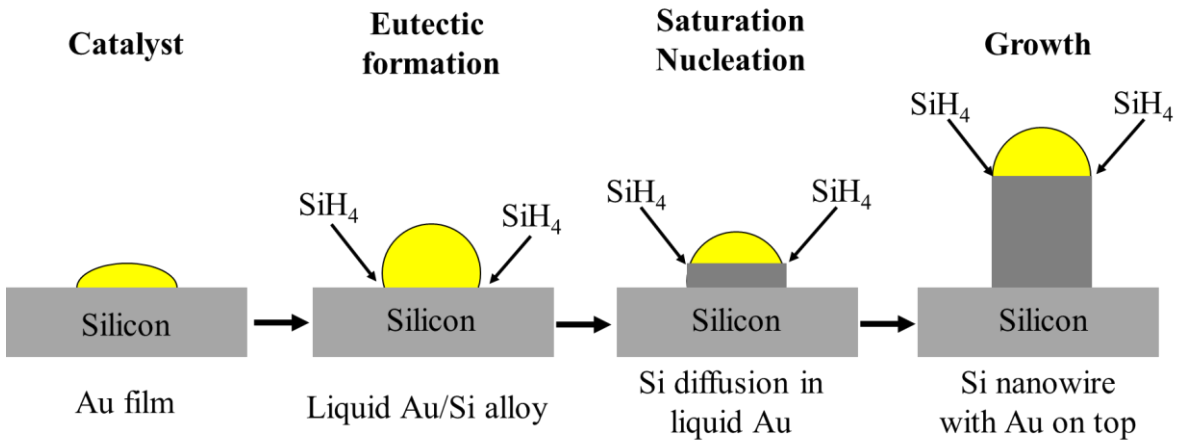

Figure 1: Schematic of silicon nanowires growth steps using VLS method via CVD method.

In case of top-down approach, the most attractive method is the metal-catalyzed electrodeless etching (MCEE), recently called metal-asssited chemical etching process (MACE) developed by Ohmi *et al.* and upgraded by Bohn *and co.* [18,19]. MACE is a simple and low-cost method for fabricating silicon nanowires with the ability to control diameter, length and cross-sectional shape. Furthermore, all procedures could be accomplished in a chemical laboratory without expensive equipment. In MACE, a silicon substrate is partly covered by a noble metal (e.g. Au, Pt) and put in an etching solution composed of fluorhydric acid (HF) and an oxidative agent generally hydrogen peroxide (H_2O_2). The silicon under the noble metal is etched faster than the silicon without noble metal coverage, so the noble metals sinks into the silicon substrate, generating pores forming nanowires. In fact, the etching rate of silicon in an etching solution without metal is as low as 0.2-0.6 nm/min against 1.5 µm/min when a metal is used as catalyst [20,21]. For the mechanism, this is well-accepted that the chemical reaction occurs preferentially near the noble metal, various possible electrochemical reactions have been proposed to describe the MACE process.

The oxidant, H_2O_2, is reduced at the metal via a cathode reaction (Equation 1):

$$H_2O_{2(l)} + 2H^+ \rightarrow 2H_2O_{(l)} + 2h^+ \quad (1)$$

In addition to Equation 1, a reduction of protons into hydrogen via another cathode reaction was proposed by Harade *et al*. [22] (Equation 2):

$$2H^+ \rightarrow H_{2(g)} \uparrow + 2h^+ \quad (2)$$

At the anode, the silicon substrate is oxidized and dissolved, various models exist for this dissolution process (anode reaction). These models could be classified in three main groups (RI, RII and RIII):

(RI) Direct dissolution of silicon in tetravalent state (Equation 3 & 4)

$$Si_{(s)} + 4h^+ + 4HF_{(l)} \rightarrow SiF_{4(g)} + 4H^{++} \quad (3)$$

$$SiF_{4(g)} + 2HF_{(l)} \rightarrow H_2SiF_{6(s)} \quad (4)$$

(RII) Direct dissolution of silicon in divalent state (Equation 5)

$$Si_{(s)} + 4HF_2^-{}_{(l)} \rightarrow SiF_6^-{}_{(l)} + 2HF_{(l)} + H_{2(g)} \uparrow + 2e^- \quad (5)$$

(RIII) silicon oxide formation followed by dissolution of oxide (Equation 6 & 7)

$$Si_{(s)} + 2H_2O_{(l)} \rightarrow SiO_{2(s)} + 4H^+ + 4e^- \quad (6)$$

$$SiO_{2(s)} + 6HF_{(l)} \rightarrow H_2SiF_{6(l)} + 2H_2O_{(l)} \quad (7)$$

However, due to the difficulty of *in-situ* exploration for the surface state, this is impossible to predict a more favourable model to describe the mechanism, so Chartier *et al.* proposed a well-accepted mixed reaction for the dissolution of silicon in MACE (Equation 8) [19]:

$$Si_{(s)} + 6HF_{(l)} + nH^+ \rightarrow H_2SiF_{6(l)} + nh^+ + (4\text{-}n/2)\, H_{2(g)} \uparrow \quad (8)$$

And the overall reaction is (Equation 9):

$$Si_{(s)} + n/2\, H_2O_{2(l)} + 6HF_{(l)} \rightarrow nH_2O_{(l)} + H_2SiF_{6(l)} + (4\text{-}n/2)\, H_{2(g)} \uparrow \quad (9)$$

Furthermore in order, to totally understand MACE process mechanism, charge transfer has to be considered for the oxidation and dissolution of silicon. In fact, the noble metal acts as a microscopic cathode on which the reduction of the oxidant occurs (cathode reaction). The generated holes are then injected into the silicon substrate in contact with the noble metal. So, the silicon atoms under the noble metal are oxidized due to the hole injection and dissolved by HF (anode reaction).

Based on the most accepted mechanism for the MACE process, all steps are described on Figure 2: (1) The oxidant is reduced at the surface of the noble metal due to the catalytic activity of the noble metal on the reduction of the oxidant. (2) The holes generated via the reduction of the oxidant diffuse through the noble metal and are injected into the silicon that is in contact with the noble metal. (3) The silicon is oxidized by the injected holes and dissolved at the Si/metal interface by HF. The reactant (HF) and the by-products diffuse along the interface between the Si and the noble metal. (4) The concentration of holes has its maximum at the Si/metal interface. Therefore, the Si that is in contact with the metal is etched much faster by HF than a bare Si surface without metal coverage would be. (5) The holes diffuse from the Si under the noble metal to off-metal areas or to the wall of the pore if the rate of hole consumption at the Si/metal interface is smaller than the rate of hole injection. Accordingly, the off-metal

areas or sidewalls of the pore may be etched and form microporous silicon, analogous to the case of electrochemical or stain etching.

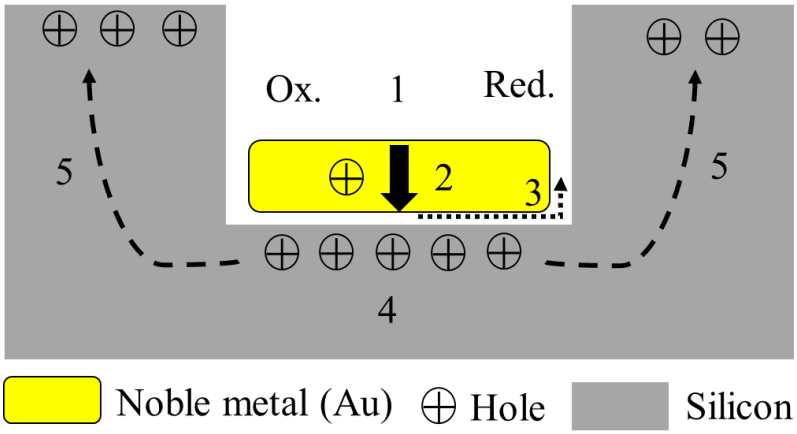

Figure 2: Schematic of the metal-assisted chemical etch process via noble metal and HF/H_2O_2 bath

MACE process was applied to silicon substrates described in Table 1 - Chapter 3 and various parameters such as noble metal nature and concentration, etching time and HF/oxidant ratio were studied in order to obtain silicon nanowires for all silicon substrates with different doping concentration. In fact, despite MACE is well-known in literature, a lot of experimental conditions are possible to obtain silicon nanowires, each laboratories using their own method/condition making it difficult to implement directly [19,23–28]. For more visibility, all results shown in the next parts were done on the same silicon substrate (Si σ=0.7 S/cm), except for the study of intrinsic properties of silicon. Experimental procedures are described in **Appendix II**.

2. Optimization of MACE procedure

2.1 Influence of noble metal and deposition method

In this study, two noble metals, gold (Au) and silver (Ag) were studied, as well as the deposition method. They could be deposited on the silicon substrate via different methods, such as spin-coating of particles, sputtering, electron beam evaporation, electrodeless deposition or thermal evaporation. The two last deposition methods, electrodeless deposition and thermal evaporation, were studied. First, electrodeless deposition methodology with nanoparticles of $AgNO_3$ and $HAuCl_4$ was used. The specific type of noble metal does not have an impact on the final morphology, in both cases silicon nanowires patterns are visible (Figure 3a &3b). These

results mean that the catalytic activity of the noble metal, in case of Au and Ag nanoparticles, does not have an influence on the etching rate and so on resulting nanostructures.

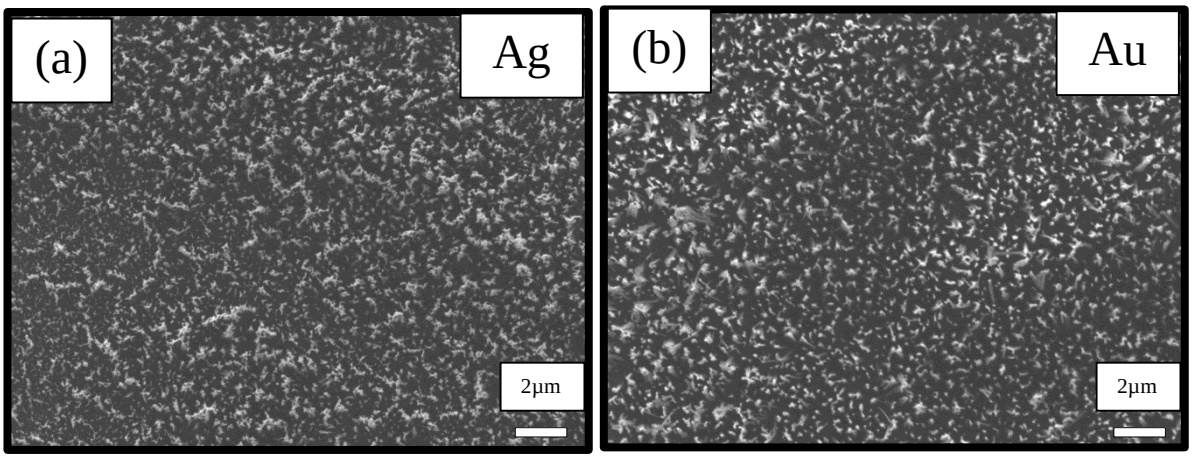

Figure 3: SEM images of Silicon wafers subjected to MACE with (a) silver particles and (b) gold particles

Then metal, Ag and Au, was deposited by thermal evaporation, a physical deposition method in vaccum (PVD), different metal thickness was tested and results are presented Figure 4. In both cases, thickness has an influence on the final silicon nano-structuration, but depending on the metal type, the final nano-structure is different. A layer of Ag film with a nominal thickness of 5 nm led to porous structure, and by increasing this nominal thickness, the pore size increases to form silicon nanowires at 20 nm of Ag thickness (Figure 4a, c, e). For a layer of Au film, the same behaviour is observed for 5 and 10 nm but when the thickness increases to 20 nm, pores are bigger but they do not form silicon nanowires (Figure 4b, d, f). So the morphology of the Ag or Au deposited by thermal evaporation depends on its nominal thickness, it varies with an increase in nominal thickness from isolated particles to continuous metal film. So the different morphologies of structures from the etching with metals can be attributed to the different shapes of distances, and packing manners of the metal particles.

For the rest of the study, despite thermal evaporation allows a more easily morphology control of the noble metal film, electrodeless deposition was preferred due to its simplicity and speed to depose noble metal. Finally, Ag nanoparticles was chosen over Au nanoparticles because they were cheaper and more easily available in the laboratory.

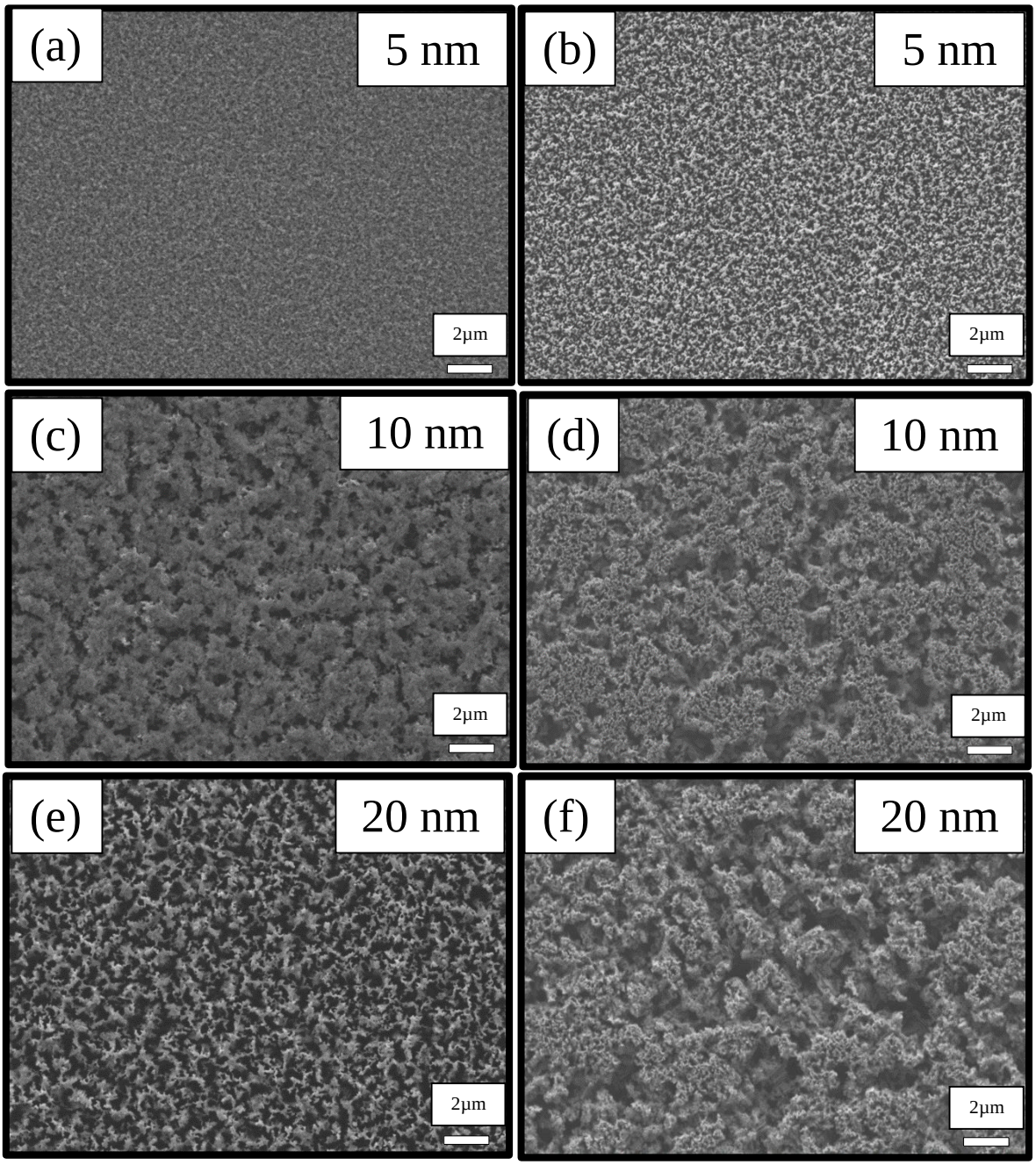

Figure 4: SEM images of Silicon wafers subjected to MACE with different noble metal thickness. (a), (c) and (e) are silver particles and (b), (d) and (f) are gold particles for 5,, 10 and 20 nm respectively.

2.2 Influence of silver nanoparticles concentration and etching time

The impact of silver nanoparticles concentration ($AgNO_3$) as well as the etching time in this solution were studied. The results shown Figure 5 are nanostructures which were formed on the silver deposited Si samples after etching in aqueous solution containing 5 M HF and 30 wt% H_2O_2 (10:1) in 30 mn at room temperature (more details in **Appendix II**). The concentration of

$AgNO_3$ in the silver deposition step strongly affects the morphology of the resulting film. Because Ag does not wet well on the Si surface, islands of Ag are deposited, and by controlling the $AgNO_3$ solution concentration and immersion time, these islands form "nanoparticles" [29]. First, when the concentration of $AgNO_3$ is less than 0.02M, the silicon nanowires arrays are not formed (Figure 5a and Figure 5b). This phenomenon is due to the formation mechanisms of silicon nanostructures in the etching solution (HF/H_2O_2) after silver deposition step [30]. The SiO_2 or Si underneath the Ag particles is etched away by HF directly, and the Ag particles enter the pits as they are forming. So, when the Ag particles are small (at low concentration), their lift-off and Brownian movement may occur during silicon dissolution, resulting in more disordered silicon nanostructures. The $AgNO_3$ concentration 0.02 and 0.05 M are appropriate for creating the vertical aligned SiNWs arrays (Figure 5c and Figure 5d). Nevertheless, when particles concentration increases, the density of nanowires decreases. The reason of this difference in density is due to a size increase of silver clusters with the concentration on the surface of silicon. So the size of the areas not covered with silver decreased, and because the Ag-coated regions of silicon etches faster, SiNWs density decreased.

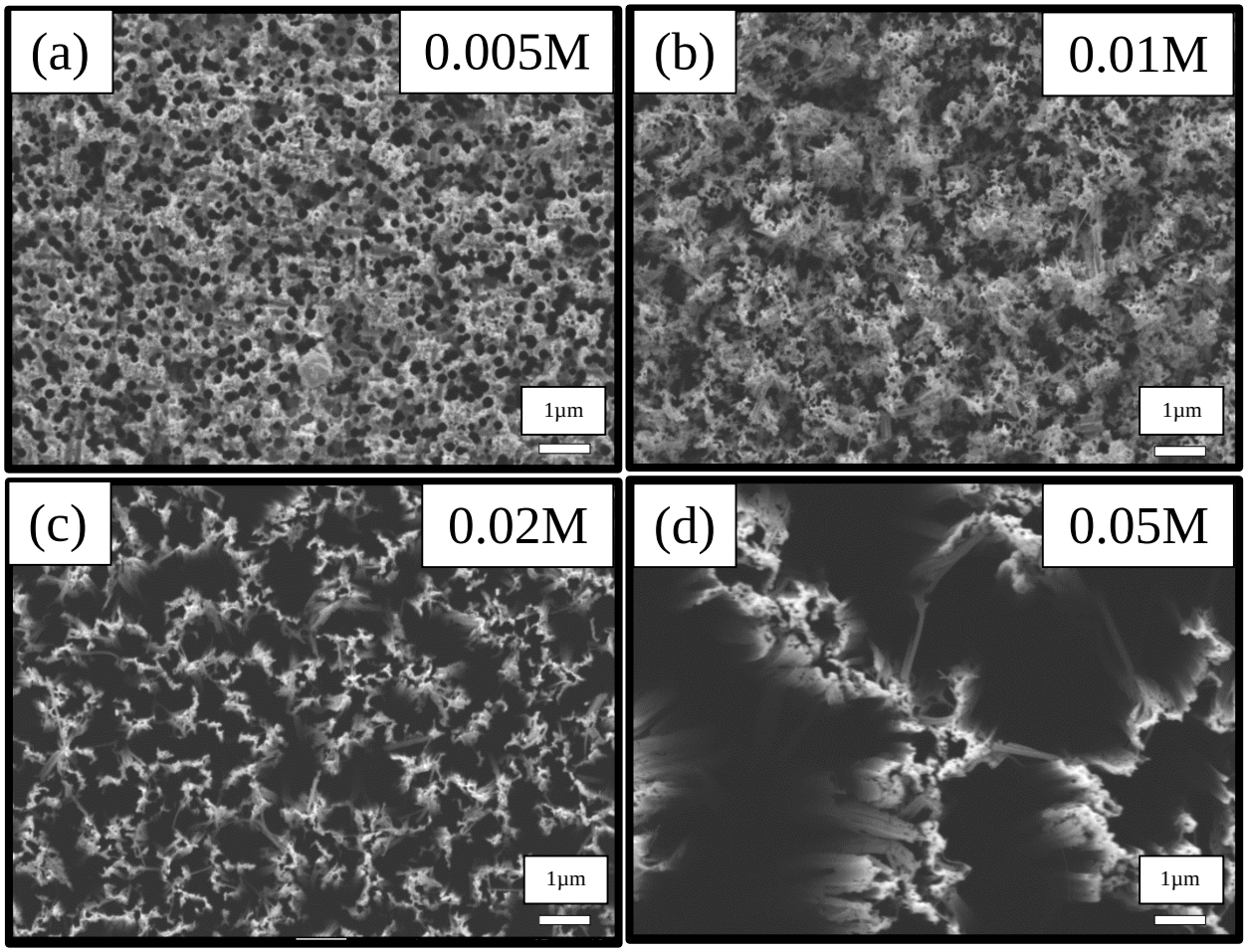

Figure 57: SEM images of silicon nanostructures fabricated with (a) 0.005 M, (b) 0.01 M, (c) 0.02 M and (d) 0.05 M of $AgNO_3$ nanoparticles concentration.

Then the influence of time in $AgNO_3$ particles bath on silicon nanostructure was studied. The $AgNO_3$ concentration was fixed at 0.02 M based on previous results. The same trend as previously is followed for etching time under 2 mn, none silicon nanowires are formed (Figure 6a and Figure 6b). The reason is similar than for $AgNO_3$ concentration, the Ag lift-off and Brownian movement occur during silicon dissolution. Silicon nanowires are formed for 2 mn in the bath, but when the time is increased to 5 or 10 mn, no nanostructure are visible (Figure 6d and Figure 6e). One of the hypothesis could be that after a long time in silver bath, "umbrella structures" could be formed, reducing the number of silver nanoparticles achieving the silicon surface, and so reducing the SiNWs formation [31].

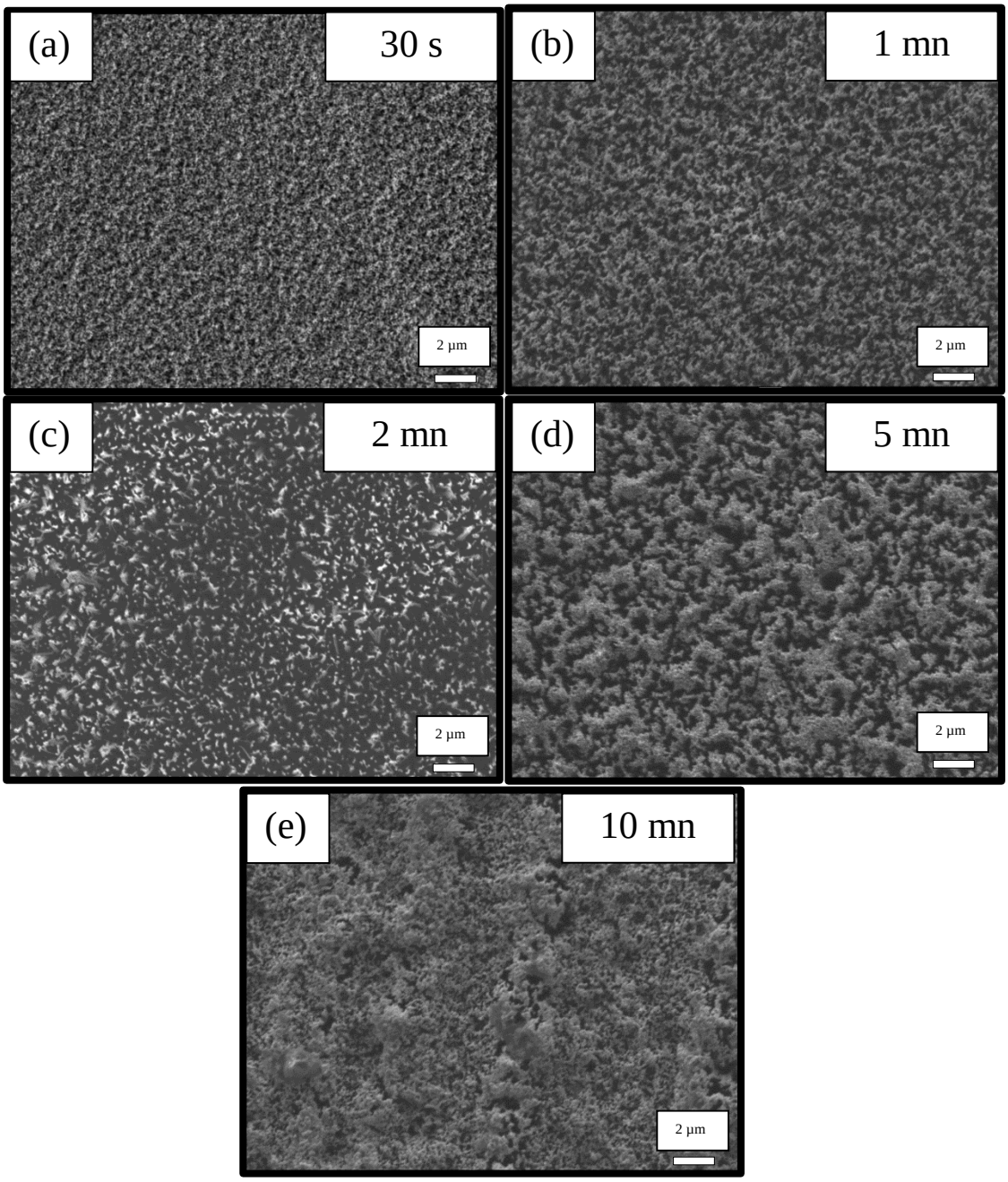

Figure 6: SEM images of silicon nanostructures fabricated with (a) 30 s, (b) 1 mn, (c) 2 mn, (d) 5 mn and (e) 10 mn of gold nanoparticles evaporation in PVD machine.

2.3 Influence of etching time in HF/H_2O_2 bath

In this part, the influence of immersion duration in HF/H_2O_2 bath was studied. The previous results obtained gave information on which noble metal have to be chosen, the concentration and immersion time in $AgNO_3$ bath. Experimental procedure details ae given in **Appendix II**. Because the influence of HF/H_2O_2 was well studied by the scientist community and HF/H_2O_2 volume ratio 10:1 is largely used in MACE procedure, it will be barely discussed here [29,31–34].

When the silicon substrates with Ag nanoparticles are immersed in etching solution (HF/H_2O_2), SiO_2 is continuously formed form the silicon in contact with Ag nanoparticles with H_2O_2 as hole donor and oxidant and dissolved by HF Equation 9). So, H_2O_2 was chosen as oxidant due to its low reduction potential versus standard hydrogen electrode (SHE) of 1.76 V compared to the reduction potential of Ag of -0.81 V versus SHE, favouring transfer of electron from Ag to H_2O_2. If the H_2O_2 concentration increases, the oxidation speed of the silicon around the Ag nanoparticles increases (more holes injected and so more oxidation occurs), resulting in the increase of the horizontal etching rate. But in case of high H_2O_2 concentration, the horizontal etching speed increases in a higher degree and overcomes the Ag nanoparticle gravity to shift its position, deviating from the vertical direction, a chaotic porous structure is obtained [33].

Naturally, the immersion time in the etching solution has a significate influence of SiNWs length as shown Figure 7a, 7b and 7c. The reason is simple, based on the Si etching mechanism, Si atoms under the silver clusters are oxidised due to the hole injection by H_2O_2 and dissolved by HF over the time. So, a longer immersion time of the substrate inside the etching solution will result in longer Si nanowires.

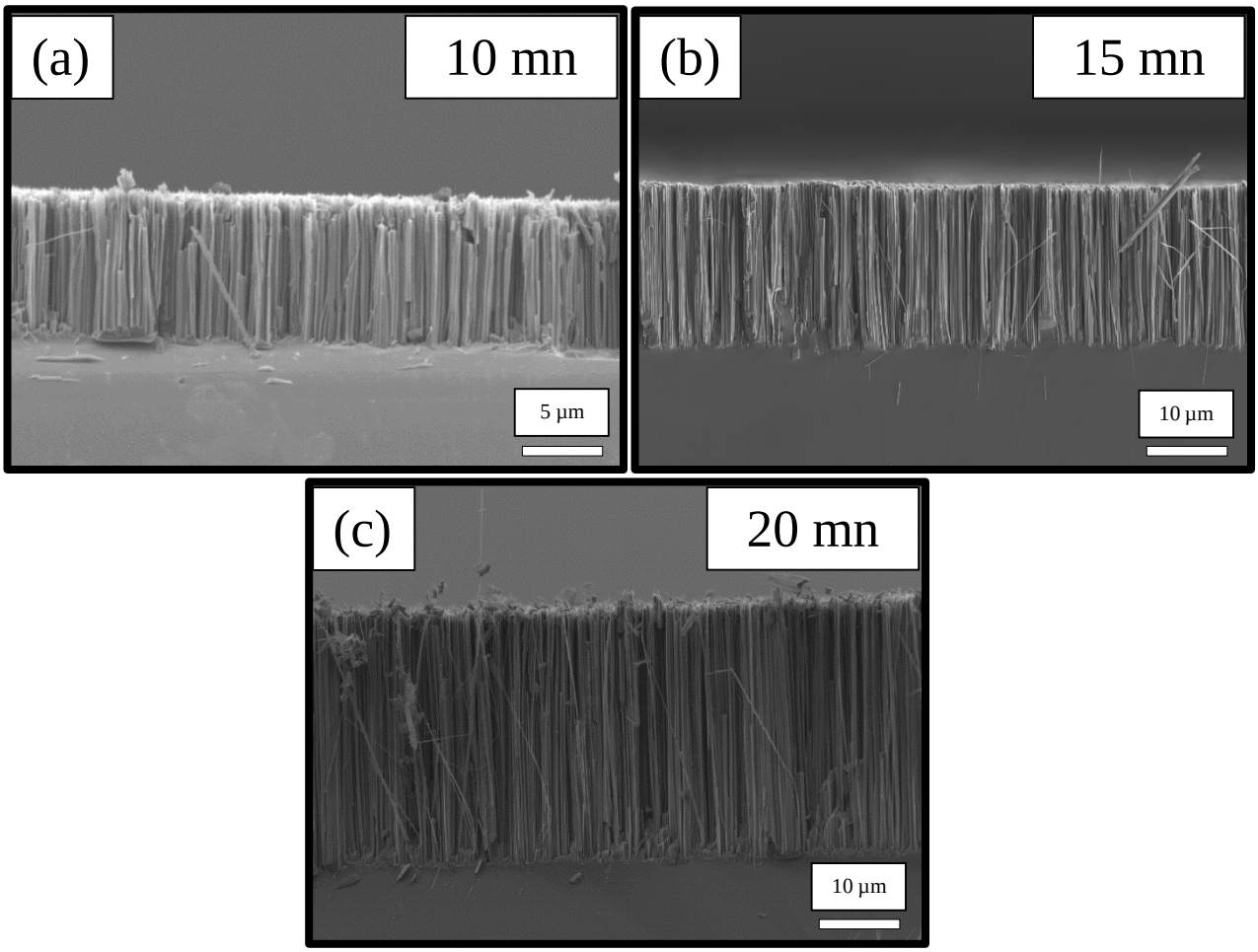

Figure 7: SEM images of silicon nanowires fabricated with (a) 10 mn, (b) 15 mn and (c) 20 mn immersion time in HF/H_2O_2 bath.

2.4 Influence of silicon intrinsic properties

Finally, when all other parameters were fixed (**Appendix II**), the intrinsic properties of silicon were studied. All results are presented Figure 8, with on the left side n-type doping silicon and p-type doping silicon on the right side. Based on these results nano-structure formation lightly depends on substrate-doping, resulting in nanowires. The reason for this behaviour could be justified by the introduction of the positive charge carriers (holes) necessary for the oxidation by the solution (H_2O_2) and not the impurities from the silicon [35]. Doping type of silicon has an influence in case of formation of mesoporous silicon nanowires, porosity rate changes with the doping type [36]. However, the doping concentration has an influence on silicon nanowires length, at a low doping concentration a deeper etching occurs (Figure 8a, 8b, 8c and 8d). Furthermore, the structure of highly doped SiNWs is different from the others, they are less structured and more porous (red circles on Figure 8g and 8h). In order to understand this

behaviour, various major mechanisms had been proposed, in all of them, a competition between vertical (SiNWs formation) and horizontal (Porosity in nanowires) etching occurs. First, dopants act as nucleation sites for pore formation (horizontal etching) during the etching of Si, so high dopant concentration will lead to more porous and structured SiNWs (hypothesis supported by Chiappini *et al*. [37]).

Hochbaum *et al.* proved that Si followed an electrochemical mechanism during MACE. So increasing the doping level of the Si results in a decrease of the energy barrier at Si/Ag^+ interface, because of the redox potential of Ag^+/Ag^0 lies below the valence band of Si. Furthermore, the insulating character of porous Si blocks the transport of holes through porous layer, instead they proceed by means of the Ag^+/Ag^0 redox pair diffusing through etched pores in Si accentuating the formation of pores [38].

On the other hand, Qu *et al.* proposed a mechanism linked with the dissolution and re-deposition of Ag [39]. Typically, Ag^+ ion cloud is crafted close of Ag particles because of the oxidation of Ag particles by H_2O_2. Ag^+ quickly reacts with the closest Si near Ag/Si interface and thus is recovered into Ag particles. So, etching is localized around Ag particles, but because Ag particles are "trapped in nano-pits created by themselves, vertical etching direction is preferred. Alongside, H_2O_2 blocks the recovering of Ag^+ into Ag nanoparticles and when the amount of out-diffusing Ag^+ ions reach a certain threshold, these Ag^+ ions may start to nucleate on the sidewall of previously formed Si near weak defective site (*e.g.*, dopants), forming new Si particles for new pathway, resulting in the pore generation. So highly doped Si will preferentially form porous silicon nanowires, with the horizontal etching faster than the vertical one, forming less long nanowires.

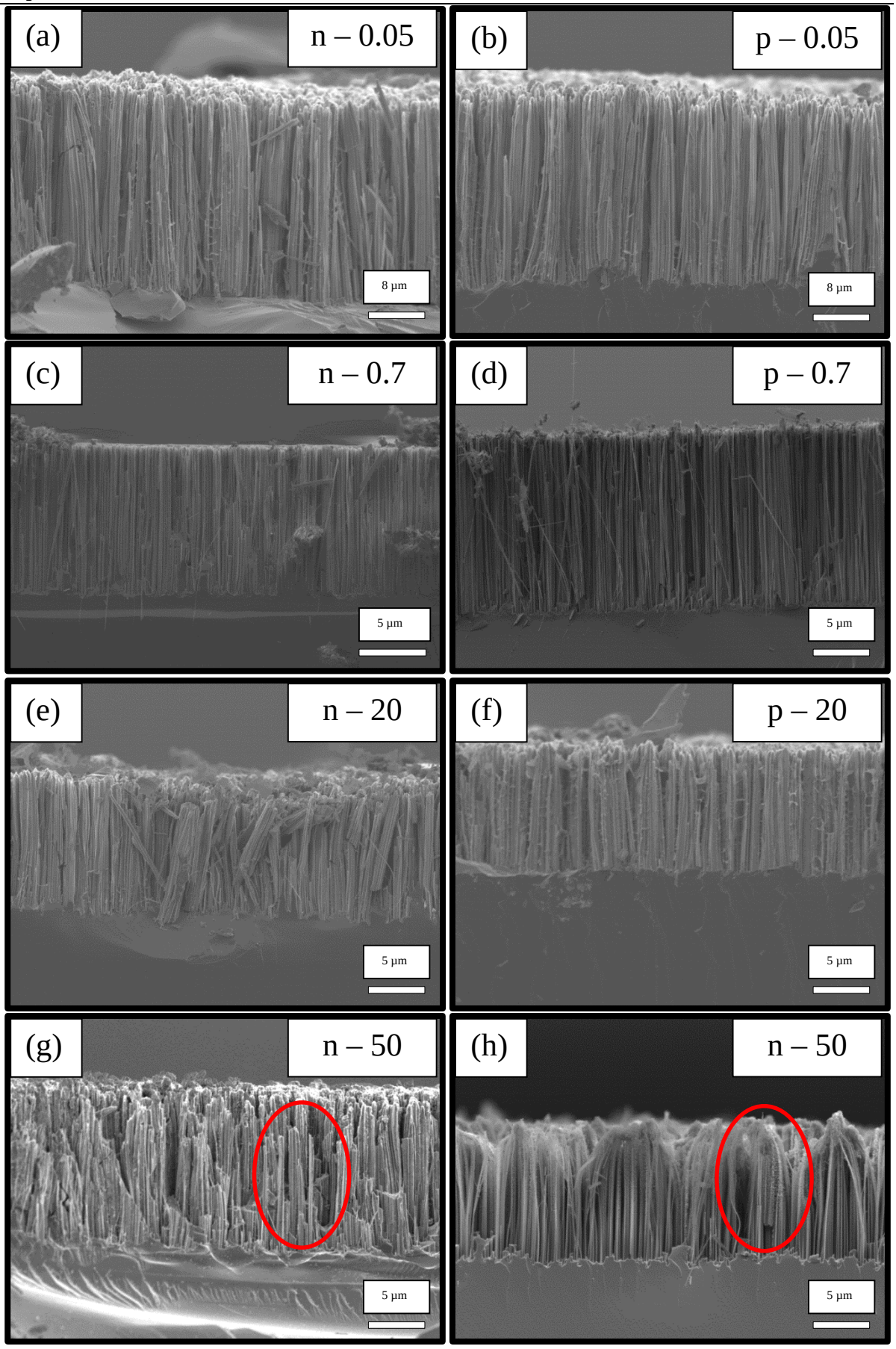

Figure 8: SEM images of silicon nanowires fabricated on (a)(b) 0.05 S/cm, (c)(d) 0.7 S/cm, (e)(f) 20 S/cm and (g)(h) 50 S/cm silicon wafers.
(a)(c)(e)(g) and (b)(d)(f)(h) are p- & n-type doping silicon, respectively.

2.5 Silicon nanowires and PEDOT:Tos hybrid material

Thanks to a fine tuning of experimental parameters, described previously, silicon nanowires were obtained for all-6 silicon substrates available in the laboratory. However, due to the high hazardous of hydrofluoric acid, the accessibility of silicon nanowire was difficult. The reproducibility of the process developed, was tested over the etching procedure of various samples and almost the same nano-structured silicon was obtained (more details in **Appendix II**). The presence of these structures was confirmed by SEM analysis of the on-top (Figure 9a), tilted (Figure 9b) and side view (Figure 9c) of etched samples.

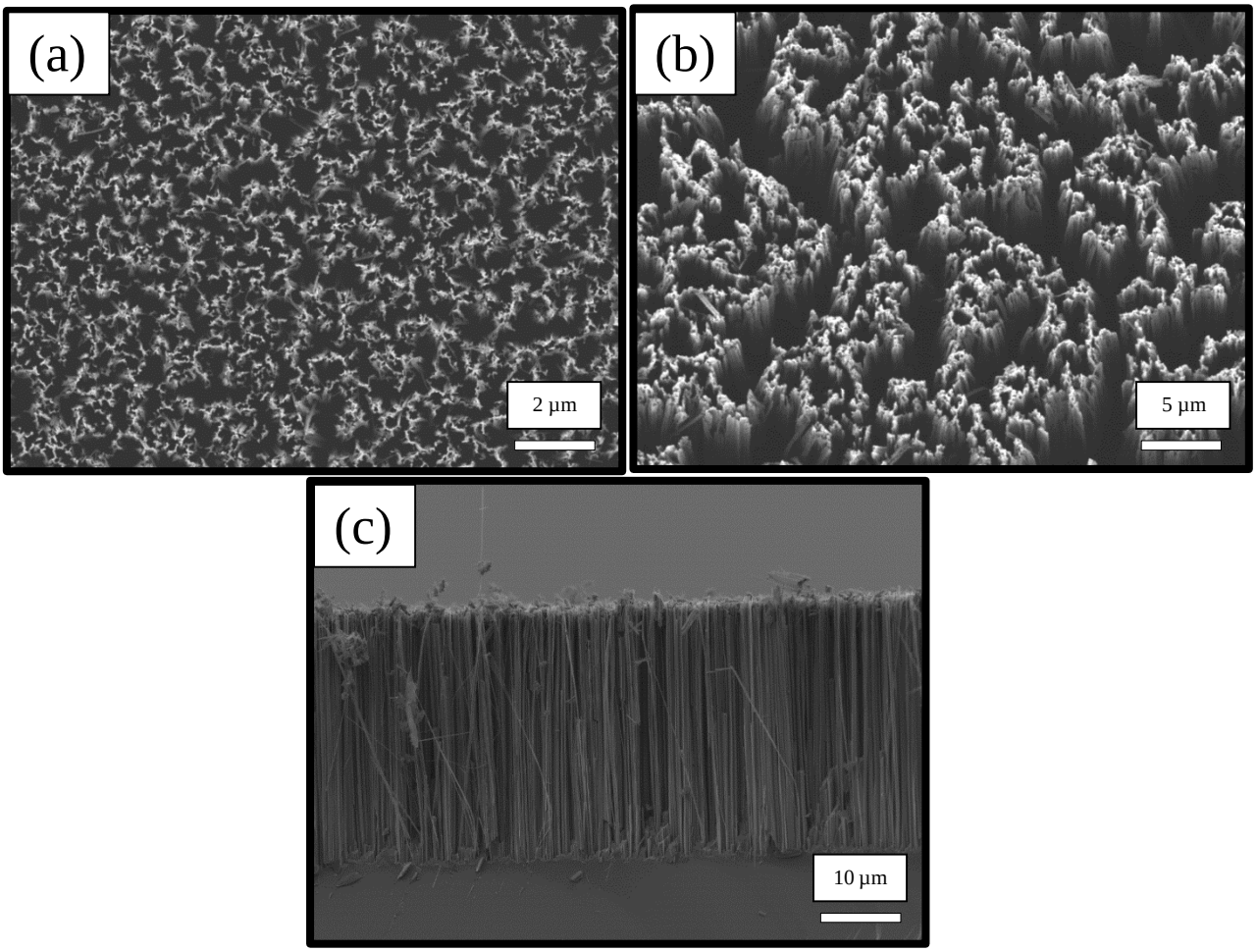

Figure 9: SEM images of silicon nanowires fabricated with optimized procedure. (a) Top view, (b) tilted view and (c) side view of the same silicon nanowires sample.

Then attempts to infiltrate polymer inside the silicon nanowires were performed. Based on results from Chapter 2 and 3, the most suitable candidate was PEDOT:Tos with DMSO and pyridine, exhibiting the best power factor on silicon substrate.

From an experimental point of view, this kind of packed nanostructures has a main drawback, a poor wettability. In fact, the top surface of the silicon nanowires is similar to the nanostructure observed for lotus leaf [40–42]. A so called Lotus effect, superhydophobicity should occur when PEDOT:Tos will be deposited on top of etched silicon substrate [41]. This phenomenon was observed during the spin-coating; none polymer was present at the end of the process. Nevertheless, the origin of this phenomenon could be attributed to an additional parameter as observed Adachi and Rusli groups [43,44]. In fact, the last treatment before the polymer deposition has an important role on the surface wettability. As explained more in details in **Appendix II**, silicon nanowires were post-treated by HF. This treatment tends to form more hydrophobic surface. The surface is therefore functionalized by Si-H termination. But when no post-treatment is made, the last bath of the etching process is a HNO_3:H_2O mixture. This "stain etching" role is to functionalize SiNWs by hydrophilic groups. In fact, the surface of SiNWs is partially oxidized by the HNO_3 solution according to the following Equation 10:

$$2x\ \mathrm{HNO_{3(l)}} + \mathrm{Si_{(s)}} \rightarrow\ \mathrm{SiO_{x(s)}} +\ 2x\ \mathrm{NO_{2(g)}} + x\ \mathrm{H_2O_{(l)}} \qquad (10)$$

The surface is therefore functionalized by the following groups: Si-O-Si, Si=O, and Si-OH.

Experimental conditions were adapted in order to avoid wettability problems (**Appendix II**), and PEDOT:Tos were successfully deposited with this new methodology. In fact, in the last procedure step, SiNWs were treated with HF to remove the oxide layer. Unfortunately, this last step made the surface hydrophobic. So, in order to successfully deposited the PEDOT:Tos on top of SiNWs, this last step wasn't performed. Furthermore, the solution (monomer with oxidant) was let 30 s on-top the substrate before spin-coating. SEM images confirmed the well deposition of PEDOT:Tos between and on-top of the SiNWs Figure 10).

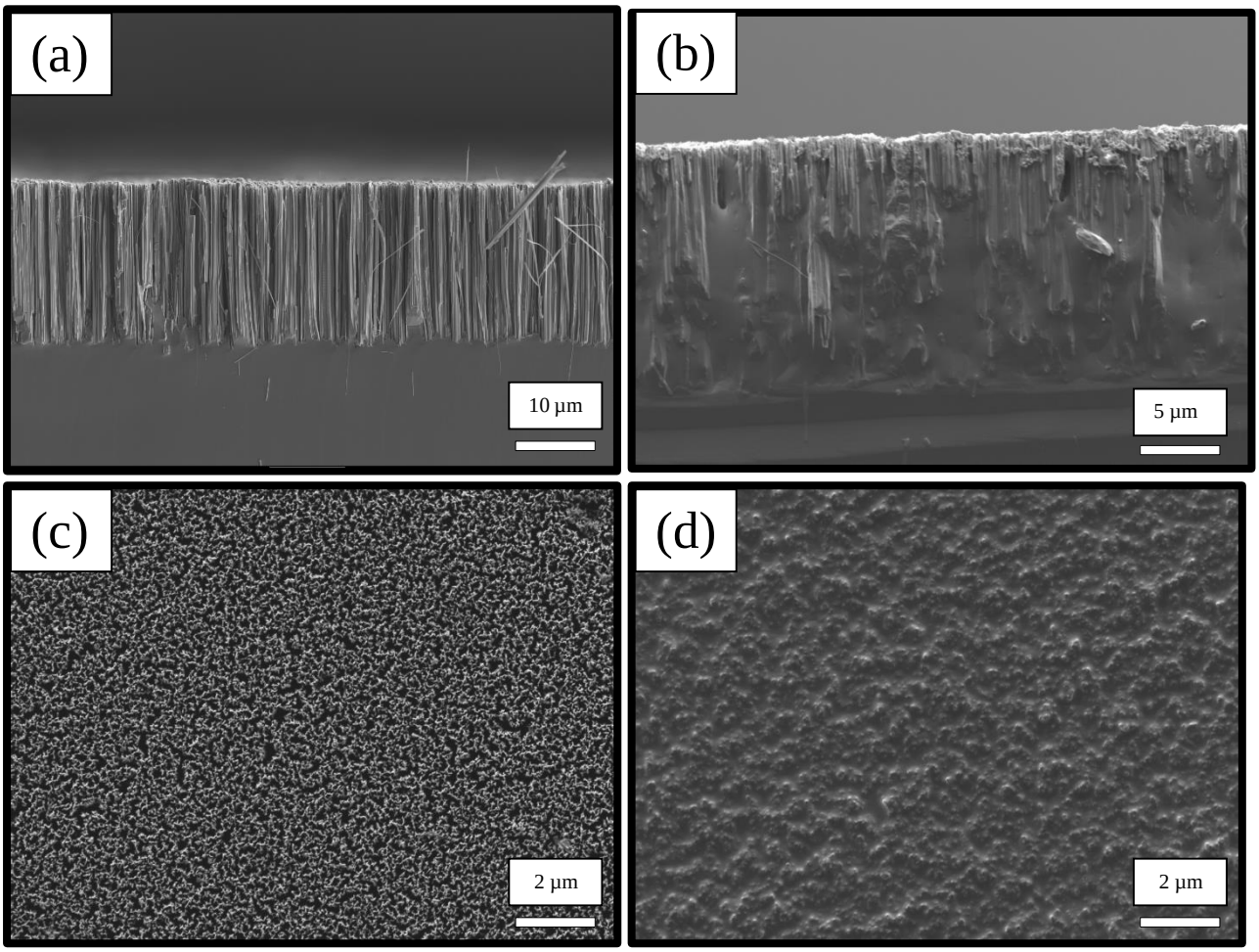

Figure 10: SEM images of bare silicon nanowires and with PEDOT:Tos on top.
(a) Side view and (c) Top view of bare silicon nanowires. (b) Side view and (d) Top view of PEDOT:Tos on silicon nanowires.

Then, PEDOT:Tos layers were stacked on top of various silicon with different conductivities, and their Seebeck coefficient, electrical conductivity and power factor were measured in agreement with results of Chapter 3 (Figure 11). All procedures are presented in **Appendix II**.

The same behaviour as previously presented in Chapter 3 for hybrid PEDOT:Tos-silicon devices is clearly visible. In Figure 11a, the Seebeck coefficient decreases rapidly to reach a plateau value for low conductive silicon (0.05 and 0.7 S/cm). In case of silicon with high conductivity (20 and 50 S/cm), Seebeck coefficient decreases more slowly when the polymer thickness increases. The same absolute Seebeck coefficient values are obtained for p- & n-type substrates with polymer on top.

In case of electrical conductivity, the doping type (positive in red and negative in blue) does not have a high effect on values regarding the experimental standard deviation (Figure 11b). But, depending on the Si substrates conductivities, the electrical conductivity values are

different. Principally, an increase of polymer thickness induces an increase of the electrical conductivity until the five PEDOT:Tos layer then a plateau is achieved. Low conductivity values are obtained for the Silicon with low conductivity and high values for high conductive Silicon with a maximum at seven layers of PEDOT:Tos. These results are similar to bare silicon with PEDOT:Tos (Chapter 3).

Finally, power factor followed the same trend than bare silicon with PEDOT:Tos (Figure 11c). When PEDOT:Tos is coated on low conductive Silicon (0.05 and 0.7 S/cm) substrates, the power factor of the hybrid devices decreases with the number of layers. This tendency is due to the negative impact of PEDOT:Tos thickness on Seebeck coefficient of Silicon with low conductivity. When Silicon substrate at 20 S/cm is used, the power factor is stable, the increase of electrical conductivity compensates the decrease of Seebeck coefficient when the PEDOT:Tos thickness increases. Finally, for high conductive Silicon (50 S/cm), the power factor increases with the number of PEDOT:Tos' layer and achieves a plateau for six layers, with a maximum at five layers.

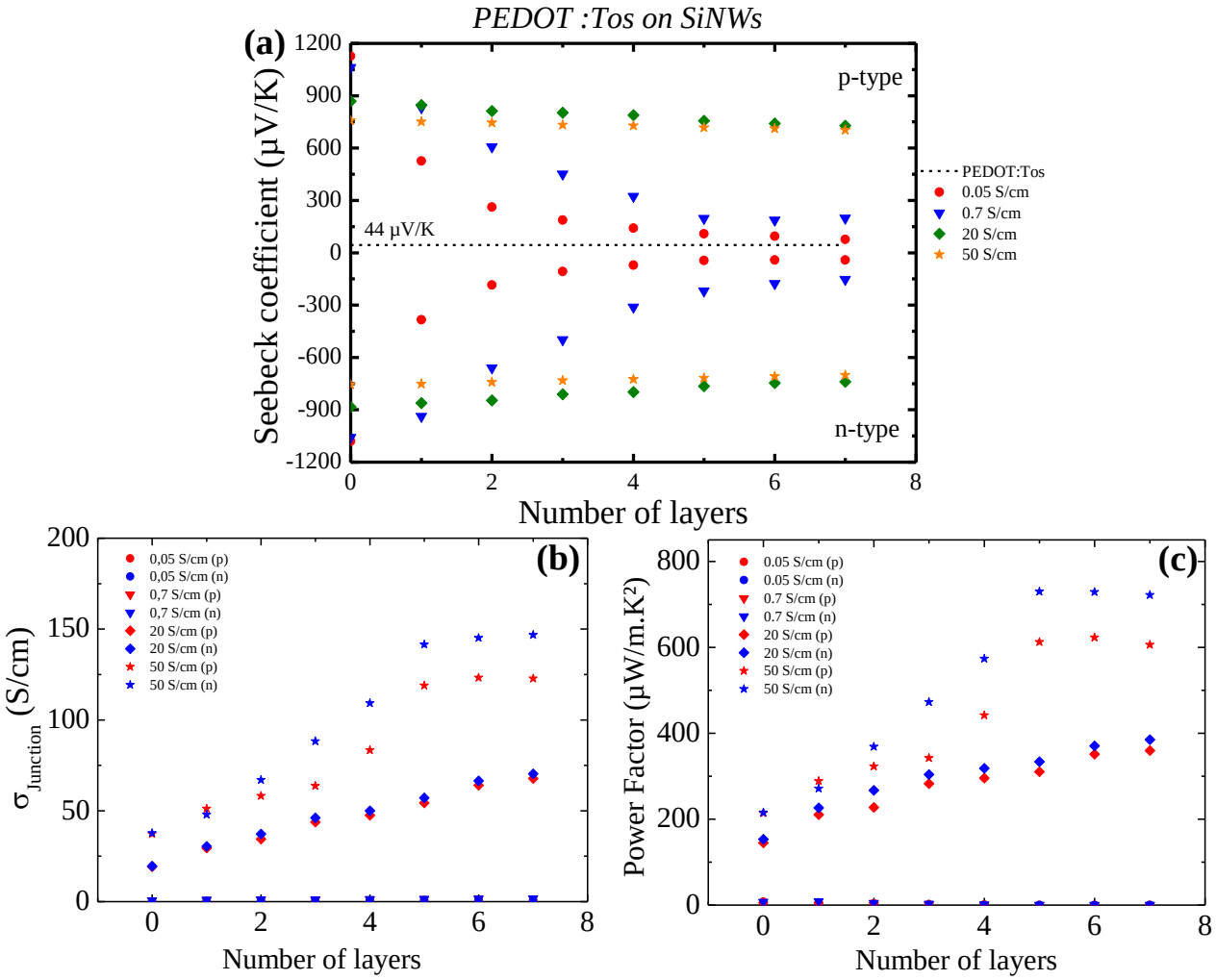

Figure 11: (a) Seebeck coefficient, (b) Electrical conductivity and (c) Power factor plotted versus number of PEDOT:Tos layer on SiNWs.
Blue symbols are for n-type silicon and red symbols are for p-type silicon.

PEDOT:Tos stacking on SiNWs products the same behaviour than PEDOT:Tos on bare silicon. In order to see if the nano-structuration of silicon had an effect on thermoelectric properties, Figure 12 reports a comparison between these two cases. A ratio between thermoelectric properties (S, σ, and PF) of hybrid material previously described with bare silicon and SiNWs were done. Full, empty, and half-full symbols represent the Seebeck coefficient, the electrical conductivity and the power factor ratio between bare silicon and SiNWs, respectively. Finally, the dashed-line correspond to unchanged thermoelectric properties.

Etching silicon surface into SiNWs has an important effect on the Seebeck coefficient and the electrical conductivity (Figure 12a). On average, Seebeck coefficient of SiNWs is 5-10% higher than Seebeck coefficient of bare silicon. However, the electrical conductivity decreased by also 5-10 % on average. But, because the contribution of Seebeck coefficient is square, the power factor increased by a 10-20% factor in case of SiNWs (Figure 12b). The enhancement of thermoelectric parameters could be due to the reduction in dimensionality on silicon. This phenomenon was pointed out by pioneers' group like Dresselhaus and co-workers [45–48], the Seebeck coefficient increases in monodimensional (nanowires) and/or bidimensional structures. In fact, the Seebeck coefficient strongly depends on the distribution in energy of charge carriers, and in particular it increases when the average difference between the carriers' energy and the Fermi energy increases. In low dimensional systems, the DoS is reshape with respect to bulk systems, in such a way that charge carriers are spread to higher energies. So, an increase in both S and σ should occur. However, as explained by Pennelli *and al*., structures must have a size of few nanometers to obtain a noticeable increase of the Seebeck coefficient with respect to its bulk value [46], which is the case in this study. Moreover, the electrical conductivity is strongly reduced by the surface scattering of charge carriers, directly confirmed by results in Figure 12b.

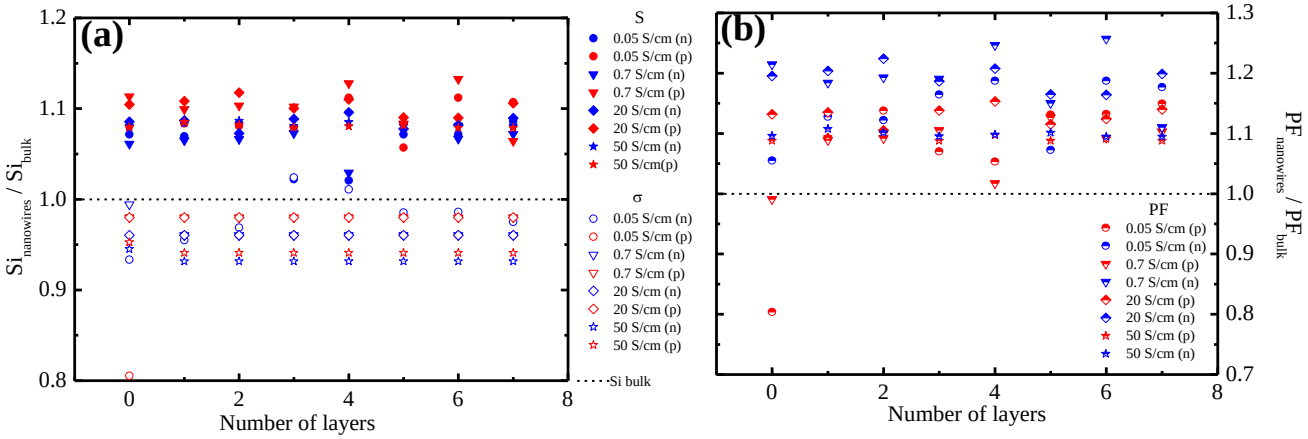

Figure 12: Comparison between (a) thermoelectric properties and (b) power of factor for bare silicon and SiNWs with different PEDOT:Tos thickness on top.
Full and empty symbols are for Seebeck coefficient and electrical conductivity, respectively.
Blue symbols are for n-type silicon and red symbols are for p-type silicon.

To conclude, SiNWs coupled with PEDOT:Tos results in a better thermoelectric properties compare to the bare silicon with PEDOT:Tos. A maximum increase of 20% of the power factor was observed. Unfortunately, the mechanism behind this enhancement was not confirmed by other analysis. The model developed in Chapter 3 isn't enough complex to describ well this new "architecture". Nakamura developed an atomistic model to predict Seebeck coefficient value of silicon nanowires on basis of first-principles calculation [49]. He proved fundamental effect of change in DoS by dimensional reduction to SiNWs, enhancing the thermoelectric performances. Finally, this is worth to note that the interface between the silicon and the polymer plays an important role in this hybrid devices.

B Porous silicon

Porous silicon (pSi) is a different form of nanostructured silicon. In 1990s, pSi generated large interest thanks to its photoluminescence properties [50,51]. Research were mainly focused on the optoelectronic applications, until Canham and Arens-Fischer's group revealed an extremely low thermal conductivity for this nanostructure [51,52]. Depending on the fraction of pores, the thermal conductivity range could be from 0.89 to 0.1 W/mK at room temperature, three orders of magnitude lower than that of the bulk silicon [52]. This low thermal conductivity opened the possibility of pSi to thermoelectric applications. Grossman *and coll*. are among some groups who studied the potential of pSi as efficient thermoelectric material [53].They found comparable *ZT* values between pSi and SiNWs, and they underlined a few possible advantages over the SiNWs. From a manufacturing point of view, pSi is easier to obtain from bulk silicon. In addition, this is more straightforward to connect pSi to electrical conductors due to its bulk nature than an array of SiNWs.

In their report, Föll *et al.* reported various mechanism for the formation of pores. The pores size, length and type are really dependant of experimental conditions [54]. In addition, these physical parameters have also a huge influence on thermoelectric properties, as shown Martin-Palma *et al.* in their recent study [55].

In this report, the pSi was obtained as a side-product during the formation of silicon nanowires. Experimental conditions for the pSi weren't studied in details, like in SiNWs case (All experimental conditions for pSi formation are described in **Appendix II**). Figure 13 shows the morphology and the size of pores on top of silicon substrate. Based on IUPAC standard [56], different pores categories could be distinguished by looking at the pore diameter and the distance between pores. In this case, macropores were obtained, geometries *i.e.* diameter and distance, are over 50 nm confirmed by SEM analysis of the on-top surface.

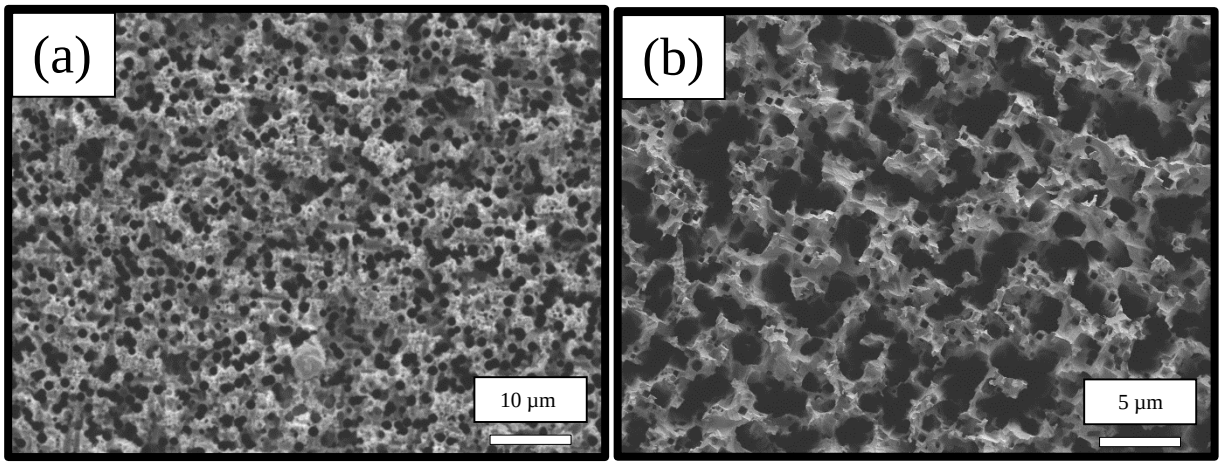

Figure 13: SEM images of porous silicon fabricated with optimized procedure.
(a) Top view and (b) magnified top view of the same porous sample.

Then attempts to deposit polymer on top of porous silicon were performed. As previously, PEDOT:Tos with DMSO and pyridine was chosen as a promising candidate. Unlike the silicon nanowires, no problem was encountered during polymer deposition. The pSi surface was perfectly wetted by the polymer solution.

So, PEDOT:Tos layers were stacked on top of various silicon with different conductivity, and their Seebeck coefficient, electrical conductivity and power factor were measured in agreement with results of Chapter 3 (Figure 14). All procedures are presented in **Appendix II**.

As previously presented for hybrid PEDOT:Tos on bare silicon and silicon nanowires, these is a clear behaviour. In Figure 14a, the Seebeck coefficient decreases rapidly to reach a plateau value for low conductive silicon (0.05 and 0.7 S/cm). The Seebeck coefficient for high conductive (20 and 50 S/cm) is almost stable with respect to increase of polymer thickness. The same absolute Seebeck coefficient values are obtained of p- & n-type substrates with polymer on top.

Electrical conductivity (Figure 14b) and power factor (Figure 14c) followed the same trend than PEDOT:Tos on bare and silicon nanowires. The doping type (positive in red and negative in blue) does not have a high effect on values regarding the experimental standard deviation. The Si substrates conductivity have an important influence on both properties. Generally speaking, an increase of polymer thickness induces an increase of electrical conductivity, and as explained for SiNWs an increase of power factor. The best results were obtained in case of high conductive silicon substrates.

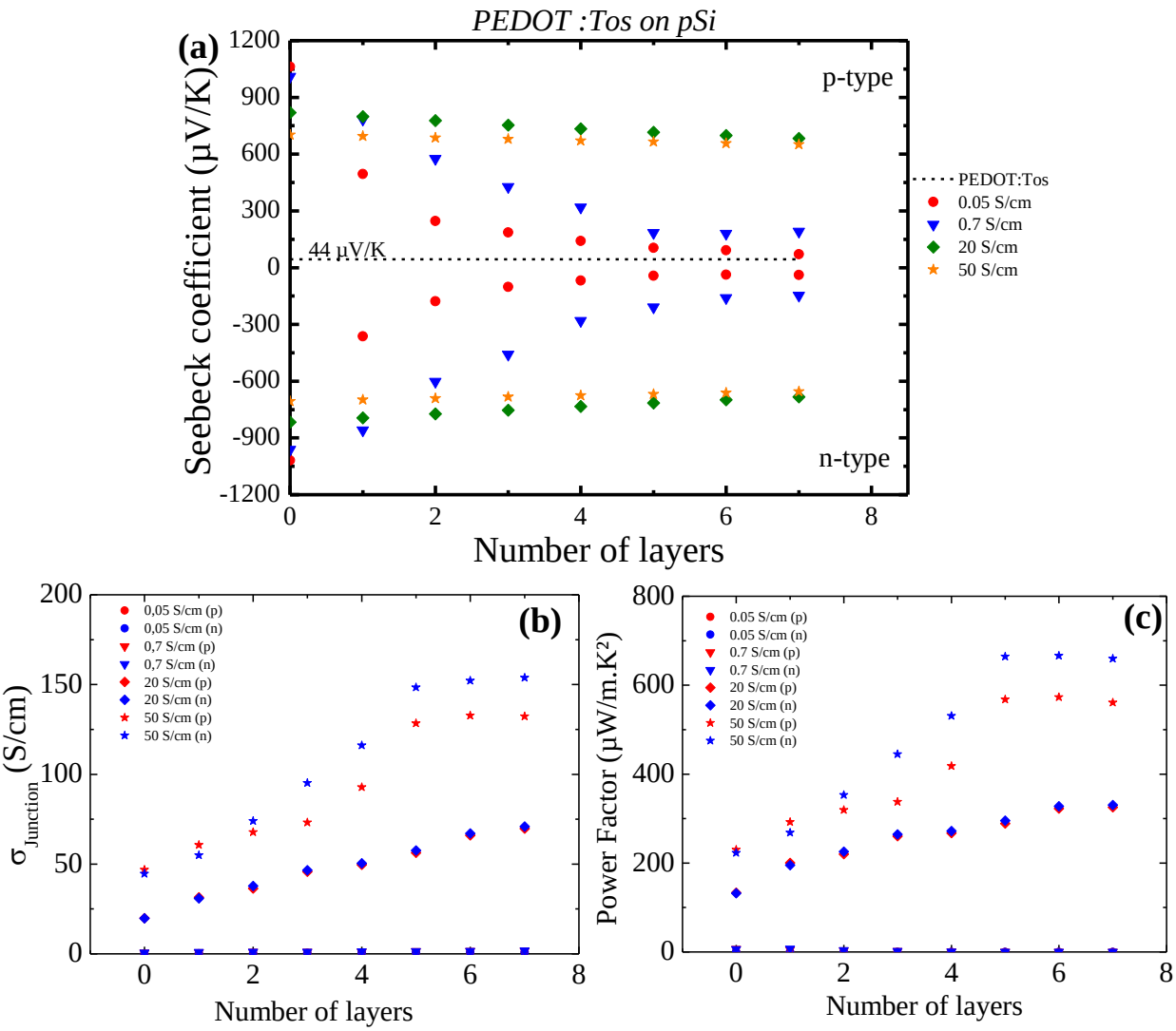

Figure 14: (a) Seebeck coefficient, (b) Electrical conductivity and (c) Power factor plotted versus number of PEDOT:Tos layer on pSi.
Blue symbols are for n-type silicon and red symbols are for p-type silicon.

PEDOT:Tos stacking on pSi products the same behaviour than PEDOT:Tos on bare silicon and SiNWs. Figure 15 shows a comparison between bare and porous silicon substrates covered by PEDOT:Tos. A ratio between thermoelectric properties (S, σ, and PF) of hybrid material previously described with bare silicon and pSi were done. Full, empty, and half-full symbols represent the Seebeck coefficient, the electrical conductivity and the power factor ratio between bare silicon and pSi, respectively. Finally, the dashed-line correspond to unchanged thermoelectric properties.

Generally speaking, pores have a lower influence on thermoelectric properties than nanowires. On average, Seebeck coefficient of pSi is <5% higher than Seebeck coefficient of bare silicon (5-10 % higher in case of SiNWs) (Figure 15a). The electrical conductivity decreased also by less than <5% on average (Figure 15a). This decrease is lower in pSi case

than SiNWs but the resulting power factor isn't higher in pSi than SiNWs (Figure 12b - 15b). The reason is the "squared" contribution of Seebeck coefficient in power factor formula.

The small enhancement of thermoelectric properties could also be due to the reduction in dimensionality on silicon, as previously described for SiNWs [45-48] (more details in SiNWs section). The decrease of electrical conductivity was due to the difficulty of transporting electron across the junctions between pores, directly confirmed by results in Figure 15b. This phenomenon was noticed in various studies on pSi [57–59].

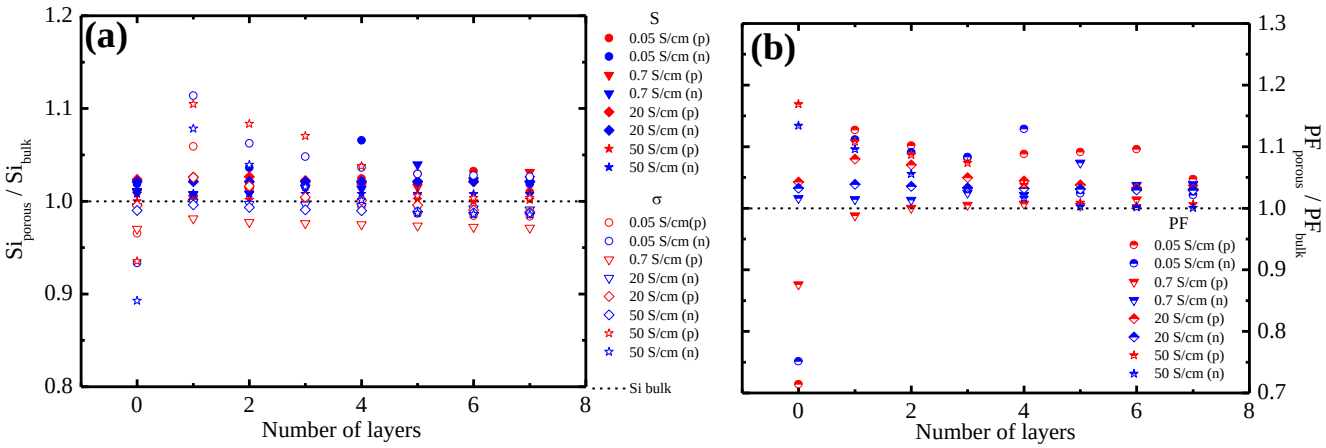

Figure 158: Comparison between (a) thermoelectric properties and (b) power of factor for bare silicon and pSi with different PEDOT:Tos thickness on top.
Full and empty symbols are for Seebeck coefficient and electrical conductivity, respectively.
Blue symbols are for n-type silicon and red symbols are for p-type silicon.

To conclude, pSi coupled with PEDOT:Tos results in a better thermoelectric properties compare to the bare silicon with PEDOT:Tos. A maximum increase of 10% of the power factor was observed. Unfortunately, the mechanism behind this enhancement was not confirmed by other analysis. On the other hand, these results were inferior to results obtained for SiNWs with PEDOT:Tos, confirming that the interface between the silicon and the polymer plays an important role in the hybrid devices. Finally, despite lower thermoelectric performances compare to SiNWs, pSi has the advantage to be tuned by filling the pores with appropriate materials, and so tune the electronic transport properties.

C Silicon pyramids

1. Theory and principle

Surface nano-structuration of crystalline silicon wafers is a process used in various fields. From optoelectronic industry [60] to biological applications [61], silicon wet etching has been studied and improved in order to address the specific requirements of technological fields challenges. Depending on the etchant or the crystalline orientation, isotropic or anisotropic etching could be achieved. Since decades, one of the most famous anisotropic wet etching is done with potassium hydroxide (KOH) [62]. The mechanism behind the etching process is described in the Equation 11 below:

$$Si_{(s)} + 4OH^-_{(l)} \rightarrow Si(OH)_{4(l)} + 4e^- \quad (11)$$

In case of <100> silicon, the nanostructure obtained is pyramid structure. The reason is due to a difference on the (100) and (111) directions since the etching rate on the (111) direction is lower than (100) direction [63,64]. For the (100) orientation, surface silicon atoms with two backbonds, connecting to two underlying silicon are present at the surface. The two dangling groups could make a nucleophilic reaction with OH radical, and so this injection of electrons will break these bonds and released a silicon-hydroxide complex (Figure 16a). In case of (111) orient plane, only one dangling bond is present for each surface silicon, thus making it harder to be etched when comparing with a (100) oriented plane (Figure 16b).

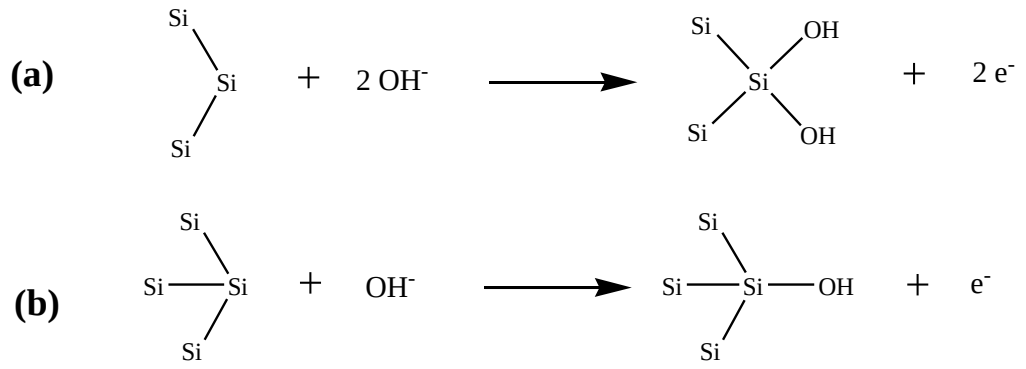

Figure 169: Etching mechanism of KOH for (a) (100) Silicon and (b) (111) Silicon substrates.

In addition, different chemicals could be used in order to interact and compete with OH radicals. Isopropyl alcohol (IPA) is the most used molecule to modulate the etching rate of specific crystallographic planes in KOH wet etching procedure. IPA acts as a mask, limiting the access of "KOH particles" to the surface of the silicon sample [65,66]. IPA slows down the reaction between the silicon surface and the hydroxide ions (OH^-) [67]. However, no chemical reaction seems to be formed between IPA and silicon atoms, thus acting as a mere modulation agent, rather than an etching stop agent [68].

The control of the pyramid shape in wet etching depends to a precise design of the etching conditions [69,70]. So, in this report, the influence of potassium hydroxide concentration, isopropyl alcohol concentration and duration time on texture of monocrystalline silicon wafers were studied and followed by SEM analysis. For more visibility, all results shown in the next parts were done on the same silicon substrate (Si σ=0.7 S/cm). Experimental procedures are described in **Appendix II**.

1.1 Influence of isopropyl alcohol concentration

In this study, the influence of IPA concentration on silicon surface, during anisotropic etching process, was studied and followed with SEM analysis. The results shown Figure 17 are nanostructures which were formed on the Si samples after 25min etching in aqueous solution containing 20wt% KOH with different concentrations of IPA (3, 5, 7 and 9 wt%) at 80°C (more details in **Appendix II**). As described in Equation 11, the silicon wet etching reaction comes from by-products, silicates. When these silicates aren't dispersed from the surface of the silicon, they act as pseudo-masks preventing the continuous etching and promoting a very rough and heterogeneous etching. Assuring a constant flow between these silicates and fresh OH radicals allows for a better control of the process, improving both smoothness and homogeneity across the sample. KOH wet etching was performed inside a large beaker with external temperature control under magnetic stirring. The magnetic stirring during the etching process increases the homogeneity, in fact by creating an internal spiral flow, silicates are diluted and a continuous OH radical could access to the silicon substrate. Then the temperature was set at 80 °C to give energy to the system to accelerate the etching process.

As shown in Figure 17, IPA concentration has an important influence on number and morphology of pyramids on top of treated silicon surface. From 3 to 7 wt%, the pyramids completely cover the entire surface, only the size of pyramids changed. At 9 wt%, this is clearly visible that the surface isn't totally covered by pyramids. In fact, the density of the formed

pyramids is limited by the etching reaction rate. At high reactions rates, the density of pyramids covering the surface is reduced, and lead to the breaking of the hydrogen bonding network by the collected alcohol. So, silicates and isopropyl alcohol formed a near surface layer that hinders the formation of any more pyramids [71]. A concentration of 5 wt% of IPA was chosen for the rest of this study, offering a perfect balance between surface covering and pyramids size.

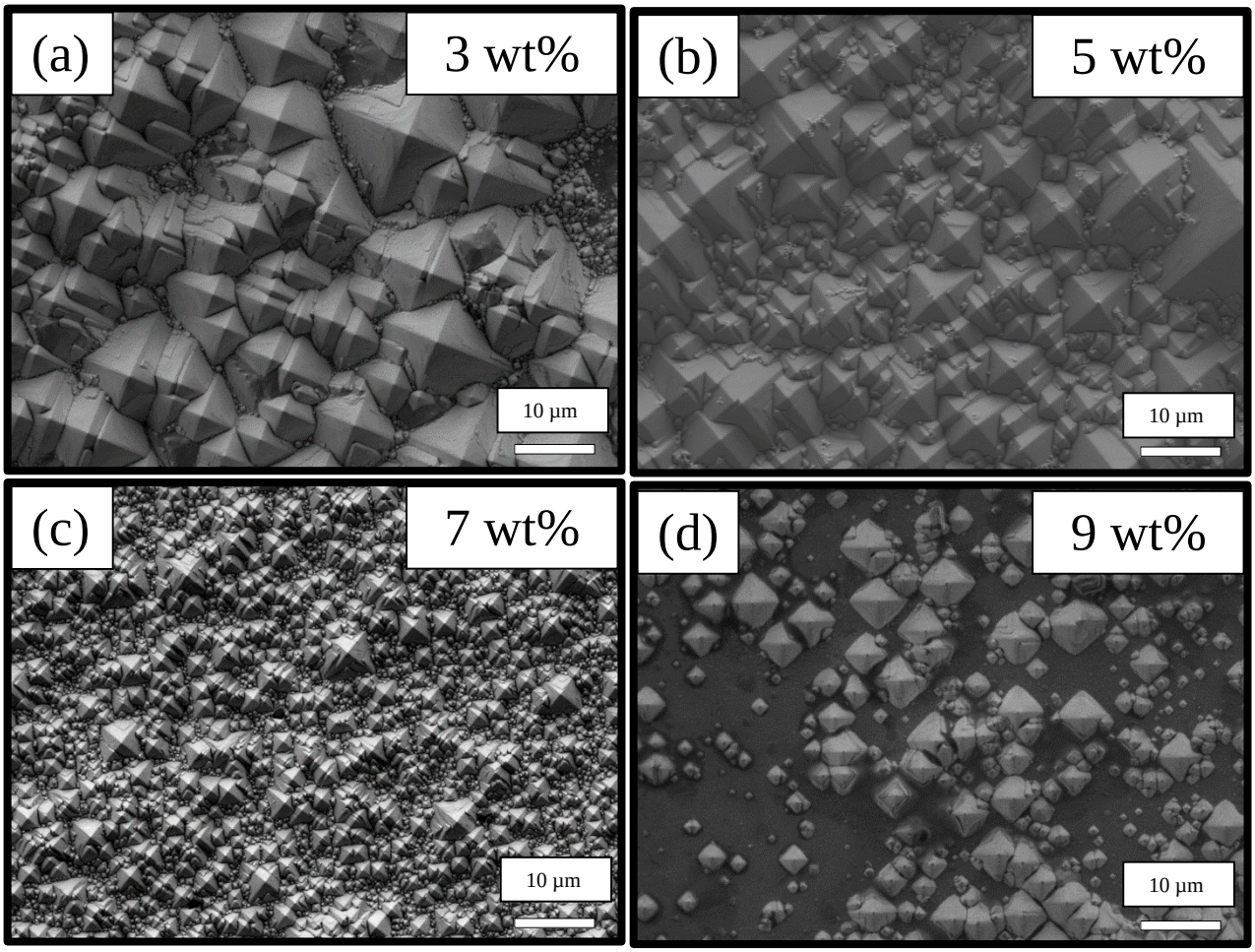

Figure 17: SEM images of silicon nanostructures fabricated with (a) 3, (b) 5, (c) 7 and (d) 9 wt% of IPA.

1.2 Influence of potassium hydroxide concentration

KOH concentration was changed from 15 to 30 wt% in order to study its influence on silicon surface. SEM analysis was used to follow the top structural change of the silicon surface, all results are presented in Figure 18. Si samples were etched 25 min with 5wt% of IPA at 80 °C. The shape and the surface coverage of the pyramids clearly depend on the concentration of the KOH concentration. At 15 wt%, all the surface is covered but the shape of the pyramids isn't well defined, the amount of KOH should not be enough to completely form pyramids (Figure 18a). Then, at 20wt%, all the surface is also covered by pyramids and their shape are

more uniform and sharp compare to 15 wt% of KOH (Figure 18b). But when the concentration is increased, as shown Figure 18c and Figure 18d, the etching rate decreased and the pyramids became smaller and did not fully fill the surface. This phenomenon could be explained by the fact that the dissolution kinetics are altered with the high removal of silicon atoms from the crystalline surface. This hinders the silicates formation, and the high silicon dissolution rate is not keep up. The concentrations of the silicates complexes are also increasing, and as see previously, they acted as a protective layer near the silicon surface, preventing the etchants from accessing the surface [71]. A concentration of 20 wt% of KOH was chosen for the rest of this study, offering a perfect balance between surface covering and pyramids size.

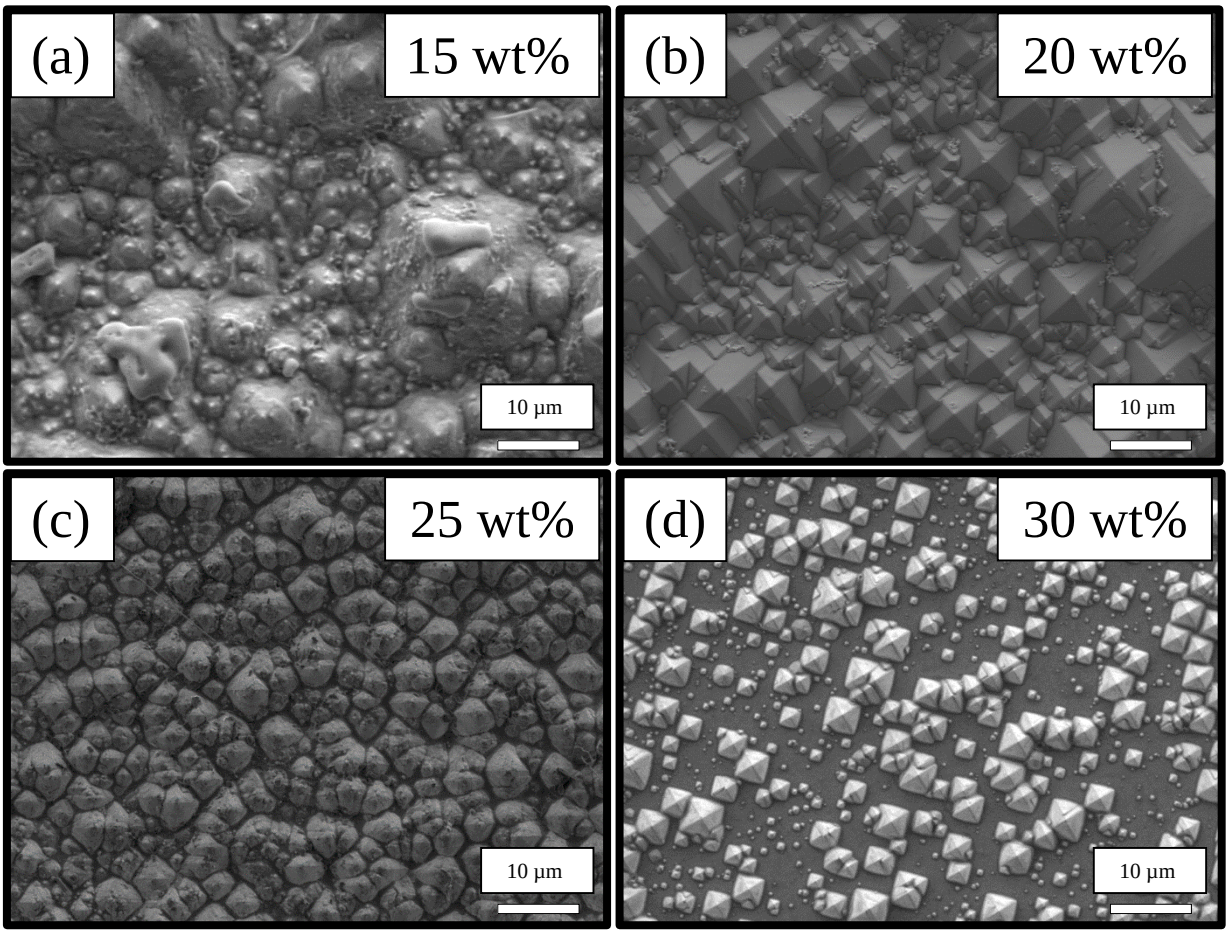

Figure 18: SEM images of silicon nanostructures fabricated with (a) 15, (b) 20, (c) 25 and (d) 30 wt% of KOH.

1.3 Influence of etching time

In this part, the influence of immersion duration in KOH/IPA bath at 80°C was studied. The results shown in Figure 19 are pyramids which were formed on the Si samples etched in aqueous solution containing 20 wt% of KOH and 5 wt% of IPA at different immersion time, from 15 to 30 min, at 80°C. This is obviously visible that etching time affects the silicon surface. At an etching time of 15 min, small pyramid patterns distributed in patches with empty regions between them are observed. These smooth empty areas could be attributed to the relatively short etching time, pyramids did not have time to be formed. At higher etching time, the surface is totally covered by pyramids. Increasing the etching time at this point plays only on pyramids size and distribution. Until 25 min, the pyramids are more uniform, and after the pyramids start to be less uniform and sharp. This problem could be related to a long immersion in the bath, in fact pyramids become attacked by the KOH which became less selective between the bare silicon surface and the pyramid surface. This result, shown in Figure 19d, is in agreement with this theory, the sharpness of the pyramids is lost in favour of heterogeneous surface on top of its.

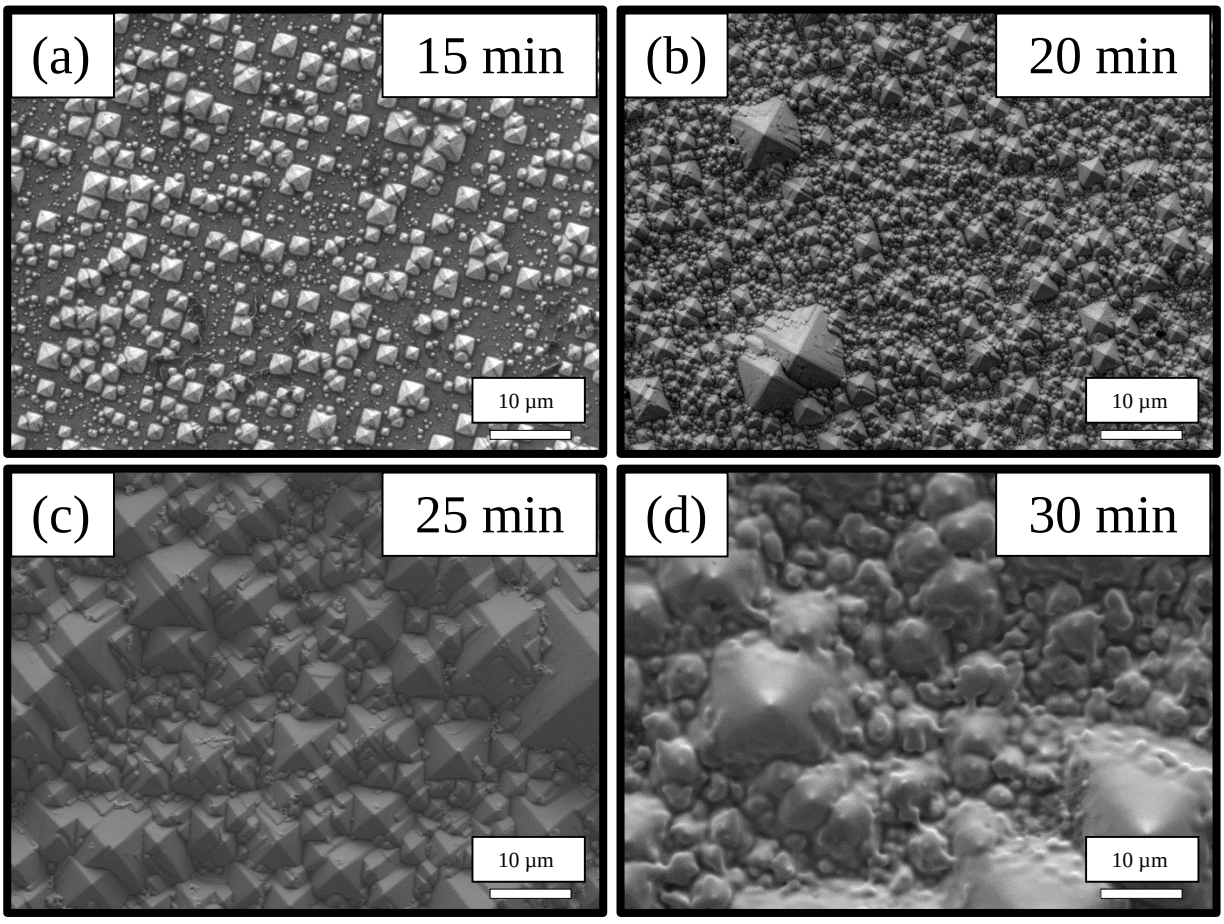

Figure 19: SEM images of silicon pyrramids fabricated with (a) 15 mn, (b) 20 mn, (c) 25 mn and (d) 30 mn immersion time in KOH/IPA bath.

1.4 Silicon pyramids and PEDOT:Tos hybrid material

The impact of KOH solution on the production of the homogeneous pyramids pattern was investigated. KOH isn't the only parameters that influence the pyramids formation, IPA concentration and etching were also investigated. Thanks to a fine tuning of experimental parameters, described previously, silicon pyramids were obtained for all-6 silicon substrates available in the laboratory. The optimum etching solution determined by this work was a solution of 25 wt% KOH with 5 wt% IPA for wet etching at a reaction temperature of 80°C with an etching time of 30 min. The reproducibility of the process developed, was tested over the etching procedure of various samples and almost the same nano-structured silicon was obtained (more details in **Appendix II**). The presence of these structures was confirmed by SEM analysis of the on-top, tilted and side view of etched samples (Figure 20).

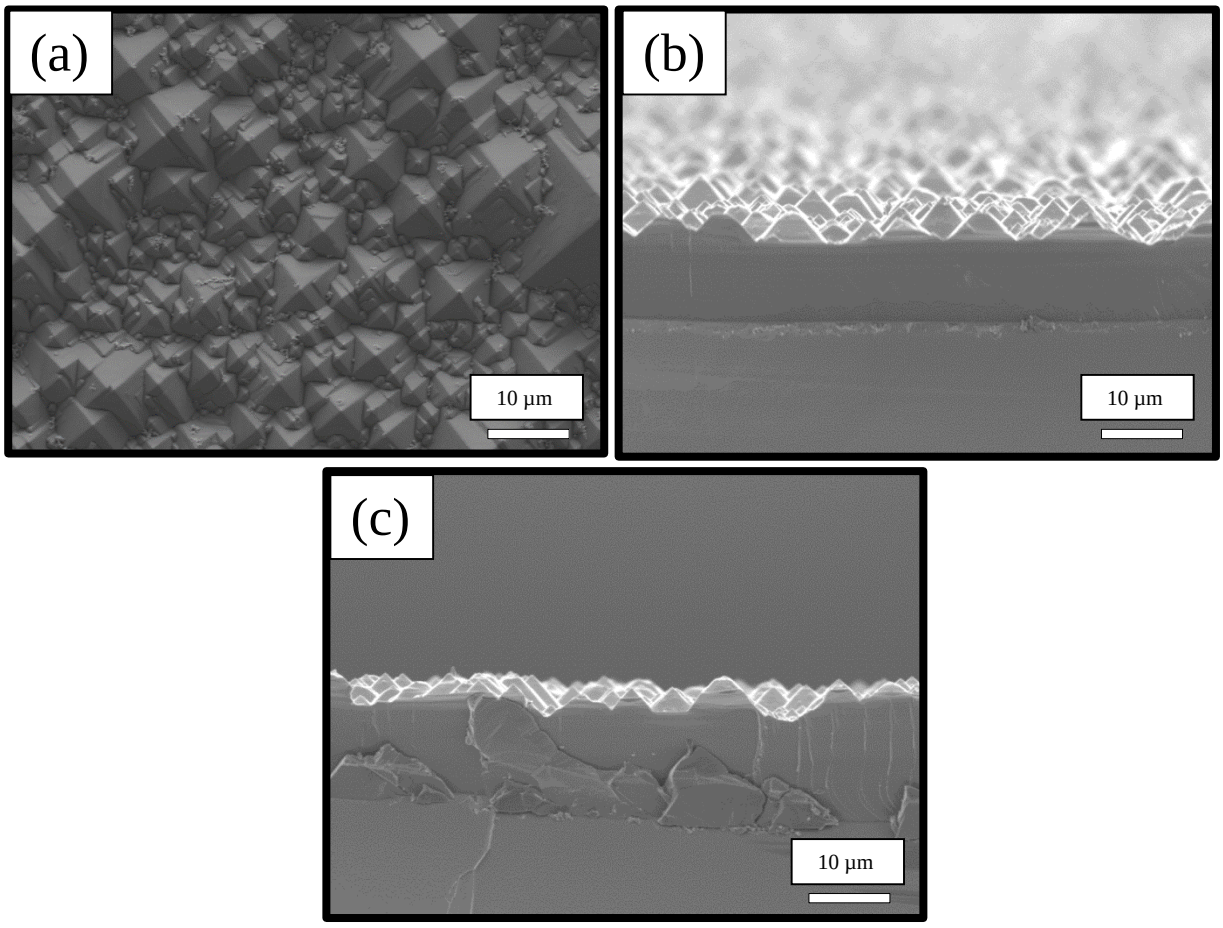

Figure 20: SEM images of silicon pyramids fabricated with optimized procedure. (a) Top view, (b) tilted view and (c) side view of the same silicon pyramids sample.

Then attempts to deposit polymer on-top of silicon nanowires were performed. Based on results from Chapter 2 and 3, the most suitable candidate was PEDOT:Tos with DMSO and

pyridine, exhibiting the best power factor on silicon substrate. Like pSi surface, the silicon pyramids surface was perfectly covered by the polymer. Unfortunately, as this is visible on Figure 21d, only the top of pyramids is covered by the polymer film, the pyramid base seems to not be in contact with the polymer. This phenomenon could be attributed to the cutting process done to obtained this side view picture and will be confirmed by thermoelectric properties investigation.

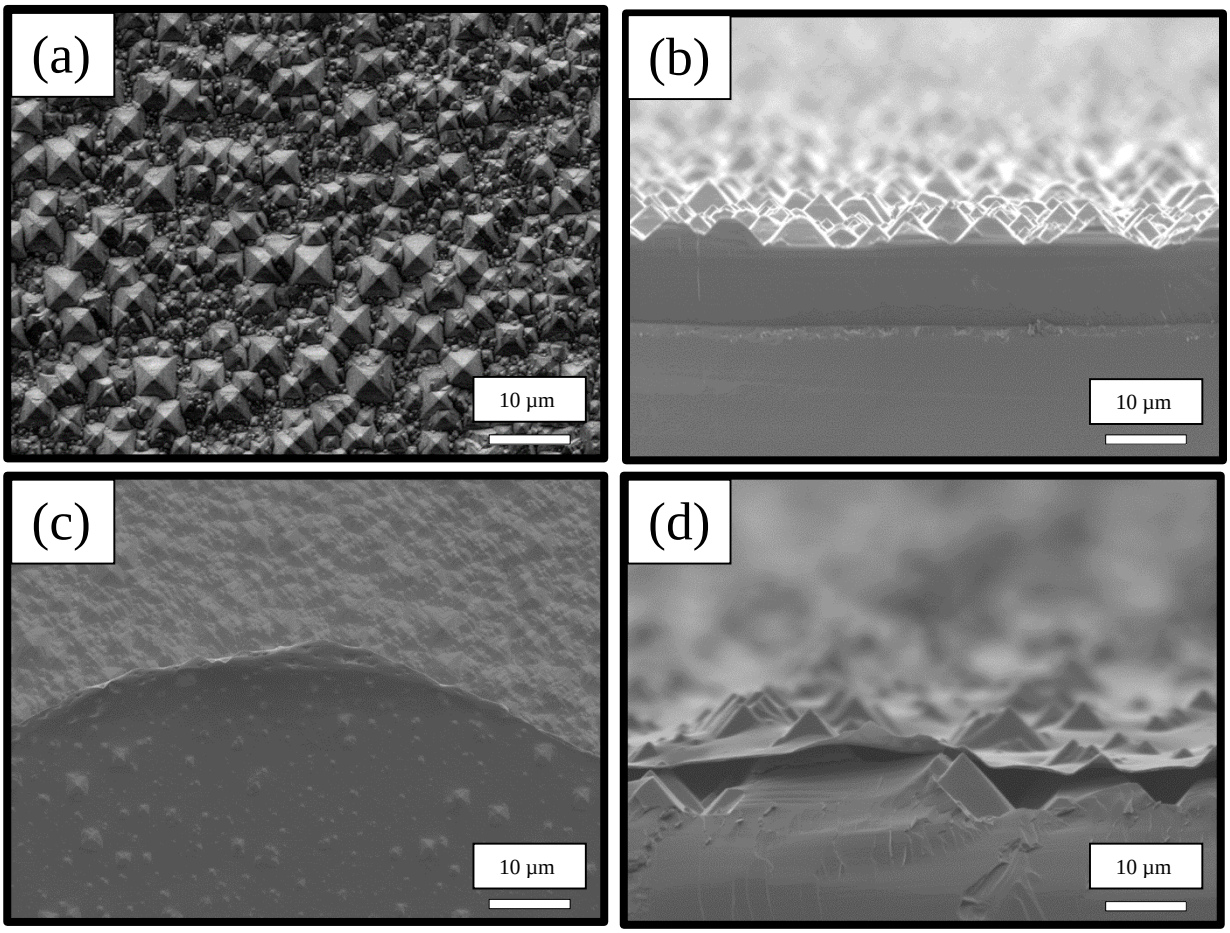

Figure 21: SEM images of bare silicon pyramids and with PEDOT:Tos on top.
(a) Side view and (c) Top view of bare silicon pyramids. (b) Side view and (d) Top view of PEDOT:Tos on silicon pyramids.

So, PEDOT:Tos layers were stacked on top of various silicon with different conductivity, and their Seebeck coefficient, electrical conductivity and power factor were measured in agreement with results of Chapter 3 (Figure 11). All procedures are presented in **Appendix II**.

As previously presented for hybrid PEDOT:Tos on nanostructured silicon surface, the identical behaviour is visible. The doping type (positive in red and negative in blue) does not have a high effect on values regarding the experimental standard deviation. In Figure 22a, the

Seebeck coefficient decreases rapidly to reach a plateau value for low conductive silicon (0.05 and 0.7 S/cm). In case of silicon with high conductivity (20 and 50 S/cm), Seebeck coefficient decreases more slowly when the polymer thickness increases. The same absolute Seebeck coefficient values are obtained for p- & n-type substrates with polymer on top.

In case of electrical conductivity (Figure 22b), the Si substrates conductivities have an influence on the resulting electrical conductivity values of hybrids devices. Principally, an increase of polymer thickness induces an increase of the electrical conductivity. Low conductivity values are obtained for the Silicon with low conductivity and high values for high conductive Silicon. These results are similar to bare silicon with PEDOT:Tos (Chapter 3) and SiNWs and pSi described previously.

Finally, power factor followed the same trend than electrical conductivity (Figure 22c). When PEDOT:Tos is coated on low conductive Silicon (0.05 and 0.7 S/cm) substrates, the power factor of the hybrid devices decreases with the number of layers. This tendency is due to the negative impact of PEDOT:Tos thickness on Seebeck coefficient of Silicon with low conductivity. When Silicon substrate of 20 S/cm is used, the power factor is stable, the increase of electrical conductivity compensates the decrease of Seebeck coefficient when the PEDOT:Tos thickness increases. Finally, for high conductive Silicon (50 S/cm), the power factor increases with the number of PEDOT:Tos' layer and achieves a plateau for 6 layers, with a maximum at 5 layers.

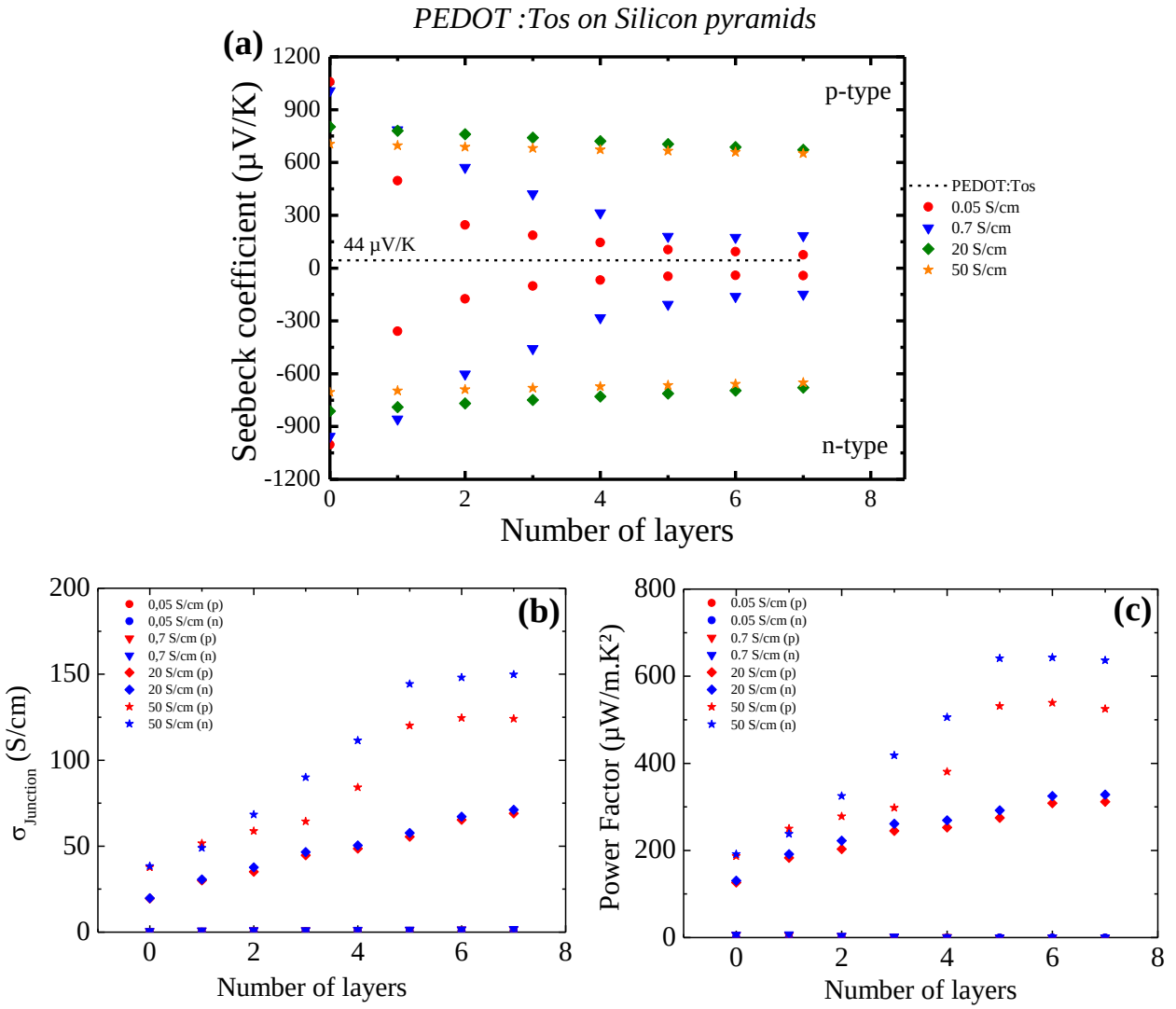

Figure 22: (a) Seebeck coefficient, (b) Electrical conductivity and (c) Power factor plotted versus number of PEDOT:Tos layer on Si pyramids.
Blue symbols are for n-type silicon and red symbols are for p-type silicon.

PEDOT:Tos stacking on silicon pyramids products a different behaviour than PEDOT:Tos on SiNWs or pSi. The behaviour is near to PEDOT:Tos on bare silicon. So, in order to compare the thermoelectric properties of bare and pyramids silicon, Figure 23 shows a comparison between these two cases. A ratio between thermoelectric properties (S, σ, and PF) of hybrid material previously described with bare silicon and Si pyramids was done. Full, empty, and half-full symbols represent the Seebeck coefficient, the electrical conductivity and the power factor ratios between bare silicon and Si pyramids, respectively. Finally, the dashed-line correspond to unchanged thermoelectric properties.

Generally speaking, pyramids have a low influence on thermoelectric properties. On average, Seebeck coefficient and electrical conductivity of Si pyramids are comparable to thermoelectric properties of the bare silicon (Figure 23a). In some cases, a negative influence

of this kind of nanostructure on thermoelectric properties is visible. So, the resulting power factor is centred around the value of in bare silicon (Figure 23b), with a majority of lower power factor by 10% in average.

This decreasing of thermoelectric properties could be due to various factor. First, as opposed to other nanostructured silicon, the dimensionality isn't reduced. The size of the pyramids being around 10 µm high represents less than 2% of the silicon substrate high (650 µm), so this is normal to do not see any influence on thermoelectric properties with respect to the standard deviation. Furthermore, as see on Figure 22d, the PEDOT:Tos polymer film isn't in contact with all the pyramids, so the interface is not optimal. This phenomenon could play a role in the decrease of electrical conductivity. In fact, the charge carriers are preferentially localized inside the polymer matrix, and their flow could be disrupted by the silicon pyramids (difficulty of transporting electron across the junctions between pyramids and PEDOT:Tos). Yang *et al.* reported a significant amount of air voids remained at the PEDOT:PSS/Si interface in the valleys of the pyramids, resulting in an incomplete interface [72]. In case of solar cells, voids in "conventional pyramids"/polymer form local shunts, which deteriorate electrical properties of the device [73]. These kinds of deteriorated properties could also occur in thermoelectric devices.

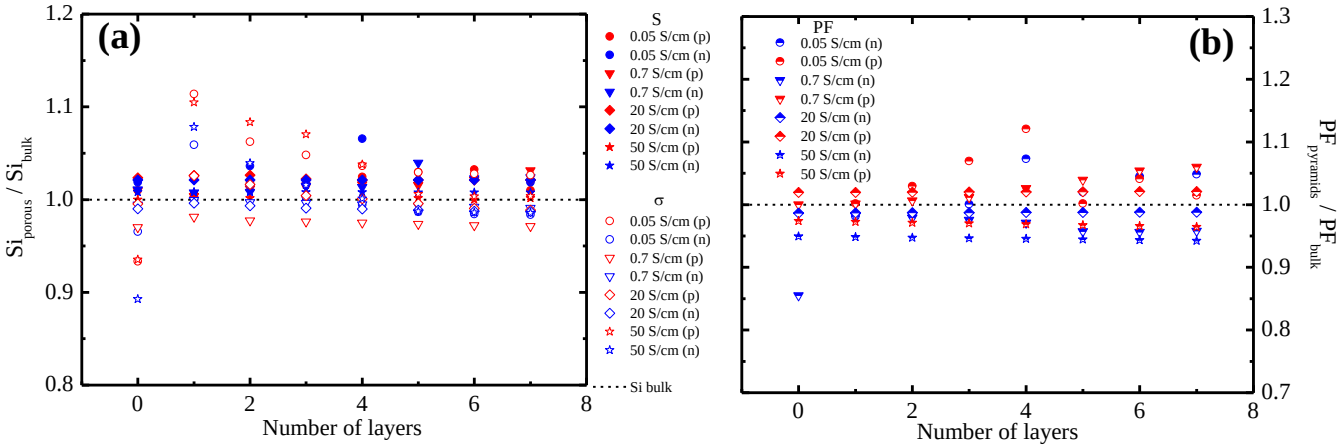

Figure 23: Comparison between (a) thermoelectric properties and (b) power of factor for bare silicon and Si pyramids with different PEDOT:Tos thickness on top.
Full and empty symbols are for Seebeck coefficient and electrical conductivity, respectively.
Blue symbols are for n-type silicon and red symbols are for p-type silicon.

To conclude, silicon pyramids coupled with PEDOT:Tos results in a lower thermoelectric properties compare to the bare silicon with PEDOT:Tos. Unfortunately, this kind of "conventional pyramids" aren't adapted to the polymer deposition. In their study, Yang *et al*. developed inverted pyramids, and showed a better covering of the nanostructured silicon [72]. The formation of inverted pyramids is simple, the etching process occurs via copper-nanoparticles in HF/H_2O_2 bath, this interesting methodology was not applied in this work [74].

D Conclusion

Through various etching procedures, three different silicon nanostructures were obtained. A fine tuning of these etching parameters allowed to make reproducible nanowires, pores and pyramids on top of silicon substrates. The best polymer developed in Chapter 2, PEDOT:Tos with DMSO and pyridine, was deposited on the nanostructured silicon. All etching procedures and polymer deposition were followed with SEM analysis.

Then the thermoelectric properties of all three hybrid nanostructured silicon with PEDOT:Tos on top devices were compared to the devices made in Chapter 3, bare silicon with the same polymer. Porous silicon and silicon nanowires showed the best power factor enhancement compare to bare silicon. Thanks to a decreasing of the dimensionality, a higher Seebeck coefficient was obtained, and despite a decreasing of the electrical conductivity, the power factor was increased by a 10 to 20 % factor in best cases. Unfortunately, conventional pyramids didn't show the same behaviour, in fact due to a low covering of polymer on top of silicon surface, a decreasing of power factor was noticed.

Finally, the interface between the polymer and the nanostructured silicon shown an important effect. By increasing the specific surface, hybrid devices provided very high power factor (Figure 24) and this should result in efficient thermoelectric generator, described in Chapter 5. Some improvements, about the silicon nanostructuration, are provided in perspectives section such as the formation of inverted pyramids covered by nanowires (the resulting specific area should be the maximum obtainable) [75].

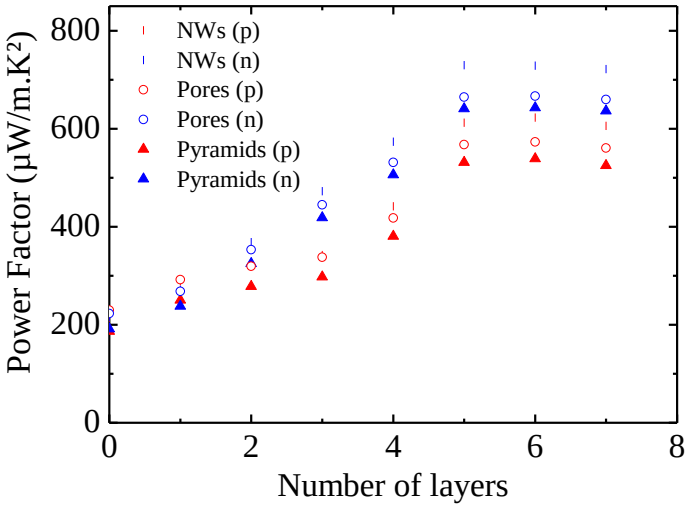

Figure 24: Influence of different silicon nanostructure on Power factor of hybrid PEDOT:Tos-Silicon (σ=50S/cm). Vertical lines, empty dots and pyramids correspond to nanowires, pores and pyramids nanostructures respectively. Blue symbols are for n-type silicon and red symbols are for p-type silicon.

References

[1] L. E. Bell, *Science* **2008**, *321*, 1457.
[2] K. Yazawa, A. Shakouri, *Environ. Sci. Technol.* **2011**, *45*, 7548.
[3] S. LeBlanc, S. K. Yee, M. L. Scullin, C. Dames, K. E. Goodson, *Renew. Sustain. Energy Rev.* **2014**, *32*, 313.
[4] B. M. Curtin, E. A. Codecido, S. Krämer, J. E. Bowers, *Nano Lett.* **2013**, *13*, 5503.
[5] J. Tang, H.-T. Wang, D. H. Lee, M. Fardy, Z. Huo, T. P. Russell, P. Yang, *Nano Lett.* **2010**, *10*, 4279.
[6] L. Weber, E. Gmelin, *Appl. Phys. A* **1991**, *53*, 136.
[7] K. Kim, C. Park, D. Kwon, D. Kim, M. Meyyappan, S. Jeon, J.-S. Lee, *Biosens. Bioelectron.* **2016**, *77*, 695.
[8] E. Garnett, P. Yang, *Nano Lett.* **2010**, *10*, 1082.
[9] A. I. Hochbaum, R. Chen, R. D. Delgado, W. Liang, E. C. Garnett, M. Najarian, A. Majumdar, P. Yang, *Nature* **2008**, *451*, 163.
[10] D. Li, Y. Wu, R. Fan, P. Yang, A. Majumdar, *Appl. Phys. Lett.* **2003**, *83*, 3186.
[11] J. Lee, W. Lee, J. Lim, Y. Yu, Q. Kong, J. J. Urban, P. Yang, *Nano Lett.* **2016**, *16*, 4133.
[12] A. I. Boukai, Y. Bunimovich, J. Tahir-Kheli, J.-K. Yu, W. A. Goddard Iii, J. R. Heath, *Nature* **2008**, *451*, 168.
[13] E. Krali, Z. A. K. Durrani, *Appl. Phys. Lett.* **2013**, *102*, 143102.
[14] J. Kim, Y. Hyun, Y. Park, W. Choi, S. Kim, H. Jeon, T. Zyung, M. Jang, *J. Nanosci. Nanotechnol.* **2013**, *13*, 6416.
[15] V. Schmidt, J. V. Wittemann, S. Senz, U. Gösele, *Adv. Mater.* **2009**, *21*, 2681.
[16] X. Duan, C. M. Lieber, *J. Am. Chem. Soc.* **2000**, *122*, 188.
[17] R. S. Wagner, W. C. Ellis, *Appl. Phys. Lett.* **1964**, *4*, 89.
[18] *Proceedings of the Fourth International Symposium on Cleaning Technology in Semiconductor Device Manufacturing*; Novak, R. E.; Ruzyłło, J.; Electrochemical Society, Eds.; Proceedings; Electrochemical Society: Pennington, NJ, **1996**.
[19] C. Chartier, S. Bastide, C. Lévy-Clément, *Electrochimica Acta* **2008**, *53*, 5509.
[20] K. Choi, Y. Song, I. Oh, J. Oh, *RSC Adv.* **2015**, *5*, 76128.
[21] C. Gondek, M. Lippold, I. Röver, K. Bohmhammel, E. Kroke, *J. Phys. Chem. C* **2014**, *118*, 2044.
[22] Y. Harada, X. Li, P. W. Bohn, R. G. Nuzzo, *J. Am. Chem. Soc.* **2001**, *123*, 8709.
[23] M.-L. Zhang, K.-Q. Peng, X. Fan, J.-S. Jie, R.-Q. Zhang, S.-T. Lee, N.-B. Wong, *J. Phys. Chem. C* **2008**, *112*, 4444.
[24] S. K. Srivastava, D. Kumar, S. W. Schmitt, K. N. Sood, S. H. Christiansen, P. K. Singh, *Nanotechnology* **2014**, *25*, 175601.
[25] K.-Q. Peng, X. Wang, L. Li, Y. Hu, S.-T. Lee, *Nano Today* **2013**, *8*, 75.
[26] K. A. Gonchar, L. A. Osminkina, R. A. Galkin, M. B. Gongalsky, V. S. Marshov, V. Yu. Timoshenko, M. N. Kulmas, V. V. Solovyev, A. A. Kudryavtsev, V. A. Sivakov, *J. Nanoelectron. Optoelectron.* **2012**, *7*, 602.
[27] S. Gielis, M. V. der Veen, S. D. Gendt, P. M. Vereecken, *ECS Trans.* **2011**, *33*, 49.
[28] L. U. Vinzons, L. Shu, S. Yip, C.-Y. Wong, L. L. H. Chan, J. C. Ho, *Nanoscale Res. Lett.* **2017**, *12*, 385.
[29] J. Kumar, S. Ingole, *J. Electron. Mater.* **2018**, *47*, 1583.
[30] K. Q. Peng, J. J. Hu, Y. J. Yan, Y. Wu, H. Fang, Y. Xu, S. T. Lee, J. Zhu, *Adv. Funct. Mater.* **2006**, *16*, 387.

[31] S. Li, W. Ma, Y. Zhou, X. Chen, Y. Xiao, M. Ma, W. Zhu, F. Wei, *Nanoscale Res. Lett.* **2014**, *9*, 196.
[32] F. Toor, J. B. Miller, L. M. Davidson, L. Nichols, W. Duan, M. P. Jura, J. Yim, J. Forziati, M. R. Black, *Nanotechnology* **2016**, *27*, 412003.
[33] Y. Liu, G. Ji, J. Wang, X. Liang, Z. Zuo, Y. Shi, *Nanoscale Res. Lett.* **2012**, *7*, 663.
[34] H. Omar, A. M. Md. Jani, M. Rusop, S. Abdullah, *AIP Conf. Proc.* **2016**, *1733*, 020016.
[35] C. Chiappini, In *Handbook of Porous Silicon*; Canham, L., Ed.; Springer International Publishing: Cham, **2014**; pp. 171–186.
[36] W. McSweeney, O. Lotty, N. V. V. Mogili, C. Glynn, H. Geaney, D. Tanner, J. D. Holmes, C. O'Dwyer, *J. Appl. Phys.* **2013**, *114*, 034309.
[37] C. Chiappini, X. Liu, J. R. Fakhoury, M. Ferrari, *Adv. Funct. Mater.* **2010**, *20*, 2231.
[38] A. I. Hochbaum, D. Gargas, Y. J. Hwang, P. Yang, *Nano Lett.* **2009**, *9*, 3550.
[39] Y. Qu, L. Liao, Y. Li, H. Zhang, Y. Huang, X. Duan, *Nano Lett.* **2009**, *9*, 4539.
[40] H. J. Ensikat, P. Ditsche-Kuru, C. Neinhuis, W. Barthlott, *Beilstein J. Nanotechnol.* **2011**, *2*, 152.
[41] A. Marmur, *Langmuir* **2004**, *20*, 3517.
[42] W. Barthlott, In *Klima- und Umweltforschung an der Universität Bonn*; 1992; pp. 117–120.
[43] A. S. Togonal, L. He, P. Roca i Cabarrocas, Rusli, *Langmuir* **2014**, *30*, 10290.
[44] Y. Kato, S. Adachi, *J. Electrochem. Soc.* **2011**, *158*, K157.
[45] G. Liang, W. Huang, C. S. Koong, J.-S. Wang, J. Lan, *J. Appl. Phys.* **2010**, *107*, 014317.
[46] G. Pennelli, M. Macucci, *J. Appl. Phys.* **2013**, *114*, 214507.
[47] L. D. Hicks, M. S. Dresselhaus, *Phys. Rev. B* **1993**, *47*, 16631.
[48] L. D. Hicks, M. S. Dresselhaus, *Phys. Rev. B* **1993**, *47*, 12727.
[49] K. Nakamura, *Jpn. J. Appl. Phys.* **2017**, *56*, 06GH04.
[50] L. T. Canham, W. Y. Leong, M. I. J. Beale, T. I. Cox, L. Taylor, *Appl. Phys. Lett.* **1992**, *61*, 2563.
[51] A. G. Cullis, L. T. Canham, P. D. J. Calcott, *J. Appl. Phys.* **1997**, *82*, 909.
[52] G. Gesele, J. Linsmeier, V. Drach, J. Fricke, R. Arens-Fischer, *J. Phys. Appl. Phys.* **1997**, *30*, 2911.
[53] J.-H. Lee, G. A. Galli, J. C. Grossman, *Nano Lett.* **2008**, *8*, 3750.
[54] H. Föll, M. Christophersen, J. Carstensen, G. Hasse, *Mater. Sci. Eng. R Rep.* **2002**, *39*, 93.
[55] R. J. Martín-Palma, H. Cabrera, B. Martín-Adrados, D. Korte, E. Pérez-Cappe, Y. Mosqueda, M. A. Frutis, E. Danguillecourt, *Mater. Res. Express* **2018**, *5*, 015004.
[56] IUPAC, (2019), *Databases - IUPAC Int. Union Pure Appl. Chem*, view on https://iupac.org/what-we-do/databases/ (July, **2019**).
[57] M. Bouaïcha, M. Khardani, B. Bessaïs, *Mater. Sci. Eng. B* **2008**, *147*, 235.
[58] P. V. More, S. Jeong, J.-Y. Lee, Y.-H. Seo, B.-H. Ryu, Y. Choi, *J. Mater. Chem.* **2012**, *22*, 23553.
[59] Z. H. Khan, *Appl. Surf. Sci.* **2009**, *255*, 8874.
[60] U. Gangopadhyay, K. Kim, S. K. Dhungel, P. K. Basu, J. Yi, *Renew. Energy* **2006**, *31*, 1906.
[61] S. Indermun, R. Luttge, Y. E. Choonara, P. Kumar, L. C. du Toit, G. Modi, V. Pillay, *J. Control. Release Off. J. Control. Release Soc.* **2014**, *185*, 130.
[62] H. Seidel, L. Csepregi, A. Heuberger, H. Baumgärtel, *J. Electrochem. Soc.* **1990**, *137*, 3612.

[63] K. C. Vernon, T. J. Davis, F. H. Scholes, D. E. Gómez, D. Lau, *J. Raman Spectrosc.* **2010**, *41*, 1106.
[64] D. Kim, *J. Korean Phys. Soc.* **2009**, *55*, 1767.
[65] I. Zubel, M. Kramkowska, *Sens. Actuators Phys.* **2004**, *115*, 549.
[66] K. P. Rola, I. Zubel, *Microsyst. Technol.* **2013**, *19*, 635.
[67] H. Park, S. Kwon, J. S. Lee, H. J. Lim, S. Yoon, D. Kim, *Sol. Energy Mater. Sol. Cells* **2009**, *93*, 1773.
[68] E. D. Palik, H. F. Gray, P. B. Klein, *J. Electrochem. Soc.* **1983**, *130*, 956.
[69] Weihua Han, Xiang Yang, Ying Wang, Fuhua Yang, Jinzhong Yu, In *2008 5th IEEE International Conference on Group IV Photonics*; 2008; pp. 146–148.
[70] C. Trompoukis, I. Abdo, R. Cariou, I. Cosme, W. Chen, O. Deparis, A. Dmitriev, E. Drouard, M. Foldyna, E. G.- Caurel, I. Gordon, B. Heidari, A. Herman, L. Lalouat, K.-D. Lee, J. Liu, K. Lodewijks, F. Mandorlo, I. Massiot, A. Mayer, V. Mijkovic, J. Muller, R. Orobtchouk, G. Poulain, P. Prod'Homme, P. R. i Cabarrocas, C. Seassal, J. Poortmans, R. Mertens, O. E. Daif, V. Depauw, *Phys. Status Solidi A* **2015**, *212*, 140.
[71] A. M. Al-Husseini, B. Lahlouh, *Bull. Mater. Sci.* **2019**, *42*.
[72] L. Yang, Y. Liu, W. Chen, Y. Wang, H. Liang, Z. Mei, A. Kuznetsov, X. Du, *ACS Appl. Mater. Interfaces* **2016**, *8*, 26.
[73] T.-G. Chen, B.-Y. Huang, E.-C. Chen, P. Yu, H.-F. Meng, *Appl. Phys. Lett.* **2012**, *101*, 033301.
[74] Y. Wang, L. Yang, Y. Liu, Z. Mei, W. Chen, J. Li, H. Liang, A. Kuznetsov, D. Xiaolong, *Sci. Rep.* **2015**, *5*, 10843.
[75] H.-Y. Chen, H.-L. Lu, Q.-H. Ren, Y. Zhang, X.-F. Yang, S.-J. Ding, D. W. Zhang, *Nanoscale* **2015**, *7*, 15142.

Chapter 5

Thermoelectric generator:

Novel hybrid organic-inorganic approach

In our modern society, electricity production is a global issue. Another important topic is the waste of heat (energy), especially during the electricity production. Coupled to recent environmental considerations, thermoelectric generators (TEGs) modules should be a part of the solution. A typical TEG is composed of thermoelectric materials couples (p- & n-type materials) connected together electrically in series and thermally in parallel, converting a part of the thermal energy passing through them into electricity. TEGs allow to obtain a direct energy conversion without any moving parts nor working fluids inside. However, their low efficiency compared to others energy-conversion technologies, due to the low performance of thermoelectric material, is an issue (Figure 1) [1].

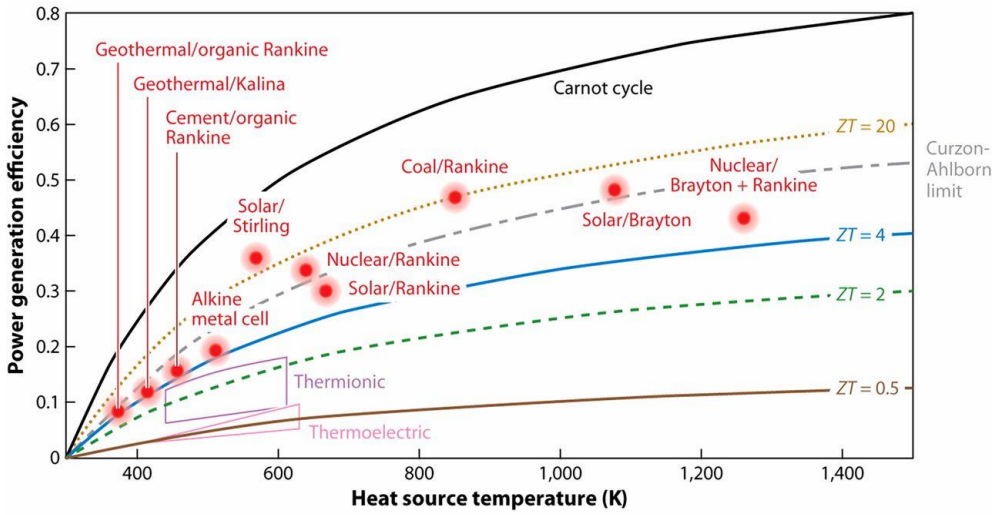

Figure 1: Thermoelectrics in the global landscape of energy conversion. The efficiency comparison of thermoelectrics and other energy-conversion technologies as a function of the heat-source temperature. The ZT values are assumed to be temperature independent, and the heat-sink temperature is set at room temperature.

Actually in the market, most TEGs are fabricated from inorganic materials, and can reach $ZT>1$ at room temperature [2]. Inorganic thermoelectric generators could be classified as function of their application fields:

- Electricity generation in extreme environments: historically space exploration was a springboard for thermoelectricity, with thermal generator based on nuclear technology. This system is called radioisotope thermoelectric generators (RTGs). The natural disintegration of radioactive atoms releasing heat that is converted in electricity [3,4].

- Waste heat harvesting: all energy-conversion system has not perfect yield, losses are present and mostly thermal. The most attractive sector for TEGs is the automobile sector

where 40% of the gasoline combustion is break down as exhaust gas and heat [5]. Nowadays, this technology is no longer an idea but became real. Famous automobile constructors, Ford or BMW, developed TEGs prototypes with high power output around few hundreds of watts [6]. Aircraft and ships are also fields where TEGs are studied [7,8].

- Decentralized domestic power: in developed countries, an estimated 1.2 billion – 17% of the global population – do not have access to the electricity grid. Biomass is the main energy source. Different societies and scientist groups started the marketing of small combustion stoves with efficient combustion [9–11].

- Micro-generation for microelectronics: Recent advances in microelectronics have led to the rapid emergence and development of micro-actuators and intelligent wireless sensors in the industry. Today, these devices can work with only a few hundred milliwatts. Industrialists are therefore looking for micro-generator producing a few milliwatts to supply and make these micro-instruments stand alone. In industrial environments, heat sources are very numerous: hot fluid pipes, furnaces, steam pipes, motors, air conditioning, heating, bearings ... TEGs are therefore a prime candidate for this challenge. Low maintenance and good behavior in difficult environments are important assets for TEGs. For example, Micropelt MPG-D751 modules with sizes of 3.3x4.2x1.1 mm^3 can produce more than 1 mW for a temperature difference of 10 °C and more than 10mW for a difference of 30 °C [12].

- Solar TEG: Thermally, the most abundant source is undoubtedly the sun, which could be consider as a source of heat for a TEG. The main problem of this technology is the low thermal flux (around 103 W/m² on average), which requires the establishment of a flux concentration system to achieve satisfactory yields. McEnaney *et al.* developed a solar thermoelectric generator giving 10% efficiency based on a geometric optical concentration ratio of 45.

Despite their dominant presence in previous cited fields, inorganic TEGs have some drawbacks [13]. The main drawback is the low abundance of inorganic elements in Earth's crust and in oceans. For example, the most used inorganic material in TEGs, Bi_2Te_3, is composed of two rarest "metals" [14]. Furthermore, weight is also a limitation for embedded applications. Finally, their low processability, high toxicity and high cost ($806/kg) [15] limit their

development. Another recent way to fabricate TEGs is the use of organic conducting materials (mostly conducting polymers) [16,17]. Conducting polymer's strength lie in an intrinsic low thermal conductivity, a high electrical conductivity (with a proper structure tuning), a high processability (printable technics available) and a low cost [18,19]. However, their low efficiency compare to inorganic TEGs limits their application to low powered devices as shown in Figure 2. The record value for an organic TEG was claimed by Fujifilm, at the Nanotech 2013, where they showed a person pressing his hand against a device that caused a toy car to begin circling around a track [20]. The power applied to this toy was around 1 mW.

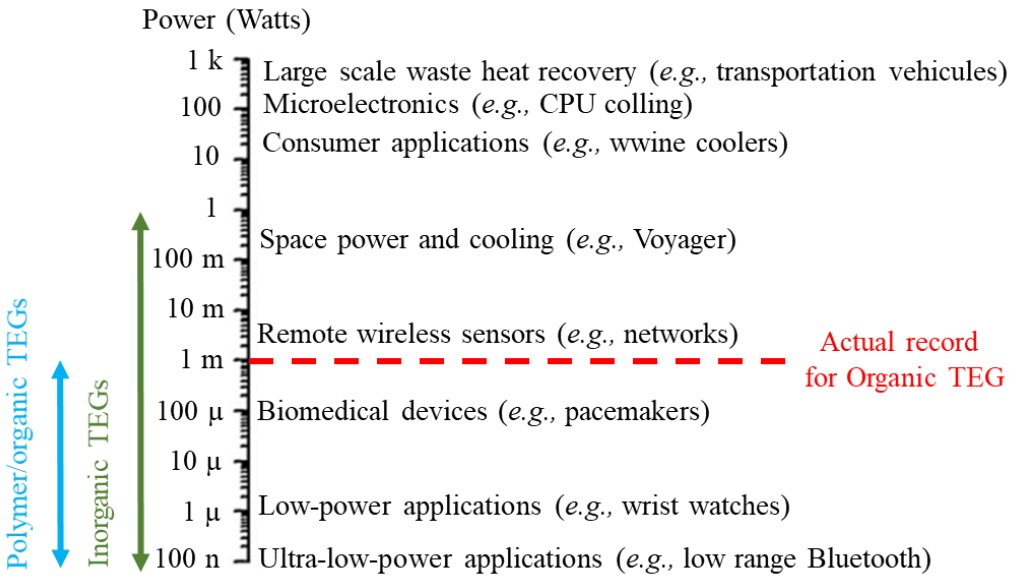

Figure 2: Power consumption scale by energy sources for thermoelectric generators [12]

One more application field, where organics TEGs could shine, is near room temperature applications. The body heat could be used by wearable thermoelectric modules to power mobile devices claiming low power [21]. In fact, the electrical power requirements for this kind of devices are not so high, for example 0.1 mW are enough for electronic tracking tags. However, the temperature difference between the body and the outside environment is small, and therefore, TEGs will have to be coupled with battery. Since thermoelectric energy harvesting can be continuous, 10 µW generator can power up a 100 mW-class device that uses a battery and senses or transmits for one second in every 3 h. An enhancement of thermoelectric performance needs to be realized; the higher the thermoelectric performance, the wider are power generation applications of thermoelectric. Nevertheless, it has been shown [16,22] that with rigorous and strategic material design, polymers and organic materials can rival the efficiencies of their inorganic counterparts.

First, TEGs modules architectures will be discussed and a small theoretical part will explain the way to compare them. Then, based on work done in Chapter 2, 3 and 4, all materials developed will be used as “brick” to build TEGs modules. Two different architectures were used, one with only one kind of material and the other with a couple of p- & n-type materials. So full organic TEGs were made with all p- & n-type materials and their performances were studied. Furthermore, polymer/inorganic hybrid materials, developed in Chapter 3 and 4, will be presented, the inorganic part offsetting the weaknesses of organic part, and vice versa. The effect of nano-structuration of silicon on TEGs devices efficiency was also studied. Finally, as proof of concept, a full flexible organic TEG was developed and tested in our laboratory.

A Fundamentals on Thermoelectric generators

The design of a regular thermoelectric module requires the assembly of two thermoelectric semi-conducting materials, p-type and n-type, connected electrically in series and thermally in parallel as schematized in Figure 3. The part composed of the p- or n-type material is called a "leg".

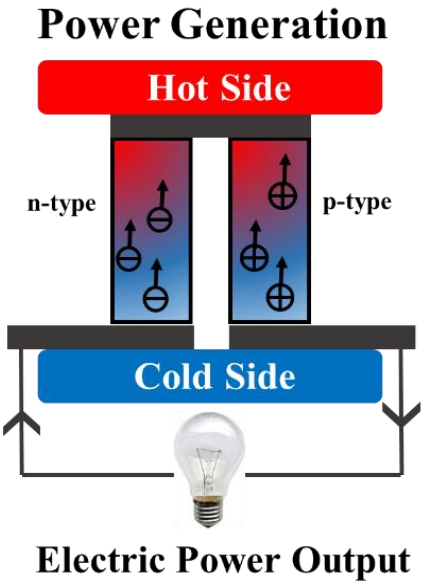

Figure 3: A thermoelectric circuit composed of materials of different Seebeck coefficient (p-doped and n-doped semiconductors), configured as a thermoelectric generator.

Obviously, module performances are dependent on the material properties such as geometrical considerations of the individual legs [23]. To predict the device performances, the efficiency of the thermoelectric material for each single thermocouple (connected p- & n- leg) have to be considered. Generally, interface thermal and electrical resistances at the metal interconnects are neglected, even if in practice they are presents. Furthermore, when a temperature gradient is applied, part of the heat flow through the thermoelectric element is lost to thermal conduction through the material, $\kappa(T_H - T_C)$, and Joule heating (I^2R) generated by the induced thermoelectric current, I, flowing through the leg of resistance, R. Joule heating occurs uniformly throughout the material; therefore, half the heat is transported to the hot side and half to the cold side. There is also Peltier heat absorption, SIT_H, from the hot side and heat generation, SIT_C, at the cold side as a result of the current going from the hot side to the cold side (more details on Peltier effect in **Appendix I**).

Hence, in order to obtain the thermal balance, the heat flow into thermocouple at the hot side and out of it at the cold side have to be considered. This is the combination of the Peltier heating, Joule heating, and thermal conduction contributions. The heat Q_H goes mostly from hot side to cold side though thermoelectric legs, and the thermal resistance between contacts is neglected to simplify the next Equation 1. The heat flow, parallel to charge carriers' displacement, could be expressed as followed thanks to the Fourier law, $K\Delta T$, Equation 1:

$$K = \frac{\kappa S}{\mathrm{L}} \tag{1}$$

Where, K is the thermal conductance, S is the cross section and L is the length of the thermocouple legs. Then, electrical flow heat dissipation by Joule effect could be written as $1/2RI^2$ (R is the electrical resistance of thermocouple legs). The power corresponding to the electrical energy dissipation of charge carriers per Peltier effect could be expressed as SIT_H (hot side) or SIT_C (cold side).

Finally, the resulting thermal power is expressed in Equation 2 and Equation 3:

$$Q_{in} = ST_H I - 0.5\, R_{internal} I^2 + \kappa(T_H - T_C) \tag{2}$$

$$Q_{out} = ST_C I + 0.5\, R_{internal} I^2 + \kappa(T_H - T_C) \tag{3}$$

$R_{internal}$ is the total resistance of each p- & n-leg (without any contact resistance), given by the Equation 4:

$$R_{internal} = R_n + R_p = \left(\sigma_n \frac{A_n}{L_n}\right)^{-1} + \left(\sigma_p \frac{A_p}{L_p}\right)^{-1} \tag{4}$$

R is the resistance, σ is the electrical conductivity, A is the cross-sectional area and L is the length of each p- & n-leg. Thus, based on these previous equations, the resulting power produced is:

$$P_{produced} = Q_{in} - Q_{out} = SI(T_H - T_C) - R_{internal}I^2 \quad (5)$$

From a practical point of view, one simple way to measure the electrical power of a TEG module is by making measurement of the voltage and the current for the corresponding closed circuit when a temperature gradient is applied. The open circuit voltage for the thermocouple is:

$$V_{OC} = (S_p - S_n)(T_H - T_C) \quad (6)$$

S_p and S_n are the Seebeck coefficient of each leg type. So, in order to obtain the best V_{oc} value, Seebeck coefficient must be of different signs. This is the main reason why thermocouples are composed of two different semi-conductors doping type for each leg.

If the TEG is used to convert the temperature gradient into electricity in a device, the resistive load, R_{Load}, has to be considered, and so the resulting close-circuit current is expressed as followed:

$$I_{SC} = \frac{(S_p - S_n)(T_H - T_C)}{R_{Internal} + R_{Load}} \quad (7)$$

Substituting Equation 7 into Equation 5 yields an expression for the electrical power generated:

$$P_{elec} = [(S_p - S_n)(T_H - T_C)]^2 \frac{R_{Load}}{(R_{Internal} + R_{Load})^2} \quad (8)$$

A thermoelectric module generates maximum power when the internal resistance is equal to the load resistance [24]. It follows that maximum power, P_{max}, is given by:

$$P_{max} = \frac{[(S_p - S_n)(T_H - T_C)]^2}{4R_{Internal}} = \frac{A[(S_p - S_n)(T_H - T_C)]^2}{8\rho L} \quad (9)$$

Based on Equations 8 and 9, the power produced by each thermocouple are proportional to the cross-sectional area, and inversely proportional to length of each leg. Therefore, power produced by an entire module is dependent on the number of couples, as well as the ratio of the load resistance to that of the TEG itself. It should also be kept in mind that the internal resistance of a thermoelectric module varies with temperature due to a variation in resistivity and the number of legs.

For a TEG module, the efficiency is calculated from the ratio of the output electrical power ($P_{produced}$) over the input energy flow rate (Q_{in}):

$$\eta = \frac{P_{produced}}{Q_{in}} = \frac{R_{Load} I^2}{ST_H I - 0.5\, R_{internal} I^2 + \kappa(T_H - T_C)} \quad (10)$$

The Equation 10 could be simplified by using two terms; $M = R_{Load}/R_{internal}$ and the Figure of Merit $Z = (S^2/\kappa R_{internal})$, described in Chapter 1.

$$\eta = \left[\frac{T_H - T_C}{T_H}\right] * \left[\frac{M}{M + 1 + \frac{M^2}{ZT_H} - 0.5\, \frac{T_H - T_C}{T_H}}\right] \quad (11)$$

The efficiency is then expressed as a product of the reversible Carnot efficiency, $\frac{T_H - T_C}{T_H}$, and an irreversible factor, $\frac{M}{M+1+\frac{M^2}{ZT_H} - 0.5\,\frac{T_H - T_C}{T_H}}$. The maximum efficiency occurs only for the solution to $\frac{\partial \eta}{\partial M} = 0$, this solution is expressed in Equation 12:

$$\eta_{max} = \left[\frac{T_H - T_C}{T_H}\right] * \left[\frac{M_\eta - 1}{M_\eta + \frac{T_C}{T_H}}\right] = \eta_{Carnot} * \left[\frac{M_\eta - 1}{M_\eta + \frac{T_C}{T_H}}\right] \quad (12)$$

With $M_\eta = [\,1 + ZT]^{1/2}$ where $T = \left[\frac{T_H + T_C}{2}\right]$.

In this last equation, the first term is related to the Carnot efficiency for reversible processes. The second term represents thermoelectric system performances directly linked to physical properties of the materials. If the thermoelectric cycle was reversible, the conversion efficiency should be equal to the maximum Carnot efficiency. However, in reality, thermoelectric conversion is limited by the irreversible process expressed as function of Figure of Merit *ZT*.

In this work, TEG will be compared with their respective maximum Power output (P_{out}) in closed circuit. With this ideal configuration, no load resistance will be used, due to the lack of rheostat in laboratory. In a more practical way, V_{oc} was measured without current (0 A) as the I_{sc} was measured without tension (0 V) at different temperature gradient. The resulting maximal P_{out} was obtained with the following expression: V_{oc} x I_{sc} [25,26]. For the efficiency calculation, the thermal conductivity is mandatory, Figure of Merit *ZT* being expressed in the Equation 12, yet this parameter was not measured during this work. Based on the particular architecture of the hybrid silicon/polymer devices and the difficulty to measure the thermal conductivity in thin film, only calculated value could be used. However, since this option offers only an indicative value that does not take fully into account the complex contribution of organic and inorganic materials in this hybrid device, no "calculated" thermal conductivity will be used in this work.

B Module design and architectures

Depending on the shape of the heat recovery surface in contact, various TEGs architectures could be employed. Thermoelectric properties and Power generation are obviously linked to the architecture of TEGs modules. The first objective of any TEG architecture is to minimize the heat loss and the contact thermal resistance, in relation to the cost considerations.

1. Flat bulk thermoelectric device

Inorganic TEG modules are commonly built with a flat bulk architecture. In this architecture, the longitudinal Seebeck effect is maximized for high power generation [27]. The flat bulk TEGs are mostly cuboid in shape and constructed with alternating legs of p-type and n-type, electrical and thermal current running parallel to each other. Inorganic flat bulk TEGs have been used in experiments in the automotive field and generated up to 1 kW from waste heat [28]. An example of TEGs with square TE legs is illustrated in Figure 4.

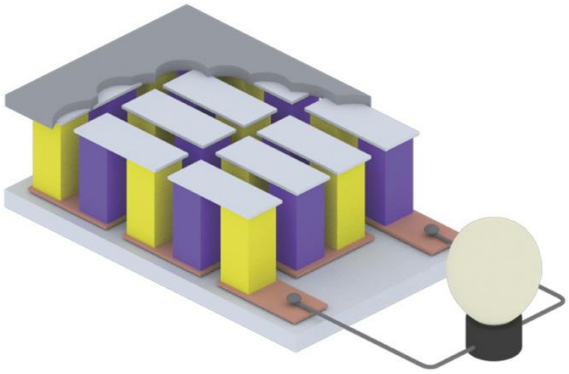

Figure 4: Schematic representation of a TEG with a flat bulk square legs. [29]

In 2011, the first thermoelectric device using polymers as active elements used flat bulk architecture was developed by Bubnova *et al.*. PEDOT:Tos (p-type) and TTF-TCNQ (n-type) were used as thermoelectric materials (Figure 5). This bulk configuration allowed to obtain 0.128 µW with $\Delta T = 10$ K at room temperature [30].

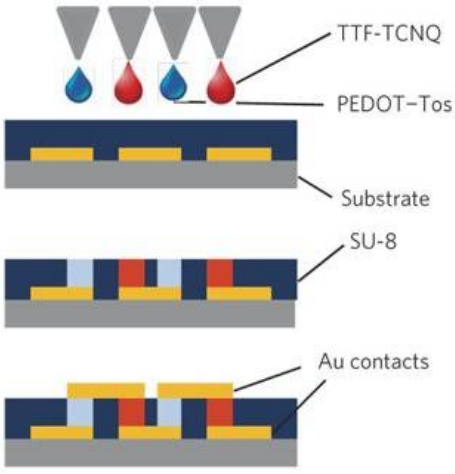

Figure 5: Manufacturing process of an organic thermoelectric generator.

2. Cylindrical Bulk thermoelectric device

Another design of bulk TEG is a cylindrical shape. Cylindrical bulk TEGs are suitable to extract power from cylindrical objects such as oil pipelines for example. In 2015, a company named Gentherm developed prototypes of cylindrical inorganic TE modules and applied them to boost the power efficiency of vehicles, and an output power of ≈30 W was obtained for the individual module under optimal conditions (Figure 6) [31].

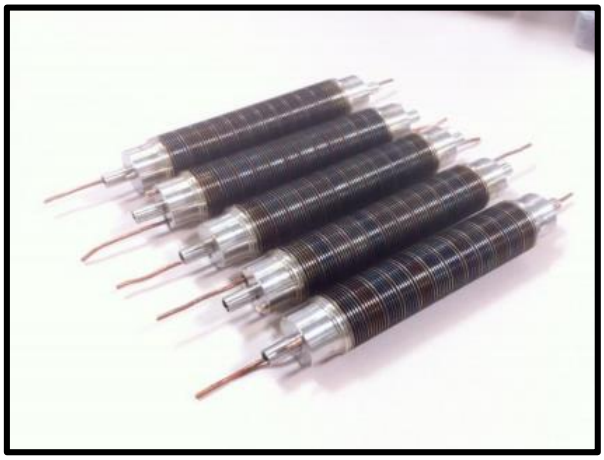

Figure 6: Cylindrical thermoelectric generator developed by Gentherm.

A similar architecture was used by Menon *et al.*, where they fabricated a radial thermoelectric device (Figure 7), which accommodates a fluid as a heat source and can be operate under natural heat convection [32,33]. With such configuration, the authors managed to produce 85 mV open circuit voltage and a power density of 15 nW/cm².

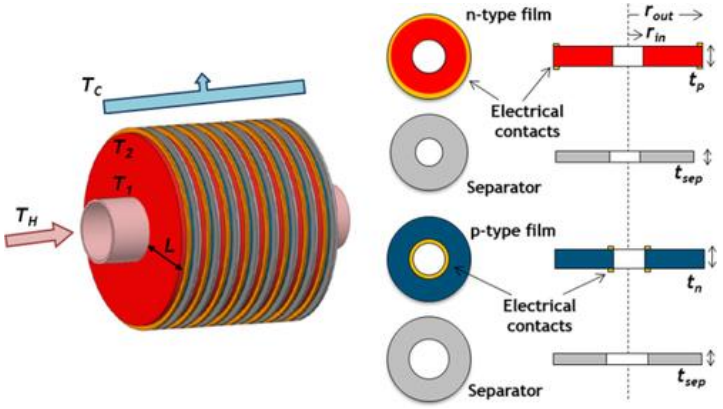

Figure 7: Schematic representation of a TEG with a radial geometry.

3. Thin film thermoelectric device

The development of low cost and easy manufacturing techniques comprising printing technologies, allows to experiment with different forms and architectures of thermoelectric devices. Thanks to this freedom of design and realization in the architecture of the devices, this is now possible to go beyond the bulk geometries, and thus develop TEGs in thin layers. Therefore, TE devices made from organic electronics are currently an emerging topic, with the focus on flexible electronics [13,16,22,34].

So, contrary to inorganic modules constructed with thick legs to harness a temperature gradient from the through-plane temperature difference, easily cast solution-processable organic thermoelectric materials allow consideration of modules that can be constructed in such unconventional geometries, like the "π structure" (Figure 8).

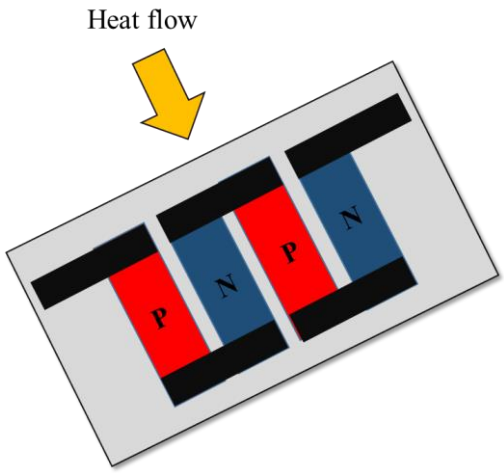

Figure 8: Schematic representation of a thin film "π structure" thermoelectric generator.

This "π structure" is inspired from the classical form of inorganic TEGs. The materials are deposited in thin layers to obtain two-dimensional devices. The heat applied to the section of the thin layer propagates along the layer. For example, Jia *et al*. developed this kind of module via inkjet printing (Figure 9), and reported a TE voltage reaching 15 mV under 25°C temperature gradient [35].

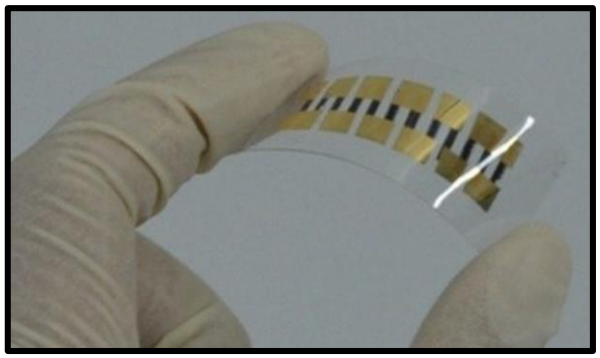

Figure 9: Picture of an organic thin film "π structure" thermoelectric generator

For the rest of this work, the "π structure" was chosen as TEGs architecture. This kind of architecture is fully compatible with the deposition techniques (spin-coating and drop casting) of developed materials described in Chapter 2. All experimental details on the TEG module specifications are available in **Appendix II**.

C Manufacture of thermoelectric devices

The difficulty to obtain a homogeneous standalone polymer film, via common printing techniques, forces to use a substrate to build the thermoelectric generators. Three different substrates were used:

- Glass substrate, offering easy polymer processability, acquisition of TE properties for polymer materials, and low cost;
- Silicon (bare and nanostructured) substrates, despite a loss in flexibility compare to polymer materials, much higher performances are expected for the association with them based on Chapter 3 and 4 results. Furthermore, the resulting n-type material are stable in the air contrary to n-type polymer/organic material;
- PolyEthylene Terephthalate (PET) substrate, the main advantage lies in its compatibility with the flexibility of polymers.

Due to size constraints for measurements (in case of non-flexible substrates), only three-legs generators will be realized during this study.

1. TEG based on glass substrate

As described previously, the most conventional TEG architecture consists of two, p- & n-type semiconductors materials, connected thermally in parallel and electrically in series. Nevertheless, this architecture requires two materials with similar thermoelectric properties, *i.e.* power factor. The material with lower power factor can potentially affect the overall performances of the module. In this work, the best p- & n-type polymers have very different power factors, PF (PEDOT) = 240 µW/mK² and PF (PCBM) = 2.44 µW/mK², as shown studies in Chapter 2.

A solution developed by several scientist groups was to make TEG modules with only one material [36–39]. In order to have a functional device, a different architecture has to be realized. The top electrode of each individual thermoelectric leg had to be connected to the bottom electrode of the next individual leg, *i.e.* all legs are connected in a series configuration, as presented in Figure 10. This architecture is called unileg thermoelectric generator, and this was applied for all p- & n-type materials available.

Figure 10: Picture of an unileg thermoelectric generator with only p-type legs made of PEDOT:Tos on glass

As described previously, only the Power Output of the different TEGs modules at different temperature differences were studied (Figure 11a and 11b). Maximal Power Output was obtained by the following formula $P_{out} = V_{oc} \times I_{sc}$, these parameters were measured in a closed circuit, and for more visibility only P_{out} versus the temperature difference are presented in Figure 11.

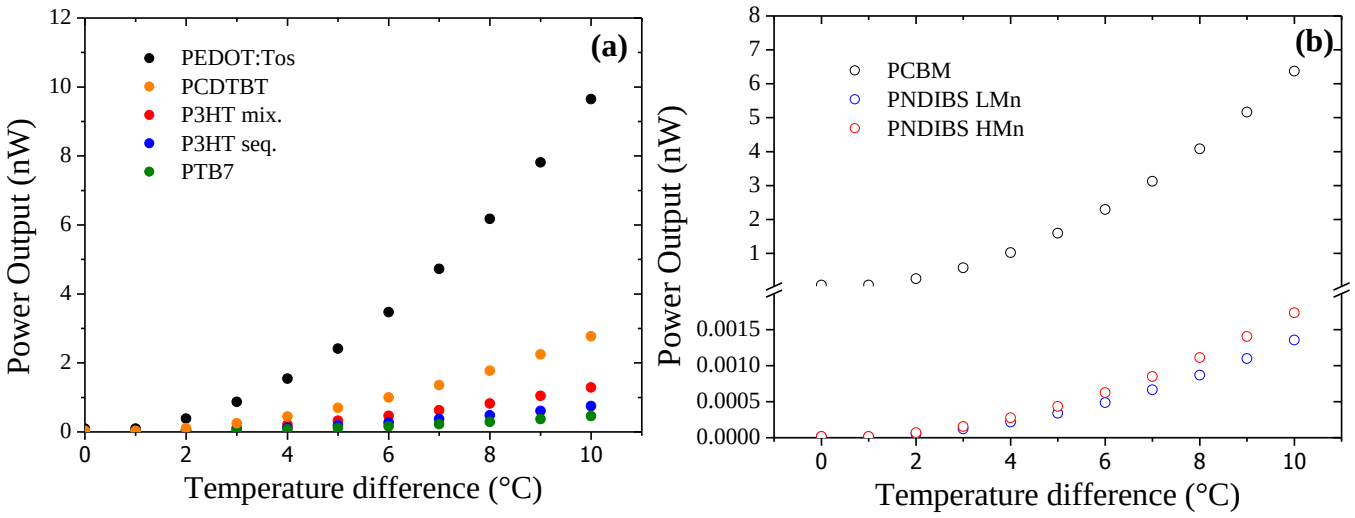

Figure 11: Power Output for the various TEGs, plotted against the applied temperature difference, at room temperature. (a) Unileg p-type and (b) Unileg n-type TEGs.

The best results for p- & n-type unileg TEGs were obtained for PEDOT:Tos and PCBM, respectively. In all cases, the Power Output follows a pseudo-exponential trend with the increase of the temperature difference. In fact, the Power Output could be also expressed as a function of the Seebeck coefficient, the temperature difference and the internal resistance, all squared (Equation 8, rewritten below) [40].

$$P_{elec} = [(S_p - S_n)(T_H - T_C)]^2 \frac{R_{Load}}{(R_{Internal} + R_{Load})^2} \quad (8)$$

Furthermore, data obtained confirm that the material with the better Power factor will give the TEG with the best performances. However, the maximal P_{out} values obtained are low, only a few nanowatts. The problem came from device design, carbon paste replacing the leaking material could hamper charge carrier displacement between each leg. It is probable that main charge carriers are dissipated in this carbon paste. The small difference in performance between the generators made from PEDOT: Tos and PCBM, allows to consider that their association will not be harmful.

Three-legs generators alternating p-n-p and n-p-n legs junctions were made (Figure 12). The number of legs was chosen to optimize the TEG fabrication from hybrid materials (Schematic in **Appendix II**). Indeed, with one device of both p- & n-type materials, two TEGs (p-n-p and n-p-n) could be build. A higher number of legs could be more complex regarding to the size

restriction with our measurement equipment (**Appendix II**). Furthermore, based on Equation 8, the increase of the number of legs will result in an increase of the first term $(S_p\text{-}S_n).(T_H\text{-}T_C)^2$ but also of the global electrical resistance. So depending of the resistance value for one leg, increasing the number of legs could have a negative impact on the Power generated. Finally, based on Chapter 2 and previous results, only PCBM were used as n-type material.

Figure 12: Picture of p-n-p three-legs thermoelectric generator with p-type legs made of PEDOT:Tos and n-type leg made with PCBM on glass

Unfortunately, as predicted, a mixture of p- & n-type legs had a negative effect on the maximal P_{out} measured (Figure 13). By comparing results obtained for p-n-p and n-p-n junction, p-type polymer does not affect the performance. PCBM is the material which has a negative impact on performances, as proven by the fact that n-p-n junction is worse than p-n-p one. The difference in thermoelectric properties is detrimental for the construction of efficient TEG, materials must have the same thermoelectric properties. It is noteworthy that all TEGs with PCBM were tested under controlled atmosphere, inside a glovebox. When the measurements were conducted outside the glovebox, with air and moisture, no performances were obtained. Indeed, it is recognized that PCBM is sensible to oxygen. Studies have been performed on the photo-oxidation of C_{60} molecules by Xia *et al.* where they have reported that interaction between oxygen and C_{60} molecules, induced by irradiation, may occur and can be described as $C_{60} \rightarrow C_{60}O_n + O_2$, (n = 1–5) [41]. The properties of fullerene to trap the radicals by the reaction of radical addition lead to the formation of radical sites which can initiate its own degradation and disturb the charge carriers' displacement.

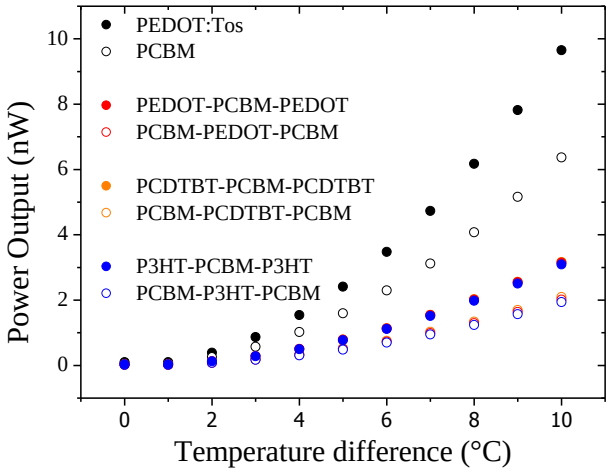

Figure 1310: Power Output for the various TEGs, plotted against the applied temperature difference, at room temperature.
Black symbols correspond to unileg PEDOT:Tos (full) and PCBM (empty). Then, full and empty colored symbols represent p-n-p and n-p-n three-legs TEGs on glass, respectively.

2. TEG based on silicon substrate

In the previous part, low performances and poor stability were obtained for polymer/organic TEGs. Furthermore, this study showed the importance of having two materials with the same thermoelectric properties. The strategy developed in our laboratory was the use of silicon as a substrate to overcome these drawbacks. Silicon substrates were chosen as semi-conducting inorganic material due to their important role in electronic and industrial field [42], their high range of impurities concentration (doping concentration) accessible [43], their good thermoelectric properties (S ≈ 500-1200 µV/K when correctly doped) at room temperature [44] and their air stability even for n-type silicon. Different polymers combined with silicon substrates with various electrical conductivities and Seebeck coefficients [45] , described in Chapter 3 and 4, were used as material for TEG construction. The corresponding hybrid materials should benefit from the advantages of the two components, hindering their corresponding drawbacks.

The compatibility between thermoelectric properties being essential, thermoelectric generators were made with an alternation of p- & n-type silicon substrates with the same electrical conductivity. In Chapter 3, the study of the influence of polymer thickness on the thermoelectric properties has showed that the same absolute value, Seebeck coefficient and electrical conductivity, were obtained whatever the silicon doping nature. So, thermoelectric generators based on these results were made, and their performances were evaluated. Thanks to the air stability of silicon, most of the devices were tested outside a glovebox, yet PCBM samples have been measured inside the glovebox.

All the results are presented on the next Figures (Figure 15, 16, and 17). The thermoelectric generators are composed of three legs of silicon substrates covered with the same material in order to have the same thermoelectric properties. The four silicon substrates were presented in Chapter 3, and had the following electrical conductivities: σ= 0.05, 0.7, 20 and 50 S/cm. The polymer and organic material were presented in Chapter 2, only PEDOT:Tos, PCDTBT, P3HT mixed and PCBM will be used in this part. The architecture of this TEG is described in **Appendix II**, a "π-design" of p-n-p junction were arbitrarily chosen.

Each Figure is related to a particular silicon substrate electrical conductivity. Inside one Figure, the four graphs represent one kind of polymer or organic material deposited on top of a silicon substrate. Eight three-legs thermoelectric generators were made for each compound, the main difference was organic/polymer thickness on top, from zero to seven layers. The same colour scheme depending on number of layer has been applied on all schemes (red, orange, green, blue, purple, pink and dark yellow corresponding to 1, 2, 3, 4, 5, 6 and 7 layers, respectively). An example of TEG made with silicon and seven layers of PEDOT:Tos is presented Figure 14. The same architecture for couple thermoelectric material (p- & n-type), was used.

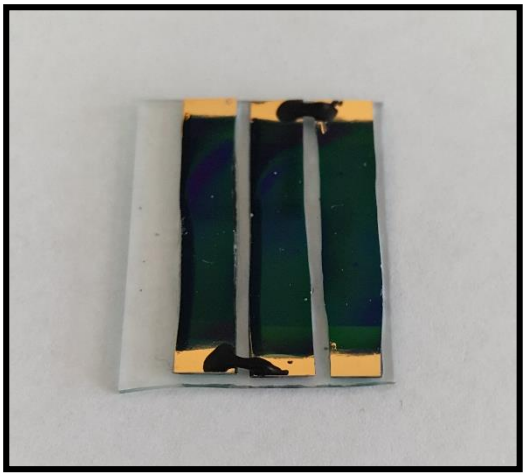

Figure 14: Picture of p-n-p three-legs thermoelectric generator with p-type and n-type legs coated with seven layers of PEDOT:Tos on silicon substrate.
P-type legs are made on p-type silicon and n-type legs are made on n-type silicon.

The Figure 15 represents results obtained on silicon with σ = 0.05 S/cm. Regardless of polymer or organic material on silicon substrates (colour symbols), this last has a negative effect on performances of TEGs compare to bare silicon (black symbols). The main reason is the huge decrease of Seebeck coefficient as function of organic material thickness shown in Chapter 3.

However, a slight difference between all the Power Output obtained for TEG could be explained by the difference of electrical conductivity of the organic material.

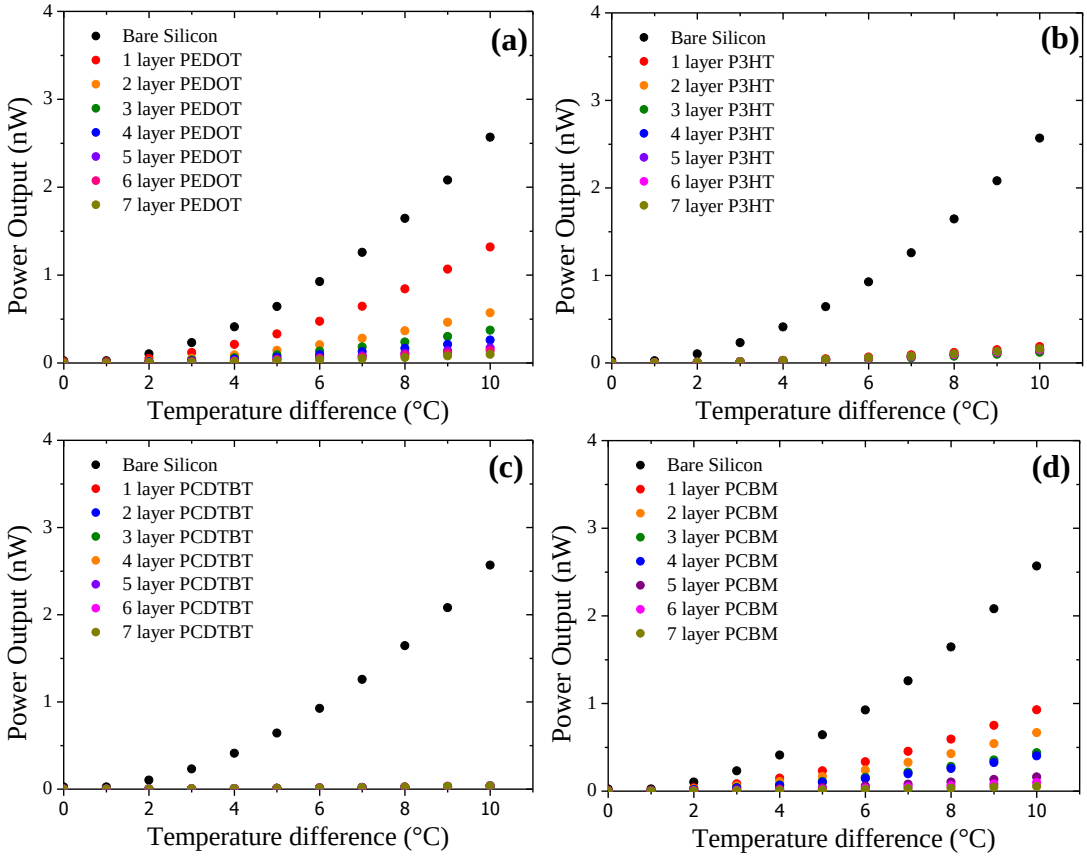

Figure 15: Power Output for the various TEGs, plotted against the applied temperature difference, at room temperature.
p-n-p three-legs TEGs on silicon substrate (σ=0.05 S/cm) with (a) PEDOT:Tos, (b) P3HT, (c) PCDTBT and (d) PCBM with different thickness coated on top.

Thereafter, silicon with an electrical conductivity of σ = 0.7 S/cm was used as substrate in the study of the influence of organic material thickness on TEG performances (Figure 16). Organic materials have still a negative impact on performances of TEG hybrid devices. The most remarkable case is the TEG with PCBM, despite the low electrical conductivity of the latter, the negative effect is not very important (compare to the PCDTBT or P3HT with barely the same electrical conductivity). This is important to note that this effect is less important compared to TEG made with lower conductive silicon. In the first approximation, this is possible to say that the thermoelectric properties of the substrate are very important for the hybrid assembly. Indeed, the substrate accounts for more than 90% of the thickness of the device.

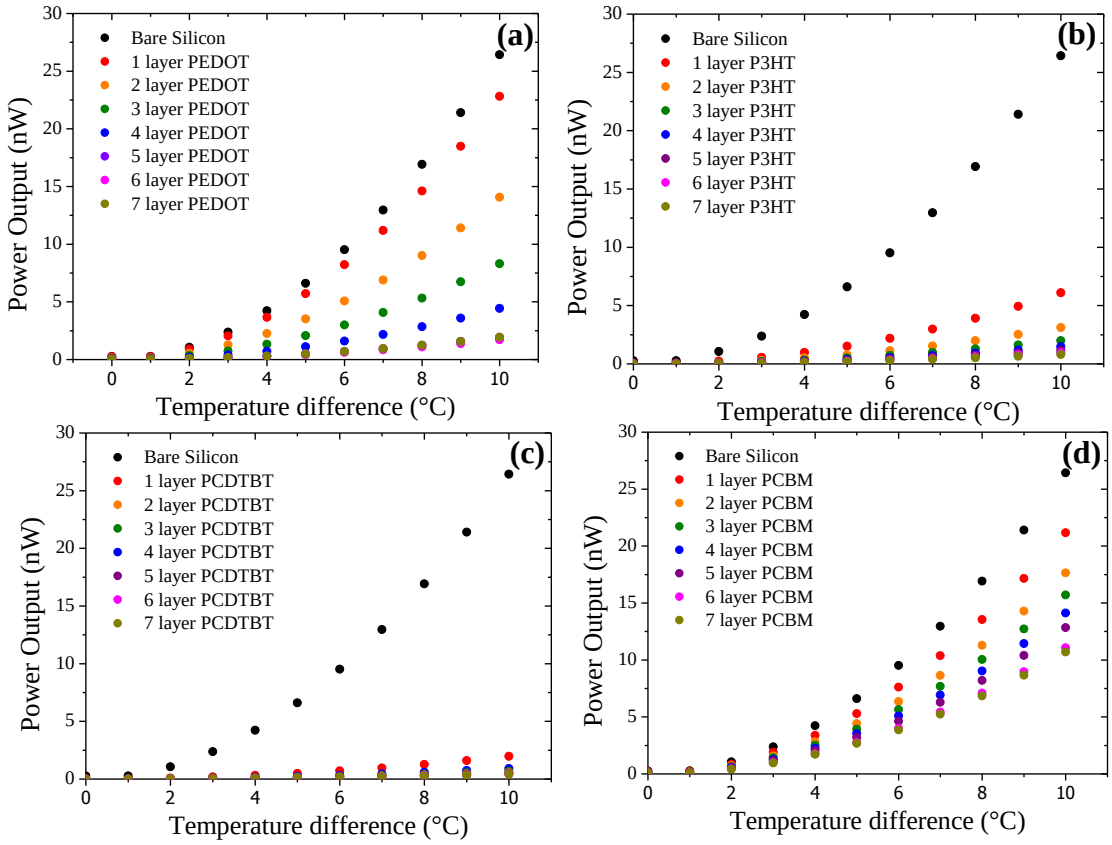

Figure 16: Power Output for the various TEGs, plotted against the applied temperature difference, at room temperature. p-n-p three-legs TEGs on silicon substrate (σ=0.7 S/cm) with (a) PEDOT:Tos, (b) P3HT, (c) PCDTBT and (d) PCBM with different thickness coated on top.

Finally, Figure 17 gathers the results for hybrid TEGs based on silicon with electrical conductivity of σ = 20 and 50 S/cm. In all cases, PCDTBT has a negative effect on Power Output. Then, following the electrical conductivity of the silicon substrate, P3HT and PCBM obtained different results. For the silicon substrate at σ = 20 S/cm, the same behaviour as low conductive silicon (σ =0.05 and 0.7 S/cm), were obtained for P3HT, the stacking of polymer layers on top of the substrate decreases the TEG performance. The PCBM thickness does not have any impact on TEG performances for silicon with σ = 20 S/cm. For the silicon substrate at σ = 50 S/cm, opposing behaviours are worth noting. In fact, the P3HT has a positive effect on the performance of the hybrid TEG, whereas in the case of the PCBM a decrease occurs. This decrease in performance is surprising, based on the previous results, an increase may occur. This effect could be attributed to an experimental problem related to the thermoelectric generator itself (contact problems for example). The best effects were obtained for PEDOT:Tos on both silicon (σ = 20 and 50 S/cm). When the Seebeck coefficient stays constant while the electrical conductivity increases, a better power factor is obtained, and so the Power Output resulting is better. Record value of 1795 nW at ΔT = 10K was obtained for five layers of PEDOT:Tos on silicon with an electrical conductivity of 50 S/cm.

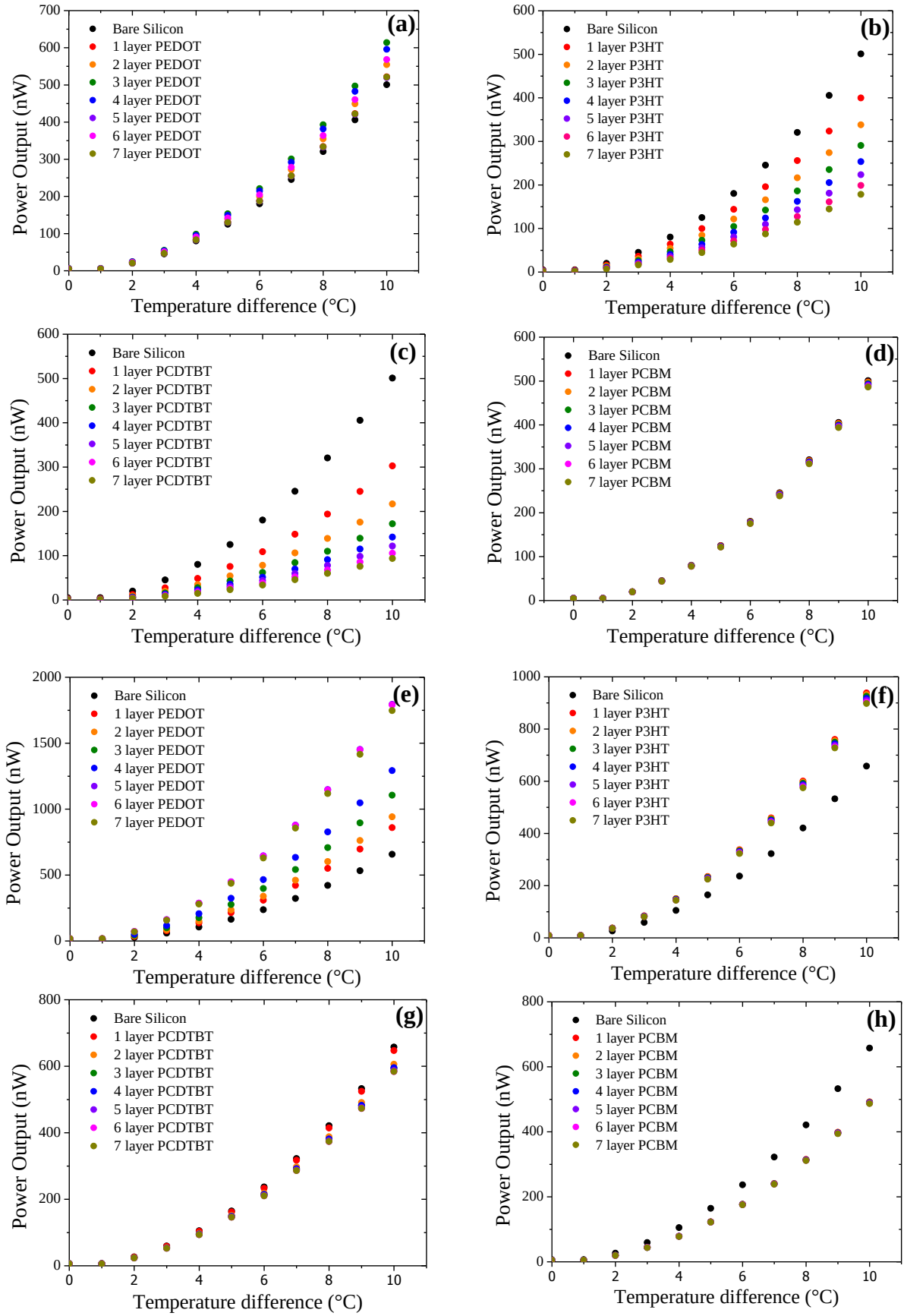

Figure 17: Power Output for the various TEGs, plotted against the applied temperature difference, at room temperature.
p-n-p three-legs TEGs on silicon substrate (σ=20 S/cm) with (a) PEDOT:Tos, (b) P3HT, (c) PCDTBT and (d) PCBM with different thickness coated on top.
p-n-p three-legs TEGs on silicon substrate (σ=50 S/cm) with (e) PEDOT:Tos, (f) P3HT, (g) PCDTBT and (h) PCBM with different thickness coated on top.

Like in the case of TEG on glass, a silicon TEG was made with two organic materials, p- & n-type (Figure 18). The best organic materials were used, PEDOT:Tos as a p-type and PCBM as a n-type material. So each of these compounds were deposited on silicon with the same majority charge carriers. The same three-legs "π-architecture" with p-n-p junctions was done. The results are all presented in Figure 18. Figure 18a compares efficiency of full PEDOT:Tos device (empty dots) and PEDOT:Tos / PCBM devices (full dots), while Figure 18b compares efficiency of full PCBM (empty squares) and PEDOT:Tos / PCBM devices (full dots). If the thermoelectric properties of the two organic materials had been similar, an increase in Power Output would have to happen. As this is not the case, the PCBM has a "negative" impact on the overall performance of the device. This effect is even more true that the PEDOT has a positive effect, when compared with the device made entirely with PCBM. These results, highlighted by the previous results (Figure 13), have also again shown the importance of having very similar thermoelectric characteristics.

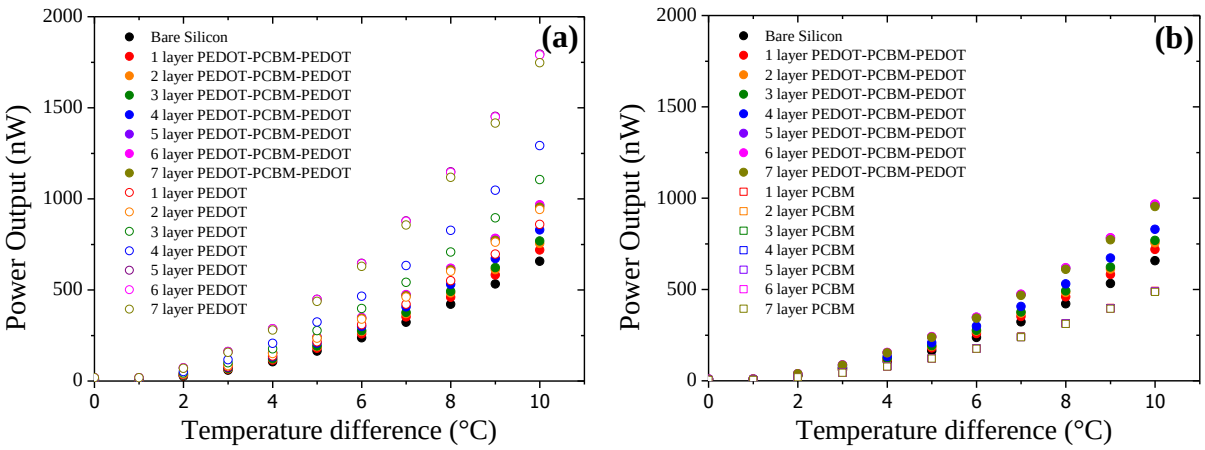

Figure 18: Power Output for the various TEGs, plotted against the applied temperature difference, at room temperature.
Comparison of p-n-p three-legs TEGs on silicon substrate (σ=50 S/cm)[full symbols] versus (a) unileg PEDOT:Tos and (b) unileg PCBM TEGs [empty symbols].

Of all the organic materials synthesized or provided in Chapter 3, the p-type materials showed the best results. PEDOT:Tos which after a fine optimization showed a high power factor resulting from his good thermoelectric. Subsequently, the results of thermoelectric generators based on silicon, showed the importance of substrate intrinsic properties.

So silicon with high surface area, developed in Chapter 4, were used as substrates to obtain more efficient hybrid TEGs. Only PEDOT:Tos which obtain the best thermoelectric performances will be deposited on nanostructured silicon. Figure 19 presents the efficiency of TEGs built with this nanostructured silicon and different PEDOT:Tos thicknesses. As a

reference, Figure 19a is the result obtained for bare silicon with PEDOT:Tos. As described in Chapter 4, the increase in the area between the polymer and the substrate induces an increase in thermoelectric properties. Thus, the best results were obtained for TEGs based on SiNWs coated with 6 layers of PEDOT: Tos, P_{out} = 2350 nW. By modifying the silicon structure at a nanometric scale, a 25 % increase of the Power Output was realized. It is noteworthy that as expected the increase of temperature difference has a direct impact on the Power Output. The first term of the Equation 8, $(S_p-S_n).(T_H-T_C)^2$, explains this phenomenon, the temperature has the same impact than the Seebeck coefficient difference.

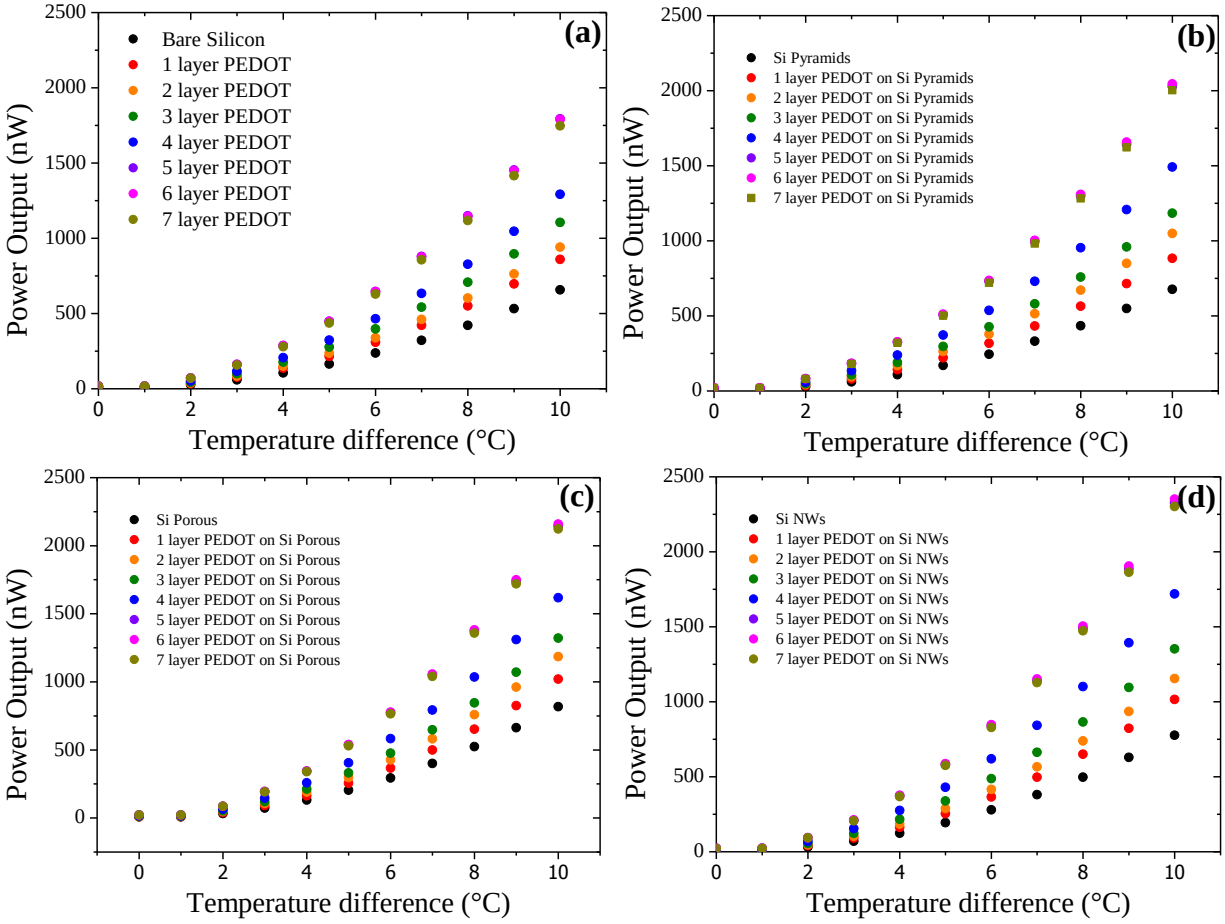

Figure 19: Power Output for the various TEGs, plotted against the applied temperature difference, at room temperature.
Comparison of p-n-p three-legs TEGs on silicon substrate (σ=50 S/cm), (a) bare silicon, (b) silicon pyramids, (c) porous silicon and (d) silicon nanowires with different PEDOT:Tos thickness coated on top.

3. TEG on flexible PET

Powerful thermoelectric generators have been realized thanks to the coupling of polymers and silicon. However, despite a notable gain in term of performances, this type of device has a disadvantage. Indeed, one of the main assets of polymers has been lost, at the expense of performance, the flexibility. Nowadays, scientists are looking to develop flexible thermoelectric devices, especially in the textile field. In 2014, Kim's group have developed wearable thermoelectric generators consisting of twelve thermocouples ($Bi_{0.5}Sb_{1.5}Te_3$ (p-type) and $Bi_2Se_{0.3}Te_{2.7}$ (n-type), where the device produced 224 nW for a temperature difference of 15 K [46]. This TEG showed the feasibility of a wearable device in the form of clothing. By applying to clothing for different parts of the body, the generate electrical energy could be enough to use low-power devices. More recently, Wang *et al.* demonstrate a facile approach to synthesize novel organic/inorganic heterostructures with ZT~0.3 at 400 K [47]. The assembled organic/inorganic hybrid can serve as an ink for scalable printing of flexible.

In order to have a functional flexible device, a home-made procedure was developed (**Appendix II**), and the "π-architecture" was chosen for all flexible TEGs. Thermoelectric generators with p- & n-type organic materials thermocouples were realized on PET substrate. Thanks to greater freedom in the realization, TEGs with three and five-legs have been fabricated. Figure 20 shows a flexible 5-legs all organic TEG with PCDTBT and PCBM as p- & n-type material, respectively.

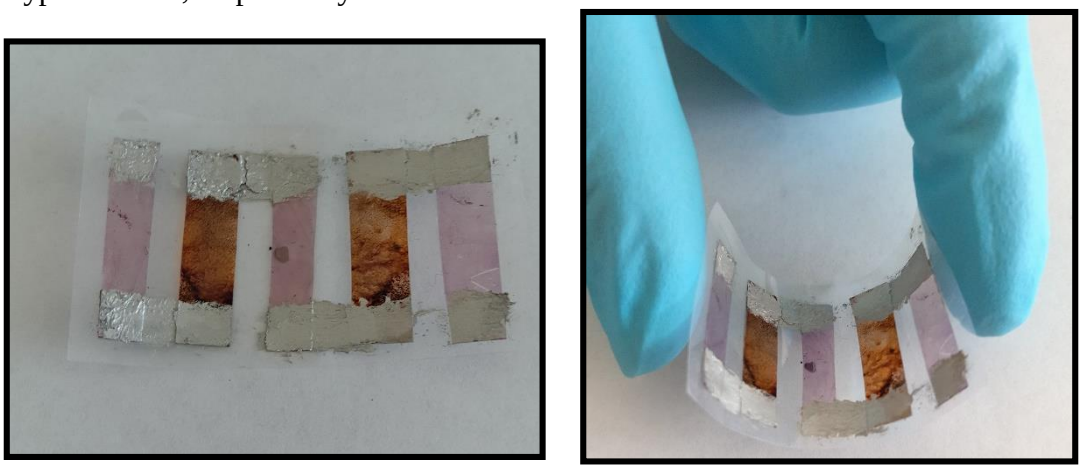

Figure 20: Pictures of p-n-p-n-p 5-legs thermoelectric generator with p-type and n-type legs coated with one layer of PCDTBT and PCBM on PET substrate.
P-type legs are made with PCDTBT and n-type legs are made with PCBM.

Then the thermoelectric performances of these flexible devices were studied. Black dots represent TEG on glass and red dots TEG on PET (Figure 21). This is important to note that whatever the support, the same thermoelectric performances were obtained with the same pair

of materials. Some measurements were done under a small bending between fingers as proof of concept. TEGs were still working without any loss in performances until the electrodes break. In fact, electrodes were deposited manually and they were very fragile. Design improvements are to be expected such as silver electrode deposited by thermal evaporation.

In addition, the increase of the number of legs allows an increase in Power Output (Figure 21, blue dots). However, as explain previously, increasing the number of legs will not necessarily increase the resulting Power Output. By increasing the number of legs, the internal resistance of the device also increases. It is, therefore, logical to think that despite the increase in the voltage generated (addition of legs, so the addition of Seebeck coefficient), the resistance of the device is an issue. This reason explains why few generators with a large number of legs (more than 1000 legs) are developed (internal electrical and contact resistance are very high) [48–51].

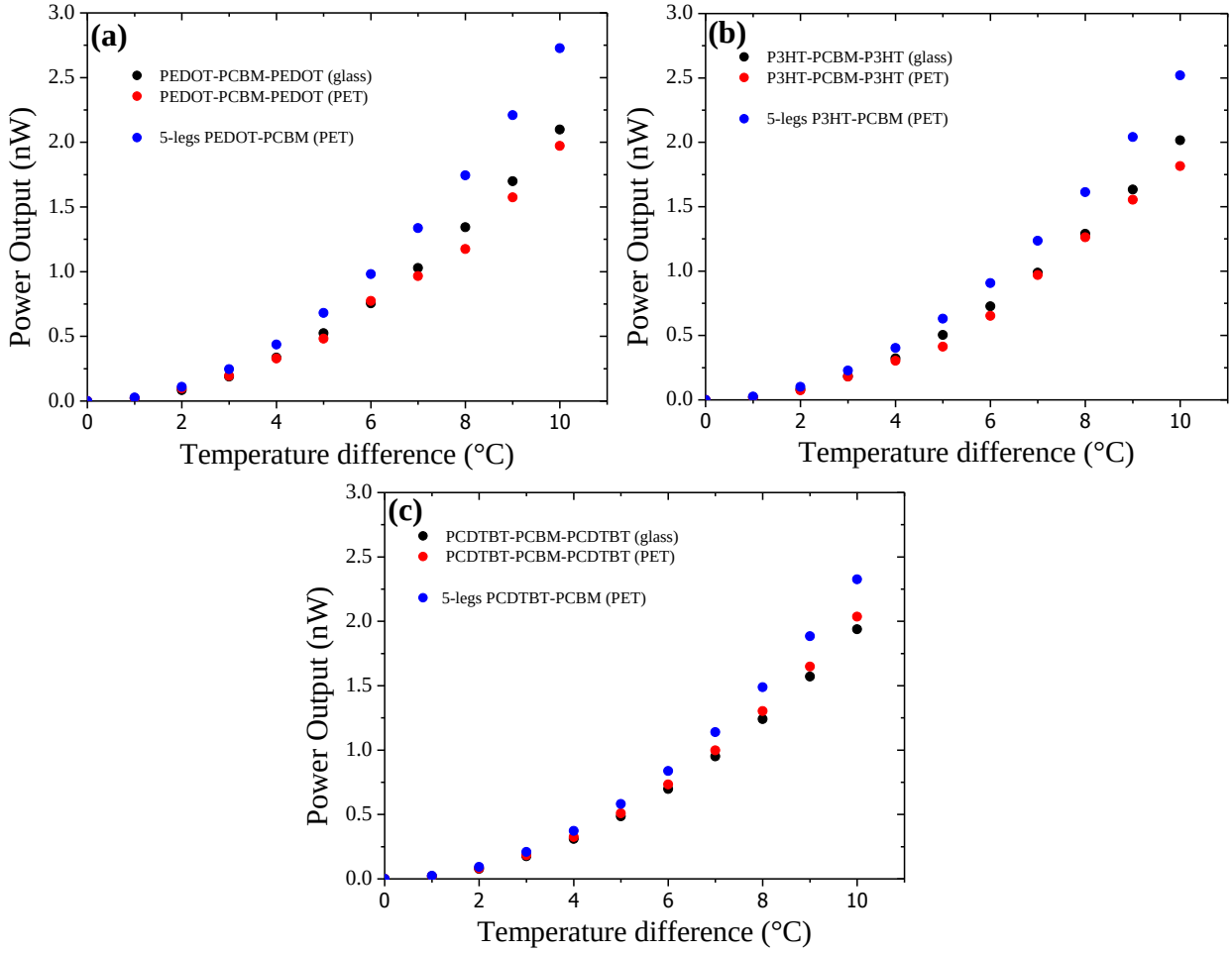

Figure 21: Power Output for the various TEGs, plotted against the applied temperature difference, at room temperature.
Comparison of p-n-p three-legs TEGs on glass vs PET substrates with (a) PEDOT:Tos, (b) P3HT and (c) PCDTBT.

D Conclusion

In this present study, thermoelectric generators on various support were developed for near room temperature application. Full organic TEGs, on glass and PET, showed similar performances. Despite their low Power Output, this kind of devices are proof of concept to develop more efficient material. The main issue was the low stability (absence of electrical conductivity) of the n-type material resulting in low performances.

In parallel, TEGs on silicon substrates were fabricated. In case of high conductive silicon, the coupling with organic material achieved to obtain an enhancement of device performances. Furthermore, the interface between the organic material and the substrate had a crucial role in this phenomenon. By nanostructuring silicon surface, better performances were obtain for hybrid PEDOT:Tos-silicon thermoelectric generators. An increase was achieved thanks to this fine tuning of interface between silicon and organic material. To explain this enhancement, a charge transfer at the silicon-organic interface was suspected [17], thus resulting to a record high power of 2350 nW, for three-legs generator at $\Delta T = 10K$ near room temperature.

Unfortunately, this enhancement could not be verified even with high analytical techniques. These results are in agreement with recent studies on hybrid systems. Scientists have focused on the use of various strategies (interfacial transport and structural/morphological effects) to improve the thermoelectric performance. However, it was proven difficult to establish the fundamental physics driving these performance enhancements [52,53]. The development of the next generation hybrid thermoelectric materials and device requires an improvement in the understanding of the carrier transport physics in complex multiphase systems.

Finally, it would be wise to homogenize the reporting of results related to TEGs. Indeed, it is difficult to compare the performance of TEGs at present. Each team uses its own architecture, the size and number of legs are rarely similar. It is especially in the conditions of analysis, that the greatest differences occur. Performances can be drastically changed if the temperature gradient is achieved at room temperature or under heating. Data that is rarely provided by the authors [16,54,55].

References

[1] J. He, T. M. Tritt, *Science* **2017**, *357*, eaak9997.

[2] L.-D. Zhao, G. Tan, S. Hao, J. He, Y. Pei, H. Chi, H. Wang, S. Gong, H. Xu, V. P. Dravid, C. Uher, G. J. Snyder, C. Wolverton, M. G. Kanatzidis, *Science* **2016**, *351*, 141.

[3] V. J Lyons, G. A. Gonzalez, M. G. Houts, C. J. Iannello, J. H. Scott, S. Surampudi, *DRAFT* Space Power and Energy Storage Roadmap - Technologye area 03, NASA, **2010**.

[4] R. L. Cataldo, G. L. Bennett, *Radioisot. - Appl. Phys. Sci.* **2011**.

[5] M. Brignone, A. Ziggiotti, *AIP Conf. Proc.* **2012**, *1449*, 493.

[6] B. Mazar (March 21 **2012**), State *of the art prototype vehicle with a thermoelectric generator*, BMW Group, view on: https://www1.eere.energy.gov/vehiclesandfuels/pdfs/thermoelectrics_app_2012/wednesday/mazar.pdf (July, **2019**).

[7] M. Brunetti, A. Cogliati, D. Iannucci, A. Scandroglio, *Aircraft capable of hovering having an exhaust duct with thermoelectric conversion circuit*, **2015**.

[8] N. R. Kristiansen, G. J. Snyder, H. K. Nielsen, L. Rosendahl, *J. Electron. Mater.* **2012**, *41*, 1024.

[9] BioLite Inc., CampStove 2 view on: https://eu.bioliteenergy.com/products/campstove-2 (July, **2019**).

[10] D. Champier, J. P. Bedecarrats, M. Rivaletto, F. Strub, *Energy* **2010**, *35*, 935.

[11] G. F. Rinalde, L. E. Juanicó, E. Taglialavore, S. Gortari, M. G. Molina, *Int. J. Hydrog. Energy* **2010**, *35*, 5818.

[12] M. F. Silva, J. F. Ribeiro, J. P. Carmo, L. M. Gonçalves, J. H. Correia, In *Scanning Probe Microscopy in Nanoscience and Nanotechnology 3*; Bhushan, B., Ed.; NanoScience and Technology; Springer Berlin Heidelberg: Berlin, Heidelberg, **2013**; pp. 485–528.

[13] M. Orrill, S. LeBlanc, *J. Appl. Polym. Sci.* **2017**, *134*.

[14] Gordon B. Haxel, James B. Hedrick, and Greta J. Orris, *USGS* **2002**, Fact Sheet 087-02.

[15] N. Lowhorn, W. K. Wong-Ng, J. Lu, E. L. Thomas, M. Otani, M. L. Green, N. Dilley, J. Sharp, T. N. Tran, *Appl. Phys. -Mater. Sci. Process.* **2009**, *96*.

[16] B. Russ, A. Glaudell, J. J. Urban, M. L. Chabinyc, R. A. Segalman, *Nat. Rev. Mater.* **2016**, *1*, 16050.

[17] Y. Zhang, S.-J. Park, *Polymers* **2019**, *11*.

[18] S. M. Haque, J. A. A. Rey, A. AbubakarMasúd, Y. Umar, R. Albarracin, *Prop. Appl. Polym. Dielectr.* **2017**.

[19] B. Russ, A. Glaudell, J. J. Urban, M. L. Chabinyc, R. A. Segalman, *Nat. Rev. Mater.* **2016**, *1*, 16050.

[20] Hideyoshi Kume (Feb6, **2013**), *Fujifilm Shows High-efficiency Thermoelectric Converter Using Organic Material*, view on: https://tech.nikkeibp.co.jp/dm/english/NEWS_EN/20130206/264517/ (July, **2019**)

[21] R. Tian, C. Wan, N. Hayashi, T. Aoai, K. Koumoto, *MRS Bull.* **2018**, *43*, 193.

[22] R. Kroon, D. A. Mengistie, D. Kiefer, J. Hynynen, J. D. Ryan, L. Yu, C. Müller, *Chem. Soc. Rev.* **2016**, *45*, 6147.

[23] C. E. Kinsella, S. M. O'Shaughnessy, M. J. Deasy, M. Duffy, A. J. Robinson, **2014**.

[24] D. M. Rowe, G. Min, *J. Power Sources* **1998**, *73*, 193.

[25] C. Goupil, W. Seifert, K. Zabrocki, E. Müller, G. J. Snyder, *Entropy* **2011**, *13*, 1481.
[26] O. Bubnova, X. Crispin, *Energy Environ. Sci.* **2012**, *5*, 9345.
[27] K. Uchida, M. Ishida, T. Kikkawa, A. Kirihara, T. Murakami, E. Saitoh, *J. Phys. Condens. Matter* **2014**, *26*, 343202.
[28] Y. Kishita, Y. Ohishi, M. Uwasu, M. Kuroda, H. Takeda, K. Hara, *J. Clean. Prod.* **2016**, *126*, 607.
[29] P. M. Kumar, V. Jagadeesh Babu, A. Subramanian, A. Bandla, N. Thakor, S. Ramakrishna, H. Wei, *Designs* **2019**, *3*, 22.
[30] O. Bubnova, Z. U. Khan, A. Malti, S. Braun, M. Fahlman, M. Berggren, X. Crispin, *Nat. Mater.* **2011**, *10*, 429.
[31] V. Jovovic, *Thermoelectric Waste Heat Recovery Program for Passenger Vehicles*; Gentherm Incorporated, Azusa, CA (United States), **2015**.
[32] A. K. Menon, S. K. Yee, *J. Appl. Phys.* **2016**, *119*, 055501.
[33] A. K. Menon, O. Meek, A. J. Eng, S. K. Yee, *J. Appl. Polym. Sci.* **2017**, *134*.
[34] F. Suarez, A. Nozariasbmarz, D. Vashaee, M. C. Öztürk, *Energy Environ. Sci.* **2016**, *9*, 2099.
[35] F. Jiao, C. Di, Y. Sun, P. Sheng, W. Xu, D. Zhu, *Philos. Transact. A Math. Phys. Eng. Sci.* **2014**, *372*, 20130008.
[36] I. Dani, A. Roch, L. Stepien, C. Leyens, M. Greifzu, M. von Lukowicz, In *Digital Product and Process Development Systems*; Kovács, G. L.; Kochan, D., Eds.; IFIP Advances in Information and Communication Technology; Springer Berlin Heidelberg, **2013**; pp. 181–184.
[37] K. Suemori, S. Hoshino, T. Kamata, *Appl. Phys. Lett.* **2013**, *103*, 153902.
[38] S. Hwang, W. J. Potscavage, R. Nakamichi, C. Adachi, *Org. Electron.* **2016**, *31*, 31.
[39] W. Wijesekara, L. Rosendahl, D. R. Brown, G. J. Snyder, *J. Electron. Mater.* **2015**, *44*, 1834.
[40] F. Cheng, *Thermoelectr. Power Gener. - Look Trends Technol.* **2016**.
[41] A. D. Xia, S. Wada, H. Tashiro, *Appl. Phys. Lett.* **1998**, *73*, 1323.
[42] L. Venema, *Nature* **2011**, *479*, 309.
[43] Bar J. Van Zeghbroeck (**1996-1997**), *2.9 Mobility - Resistivity - Sheet Resistance*, Colorado University, view on: http://ecee.colorado.edu/~bart/book/mobility.htm (July, **2019**).
[44] J. Zhou, B. Liao, B. Qiu, S. Huberman, K. Esfarjani, M. S. Dresselhaus, G. Chen, *Proc. Natl. Acad. Sci.* **2015**, *112*, 14777.
[45] A. W. Van Herwaarden, *Sens. Actuators* **1984**, *6*, 245.
[46] M.-K. Kim, M.-S. Kim, S. Lee, C. Kim, Y.-J. Kim, *Smart Mater. Struct.* **2014**, *23*, 105002.
[47] L. Wang, Z. Zhang, L. Geng, T. Yuan, Y. Liu, J. Guo, L. Fang, J. Qiu, S. Wang, *Energy Environ. Sci.* **2018**, *11*, 1307.
[48] Y. Wang, S. M. Zhang, Y. Deng, *J. Mater. Chem. A* **2016**, *4*, 3554.
[49] L. Wang, Q. Yao, W. Shi, S. Qu, L. Chen, *Mater. Chem. Front.* **2017**, *1*, 741.
[50] H. Fang, B. C. Popere, E. M. Thomas, C.-K. Mai, W. B. Chang, G. C. Bazan, M. L. Chabinyc, R. A. Segalman, *J. Appl. Polym. Sci.* **2017**, *134*.
[51] A. Fabian-Mijangos, J. Alvarez-Quintana, *Bringing Thermoelectricity into Realality* **2018** (*DOI: 10.5772/intechopen.75790*).
[52] N. E. Coates, S. K. Yee, B. McCulloch, K. C. See, A. Majumdar, R. A. Segalman, J. J. Urban, *Adv. Mater.* **2013**, *25*, 1629.
[53] J. Choi, J. Y. Lee, S.-S. Lee, C. R. Park, H. Kim, *Adv. Energy Mater.* **2016**, *6*, 1502181.
[54] H. Wang, C. Yu, *Joule* **2019**, *3*, 53.
[55] L. C. Ding, A. Akbarzadeh, L. Tan, *Renew. Sustain. Energy Rev.* **2018**, *81*, 799.

General Conclusion

Organic and hybrid thermoelectricity is a field that is still in its infancy and presents a lot of exploration opportunities. The recent emergence of connected and communication technologies, as well as energy issues and the threat of global warming, could make organic and hybrid thermoelectric devices an important market. For thermoelectric products to find their place in this context of emerging new technologies, it is still necessary to overcome barriers related to the performance and manufacturing processes of thermoelectric devices.

The main objective of this Ph.D. thesis, the fabrication of an efficient polymer thermoelectric material was successfully tackled. The basic philosophy of the work was to optimize the thermoelectric properties of various organic materials towards efficient thermoelectric design. Then, the interfacial effects between the silicon substrate and organic materials were utilized to fabricate a hybrid thermoelectric generator thanks to a novel approach developed.

P-type polymers synthesized were tuned via various different methods, all of which had played on the doping level analog to the carrier concentration of the material. The n-type organic materials were characterized, and despite poor air stability, they showed interesting thermoelectric properties with respect to literature values. Thanks to a fine tuning of electronic properties, PEDOT:Tos with a power factor of 240 µW/mK² and PCBM with a power factor of 2.44 µW/mK² were the best materials for p- & n-type series. It is noteworthy that a new n-type polymer PNDIBS with selenium atoms, developed by Prof. Jenekhe's group, obtained similar results than standard PNDI(2OD)2T n-type polymer. Unfortunately, no air stable n-type organic material was recorded.

In Chapter 3, all organic materials were combined with p and n type silicon wafers. Thermoelectric properties, Seebeck coefficient, electrical conductivity and power factor were measured for each hybrid material. The results showed an interesting behaviour via increasing the thickness of the polymer layer, in fact thermoelectric properties could be tuned with this strategy. Although the origin of this behaviour is not completely clarified, it could be appointed to interfacial charge transfer phenomena.

The shortage of n-type thermoelectric materials (strongly related to their instability to ambient air) has forced to propose new synthesis approaches for these materials. The novel approach, with silicon substrate and organic material on top, enabled the development of an

efficient air stable n-type material for thermoelectric applications. In fact, the impurities inside the silicon substrate greatly influenced the charge carrier type in the hybrid material. Thus, with negatively doped silicon, the corresponding devices were of n-type (regarding its Seebeck coefficient), despite the fact that organic material of p-type had been deposited above them. The hybrid PEDOT:Tos/n-type silicon reached a record value of 0.65 mW/mK^2, one of the best value reported for hybrid n-type material.

Chapter 4, where the silicon surface was nanostructured, provided further insight on the interface role in properties. In fact, increasing the specific area produces an enhancement of the thermoelectric properties compared to bare silicon. Despite only employing PEDOT:Tos, this strategy is suspected to be applied to any organic material, and the same enhancement should be obtained.

Finally, thermoelectric generators were fabricated by using these hybrid systems and their behaviour was recorded with respect to the temperature difference. The best power output, 2350 nW, was obtained for three-legs TEG of six PEDOT:Tos layers on silicon nanowires at temperature difference of 10K. Furthermore, as proof of concept, full organic flexible TEGs were developed, the same performances under binding were obtained compared to TEGs on glass.

Perspectives

Our study was designed to address different aspects and problems of thermoelectricity in the organic field. Each of them still requires additional studies. The prospects are numerous, and listed below:

- As far as materials are concerned, the thermal conductivity of the different organic and hybrid materials presented in this study should first be determined. In addition, it would be necessary to increase the thermoelectric performance of p- & n-type materials. In the case of n-type materials, new approaches need to be developed to make them more air-stable [1]. For example, Pei's group by a rational design strategies obtained high performances for an air stable n-type polymer [2]. Thanks to a rigid coplanar backbone through carbon–carbon double-bond connections and intramolecular hydrogen bonds, stronger interchain interactions, and longer polaron delocalized length were achieved. Furthermore, with two electron-deficient building blocks with low LUMO levels, down to 4.49 eV, greatly contributing to their high doping efficiency and good air stability.

- Silicon has shown its many advantages as a substrate in this study. It would be interesting to test other inorganic substrates in order to compare the results and better understand the phenomena related to the interfaces. Gallium arsenide appears to be a prime candidate [3,4]. It has a higher saturated electron velocity and higher electron mobility, allowing gallium arsenide transistors to function at frequencies in excess of 250 GHz. GaAs devices are relatively insensitive to overheating, owing to their wider energy bandgap, and they also tend to create less noise (disturbance in an electrical signal) in electronic circuits than silicon devices, especially at high frequencies. This is a result of higher carrier motilities and lower resistive device.

- Hybrid assemblies between silicon and organic materials have resulted in improved thermoelectric properties. However, this improvement occurred at the expense of the flexibility offered by organic materials. It would be interesting to evaluate the effect with flexible silicon. Some groups have already used flexible silicon in the design of solar cells [5,6], and performances similar to bare silicon have been obtained. Recently, Prof. Hussain has developed a flexible thermoelectric generator [7]. Flexible and semi-transparent high performance thermoelectric energy harvesters were fabricated on low

cost bulk mono-crystalline silicon (100) wafers. The released silicon was only 3.6% as thick as bulk silicon reducing the thermal loss significantly and generating nearly 0.14 µW at temperature difference of 20K. These results are promising for our approach.

- The silicon nanowires could be used as fillers in the PEDOT: Tos films (**Appendix III**), for example. Thus the number of interfaces between the polymer and the inorganic compound would be greater, and therefore better thermoelectric performance would be obtained. Galliani *et al.* already performed the tuning of PEDOT:Tos thermoelctric properties through Mn_3O_4 nanoparticles inclusion [8]. Unfortunately, when nanoparticles sit aside the chains, nanoparticle size impacts on chain packing, leading to lower interchain hopping. As a result, hole mobility decreased upon increasing of nanoparticle concentration. Since the issue is related to the structural reorganization of the polymer upon the formation of the nanocomposite, one may implement polymerization and post-polymerization treatments that favour the rearrangement of NPs [9], with the aim of promoting their location at the chain ends instead that aside chains. So the size of silicon nanowires will be detrimental to achieve an enhancement of thermoelectric properties.

- Another possible improvement could come from the TEG design. New architectures could be developed following the example of Yee's group with their radial thermoelectric generator fabricated from n- & p-type conducting polymers [10]. However, the contacts remain an issue in the design of efficient thermoelectric generators. The contact resistance is an underestimated research axis but has a great influence on the device performance. Nielsch *et al*. have focused to better understand the latter [11].

- Finally, the most promising improvement would be to make block copolymers (BCP) comprising p-type and n-type material in the same backbone. Work on the subject already exists, so block copolymers based on P3HT-*b*-P(NDI2OD-T2) have been synthesized successfully [12]. Each block was doped, and the electrical conductivity of p-doped BCP was 1.4×10^{-3} S/cm, whereas, for n-doped BCP, the film conductivity is 1.7×10^{-3} S/cm. In addition, the sign of the Seebeck coefficients of doped BCP obtained using either p- or n-dopants were quite different from each other, *i.e.*, 596 and −602 µV/K. The use of a block copolymer with well-defined conjugation units, in blends with a fully conjugated polymer, could offer a new strategy for developing

organic-based thermoelectric materials. Then such a material could be used to make nanoscale thermoelectric generator [13]. This strategy was already used for inorganic thermoelectric generator, Snyder *et al.* developed self-assembled nanometer lamellae of PbTe and Sb_2Te_3 [14]. They managed to have exceptionally high thermoelectric efficiency (Seebeck 30 µV/K and electrical resistivity 4×10^{-4} Ω/cm). Applying to organic material, where the direct self-auto assembly is well studied [15], could achieve interesting results.

References

[1] Y. Lu, J.-Y. Wang, J. Pei, *Chem. Mater.* **2019**.

[2] Y. Lu, Z.-D. Yu, R.-Z. Zhang, Z.-F. Yao, H.-Y. You, L. Jiang, H.-I. Un, B.-W. Dong, M. Xiong, J.-Y. Wang, J. Pei, *Angew. Chem. Int. Ed.* **2019**, *58*, 11390.

[3] M. Kuwata-Gonokami, In *Comprehensive Semiconductor Science and Technology*; Bhattacharya, P.; Fornari, R.; Kamimura, H., Eds.; Elsevier: Amsterdam, **2011**; pp. 213–255.

[4] T. E. Schlesinger, In *Encyclopedia of Materials: Science and Technology*; Buschow, K. H. J.; Cahn, R. W.; Flemings, M. C.; Ilschner, B.; Kramer, E. J.; Mahajan, S.; Veyssière, P., Eds.; Elsevier: Oxford, **2001**; pp. 3431–3435.

[5] A. Augusto, P. Balaji, H. Jain, S. Y. Herasimenka, S. G. Bowden, *MRS Adv.* **2016**, *1*, 997.

[6] S. Thiyagu, C.-C. Hsueh, C.-T. Liu, H.-J. Syu, T.-C. Lin, C.-F. Lin, *Nanoscale* **2014**, *6*, 3361.

[7] G. A. T. Sevilla, S. B. Inayat, J. P. Rojas, A. M. Hussain, M. M. Hussain, *Small* **2013**, *9*, 3916.

[8] D. Galliani, S. Battiston, D. Narducci, *J. Nanosci. Nanotechnol.* **2017**, *17* (3), 1579-585.

[9] J. Heinze, B. A. Frontana-Uribe, S. Ludwigs, *Chem. Rev.* **2010**, *110*, 4724.

[10] A. K. Menon, O. Meek, A. J. Eng, S. K. Yee, *J. Appl. Polym. Sci.* **2017**, *134*.

[11] R. He, G. Schierning, K. Nielsch, *Adv. Mater. Technol.* **2018**, *3*, 1700256.

[12] J.-S. Kim, S.-Y. Ku, N. J. Economou, W. Jang, D. H. Wang, *Nanoscale Microscale Thermophys. Eng.* **2019**, *23*, 222.

[13] S. Yazdani, M. T. Pettes, *Nanotechnology* **2018**, *29*, 432001.

[14] T. Ikeda, L. A. Collins, V. A. Ravi, F. S. Gascoin, S. M. Haile, G. J. Snyder, *Chem. Mater.* **2007**, *19*, 763.

[15] A. P. Upadhyay, D. K. Behara, G. P. Sharma, R. G. S. Pala, S. Sivakumar, In *Advanced Theranostic Materials*; John Wiley & Sons, Ltd, **2015**; pp. 297–335.

Publications and communications

Publications

Aqueous PCDTBT:$PC_{71}BM$ Photovoltaic Inks Made by Nanoprecipitation, G. Prunet, L. Parrenin, G. Pecastaings, C. Brochon, G. Hadziioannou, and E. Cloutet, *Macromol. Rapid Commun.*, **2018**, *39*, 1700504.

Tailoring Silicon – Conducting Polymer Hybrid Thermoelectric Generator Properties, G. Prunet, I. Petsagkourakis, S. Perrot, A. Sharma, E. Pavlopoulou, S. Dilhaire, S. Grauby, Mats, Fahlman, E. Cloutet, G. Fleury and G. Hadziioannou, *to be submitted*.

Communications

January 2018: (**Poster**) International Conference on Organic and Hybrid Thermoelectrics (**ICOT2018**), Valencia, SPAIN. *Improvement of thermoelectric properties of PEDOT:Tos based devices* – G. Prunet, I. Petsagkourakis, E. Cloutet, E. Pavlopoulou, G. Fleury, S. Grauby, S. Dilhaire and G. Hadziioannou.

May 2018: (**Poster**) Bordeaux Polymer Conference (**BPC2018**), Bordeaux, FRANCE. *Improvement of thermoelectric properties of hybrid polymer/silicon devices* – G. Prunet, I. Petsagkourakis, E. Cloutet, E. Pavlopoulou, G. Fleury, S. Grauby, S. Dilhaire and G. Hadziioannou.

October 2018: (**Oral contribution**) Groupement de recherche sur Organic Electronics for the new eRA (**GDR OERA**), Aix-en-Provence, FRANCE. *Polymer Electronic Materials & Devices* – G. Prunet, E. Cloutet and G. Hadziioannou.

March 2019 (**Oral contribution**) Interfaces in Organics and Hybrid Thin-Film Optoelectronics (**INFORM19**), Valencia, SPAIN. *High performance polymer and polymer/inorganic thermoelectric materials* – G. Hadziioannou, G. Prunet, I. Petsagkourakis, S. Perrot, A. Sharma, E. Cloutet, G. Fleury, E. Pavlopoulou, S. Grauby, S. Dilhaire., G. Portale, M. Fahlman, X. Crispin, M. Berggen.

June 2019: (**Poster**) 14th International Symposium on Functional π-Electron Systems (**Fπ14**), Berlin, GERMANY. *Improvement of thermoelectric properties of hybrid polymer/silicon devices* – G. Prunet, I. Petsagkourakis, E. Cloutet, E. Pavlopoulou, G. Fleury, S. Grauby, S. Dilhaire and G. Hadziioannou.

Appendix I:

Theoretical background

A Thermoelectric theory

1. Peltier effect

The Peltier effect is the presence of heating or cooling at an electrified junction of two different conductors, and is named after Jean Charles Athanase Peltier, who discovered it in 1834 [1]. When a current is made to flow through a junction between two conductors, A and B, heat may be generated or removed at the junction (Figure 1, Thermoelectric cooler example).

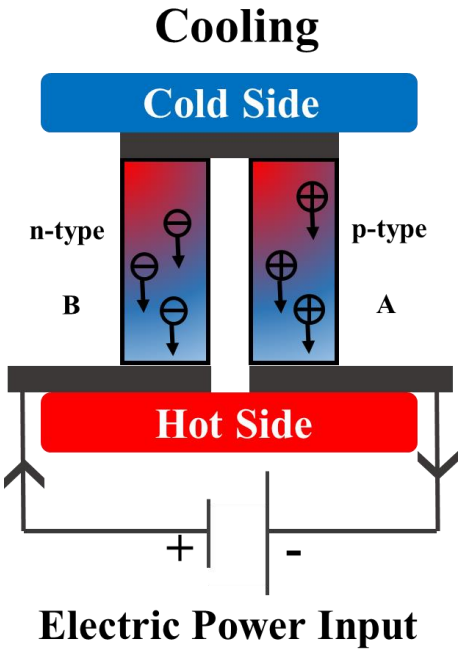

Figure 1: A thermoelectric circuit composed of materials of different Peltier coefficient (p-doped and n-doped semiconductors), configured as a thermoelectric cooler.

A potential gradient generates both a charge flow and a heat flow. The Peltier heat generated at the junction could be written as Equation 1:

$$Q = (\Pi_a - \Pi_b).I \quad (1)$$

With Q the heat flux, Π_a and Π_b are the Peltier coefficients of conductors A and B, and I is the electric current (from A to B). This phenomenon can be understood qualitatively by noting that the particles conducting the current are also those that carry the energy. Thus, if an electric current appears then the particles move carrying with them their energy.

The Peltier effect can be considered as the back-action counterpart to the Seebeck effect if a simple thermoelectric circuit is closed, then the Seebeck effect will drive a current, which in turn (by the Peltier effect) will always transfer heat from the hot to the cold junction. The close relationship between Peltier and Seebeck effects can be seen in the direct connection between their coefficients (Equation 2):

$$\Pi = T.S \tag{2}$$

2. Thomson effect

Thomson effect combines Seebeck and Peltier coefficient. In fact, a heat transfer happens when a material is crossed by an electrical field under a temperature gradient. This Thomson effect was predicted and subsequently observed in 1851 by Lord Kelvin (William Thomson) [2]. It describes the heating or cooling of a current-carrying conductor with a temperature gradient. The heat flux emitted or absorbed per unit volume can be quantified as follows:

$$Q = -K.J.\vec{\nabla}T \tag{3}$$

Where Q is the heat flux, J is the current density, T is the temperature gradient, and K is the Thomson coefficient.

Since this effect is a combination of the two previous effects, it is not surprising that the latter coefficient is related to the Seebeck and Peltier coefficients. Lord Kelvin thus showed the following equalities:

$$\begin{cases} \pi = S.T \\ K = T.\dfrac{dS}{dT} \end{cases} \tag{4}$$

These equations show that the less the Seebeck coefficient will be dependent on the temperature and the less the Thomson effect will be important. In practice, the variation of the

coefficient with the temperature has a look of a parabola. However, the final equation, neglects Joule heating and ordinary thermal conductivity, the full equation is presented in a next part.

3. Joule effect

Joule's law was developed by Joule between the years 1840 and 1843 [3]. The circulation of an electric current through a resistive material causes the creation of a heat flux Q:

$$Q = \rho . J^2 \tag{5}$$

With Q the heat flux, ρ the electrical resistivity of the material and J the current density. The flow of charge appears here squared, and the electrical resistivity is always positive which imposes a heat flow Q> 0. Unlike the Peltier and Thomson effects, the Joule effect is irreversible and can only create heat and not absorb it.

4. Full thermoelectric equations

To understand the Peltier (Π), Seebeck (S), and Thomson (K) effects more precisely, the full equations of heat and charge flow are needed. In fact, more than one of the above effects is involved in the operation of a thermoelectric device. All these effects can be gathered together in a consistent and rigorous way. The following Equation 6, describes the relation between current density and Seebeck coefficient [4]. (this equation is the simplified version to have a better understanding of the related phenomenon):

$$J = \sigma(-\nabla V - S\nabla T) \tag{6}$$

To describe the Peltier and Thomson effects the flow of energy must be considered. To start, the dynamic case where both temperature and charge may be varying with time can be considered. The full thermoelectric equation for the energy accumulation, ė, is [4]:

$$\dot{e} = \nabla . (\kappa \nabla T) - \nabla . (V + \Pi) J + q_{ext} \tag{7}$$

Where κ is the thermal conductivity. The first term is the Fourier's heat conduction law, and the second term shows the energy carried by currents. The third term, q_{ext}, is the heat added from an external source (if applicable).

B Semi-conducting polymers theory

1. Fundamentals on semi-conducting physics and band energy theory [5–8].

Charge transport in material happens thanks to charge carrier displacement which induce an electrical current. The most frequent charge carrier is electron particularly in metals. However, in semi-conducting materials, two kind of charge carriers can be present electrons and holes. Classical Mechanics can't explain all properties of atomic dimensions, that's why by using Quantum Mechanics, more accurate model can describe these properties. So, in case of an isolated atom, each electron has a defined energy quantity (Figure 2), and is forced to occupy a certain energy level, there is a quantification of energy. When electron absorb or transmit energy corresponding to the energy difference between two states, electron moves from one to another.

By conceptual way, bringing closer N atoms, inter-atomics forces lead to an overlap of atomic orbitals and an increase/broadening of permitted energy. This broadening creates energy bands, that is a group of permitted energy states slightly space (Figure 2). Highest energy band is called conduction band (CB), while lower energy band is called valence band (VB). In materials, insulators and semi-conductors, these two bands are separated by a forbidden band (Eg), also called band gap. Charge carriers are associated to electrons in CB and to holes in VB. During filling of permitted energy states, electrons and holes tend towards unoccupied states of lower energies. To note because of Pauli exclusion principle, energy levels are restricted at only two electrons, so electrons fill in first VB. In intrinsic semi-conductors, at T ≈ 0K, VB is full of electrons and CB is completely empty (Figure 2).

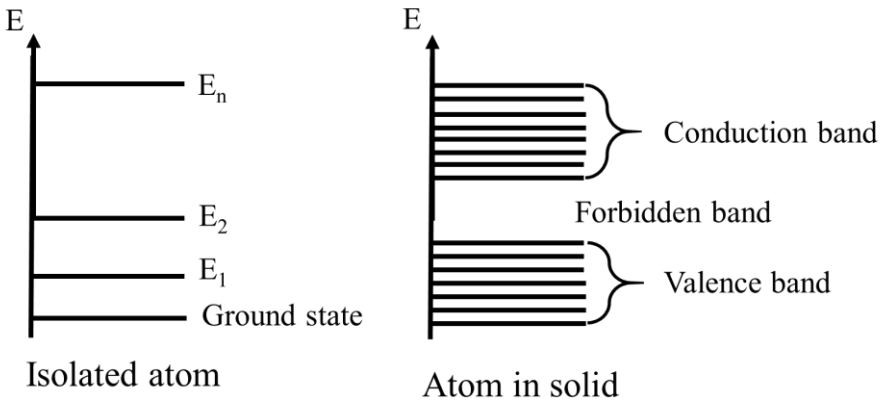

Figure 2: Energy diagram of an isolated atom and atom in solid.

Under an electric disruption, charges could freely move in corresponding energy band without modification of charge carrier concentration inside the same band. But, when VB is full and CB is empty, it's impossible to obtain any electrical current, this is linked to charge carrier absence. Under a more powerful excitation, charge carrier concentration inside a band will be modified, increasing number of electrons in CB and holes in VB. That's why two kinds of charge carriers, electrons (negatively charged) and holes (positively charged) are present.

In order to move an electron from VB to CB, an energy equal to Eg, principal parameter for classification and distinction of material, is mandatory. When Eg is higher than 2 eV, the material is an insulator with low concentration of charge carrier, implying a very bad electrical conductivity and the Fermi Level (Ef) exists inside one of these two bands. For metals, Eg nonexistent / almost nonexistent thanks to overlapping of VB with CB. Finally, semi-conducting materials, are considered intermediary because Eg is lower than 2 eV. In their case, at room temperature, thermal energy is enough to excited a small number of electrons from VB to CB. (Figure 3)

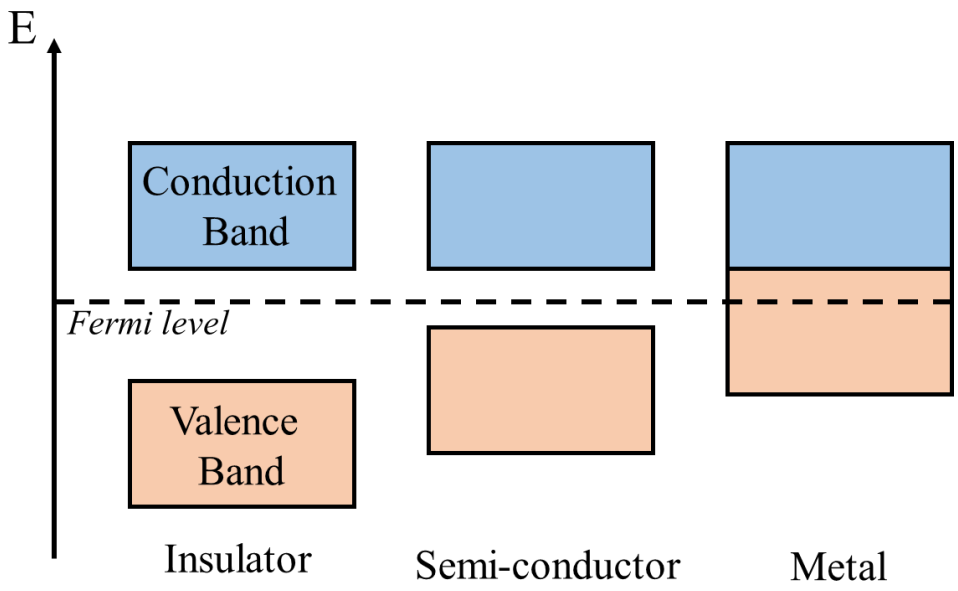

Figure 3: Band theory of insulator, semi-conductor and metal

To have a better comprehension of semi-conducting materials and to understand why they are a great class for thermoelectric application, Density of States (*DoS(E)*) have to be explained. *DoS(E)* is defined as the number of possible states that an electron can occupy per unit volume and per energy interval. This is a mathematical concept, its filling and shape can be used to evaluated properties of a material (electrical, electronic and thermoelectric).

As explain before, in electron rich systems, energy levels are formed, separated by Eg, and at 0 K, charge carriers fill the lowest level first, inside VB, while the highest filled energy state is called the Fermi Level, Ef (electronic band above Ef is CB, separated by Eg). To described the possibility of an electron to fill at a certain available level of these bands at an absolute temperature T, Fermi-Dirac distribution f0(E) is used [9]:

$$f_0(E) = \frac{1}{1 + e^{\frac{E-\mu}{kBT}}} \quad (1)$$

where μ is the chemical potential (At T ≈ 0 K, μ = Ef)[10] and kB the Boltzmann constant.

Thanks to *DoS(E)*, the number of available states that charge carriers can fill, and f0(E), the probability of an electron to fill a state, this is possible to obtain the actual number of charge carriers per volume in the system (N, also called carrier concentration or charge carrier density) with the integral of their product. Hence, for T>0 and with energy E in the system [9–11]:

$$N = \sigma \int_0^{\infty} f_0(E) \, . DoS(E) \, dE \quad (2)$$

N is one of the key parameter in order to tune properties of semi-conducting materials.

In previous part, it was explained that material can be classified (insulator, metal or semi-conductor) based on its band gap, but *DoS(E)* have to be also considered. Band structures for insulator, semi-metal, metal and semi-conductor are presented in Figure 4 [10,12].

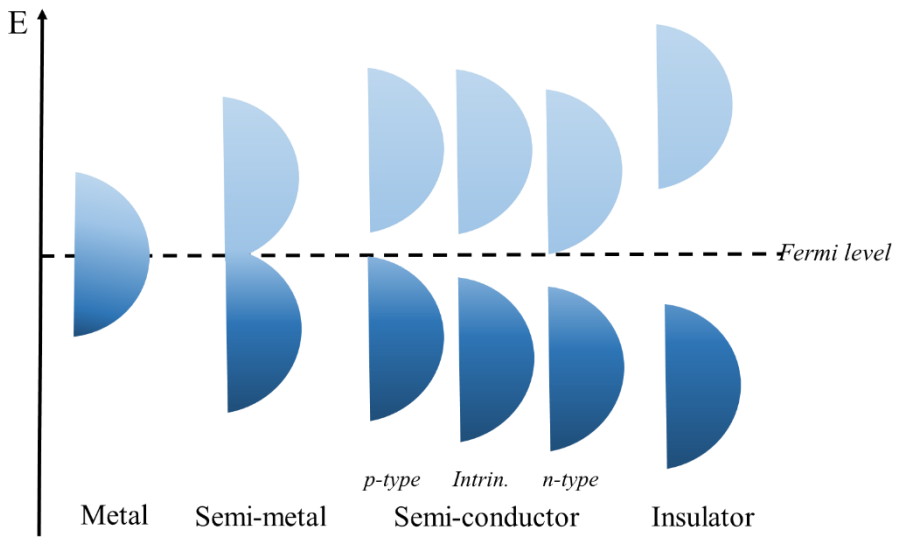

Figure 4: Filling of the electronic states in various types of materials for a metal, a semi-metal, semi-conductors (p, n & intrinsic) and insulator. (Dark Blue = alls states filled and Light Blue = no state filled following Fermi-Dirac distribution).

So a semi-conductor has a Eg (< 2 eV), and by considering *DoS(E)* filling, two consequences are possible resulting in p- or n-type semi-conductor. When CB is unfilled and VB is semi-filled, the material is a p-type semiconductor, holes are the main charge carriers. On another hand, semi-conductor that conducts electrons is n-type semi-conductor. Its VB is fully filled and there are also filled states in CB. This partial filling of bands in semiconductors allows to finely tune the band structure. This tuning can occur either by filling/emptying the states or by modifying the shape of the Density of States [9,11,12].

A correlation is possible between modification in *DoS(E)* and macroscopic properties of the materials, when they are expressed as a function of *DoS(E)*. The electric current, $\overrightarrow{J_e}$, can be expressed as [9]:

$$\overrightarrow{J_e} = \frac{q}{3} \cdot \int v^2 . \tau \cdot \left(q\epsilon \frac{\partial f_0}{\partial E} \right) D(E) dE + \frac{q}{3} \cdot \int v^2 . \tau \cdot \left(\frac{\partial f_0}{\partial x} \right) D(E) dE \qquad (3)$$

where ϵ is the one-dimensional of field $\vec{E}$, τ is the relaxation time and v the drift velocity of the charge carrier in the system. This Equation (3) can also be reformulated as:

$$\overrightarrow{J_e} = \mathrm{q} \,.\, \mathrm{N} \,.\, \mu_e . \epsilon + q \,.\, a \,.\, \frac{\partial N}{\partial x} \tag{4}$$

where, N, is the carrier concentration as defined in Equation (2), μ_e is the charge carrier mobility (m^2/Vs) and a is the carrier diffusivity (m^2/s). Equation (4) is also called the drift-diffusion equation [9]. In the first part of the relationship, the electrical conductivity can be identified as:

$$\sigma = \mathrm{q} \,.\, \mathrm{N} \,.\, \mu_e \tag{5}$$

where:

$$\mu_e = \frac{\frac{q}{3} \,.\, \int_0^\infty v^2 \,.\, \tau \,.\, \left(\frac{\partial f_0}{\partial E}\right) . D(E) dE}{\int_0^\infty f_0\,(E) . D(E) dE} \tag{6}$$

Consequently, the electrical conductivity can be defined as:

$$\sigma = \frac{q}{3} \,.\, \int_0^\infty v^2 \,.\, \tau \,.\, \left(\frac{\partial f_0}{\partial E}\right) . D(E) dE \tag{7}$$

The importance of the shape and the filling of the Density of States to material properties is highlighted in the extracted relationships for electrical conductivity and charge carrier mobility. Practically speaking, the electrical conductivity of a semiconducting material can be increased either by increasing the carrier concentration (i.e. the filling the states) or by increasing the carrier mobility. Considering that the carrier mobility is the measure of the mobile properties of individual electrons in the system, tuning of μ_e can be achieved by modifications of the material structure. For example, the mobility of an amorphous semiconductor is lower than the mobility of a semi-crystalline or crystalline one as the amorphous material exhibits more structural defects inhibiting the transport of electrons.

Furthermore, following Equation (4), the diffusivity of the charge carriers can be written as:

$$a = \frac{\frac{1}{3}.\int_0^\infty v^2.\tau.f_0.D(E)dE}{\int_0^\infty f_0(E).D(E)dE} \approx \frac{k_B T}{q}.\mu_e \quad (8)$$

Equation (8) is called the Einstein relationship and correlates the mobility with the diffusivity. This equation is only valid when the distribution function follows a Boltzmann distribution law [9,13,14]. Additionally, the Seebeck coefficient can be derived from the Onsager relationships that connect *S* with σ, so *S* is written as:

$$S = \frac{\frac{1}{qT}\int_0^\infty v^2.\tau.(E-\mu).\left(\frac{\partial f_0}{\partial E}\right).D(E)dE}{\int_0^\infty v^2.\tau.\left(\frac{\partial f_0}{\partial E}\right).D(E)dE} \quad (9)$$

Thanks to Equation (9), the influence of *DoS(E)* on the Seebeck coefficient is evident. However, the Seebeck coefficient seems to have a strong dependence to the position of the chemical potential with the respect of the *DoS(E)*, as implied (E-μ) term inside the integral. Indeed, Equation (9) shows that Seebeck coefficient is a measure of the average energy of a carrier above the chemical potential under open circuit conditions, weighted against the differential electrical conductivity at each energy level [9].

Because when T = 0K, the value of the chemical potential is close to the Fermi Level, the charge carrier density N(E) is equal to the *DoS(E)*. Furthermore, to these assumptions, with a metallic conduction, equation (7) can be re-written as [12,15,16]:

$$\sigma = \sigma(E,T) = \frac{q}{3}.\frac{v^2.\tau}{k_B T}.D(E) \quad (10)$$

where σ(E,T) is the Mott's energy dependent electrical conductivity.

With the same assumptions, the mobility van be written as energy dependent:

$$\mu_e(E,T) = \frac{q}{3} \cdot \frac{v^2 . \tau}{k_B T} \tag{11}$$

And the diffusion coefficient:

$$a\,(E,T) = \frac{1}{3} \cdot v^2 . \tau \tag{12}$$

Subsequently, the Seebeck coefficient is derived as:

$$S\,(E,T) = \frac{\pi^2}{3} \cdot \frac{{k_B}^2 T}{q} \cdot \left(\frac{\partial \ln(\sigma(E))}{\partial E} \right)_{E=E_f} \tag{13}$$

which can be re-written as [12,15,16]:

$$S\,(E,T) = \frac{\pi^2}{3} \cdot \frac{{k_B}^2 T}{q} \cdot \left(\left(\frac{1}{\mu_e(E,T)} \cdot \frac{\partial(\mu_e(E,T))}{\partial E} \right)_{E=E_f} + \left(\frac{1}{D(E,T)} \cdot \frac{\partial(D(E,T))}{\partial E} \right)_{E=E_f} \right) \tag{14}$$

So the Seebeck coefficient is analogous to [10,12,17]:

- The slope of the Density of States at Fermi Level
- The slope of the energy dependent “metallic” mobility at Fermi Level

Nevertheless, these relationships are only effective at T close to 0 K. When the temperature starts to increase, the chemical potential is shifting away from the Fermi Level due to the presence of defects in the material (e.g. structural defects). These defects modify the distribution of carriers in the different states (i.e. the Fermi-Dirac distribution) [9,10]. As a result, the Equations (10) - (14) are strictly valid at low temperatures close to 0 K and energies near the Fermi position.

2. Conjugation

If it is energetically advantageous, atoms will bond together to from molecules. The atomic orbitals overlap, sharing their electron density, forming bonds and as a consequence decreasing the inter-atomic distance. Depending on the molecule formed, there are different types of molecular bonds:

σ bonds are rotation symmetric with respect to the axis between the two participating atoms. They are bonding orbital, stabilizing the molecule, with the shared electron density being concentrated at the center between both atoms. The electron density for the corresponding antibonding σ* orbitals with the same rotational symmetry is concentrated on opposite asides, far away from the center between the two atoms. If one were to excite an electron from a σ orbital to a σ* orbital, the bond between atoms would be cut, since the energy of the σ* orbital lies above the ionization energy.

π bonds are weaker than σ bonds, since there is less overlap of the electron densities of the participating atomic orbitals. The binding energy of a C=C double bond, which is composed of one σ and one π bond, is less than twice that two σ bonds. This means, that an electron can be excited from a filled π to an empty π* orbital without cutting the molecular bond.

Since π-conjugation is formed between the overlap of out-of-plane p-orbitals, this requires the molecule to be planar. The molecule is rigid and cannot arbitrarily bend, or rotate along the bond axis without breaking the π bonds.

This part will be focused on π-conjugated polymers. In this system, the electrons of the carbon molecules of the units are delocalized in an extended π-system due to the double bonds. The semi-conducting behavior, in π-conjugated polymer results from this delocalization and express the electronic properties of the material. So, π-bonds where the electrons are delocalized are the Highest Occupied Molecular Orbital (HOMO) of the material and the π*-anti-bonds are the Lowest Unoccupied Molecular Orbital (LUMO). In contrary with organic substance, like ethylene or benzene molecule, where the band gap is too large (insulating material), for a conjugated polymer, the extension of each π-π* bond results in the recombination of π-orbitals. This is transcribed by an addition of states to the HOMO and the LUMO, resulting in a reducing of the band gap and semi-conducting behavior [11,18,19].

For example, the simplest π-conjugated polymer (Polyacetylene), is intrinsically a semi-conducting material thanks to its alternated π-bonds. By treating this polymer with oxidative iodine vapors, radical ions rea formed on the chain, so called solitons, adding more states to the HOMO-LUMO levels, inducing an even more decrease of the band gap. In this state, Polyacetylene shows a high electrical conductivity with a metallic behavior [20–22].

On another side, other π-conjugated polymers, like polythiophenes, are not intrinsically semiconducting and must be doped in order to obtain a semiconducting behavior. The reason of this behavior is due to a localization of the electrons in the π-orbitals of a units. So, chains are oxidized (an electron is taken for p-doped polymer), or reduced (an electron is given for n-doped polymer), in order to improve the delocalization of electrons by changing the thiophene rings configuration to the quinoid form (Figure 5). Consequently, the newly formed double bonds enable the recombination of the π-orbitals, extending the π-system along the chain, and so the charge carriers (holes and electrons) are more easily delocalized, reducing the band gap (semi-conducting behavior achieved) [11,19,23,24].

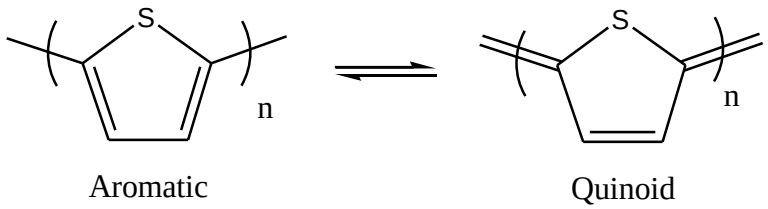

Figure 5: Aromatic to Quinoid form for thiophene

The new charge carriers formed in these "extrinsically" semi-conducting polymers are called polarons or bipolarons. Polaron are due to a chain conformation changes from the aromatic to quinoid form, during the doping, inducing a chain lattice relaxation. Polaron assists in the extension of the π-system (Figure 6). As a result, electronic states are added in the HOMO and LUMO levels (Figure 7), and are referred to polaron bands [19,23,25].

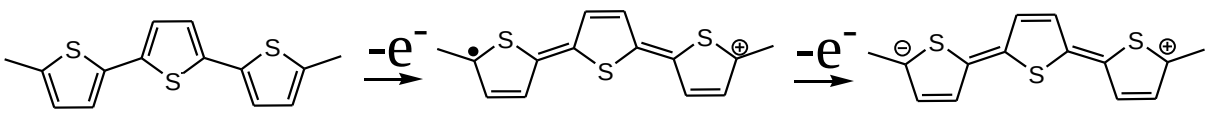

Figure 6: Formation of a polaron (center) and a bipolaron (right) for an oligothiophene

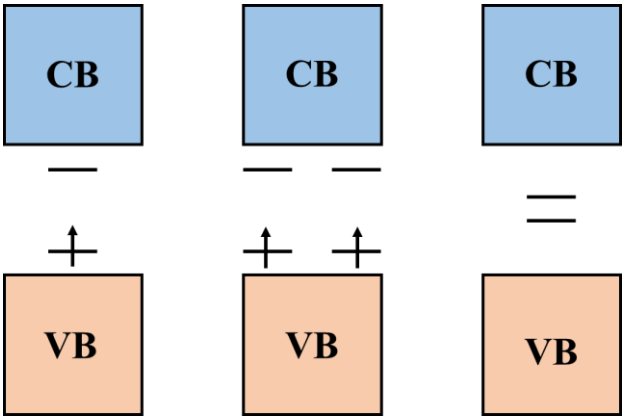

Figure 7: Band structure of one polaron (left), two polarons (center) and one bipolaron (right)

By increasing the doping, multiple polarons (on the same chain) aren't formed in the π-systems, in place a bipolaron is spontaneously created (Figure 7). A bipolaron is an extended lattice relaxation that gives an energy to the system, which is larger than the repulsion between the two ions. That's why, this is thermodynamically more favorable to form a new polaron besides the already existing polaron of the chain, than to anywhere else in the chain. Thus, a bipolaron band of higher energy is created, and by increasing dopant concentration, number of bipolatons is also increased, forming a widened bipolaron bands in the material (Figure 8) [25,26].

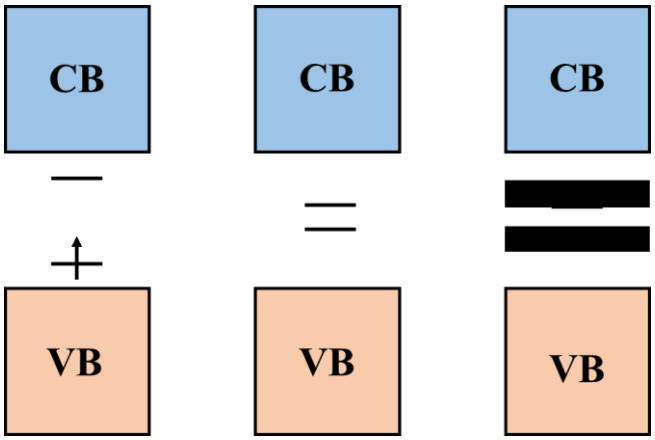

Figure 8: Evolution of the band structure for a conjugated polymer upon doping: low doping level, polaron formation (left), moderate doping level, bipolaron formation , high doping level, formation of bipolaron bands

Density of states of the polymer is constituted by all these electronic states, solitons, polarons or bipolarons, filling it with redox processes. When dopant concentration is low, Dos of the polymer is comparable to a conventional inorganic semi-conductor. By increasing the doping rate, so decreasing the band gap, the polymer DoS tend to resemble to a metal or semi-metal, where the HOMO is the work function of the material [25,26].

The formation of those new energy bands, results in band transport mechanism of the charge carrier between the different energy bands in the polymer. Although, polymers are not perfect crystal, and do not have prerequisites to band transport, so the main charge transport mechanism is a thermally activated hopping transport. Charge carriers "hop" between the different units in an inter-chain (green arrow) and intra-chain (red arrow) level (Figure 9). These hopping sites are the extended π-systems formed between the chain units, which are inherent conducting [11,24,27,28].

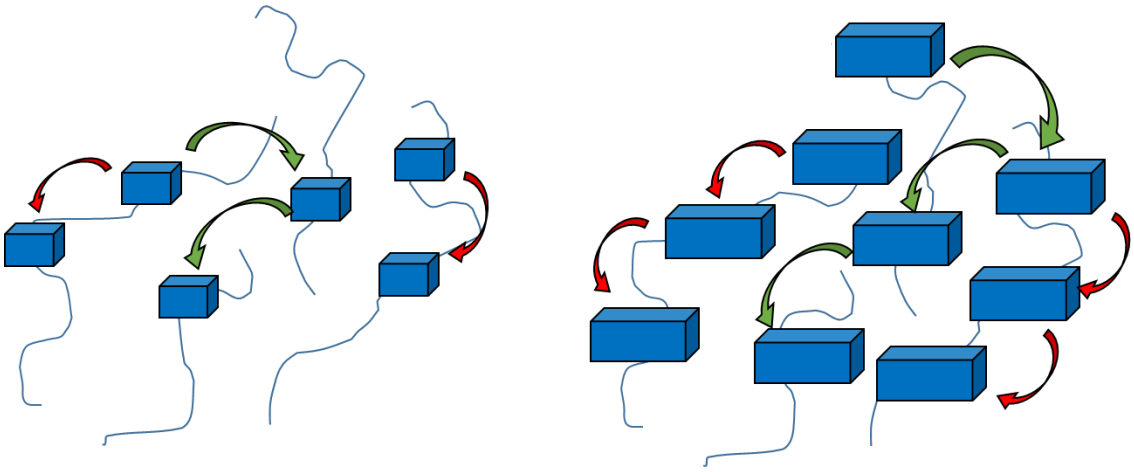

Figure 9: Hopping trnasport in a conducting polymer with low (left) and high (right) degree of crystallinity. Red arrows show the hopping transport intra-chains and green arrows show the hopping transport inter-chains. Blue blocks are crystalline parts and blue lines amorphous part of the conducting polymers.

These conducting formations are called "metallic" island and are dispersed inside the amorphous matrix [28]. The distribution of these metallic islands in amorphous matrix heavily affects the shape of the Density of States. So, the electronic structure and properties of doped polymer materials are highly dependent on the structural properties such as the degree of crystallinity and the chain orientation. When the degree of crystallinity is high, π-orbitals can recombine to extended π-system, and larger "metallic islands" are formed in the amorphous matrix making charge carrier more mobile. Also, a higher conjugation length benefits the intra-chain hopping transport. For the inter-chain, the hopping transport occurs either to level of the chain backbone or out-of-normal to the polymer backbones. This configuration is better for charge transport because π-orbitals are at a closer distance leading to an increased hopping the sites. Finally, in a conductor polymer, when all structural parameters are respected at the intra- and inter-chain level, π-orbitals can recombine into an extended π-system, called a "bipolaron network" (Figure 10) [29].

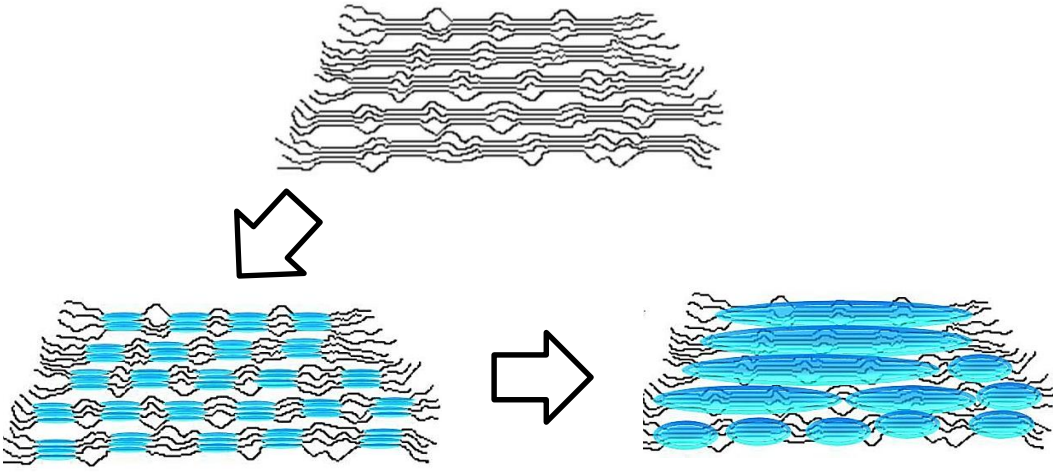

Figure 10: A « bipolaron network ». A semi-crytalline doped polymer (bipolarons as charge carriers) on top. The same polymer represented with the π-orbitals of individual doped conjugated chains in blue (left). Then with increasing the crystallinity of the same polymer, the various π-orbitals overlap with a much wider π-systems, a bipolaron network (on right).

Now, this conformation of a "bipolaron network", is an ideal conformation for thermoelectricity, because its benefits the Seebeck coefficient of the material. Thanks to the Mott's equation (Equation (13)), Seebeck coefficient is analogous to the slope of the DoS at the Fermi Level. In a doped conducting polymer with a "bipolaron network", the band edge is broader due to the extended π-system. Hence, the slope of the DoS at Fermi Level is steeper and the Seebeck coefficient of the material is higher.

Doping levels of the material have to be considered for thermoelectric optimization. Increasing the carrier concentration will add more states to the HOMO, narrowing the band gap, thus the slope of the DoS will be decreased, inducing a lower Seebeck coefficient. So, in order to achieve high thermoelectric performance, proper and detailed material design is needed [27].

In the case of highly conducting systems, like PEDOT, the electrical conductivity follows the thermally activated variable range hopping (VHR) model, proposed by Mott (Equation (15)) [12,28]:

$$\sigma = \sigma_o \cdot e^{-\left(\frac{T_0}{T}\right)^p} \quad (1519)$$

where T_0 is related to the Fermi position of the polymer and the localization length of the polymer charge carriers on the chains. The parameter p can give the type of hopping transport, in fact, it's linked to the dimensionality, d, of the hopping transport ($p = \frac{1}{1+d}$) and can be between 0.5, 0.33 and 0.25 which is related to 1-D, 2-D and 3-D hopping transport. With their semi-crystalline nature, conducting polymers are active 3-D systems. Tough, in higly crystalline materials, the hopping transport occurs either mainly along the π-stacking (thus resembling a 1-D behavior) or both along the π-stack and along the chain backbone (resembling a 2-D system) [28,30–33].

For p=0,5, the model is called Efos-Shlovski and the parameter T_0 of Equation (15) is written as:

$$T_{ES} = \frac{C\ q^2}{\varepsilon_r\ k_B\ \xi} \tag{16}$$

Where ε_r is the dielectric constant, C is a numerical constant and ξ is the charge carrier localization length [31,34,35].

This model successfully described the charge transport behavior of most conducting polymers like PEDOT:PSS [8,32–33].

C PEDOT:Tos formation mechanism

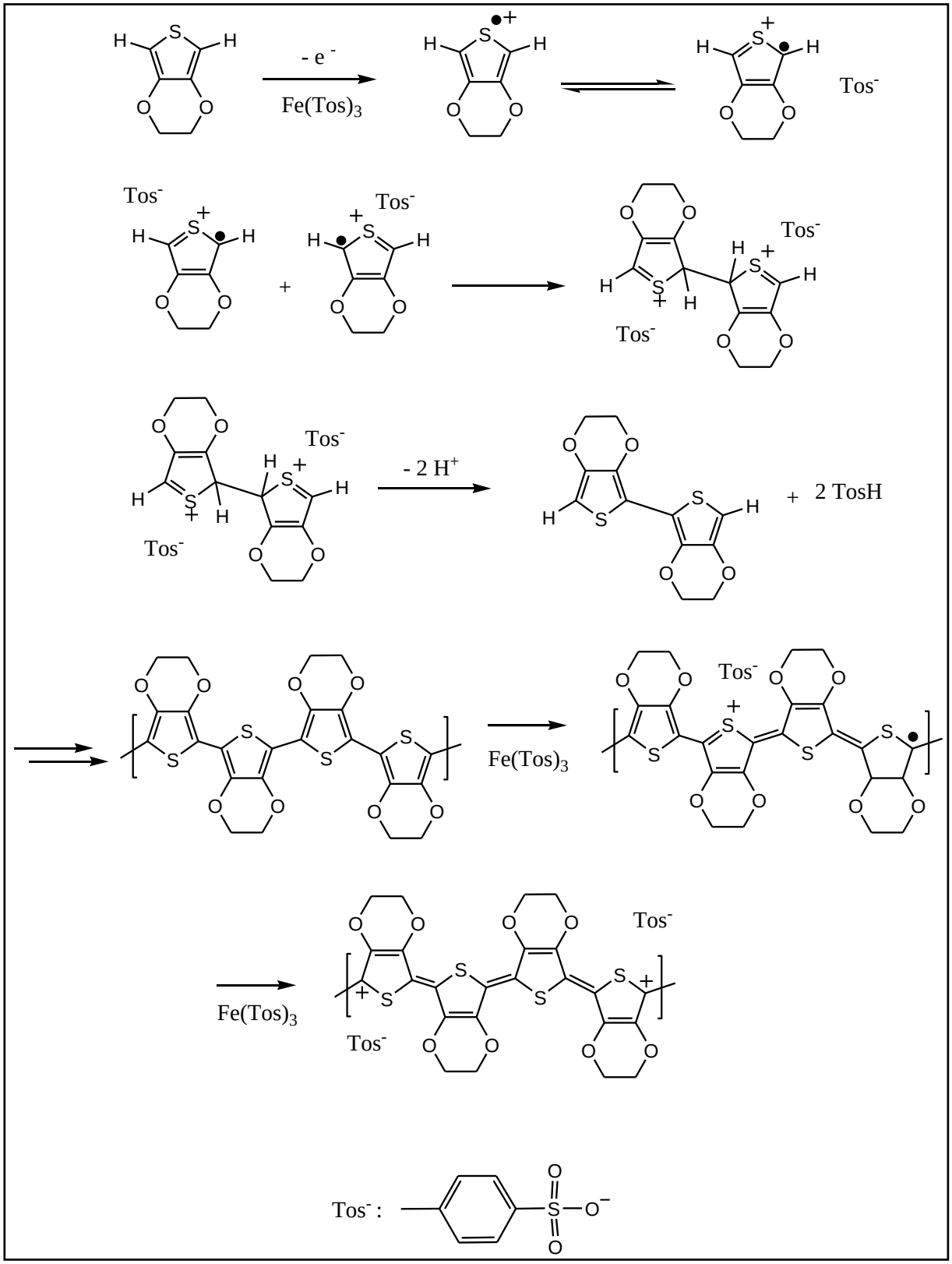

Figure 11: Polymerization mechanism of EDOT in presence of $Fe(Tos)_3$.

References

[1] J. C. A. Peltier, *Nouvelles Experiences sur la Caloricite des Courans Electriques*, Paris, First separate edition, reprinted from Annales de Chimie et de Physique, LVI, **1834**, pp. 371–386.

[2] W. Thomson, *Proc. R. Soc. Edinb.* **1857**, *3*, 91.

[3] Henry Crew, *General Physics: An Elementary Text-book for Colleges*; Third Edition, The Macmillan company, **1916**.

[4] Leon van Dommelen, *A.11 Thermoelectric effects*, FAMU-FSU College of Engineering, view on: http://www.eng.fsu.edu/~dommelen/quantum/style_a/nt_pelt.html (July, **2019**).

[5] R. F. Pierret, *Semiconductor Device Fundamentals*., 2nd Edition, Volume VI, Pearson, **2002** (ISBN 10: 978-0130617927).

[6] P.S. Kireev, *Semiconductor Physics*, Central Book Ltd, **1978**, (ISBN 13:9780714712321).

[7] S. M. Sze and K. NG. Kwok, *Physics of Semiconductor Devices*, 3rd Edition., Wiley, **2006**, (ISBN :978-0-470-06830-4).

[8] R. F. Pierret, *Semiconductor Device Fundamentals*. « 2nd Edition », Addison-Wesley, 1996 (ISBN 10: 978-0201543933).

[9] G. Chen, *Nanoscale Energy Transport and Conversion: A Parallel Treatment of Electrons, Molecules, Phonons, and Photons*; MIT-Pappalardo Series in Mechanical Engineering; Oxford University Press: Oxford, New York, **2005**.

[10] N. Ashcroft, N. D. Mermin, *Solid State Physics*, Brooks/Cole, **1976** (ISBN 10: 0030493463)

[11] M. Geoghegan, G. Hadziioannou, *Polymer Electronics*., Oxford Master Series in Physics, **2013**, (ISBN: 9780199533824)

[12] N. Mott, E. A. Davis, *Electronic Processes in Non-Crystalline Materials*, Oxford Classic Texts in the Physical Sciences, Oxford University Press: Oxford, New York, **2012**.

[13] G. A. Wetzelaer, L. J. Koster, P. W. Blom, *Phys. Rev. Lett*., **2011**, *107*, 066605.

[14] S. Xiao-Hong, S. Jiu-Xun, X. Chun-Hua, *Org. Electron.* **2016**, *35*, 65.

[15] M. Cutler, N. F. Mott, *Phys. Rev.* **1969**, *181*, 1336.

[16] M. Jonson, G. D. Mahan, *Phys. Rev. B* **1980**, *21*, 4223.

[17] S. Ihnatsenka, X. Crispin, I. V. Zozoulenko, *Phys. Rev. B* **2015**, *92*, 035201.

[18] Y. W. Park, A. J. Heeger, M. A. Druy, A. G. MacDiarmid, *The Journal of Chemical Research*, **1985**, *18*, 309-315.

[19] J. L. Brédas, F. Wudl, A. J. Heeger, *Solid State Communications*, **1987**, *63*, 577-580.

[20] R. E. Peierls, R. Peierls, *Surprises in Theoretical Physics*; Princeton University Press, 1979.

[21] A. J. Heeger, *Rev. Mod. Phys.* **2001**, *73*, 681.

[22] C. K. Chiang, C. R. Fincher, Y. W. Park, A. J. Heeger, H. Shirakawa, E. J. Louis, S. C. Gau, A. G. MacDiarmid, *Phys. Rev. Lett.* **1977**, *39*, 1098.

[23] J. L. Brédas, B. Thémans, J. G. Fripiat, J. M. André, R. R. Chance, *Phys. Rev. B* **1984**, *29*, 6761.

[24] V. Coropceanu et al., *Charge Transport in Organic Semiconductors*, **2007**, *107* 926-952.

[25] R. R. Chance, J. L. Brédas, R. Silbey, *Phys. Rev. B* **1984**, *29*, 4491.

[26] J. L. Brédas, G. B. Street, *Accounts of Chemical Research*, **1985**, *18*, 309-315.

[27] O. Bubnova, X. Crispin, *Energy Environ. Sci.* **2012**, *5*, 9345.
[28] A. B. Kaiser, V. Skákalová, *Chem. Soc. Rev.* **2011**, *40*, 3786.
[29] O. Bubnova, Z. U. Khan, H. Wang, S. Braun, D. R. Evans, M. Fabretto, P. Hojati-Talemi, D. Dagnelund, J.-B. Arlin, Y. H. Geerts, S. Desbief, D. W. Breiby, J. W. Andreasen, R. Lazzaroni, W. M. Chen, I. Zozoulenko, M. Fahlman, P. J. Murphy, M. Berggren, X. Crispin, *Nat. Mater.* **2014**, *13*, 190.
[30] A. N. Aleshin, R. Kiebooms, A. J. Heeger, *Synth. Met.* **1999**, *101*, 369.
[31] B. Skinner, T. Chen, B. I. Shklovskii, *Phys. Rev. B*, **2012**, *85*, 205316.
[32] A. J. Kronemeijer, E. H. Huisman, I. Katsouras, P. A. van Hal, T. C. T. Geuns, P. W. M. Blom, S. J. van der Molen, D. M. de Leeuw, *Phys. Rev. Lett.* **2010**, *105*, 156604.
[33] J. J. Brondijk, W. S. C. Roelofs, S. G. J. Mathijssen, A. Shehu, T. Cramer, F. Biscarini, P. W. M. Blom, D. M. de Leeuw, *Phys. Rev. Lett.* **2012**, *109*, 056601.
[34] T. Chen, K. V. Reich, N. J. Kramer, H. Fu, U. R. Kortshagen, B. I. Shklovskii, *Nat. Mater.* **2016**, *15*, 299.
[35] A. L. Efros, B. I. Shklovskii, *J. Phys. C Solid State Phys.* **1975**, *8*, L49.
[36] K. Lee *et al.*, *Nature*, **2006**, *441*, 65-68.
[37] A. N. Aleshin, *Phys. Solid State* **2010**, *52*, 2307.
[38] S. Bhadra, N. K. Singha, D. Khastgir, *Journal of Applied Polymer Sciencei*, **2007**, *104* (3), 1900-1904.

Appendix II:

Material and methods

A Chemical materials

Iron(III) p-toluenesulfonate at 40wt% in 1-butanol (named Clevios CB 40 V2) was purchased from Heraus. PCBM was purchased from Solaris (99+%). F4TCNQ was purchased from TCI chemicals. All others chemical compounds, additives and solvents were purchased from Sigma Aldrich. All chemicals were used as received unless otherwise stated.

PNDIBS were received from Prof. Samson Jenekhe's group (University of Washington).

B Polymer synthesis

1. PEDOT:Tos formulations

- High boiling point solvent formulation:

500 µL of a high boiling point solvent is added to 10 mL of oxidant solution, iron(III) tosylate in 1-butanol (40 wt%). Volume fraction of solvent additive is 5 % v/v with respect to the solution volume. The solution is stirred 12h at room temperature and stored at 4°C.

- Pyridine formulation:

0,5 eq. of pyridine are added to 1 eq. of oxidant solution, iron(III) tosylate in 1-butanol (40 wt%). The solution is stirred 12h at room temperature and stored at 4°C.

High boiling point solvent and pyridine formulation:

300 µL of pyridine is added to 10 mL of oxidant solution, iron(III) tosylate in 1-butanol (40 wt%). Then 300 µL of high boiling point solvent is added to the previous mixture. Volume fraction of each additive is 3 % wt with respect to the solution volume. The solution is stirred 12h at room temperature and stored at 4°C.

- In-situ oxidative polymerization of EDOT:

Polymerization directly takes place during the film process. 9,9 µL of EDOT were added to 300 µL of a previous oxidative formulation (Oxidant/monomer ratio = 2.3 / 1.2 eq.) The mixture was stirred 30 s before processing. On cleaned / treated substrate (see Substrate cleaning / treating procedure), oxidant/EDOT mixture, filtered with 0,45 µm PTFE filter, was spin-coated at 1500 rpm for 30 s with a ramp of 800 rpm/s². The resulted thin films were annealed on a hot plate (100°C) in ambient conditions for 15 min. Afterwards, the film was sequentially washed with two 1-butanol bath and one ethanol bath during 5 min per bath. The role of the bathing

steps is to remove the unreacted and insulating oxidant that remained after the end of the polymerization. Considering that the $Fe(Tos)_3$ used in the synthesis was dissolved in n-butanol, this solvent is chosen as a first bathing step. The second and third bathing steps are added to further remove any remaining oxidant. After the bathing steps, the films are dried with Nitrogen gas flow.

2. P3HT synthesis procedure

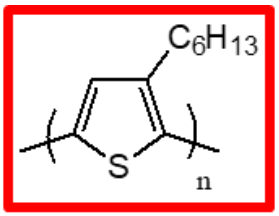

Figure 1: Poly(3-hexylthiophène)

Bulk made P3HT was synthesized according to the literature [1].

2,5-dibromo-3-hexylthiophene (0.5g, 1.5 mmol) [116971-11-0] were dissolved in 15 mL anhydrous THF in a 50 mL three-necked flask. A 2 mol/L solution of t-butylmagnesium chloride (0.75 mL, 1.5 mmol) [677-22-5] in diethyl ether was added via a purged syringe, and the reaction mixture was gently refluxed for 90 min. The reaction mixture was allowed to cool to room temperature, and Ni(dppp)Cl_2 (0.013 g, 0.023 mmol) [15629-92-2] was added to the reaction mixture. The polymerization was left to proceed under stirring for 15 min at room temperature and then quenched with degassed methanol. The reaction mixture was then concentrated by rotary evaporation (0.23 g, 89% yied). GPC: Mn = 20600 g/mol (Mn/Mw = 1.26). 1H NMR (400 MHz, CDCl3, ppm) : 6.98 (s, 1H), 2.80 (t, 2H), 1.69 (t, 2H), 1.43-1.35 (m, 6H), 0.9 (t, 3H).

3. PCDTBT synthesis procedure

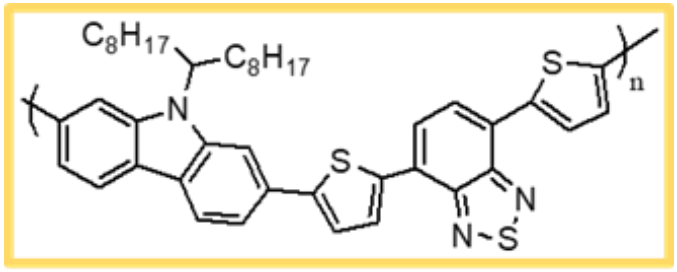

Figure 2: PCDTBT

Bulk made PCDTBT was synthesized according to the literature [2].

2,7-bis(4,4,5,5-tetramethyl-1,3,2-dioxaborolan-2-yl)-N-9-heptadecanyl-carbazole (654.4 mg, 0.966 mmol) [958261-51-3], 4,7-di(2-bromothien-5-yl)-2,1,3-benzothiadiazole (458.8 mg, 1 mmol) [288071-87-4], tris(dibenzylidedeneacetone)dipalladium(0) (4.2 mg, 0.0046 mmol) [51364-51-3] and tri(o-tolyl)phosphine (6.1 mg, 0.020 mmol) [6163-58-2] were dissolved in 3.4 mL (NH4OH)aq and 10 mL toluene in a 25 Schlenk tube. The reaction mixture was stirred at 95°C for 3 hours (temperature ramp of 5°C/5min). Then 110 µL of bromobenzene [108-86-1] were added and reacted for an hour. Finally, 120 mg of phenylboronic acid [98-80-6] in 3mL of toluene were added and reacted for another hour. The resulting mixture was precipitated into a mixture of methanol (100 mL) / water (10 mL). The precipitate was washed by Soxhlet extraction with acetone for one night followed by a day with heptane and then extracted with CHCl3. The CHCl3 portion was concentrated and washed with 500 mL of cold methanol, collected and dried in vacuum. A deep purple powder (2,25g, 90% yield). GPC: Mn = 27649 g/mol (Mn/Mw = 2.19). 1H NMR (400 MHz, CD2Cl2, ppm): 8.3-7.1 (br, 12H, ArH); 4.74 (br, 1H); 2.40 (br, 2H); 2.04 (br, 2H); 1.45-1.23 (br, 8H); 1.23-1.00 (br, 16 H); 0.78 (br, 6H).

4. PTB7 synthesis procedure

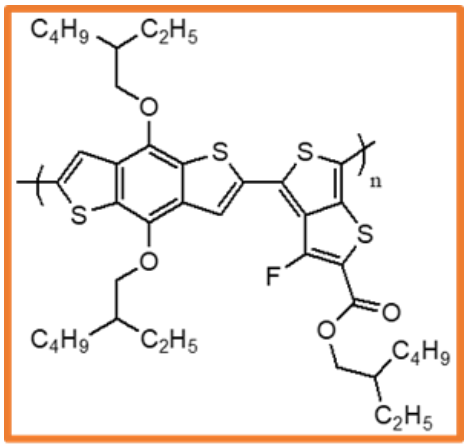

Figure 3: PTB7

Bulk made PTB7 was synthesized according to the literature [3,4].

2,6-Bis(trimethyltin)-4,8-bis(2-ethylhexyl)benzo[1,2-b:3,4-b']dithio-phene (386 mg, 0.50 mmol) [1160823-78-8] and 2-ethylhexyl-4,6-dibromo-3-uorothieno[3,2-c]thiophene-2-carboxlate (236 mg, 0.50 mmol) [1237479-38-7] were dissolved in 8 mL toluene and 4 mL dimethylformamide in a 25 mL Schlenk tube. Tetrakis-(triphenyl-phosphine)palladium(0) (25 mg, 0.05%mol.) [14221-01-3] was added and the reaction mixture was stirred at 120°C for 24 hours. The resulting mixture was poured into methanol (80 mL). The precipitate was washed by Soxhlet extraction with acetone for one day followed by a further day with heptane, and then extracted with CHCl3. The CHCl3 portion was concentrated, a deep blue powder (322 mg, 86% yield). GPC: Mn = 41567 g/mol (Mn/Mw = 2.26). 1H NMR (400 MHz, CDCl2CDCl2, ppm): 7.01-6.64 (br, 2H, ArH); 3.77-3.60 (br, 6H); 1.26-0.36 (br, 45H).

5. Substrates references

5.1 Glass substrates

Two kinds of glass substrates were used. The first one, Microscope slides washed, degreased, with raw edges from RS France (purchased on Fischer scientific) were used for Seebeck coefficient and 2-probes electrical measurement (described below). The other one, Microscope slides of 1,5 cm per 1,5 cm were used for 4-point probe resistivity measurement (described below).

5.2 Silicon substrates

Supplier	Type/dopant	Resistivity (ohm.cm)	Diameter (mm)	Thickness (µm)	Orientation	Surface	Grade
Sil'tronix	P - Boron	20	150	675 +/- 25	<100>	polished	Prime CZ
	N-Phosphorus	20	150	675 +/- 25	<100>	polished	Prime CZ
	P - Boron	1.5	150	675 +/- 25	<100>	polished	Prime CZ
	N-Phosphorus	1.5	150	675 +/- 25	<100>	polished	Prime CZ
	P - Boron	0.05	150	675 +/- 25	<100>	polished	Prime CZ
	N-Phosphorus	0.05	150	675 +/- 25	<100>	polished	Prime CZ
Si-Mat	P - Boron	0.025	100	525 +/- 25	<100>	polished	Prime CZ
	N - Antimony	0.025	100	525 +/- 25	<100>	polished	Prime CZ

Table 1: Commercial characteristics of silicon wafers

C Material processing

1. Substrate cleaning and treatment:

All glasses and silicon substrates were washed in ultrasonic baths of ethanol, isopropanol and acetone for 15 mn per washing step. Then substrates were treated by UV-O_3 for 20 min before film processing.

2. P3HT

2.1 Mixed-solution doping

P3HT solutions (20 mg/mL) and the dopant, F4TCNQ solutions (1 mg/mL) in chlorobenzene were heated to 80°C and left dissolve overnight. The mixed-solutions, P3HT:F4TCNQ, were prepared immediately prepared before spin-coating. F4TCNQ was added at 60°C to give final solutions at 10 mg/mL. 50 nm thin films, were obtained via spin-coating at 2000 rpm during 60s (acceleration speed set at 800 rpm/s²). Films were annealed on a hot plate at ≈80 °C for six hours.

2.2 Sequential doping

P3HT thin films were prepared by spin-coating previous P3HT solution (10 mg/mL, CB) to form 50 nm thin films. Doping was performed via sequential doping process, P3HT film were wetted with F4TCNQ at different concentration in acetonitrile. After 30s, the excess was remove by spin-coating at 1000 rpm. Films were annealed on a hot plate at ≈80 °C for six hours.

3. PCDTBT

PDTBT solutions (50 mg/mL) in chlorobenzene were heated to 80°C and left dissolve overnight. $FeCl_3$/chloroform solutions at different concentration were dropped wise into PCDTBT/chloroform solution to obtain final solution at 10 mg/mL. Solution were stirred at least 10 min, then spin-coated 2000 rpm during 60s (acceleration speed set at 800 rpm/s²) to form approximately 50 nm thin film. Films were annealed on a hot plate at ≈80 °C for six hours.

4. PTB7

PTB7 solutions (10 mg/mL) in 1,2,4-trichlorobenzene (TCB) were heated to 80 °C and left dissolve overnight. For solutions containing 1,8-diiodooctane (DIO), 15 mg of PTB7 were dissolved in a mixture of 970 µL of TCB and 30 µL of DIO, and stirred for at least 12 hours at 80°C. 50 nm thin films, were obtained via spin-coating at 2200 rpm during 60s (acceleration speed set at 1000 rpm/s²). Films were annealed on a hot plate at ≈120 °C for six hours.

5. PCBM

PCBM solutions (40 mg/mL) in chlorobenzene were heated to 80°C, and stirred one day. The mixed-solutions, PCBM:N-DPBI, were prepared immediately prepared before spin-coating. 5wt% of N-DPBI were added to a PCBM solution of 10 mg/mL. Then, various amount of AOB were added to this solution at 80°C. 50 nm thin films, were obtained via spin-coating at 2000 rpm during 60s (acceleration speed set at 800 rpm/s²) in a glovebox. Films were annealed on a hot plate at ≈80 °C for six hours.

6. PNDBIS

PNDBIS and the molecular dopants N-DMBI were dissolved in 1,2-dichlorobenzene (DCB) at a concentration of 10 mg/ml. PNDBIS solutions were heated at 80 °C and stirred for 1 hour. Dopants were used unheated within 12 hours of dissolution. Aliquots of dopant and polymer solution were mixed at room temperature to achieve the dopant concentrations reported. Films were spin cast from solutions described above onto substrates described in the section in a glovebox at 2000 rpm for 60 s. Films were annealed on a hot plate at ≈120 °C for six hours in the glovebox.

7. General comment

During the study of the thermoelectric properties as a function of the thickness of the organic materials, the following protocol was applied to vary the thickness. This protocol was valid for P3HT, PCDTBT, PTB7, PCBM and PNDIBS. Up to 250 nm thick films, the concentration of the deposited solution, as well as the spin-coating speed, were modified to achieve the desired thickness. In the case of thicker films, the method of drop-casting was chosen, the same proportion and concentration were kept.

PEDOT:Tos layer stacking was easier. In fact, the resulting thin film obtained with the previously described protocol is insoluble. So, after the washing step, another PEDOT:Tos

deposition was directly realized on PEDOT:Tos thin films. Each polymer layer adds 50 nm approximately.

D Device architecture

1. Substrate cleaning

All glasses and silicon substrates were washed in ultrasonic baths of ethanol, isopropanol and acetone for 15 mn per washing step.

Then, only on silicon substrate, a supplementary step was required before electrode deposition in order to remove the native oxide (SiO_2). Following the RCA procedure, silicon substrates were putted in different baths:

- Standard Clean (SC-1): 5 parts of deionized water, 1 part of ammonia water (29% wt of NH_3 in water) and 1 part of H2O2 (30% wt in water) at 80°C for 10 min;
- Oxide strip: 1 part of HF (49% wt) in 50 parts of water for 2 min;
- Standard Clean (SC-2): 6 parts of deionized water, 1 part of HCl (37% wt in water) and 1 part of H_2O_2 (30% wt in water) at 80°C for 10 min.
- Oxide strip: 1 part of HF (49% wt) in 50 parts of water for 2 min;
- Rinsing: Deionized water;
- Drying: Nitrogen flux (filtered).

2. Devices for Seebeck coefficient and electrical conductivity measurement:

On clean glass or silicon substrate, 10 nm of chromium and 100 nm of gold were deposited by Physical Vapor Deposition (PVD) thanks to a metal evaporator, Lesker Mini Spectros. The device configuration and dimensions are presented in Figure 4.

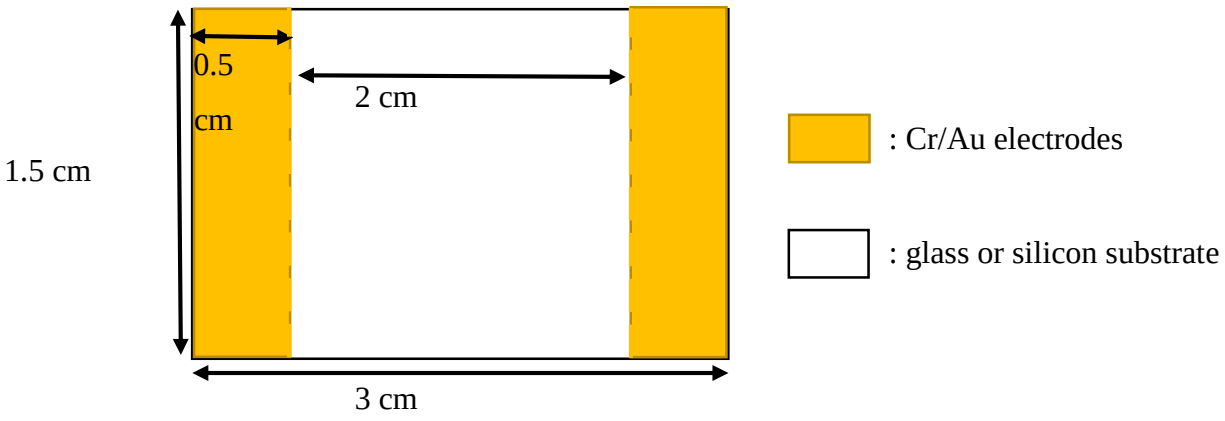

Figure 4: Schematic representation of devices for Seebeck coefficient and electrical conductivity measurement.

Polymer thin films were deposited on top of this device, and half of the polymer film on the electrode was washed out, in order to make it appear. An example with final devices of PEDOT:Tos stacking on silicon is presented below in Figure 5:

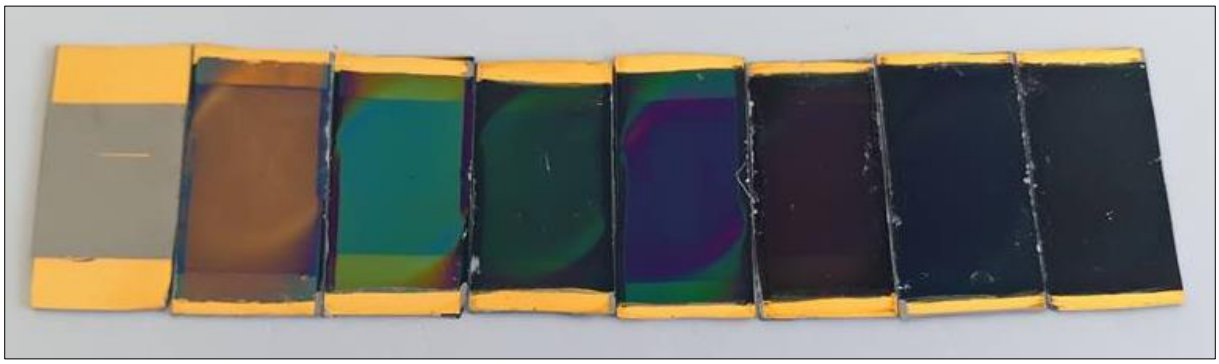

Figure 5: Picture of devices for Seebeck coefficient and electrical conductivity measurement coated with PEDOT:Tos. From left to right are presented bare silicon to 7 layers of PEDOT:Tos.

3. Thermoelectric generator

Thermoelectric converters were fabricated for demonstration of the phenomena reported in this study. Fabrication steps are described in Figure 6. First, similar devices than devices for Seebeck coefficient and electrical conductivity measurement were used for thermoelectric legs (Figure 6a). Various polymer and organic materials were deposited on top of these devices (Figure 6b). The substrate was either glass or doped silicon. The polymer + substrates were then cut with diamond cutter in dimensions 25 mm x 3mm, following dashed lines. As previously, half of the polymer film on the electrode was washed out, in order to make it appear. P-n-p legs junctions were stuck with glue on top of a glass substrate, and the connection between the legs was being made by carbon paste (Figure 6c). Example of TEGs are showed in the main manuscript part about TEGs.

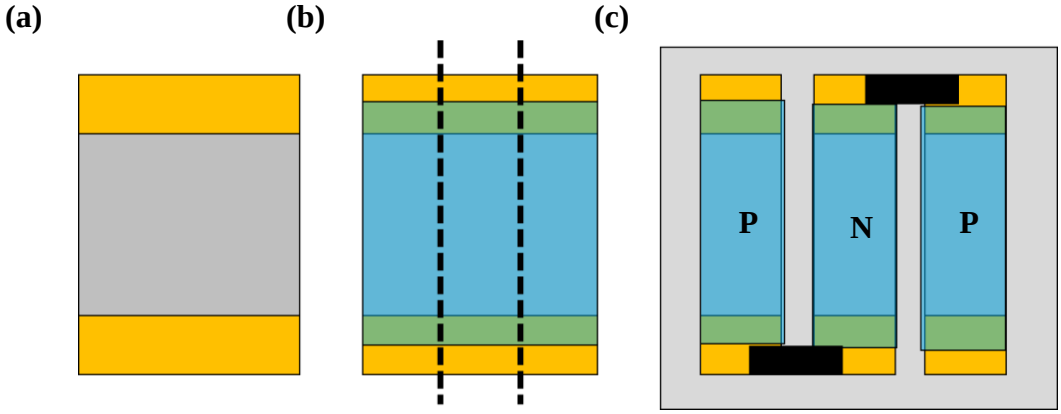

Figure 6: Schematic representation of fabrication steps for three-legs TEG.

In case of flexible TEGs, 100 µm thick flexible PET sheets were used. First, the organic material was deposited, following the previous protocol cited (Material processing section), on a small PET sheet of 25 mm x 30 mm. The organic material on PET was then cut with scissors in dimensions 25 mm x 3mm. Then, p-n-p legs junctions were stuck with glue on top of another larger PET substrate. Finally, the electrodes and connections between the legs was being made by silver paste (Figure 7).

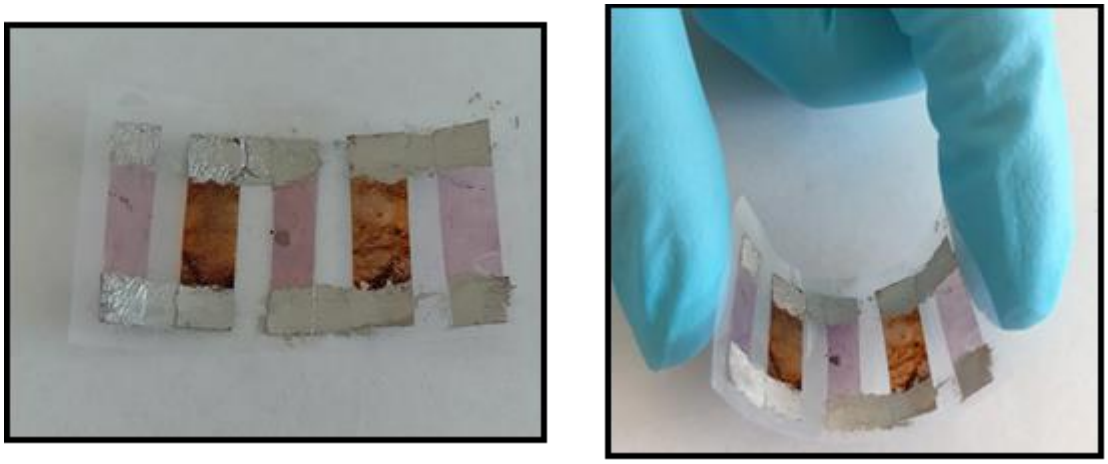

Figure 7: Pictures of p-n-p-n-p 5-legs thermoelectric generator with p-type and n-type legs coated with one layer of PCDTBT and PCBM on PET substrate.
P-type legs are made with PCDTBT and n-type legs are made with PCBM.

E Silicon etching

Silicon substrates used in this study are described in a previous section named Substrates references. All experiments were performed at room temperature unless contraindicated.

Following the RCA procedure, silicon substrates were washed in different baths before each etching process:

- Standard Clean (SC-1): 5 parts of deionized water, 1 part of ammonia water (29% wt of NH_3 in water) and 1 part of H2O2 (30% wt in water) at 80°C for 10 min;
- Oxide strip: 1 part of HF (49% wt) in 50 parts of water for 2 min;
- Standard Clean (SC-2): 6 parts of deionized water, 1 part of HCl (37ù wt in water) and 1 part of H2O2 (30% wt in water) at 80°C for 10 min.
- Oxide strip: 1 part of HF (49% wt) in 50 parts of water for 2 min;
- Rinsing: Deionized water;
- Drying: Nitrogen flux (filtered).

1. Preface

It's important to note that visual evaluation of the reflectivity gives a clue to the good realization of the etching process. In fact, Figure 8 compares bare silicon, silicon pyramids, porous silicon, and silicon nanowires. For nanostructured silicon, the mirror effect is lost, and the substrate turns black for the SiNWs.

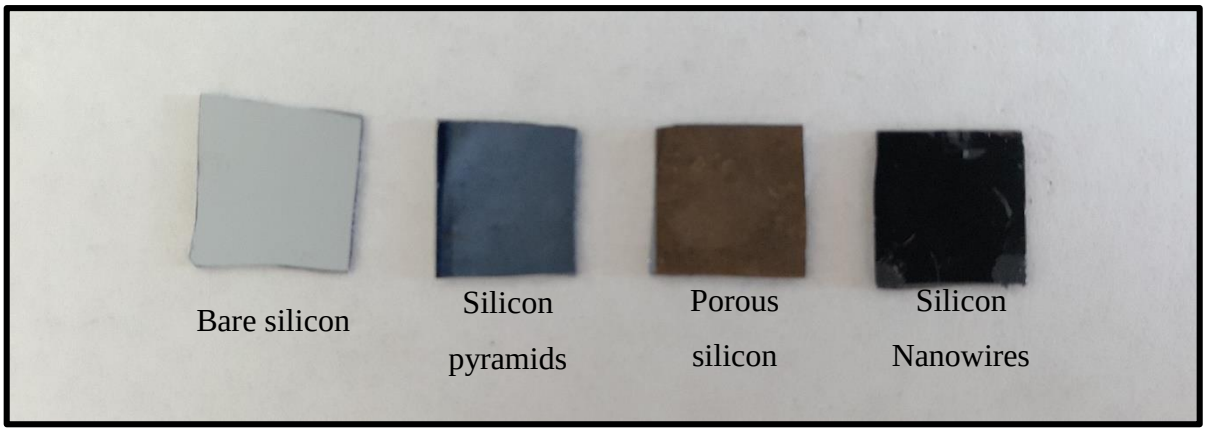

Figure 8: Picture of 1.5 cm x 1.5 cm silicon substrate.
Different etching treatment were applied from left to right, bare silicon, KOH etching, soft MACE and regular MACE.

2. Silicon nanowires

MACE process was applied to silicon substrates and various parameters such as noble metal nature and concentration, etching time and HF/oxidant ratio were studied in order to obtain silicon nanowires for all silicon substrates with different doping concentration. Step by step experiments were carried out. Only one parameter was changed for each study, the others were set to the values shown in Figure 9, thus comparable experiments were done.

In Figure 9, each colour corresponds to a specific bath, and the text writes under it are compounds names mixture, purity or concentration, and the ratio between species, respectively. Time in each bath is written inside the bath schematic. Two routes were followed, the first one with deposition of the noble metal through a wetting process. The other route was the deposition of the noble metal directly on the silicon substrate via Physical Vapour Deposition (PVD).

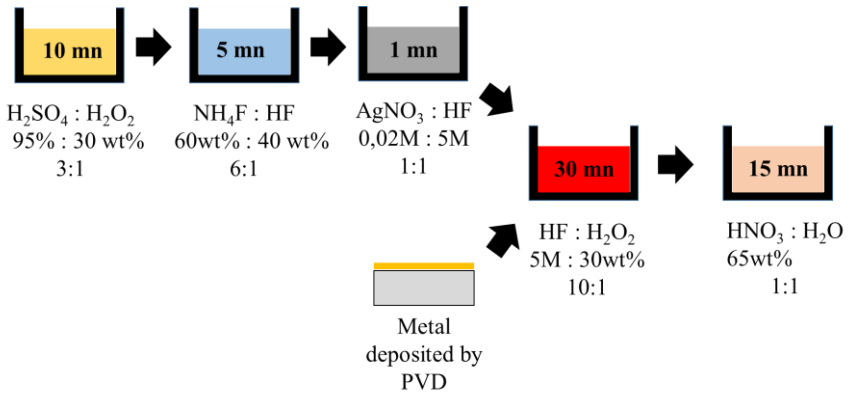

Figure 9: Schematic representation of regular MACE procedure.

Finally, the best procedure in order to obtain regular silicon nanowires are resumed below in Figure 10. Each bath was used only one time, after it was replaced. The last step, unmarked, was treated silicon nanowires with HF to remove the oxide layer. Unfortunately, this last step made the surface hydrophobic. So, in order to successfully deposited the PEDOT:Tos on top of SiNWs, this last step wasn't performed. Furthermore, during the PEDOT:Tos spin-coating, before the spin-cast starting, the solution (monomer with oxidant) was let 30 s on the substrate.

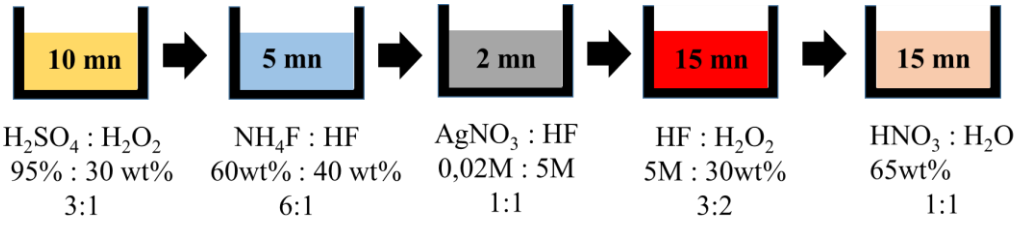

Figure 10: Schematic representation of optimized MACE procedure

3. Porous silicon

MACE process was applied to silicon substrates, and porous silicon was obtained as a side product of silicon nanowires. So the procedure Figure 11 was followed:

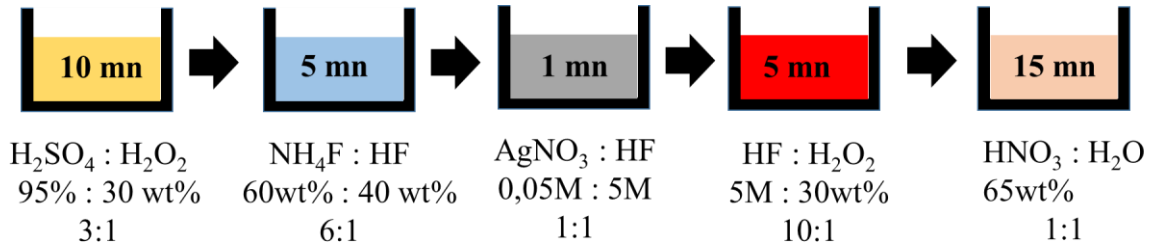

Figure 11: Schematic representation of regular soft MACE procedure

4. Silicon pyramids

KOH etching was applied to silicon substrates, isopropyl alcohol concentration, potassium hydroxide concentration and etching time were studied in order to obtain silicon pyramids for all silicon substrates with different doping concentration. Step by step experiments were carried out. Only one parameter was changed for each study, the others were set to the values shown in Figure 12, thus comparable experiments were done. Etching procedure was carried out in a beaker at 80°C under agitation. A home-made clamp system allowed to put three samples at the same time. The final step was a washing procedure with deionized water.

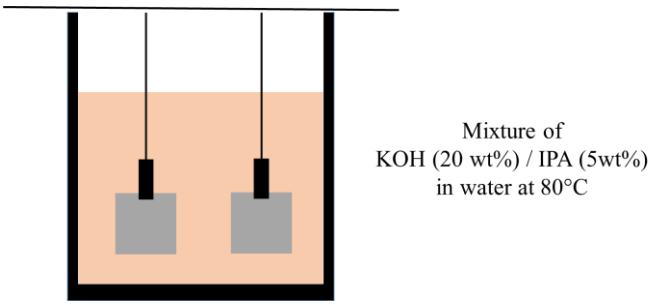

Figure 12: Schematic representation of the set up for KOH/IPA etching process.

5. General comment

Substrates with electrodes have also been etched with the previously described procedures. Except, gold can serve as a catalyst for these processes, and therefore can be degraded by them. Protection was, therefore, necessary, a Kapton tape was used to protect the different electrodes during engraving. No degradation was then noted.

F Methods and characterizations

All polymer deposits were made in clean room [according to standard ISO 14644-1] (atmosphere and temperature controlled) [5]. This clean room is classified ISO 4.

1. Thickness measurement

All film thickness, *t*, were measured with a Dektak XT stylus profilometer (Bruker). This technique is based on a sweep of the sample surface by a fine point with a diameter of 25 microns. The thickness variation is recorded by the position of the tip, the thickness of the sample is determined by measuring a step between the height of the deposited thin film and the substrate. This step can be performed mechanically by scratching with a scalpel.

2. Electrical conductivity measurement

Two different methods were used in order to determine the electrical conductivity, depending on the sample geometry or its application.

In case of bare polymer materials on 1,5 cm x 1,5 cm microscope glass slides, 4-point probe set-up utilizing a Lucas Lab S-302-4 station was used to obtain the film resistance recorded with a Keithley 2450. The name of this measurement technique is the principle of the apparatus which consists of four points (connected to a current source and a voltmeter). The four points are equidistant and aligned. Constant current is injected through two spikes and the fall of potential is measured by the voltmeter. The principle of this measurement technique is illustrated in Figure 13.

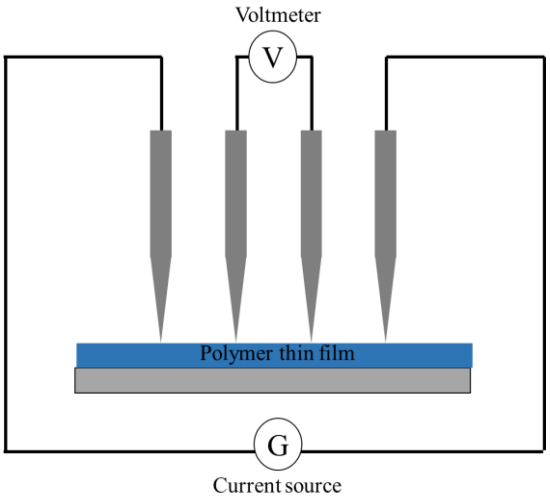

Figure 13: Schematic representation of 4-point probe set up measurement

If the thickness of the thin film, *t*, is negligible to its other dimensions, which is the case of thin layers, then the following expression (Equation 1) of the surface resistance $R_{\square}$ can be used:

$$R_{\square} = K \frac{V}{I} \quad (1)$$

$R_{\square}$ is expressed in Ω/□, I is the injected current (A), V is the measured voltage (V), and K is a geometrical factor depending on probe positioning. In thin film, $K = \pi/\ln(2) = 4.532$ [6]. Electrical conductivity σ is calculated with the following Equation 2:

$$\sigma = \frac{1}{R_{\square} . t} \quad (2)$$

While a different method was used to obtain electrical conductivity of n-type material and hybrid polymer/silicon devices. 2-probe set-up utilizing two gold-coated tungsten probes was used to obtain the film resistance recorded with a Keithley 2450. Thus, by knowing the resistance of the film *R* and its geometry (length *L*, width *w*, and thickness *t*), the electrical conductivity could be determined (Equation 3):

$$\sigma = \frac{1}{R} . \frac{L}{w\, t} \quad (3)$$

Unfortunately, this technique does not neglect the contact resistance generated between the electrodes and the probes [7]. The measured total resistance consists of several components:

$$R_T = 2R_{electrode} + 2R_c + R_{material} \quad (4)$$

where R(electrode) is the resistance due to the contact metal, R_C is associated with the metal/semiconductor interface, and R(material) is the usual resistance. The resistance of a single

contact would be R(electrode) + R_C. However, in most situations, the resistivity of the metal in the contact is so low that R_C >> R(electrode), and so R(electrode) can be ignored.

The material resistance is:

$$R_{material} = R_S \frac{L}{w} \tag{5}$$

$$R_T = \frac{R_S}{w} L' + 2R_c \tag{6}$$

These results suggest a method for measuring the contact resistance. If resistors of several different lengths are constructed (Figure 14), keeping all other details the same, the total resistances of each can measured and plotted.

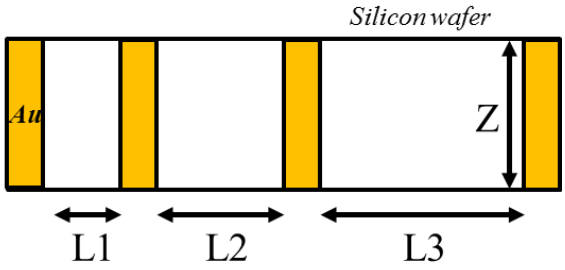

Figure 14: Schematic representation of device build to extract contact resistance

In the limit of a zero-length resistor, the residual resistance would be just twice the contact resistance. $2R_C$ can be found from the graph by extrapolating back to L = 0 (Figure 15).

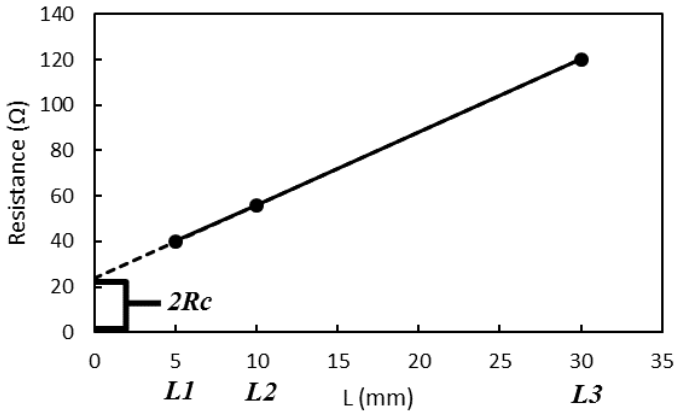

Figure 15: Plot of the resistance as function of the distance between two electrodes.

The following table resumed contact resistances between Cr/Au electrodes and probes of our two experimental measuring equipment (Table 2). The difference between these two contact resistances could be explained by the cable length, almost two times higher in case of our Home-made equipment.

Measuring equipment	**Electrical conductivity (S/cm)**	**Type/dopant**	**Contact resistance (Ω)**
Linkam	0.05	P - Boron	1
	0.05	N- Phosphorus	1
	0.7	P - Boron	1
	0.7	N- Phosphorus	1
	20	P - Boron	1
	20	N- Phosphorus	1
	50	P - Boron	1
	50	N - Antimony	1
Home-made equipment	0.05	P - Boron	5
	0.05	N- Phosphorus	5
	0.7	P - Boron	5
	0.7	N- Phosphorus	5
	20	P - Boron	5
	20	N- Phosphorus	5
	50	P - Boron	5
	50	N - Antimony	5

Table 2: Contact resistance obtained in our set up condition

3. Seebeck coefficient measurement

The Seebeck coefficient was measured in thin film geometry with two different setup depending on the main charge carrier nature of the organic material, holes (p-type) or electrons (n-type).

In case of p-type organic materials, the setup presented in Figure 16 was used (Home-made set up made with Linkam Faraday cage). Two tungsten-pins coated with gold measured the voltage, *V*, via a Keithley 2450, while the temperature, *T*, was controlled by two monitors imposing a voltage to two Peltier plates presented Figure 16c. This is possible to close the setup to minimize all outside disturbances. Substrates were coated with two 100 nm Cr/Au electrodes to ensure proper electrical contact.

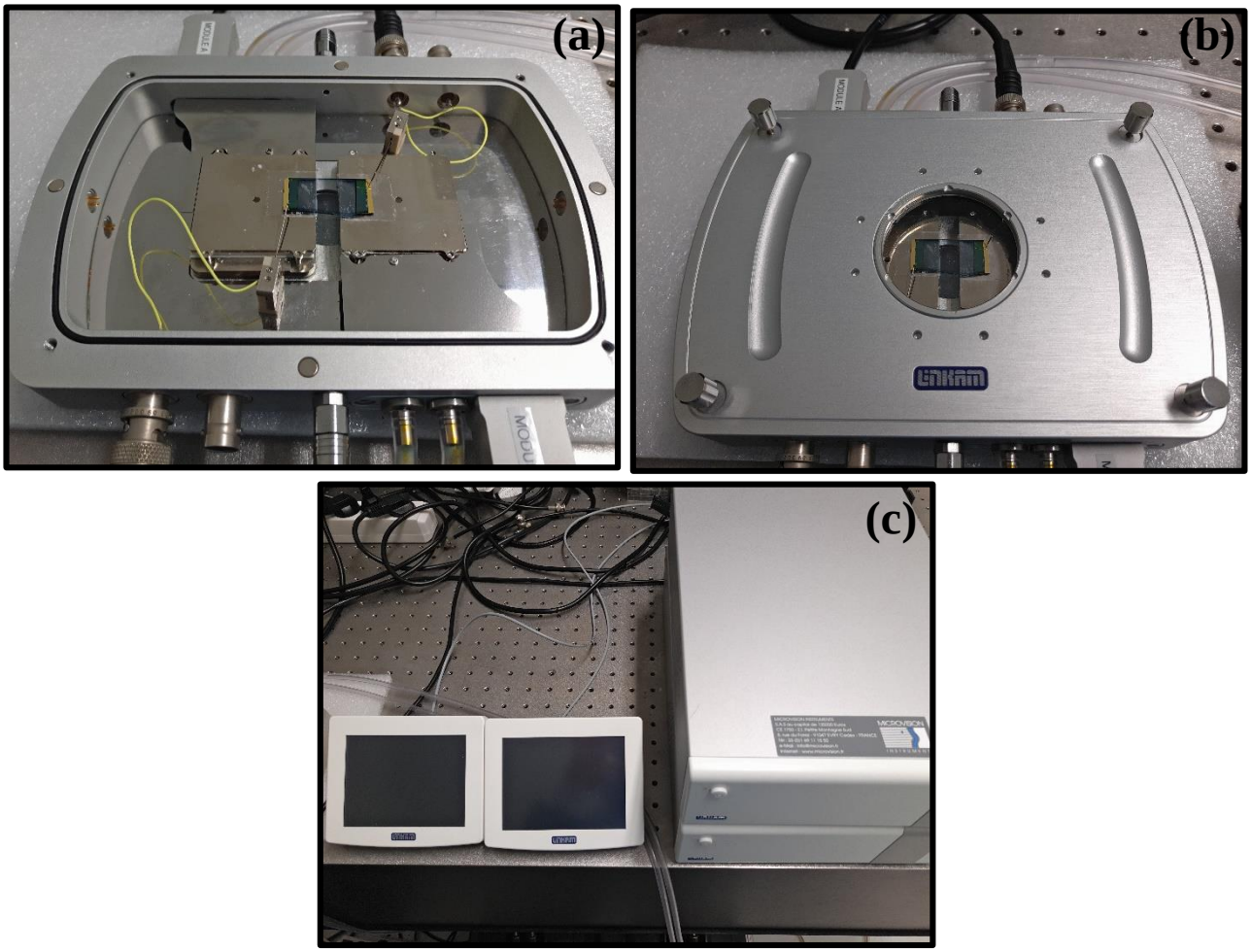

Figure 16: Picture of the home-made set up for Seebeck coefficient measurement of p-type material (air stable material).

In case of n-type organic materials, due to an instability to air and moisture, all Seebeck coefficient measurement were done in a glove box equipped with a homemade setup (Figure 17). The same tungsten-pins coated with gold measuring the voltage, *V*, via a Keithley 2450, were used. The Peltier temperature was controlled by Agilent E3632A DC Power supply and recorded with 2 T-type thermocouples (Omega T-08). Substrates were coated with two 100 nm Cr/Au electrodes to ensure proper electrical contact.

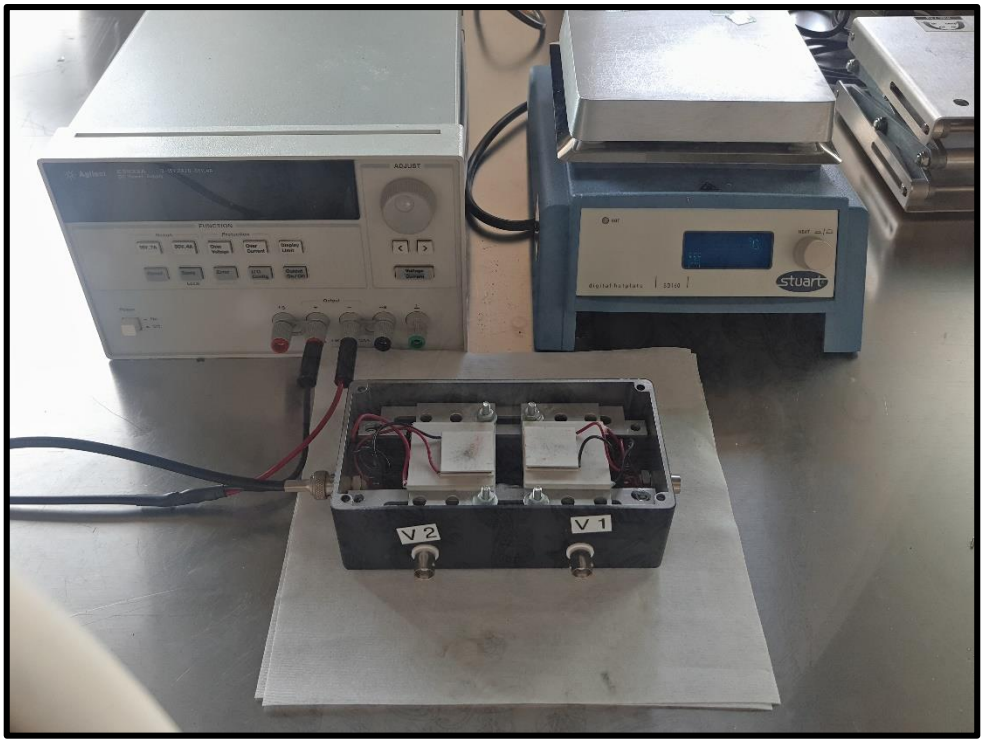

Figure 17: Picture of the home-made set up for Seebeck coefficient measurement of n-type material (air unstable material).

The Seebeck coefficient was experimentally measured as followed, Figure 18 represents an example: PEDOT:Tos film with DMSO on a top-view schematic representation of the previous set-up.

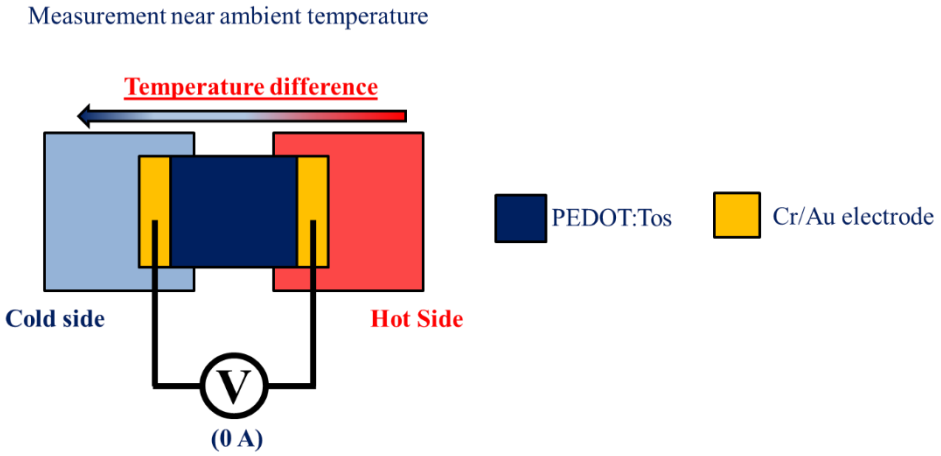

Figure 18: Schematic representation of ongoing Seebeck coefficient measurement.

Measurements were realized at ambient temperature, and the cold side temperature was set at 25°C. Only the temperature of the hot side was increased to create a temperature difference. The voltage (V_{OC}) measured, in the absence of current, is read for each temperature difference. In the following example, PEDOT:Tos with DMSO, V_{OC} was measured from 0 to 4°C of temperature difference, Figure 19a are the data obtained. Then, for each plateau, the average is calculated and plotted as a function of the temperature difference (Figure 19b). Finally, the slope of the curve gives the Seebeck efficient value generally express in µV/K.

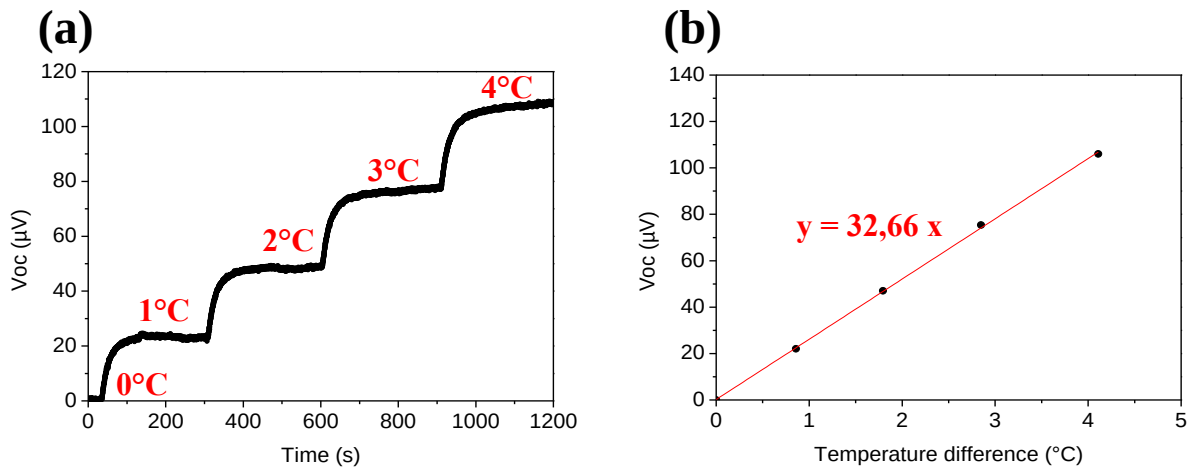

Figure 19: Plot of V_{OC} measured at different difference temperature for PEDOT:Tos with DMSO. Then, V_{OC} plotted as function of temperature difference, the slope corresponds to Seebeck coefficient.

4. Thermoelectric generator Power Output measurement

Measurements in short circuit conditions were conducted using the same two Seebeck measurement setup described above. The Power Output was subsequently calculated as the product between the short circuit current I_{SC} and the thermovoltage V_{OC} [8].

5. Thermal imaging

Thermal images taken to verify the presence of a possible Tomson effect were recorded using a FLIR TG165 infrared thermal imaging camera (Figure 20).

Figure 20: Commercial picture of FLIR TG165 infrared thermal imaging camera

6. Grazing Incidence Wide Angle X-ray Scattering (GIWAXS)

The internal structure of the PEDOT:Tos thin films was probed using Grazing Incidence Wide Angle X-ray Scattering (GIWAXS). GIWAXS measurements were performed on the Dutch-Belgian Beamline (DUBBLE CRG), station BM26B, at the European Synchrotron Radiation Facility (ESRF), Grenoble, France [9]. The energy of the X-rays was 12 keV, the sample-to-detector distance and the angle of incidence, α_i, were set at 11 cm and 0.16°, respectively. The diffracted intensity was recorded by a Frelon CCD camera and was normalized by the incident photon flux and the acquisition time (30 s). Flat field, polarization, solid angle and efficiency corrections were subsequently applied to the 2D GIWAXS images [10]. The scattering vector q was defined with respect to the center of the incident beam and has a magnitude of $q = (4\pi/\lambda)\sin(\theta)$, where 2θ is the scattering angle and λ is the wavelength of the X-ray beam. Herein we opted to present the wedge-shape corrected images where q_r and q_z are the in-plane and near out-of-plane scattering vectors, respectively. The scattering vectors are defined as follows: $q_x = (2\pi/\lambda)(\cos(2\theta_f)\cos(\alpha_f)-\cos(\alpha_i))$, $q_y = (2\pi/\lambda)(\sin(2\theta_f)\cos(\alpha_f))$, $q_z =$

$(2\pi/\lambda)(\sin(\alpha_f)+\sin(\alpha_i))$, $q_t^2 = q_x^2 + q_y^2$, where α_f is the exit angle in the vertical direction and $2\theta_f$ is the in-plane scattering angle, in agreement with standard GIWAXS notation [11].

7. X-ray Photoelectron Spectroscopy (XPS) and Ultraviolet Photoelectron Spectroscopy (UPS)

X-Ray Photoelectrons Spectroscopy (XPS) and Ultraviolet Photoelectrons Spectroscopy (UPS) were performed on the platform ELORPrintTec. Electron spectroscopy measurements were carried out in an ultrahigh vacuum chamber SPECS (10^{-9} mbar). All the samples were stored in gloves box before being analyzed by photoelectron spectroscopy in order to keep the surface in the same state than after deposition.

For UPS, a UHV surface analysis system equipped with a Scienta-200 hemispherical analyzer was used. All measurements were performed using He(I) with a low intensity UV light (21.22 eV).

In case of XPS analysiss, a monochromatized Al Kα X-ray source with an energy of 1486.6 eV allowed to obtain all results.

8. Oxidation level calculation

The oxidation level is relative to the amount of tosylate counter-anion per unit of thiophene unit. So, the ratio of the area for reacted tosylates contribution on the area for all thiophenes unit contribution gives the oxidation level [12].

$$Oxiation\ level = \frac{Area_{reacted\ Tosylate}}{Area_{Thiophene}}$$

(a)

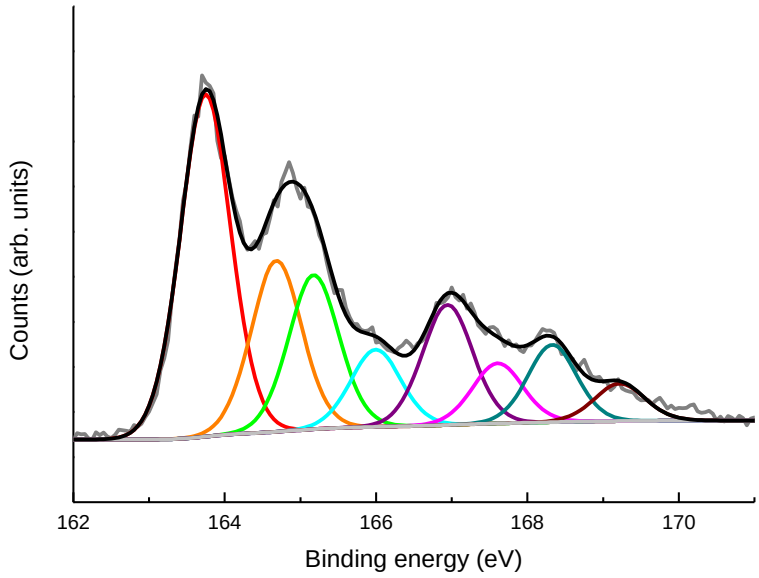

(b)

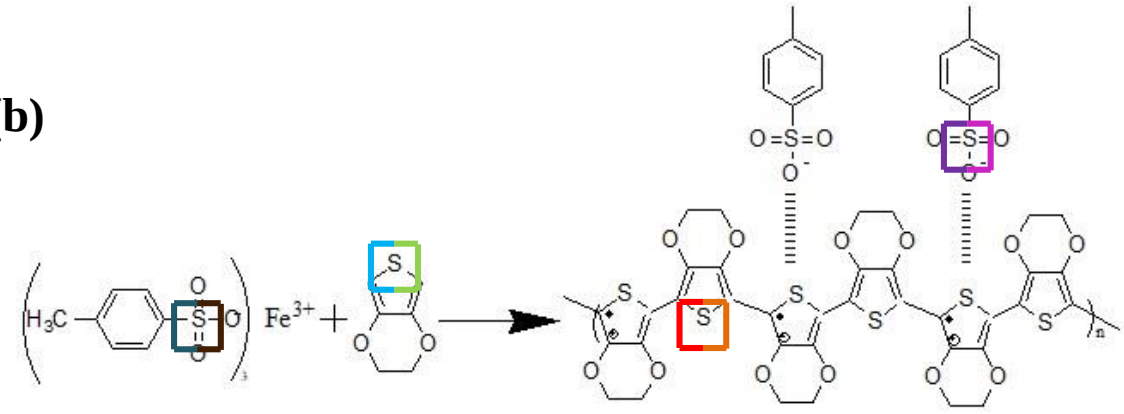

Figure 21: (a) S(2p) XPS spectra for PEDOT:Tos film. (b) Schematic PEDOT:Tos forming reaction from EDOT monomer and Fe(Tos)3. Each color represents a different sulfur: Doublet thiophene unit cation (red and orange), doublet thiophene unit (green and blue), tosylate counterion (purple and rose) and tosylate counterion charged (cyan and brown).

9. Atomic Force Microscopy (AFM)

Atomic force microscopy (AFM Dimension FastScan, Bruker) was used in tapping mode to characterize the surface morphology of the samples. Silicon cantilevers (Fastscan-A) with a typical tip radius of ≈5 nm, a spring constant of 18 $N.m^{-1}$ and a cantilever resonance frequency of about 1.4 MHz were used.

10. Scattering Electron Microscopy (SEM)

SEM images were obtained with a Scanning electron microscope – JEOL 7800 – E prime. LED detector with an acceleration of 2 kV permitted to obtain high resolution images. Analysis were done in ElorPrinTec facilities (University of Bordeaux, Building B8). The infrastructure consists of an 850m² cleanroom which houses 5 equipment clusters. The cleanroom is entirely qualified to ISO 6 conditions and temperature and humidity are strictly controlled. This guarantees optimal and very constant working conditions.

11. Transmission Electron Microscopy (TEM)

TEM images were obtained on Formvar grids with a Transmission Electron Microscope (H7650, HITACHI (accelerate voltage 120 kV)), using high contrast mode. Analysis were done in the Bordeaux Imaging Center (University of Bordeaux, Electronic Unit, Centre Génomique Fonctionnelle Bordeaux).

12. UV-Visible measurement (UV-Vis)

Absorption spectra were measured using a Shimadzu spectrophotometer UV-3600.

13. Nuclear Magnetic Resonance (NMR)

NMR spectra were recorded on a Bruker Avance III 400 spectrometer at 400 MHz for ^{1}H nucleus.

14. Size Exclusion Chromatography (SEC)

Size exclusion chromatography (SEC) was performed in TCB at 150°C with a flow rate of 1 $mL.min^{-1}$ using Agilent PL gel MIXED C column (pore size 5 µm) and an Agilent PL gel guard-column. The elution times were converted into molecular weights using a calibration curve based on low dispersity polystyrene standards.

References

[1] M. Urien, L. Bailly, L. Vignau, E. Cloutet, A. de Cuendias, G. Wantz, H. Cramail, L. Hirsch, J.-P. Parneix, *Polym. Int.* **2008**, *57*, 764.

[2] S. Beaupré, M. Leclerc, *J. Mater. Chem. A* **2013**, *1*, 11097.

[3] L. Lu, T. Zheng, T. Xu, D. Zhao, L. Yu, *Chem. Mater.* **2015**, *27*, 537.

[4] O. Moudam, N. Bristow, S.-W. Chang, M. Horie, J. Kettle, *RSC Adv.* **2015**, *5*, 12397.

[5] **NF EN ISO 14644-1**, Février 2016, view on: https://www.boutique.afnor.org/norme/nf-en-iso-14644-1/salles-propres-et-environnements-maitrises-apparentes-partie-1-classification-de-la-proprete-particulaire-de-l-air/article/783288/fa162637 (July, **2019**).

[6] H. Topsoz (Semiconductor Division), *Geometric factors in four-point resistivity measurement*, 2nd revisited Edition, Bulletin No. 472-13, **1968**.

[7] Gary Tuttle, Dept. of Electrical and Computer Engineering, Iowa State University. *Contact resistance and TLM measurements*.

[8] C. Goupil, W. Seifert, K. Zabrocki, E. Müller, G. J. Snyder, *Entropy* **2011**, *13*, 1481.

[9] W. Bras, I. P. Dolbnya, D. Detollenaere, R. van Tol, M. Malfois, G. N. Greaves, A. J. Ryan, E. Heeley, IUCr,. *J. Appl. Crystallogr.* **2003**, *36*, 791-794.

[10] P. Müller-Buschbaum, *Adv. Mater.* **2014**, *26*, 7692.

[11] G. Renaud, R. Lazzari, F. Leroy, *Surf. Sci. Rep.* **2009**, *64*, 255.

[12] M. Fabretto, K. Zuber, C. Hall, P. Murphy, H. J. Griesser, *J. Mater. Chem.* **2009**, *19*, 7871.

Appendix III:

Silicon nanowires as a filler

A Preface

Recently, improvements on the figure of merit *ZT*, have been achieved in inorganics thermoelectric materials (*e.g.*, superlattices, nano-inclusions, nano-composites, etc.) [1,2], in particular, by phonon scattering to preferentially reduce the thermal conductivity without the loss of power factor, R. [2] and by energy filtering to independently promote the Seebeck coefficient without greatly suppressing electrical conductivity [3]. However, these complex inorganic materials are generally prepared by either the ball-milling, melt-spinning method or molecular beam epitaxy, which involves high-temperature, long-term and high-cost fabrication processes [4].

So, several teams work to develop a facile and l ow-cost fabrication process for inorganic TE materials, including wet-chemical synthesis [5], solution-processable nanocomposites [4], and polymer TE materials [6]. The strategy of introducing inorganic materials interfaces to scatter phonons or filter low-energy carriers seems to also work well in polymer TE materials.

In this work, a rationally engineering of the organic–inorganic semiconductor interfaces of polymer nanocomposites were conducted to improve the Seebeck coefficient and power factor *via* the energy-filtering effect [7]. Herein, an organic–inorganic interface was created by mixing inorganic nanoparticles into a polymer matrix through a solution-processable route. Based on previous results described in this manuscript, PEDOT:Tos treated with DMSO and pyridine was chosen as organics material. This polymer obtained the best thermoelectric performances among tested organic materials. Then, as inorganic nanoparticle material, silicon nanowires were chosen due to their role in the enhancement of TE properties for hybrid polymer/silicon devices. A home-made procedure developed in the laboratory, allowed to recover a suspension of SiNWs in an organic solvent. Finally, a solution-processable fabrication of nanocomposites was also developed.

B Silicon nanowires suspension

First, silicon nanowires were prepared by following the procedure in **Appendix II**. Then, the silicon treated substrate was placed inside a small container, and immerged with 1 mL of ethanol. This container (closed) was placed 1 hour in an ultrasonic bath at room temperature. The highest ultrasounds intensity possible was set. After one hour, the ethanol turns to a trouble brown-grey solution, and the silicon substrate shows some area with the mirror effect of the

bare silicon. By repeating this process, one silicon substrate allows to obtain 0.2 mg of "silicon nanoparticles". In order to confirm the extraction of SiNWs from the substrate, SEM was performed on silicon treated substrate, results are presented in Figure 1.

Figure 1b and 1c represent the side view of SiNWs after one and three cycles inside the ultrasonic bath, respectively. This is clearly visible that some silicon nanowires parts were cut-off their basis.

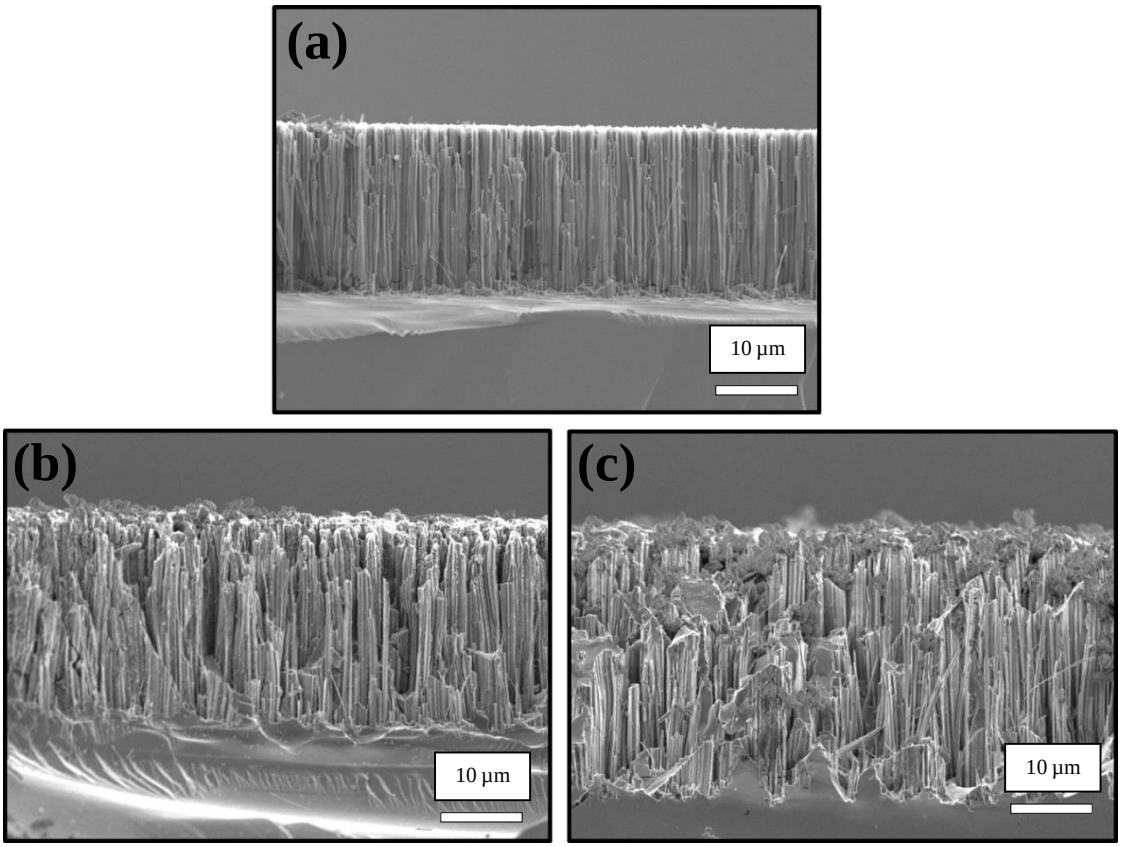

Figure 1: SEM picture of (a) bare silicon nanowires, (b) SiNWs after 1 hour in ultrasonic bath and (c) SiNWs after 3 times 1 hour in ultrasonic bath.

In parallel, the "silicon nanoparticles" in the ethanol solution were analyzed by TEM and AFM (Figure 2). Both techniques confirmed the presence of silicon nanowires. Figure 2a shows particles heterogeneity, they aren't all silicon nanowires and their size differs. Two magnification confirmed this result (Figure 2b and 2c). Finally, the silicon nanowires have been dried under Nitrogen flux.

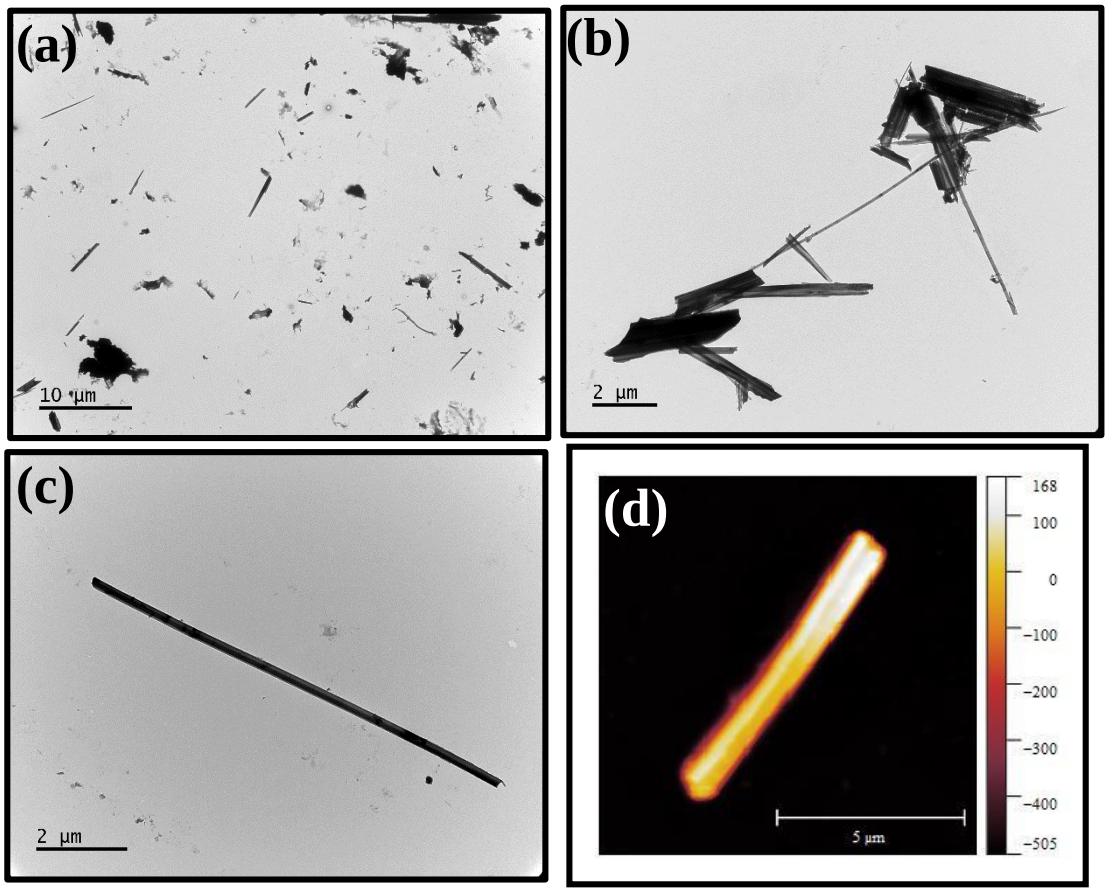

Figure 2: TEM and AFM images of SiNWs after ultrasonic bath.

C PEDOT:Tos/SiNWs film composite

The inorganic/polymer composite thin film were made following the next procedure. Polymerization directly takes place during the film process. The SiNWs were introduced inside the oxidative formulation DMSO + pyridine. Unfortunately, in view of the difficulty to recover high quantities of silicon nanowires, only 0.1 wt% (3 mg) were mixed with this oxidative formulation. So, 9,9 µL of EDOT were added to 300 µL of the oxidative formulation with 0.1 wt% of SiNWs. The mixture was stirred 30 s before processing. On cleaned / treated substrate (see Substrate cleaning / treating procedure), oxidant and SiNWs/EDOT mixture, was spin-coated at 1500 rpm for 30 s with a ramp of 800 rpm/s². The resulted thin films were annealed on a hot plate (100°C) in ambient conditions for 15 min. Afterwards, the film was sequentially washed with two 1-butanol bath and one ethanol bath during 5 min per bath. The resulting thin films was visually rougher.

The effect of silicon nanowires on PEDOT:Tos thermoelectric properties was investigated. Electrical conductivity σ, Seebeck coefficient S and power factor PF are presented Table 1. The small amount of SiNWs (0.1 wt%) have a significate impact on Seebeck coefficient, which increased at 50 µV/K. However, the electrical conductivity decreased almost by a factor of two, 1240 to 814 S/cm. The power factor, $S^2\sigma$, reached a value of 203 µW/m.K² for the film with 0.1 wt% of SiNWs.

Name	S (µV/K)	σ (S/cm)	PF (µW/m.K²)
PEDOT:Tos DMSO+pyridine	44 ± 3	1240 ± 12	240.1
PEDOT:Tos DMSO+pyridine + 0.1 wt% SiNWs	50	814	203

Table 1: Thermoelectric properties of the corresponding PEDOT:Tos films with and without SiNWs as filler

This decreasing electrical conductivity could be due to a morphological change of the semi-crystalline PEDOT:Tos thin film. SEM analysis was performed in order to investigate this phenomenon (Figure 3). No whole nanofiber is visible; only inorganic aggregates are present (pointed by white arrows). The presence of these pieces of fibers may be due to the experimental conditions, for example, agitation prior to deposition. In addition, the film is clearly inhomogeneous, this may explain the drop in electrical conductivity. As has been shown in Chapter 2, the film structure plays a fundamental role in the transport of charges, and hence the electrical conductivity.

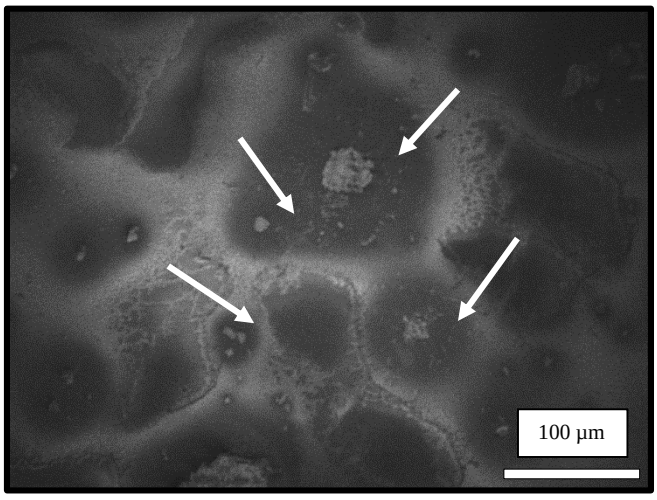

Figure 3: Top view SEM image of PEDOT:Tos with SiNWs.
White arrows point silicon aggregates.

D Conclusion

In this study, SiNWs were recovered using an ultrasonic bath. Subsequently, silicon nanoparticles were embedded in a film of PEDOT: Tos treated with DMSO and pyridine. Despite an increase in the Seebeck coefficient, the power factor of this composite film was lower than the polymer film alone. The reason could be a modification in the morphology of the film (confirmed by SEM). It would be interesting to study this approach in greater depth. For example, by controlling more finely the incorporation of these SiNWs in the film, so as not to harm the crystallinity. Finally, more of these particles should be added to see their effect. A bell-like shape could be obtained, with a maximum greater than the TE performance of the polymer alone, for higher amounts.

References

[1] F. Wu, H. Song, F. Gao, W. Shi, J. Jia, X. Hu, *J. Electron. Mater*. **2013**, *42*, 1140.

[2] R. Venkatasubramanian, E. Siivola, T. Colpitts, B. O'Quinn, *Nature* **2001**, *413*, 597.

[3] K. Koumoto, T. Mori, *Thermoelectric Nanomaterials: Materials Design and Applications; Springer Science & Business Media*, **2013**.

[4] D.-K. Ko, Y. Kang, C. B. Murray, *Nano Lett*. **2011**, *11*, 2841.

[5] J. S. Son, M. K. Choi, M.-K. Han, K. Park, J.-Y. Kim, S. J. Lim, M. Oh, Y. Kuk, C. Park, S.-J. Kim, T. Hyeon, *Nano Lett*. **2012**, *12*, 640.

[6] C. Yu, Y. S. Kim, D. Kim, J. C. Grunlan, *Nano Lett*. **2008**, *8*, 4428.

[7] K. C. See, J. P. Feser, C. E. Chen, A. Majumdar, J. J. Urban, R. A. Segalman, *Nano Lett*. **2010**, *10*, 4664.

Titre : Matériaux polymères/silicium hybrides pour des applications thermoélectriques

Résumé :

De nos jours, l'Homme cherche principalement à gérer les énergies et leurs utilisations dans une perspective de développement durable. Parmi les différentes énergies renouvelables, la thermoélectricité semble être une solution de choix pour la conversion de la chaleur en électricité, améliorant ainsi les rendements thermiques. Les matériaux thermoélectriques pour les applications à température ambiante sont dominés par les matériaux à base de tellurure de bismuth (Bi_2Te_3) qui offrent la meilleure efficacité. Cependant, leur coût et leur toxicité empêchent leur développement à grande échelle. Ces dernières années, bien que possédant des caractéristiques thermoélectriques plus faibles que le Bi_2Te_3, les matériaux polymères ont été envisagés comme une alternative prometteuse. L'objectif de cette thèse était donc de développer des matériaux polymères et hybrides (*i.e.* en combinaison avec des inorganiques) thermoélectriques performants dans le but de réaliser un générateur thermoélectrique (GTE) efficace. Nous avons choisi d'étudier le PEDOT, le P3HT et le PCDTBT comme polymères, et le Silicium comme matériau inorganique. Plusieurs voies d'optimisation ont ainsi été explorées, soit en ajustant le niveau de dopage, soit en adaptant la surface des matériaux inorganiques et leurs interfaces. Des GTEs ont été développés pour des applications proches de la température ambiante. Le couplage entre un matériau polymère et le silicium a notamment permis d'obtenir une amélioration significative des performances et d'atteindre une valeur record par rapport à l'état de l'art du domaine.

Mots clés : Thermoélectricité, Polymère, Silicium, Générateur

---

Title: Hybrid polymer/silicon materials for thermoelectric applications

Abstract:

Nowadays, human beings seek mainly to manage energy and their uses toward sustainable development. Among the various renewable energies, thermoelectricity is the solution for the conversion of heat losses into electricity, and therefore the improvement of thermal efficiency. Thermoelectric materials for room-temperature applications are dominated by bismuth telluride (Bi_2Te_3) based materials offering higher efficiencies. Nevertheless, their cost and toxicity prevent large-scale applications. In recent years, polymer materials have been considered as alternatives for Bi_2Te_3, although their thermoelectric properties are significantly lower. The aim of this thesis was therefore to develop an efficient thermoelectric polymer, in combination with an inorganic material in order to obtain an efficient thermoelectric generator. PEDOT, P3HT and PCDTBT were chosen as p-type polymers and silicon substrates as semi-conducting inorganic materials due to their high importance and performance in their respective fields. Several optimization routes have been investigated, either by fine-tuning the doping level parameters or by tailoring the surface of the inorganic materials. Hybrid thermoelectric generators (TEGs) were developed for near room temperature application. The coupling with polymer material achieved to obtain an enhancement of device performances resulting in record value.

Keywords: Thermoelectricity, Polymers, Silicon, Generator

Laboratoire de Chimie des Polymères Organiques

UMR 5629, 16 Avenue Pey-Berland, Pessac Cedex, F-33607, France.